

The use of layered double hydroxides and mixed oxides for stabilization of metals and metalloids in contaminated soils

Ph.D. Thesis

Thesis supervisor: Prof. Michael Komárek, Ph.D.

Thesis reviewers: Vojtěch Ettler, Ph.D.
Professor
(Charles University in Prague, Czech Republic)

Rémi Marsac, Ph.D.
Associate Professor
(CNRS, Rennes, France)

Daniel C.W. Tsang, Ph.D.
Associate Professor
(Hong Kong Polytechnic University, Hong Kong)

Czech University of Life Sciences Prague
Faculty of Environmental Sciences
Department of Environmental Geosciences

Prague, 2018

The use of layered double hydroxides and mixed oxides for stabilization of metals and metalloids in contaminated soils

Barbora Hudcová

Thesis

This thesis is submitted in fulfillment of the requirements for the Ph.D. degree at the Czech University of Life Sciences Prague, Faculty of Environmental Sciences.

The use of layered double hydroxides and mixed oxides for stabilization of metals and metalloids in contaminated soils

Barbora Hudcová

Czech University of Life Sciences Prague (2018)

Acknowledgement

I would like to thank my supervisor Prof. Michael Komárek for his guidance, support and useful critics during my Ph.D. studies. It was a real privilege for me to perform my research at the Department of Environmental Geosciences under his supervision. I also would like to thank other colleagues at the Environmental and Isotope Geochemistry Group for their useful advices during my research, especially Dr. Martina Vítková, Dr. Zuzana Michálková and Dr. Veronika Veselská. Special thanks come to Dr. Jan Filip and Dr. Milan Erben to participate on my research. I also appreciate Dr. Radek Fajgar, Dr. Petr Drahota, Marie Králová, Neomi Meszarošová, Hana Šnajdaufová, Sylva Číhalová, Ondřej Tomanec and Jiří Tuček for their analytical work. I would like to thank to my parents and my grandmother for their support during my Ph.D. studies. Finally, I would like to thank my boyfriend Jiří Böserle for his love, help and knowledge.

The experimental work included in this Ph.D. thesis was funded by the following research projects:

15-07117S (Czech Science Foundation)

18-24782Y (Czech Science Foundation)

TJ01000015 (Technology Agency of the Czech Republic),

CZ.07.1.02/0.0/0.0/16_040/0000368 (Operational Programme Prague – Growth Pole of the Czech Republic)

CIGA 20154202 (Czech University of Life Sciences)

IGA 4240013123159 (Internal Grant Agency of the Faculty of Environmental Sciences, CULS Prague)

IGA 4240013123119 (Internal Grant Agency of the Faculty of Environmental Sciences, CULS Prague)

Abstract

The main aim of the thesis was to evaluate the (ad)sorption mechanisms of metals and metalloids onto Mg-Fe layered double hydroxides (LDHs) and mixed oxides (CLDHs) using mechanistic/modeling approaches and describe the stability and stabilizing efficiency of these materials in contaminated soils. The (ad)sorption properties of materials were studied by basic (ad)sorption modeling and surface complexation modeling (diffuse layer model). To further differentiate between individual (ad)sorption processes, various solid-state analyses were used, e.g., X-ray diffraction analysis (material/phase identification), electron microscopy analysis (morphology of materials), elemental mapping (distribution of elements on the material surface), infrared spectroscopy and X-ray photoelectron spectroscopy (binding arrangements) and low-temperature ^{57}Fe Mössbauer spectroscopy (other structural changes). In general, the As(V) and Sb(V) (ad)sorption processes onto Mg-Fe LDHs included surface complexation (As, Sb), anion exchange (As, minorly for Sb), the formation of brandholzite-like structures (Sb). In the case of Mg-Fe CLDHs, the predominant effect of surface complexation was observed since the possible metalloid incorporation in the interlayer region *via* the material reconstruction took place only at low metalloid loadings. The (ad)sorption mechanisms of Pb(II) and Zn(II) were influenced by surface complexation, (surface) precipitation (Pb, Zn) and isomorphic substitution (minorly for Zn). In the case of Mg-Fe CLDHs, similar mechanisms were observed; however, the reconstruction ability was significantly limited at higher Pb(II) and Zn(II) loadings. Afterwards, the application of Mg-Fe LDHs and CLDHs to soil solutions and soils with highly elevated As(V), Pb(II) and Zn(II) concentrations was performed. Although Mg-Fe CLDHs were more effective/stable in aqueous solutions, Mg-Fe LDHs showed more promising results after their direct soil incubation. The buffering effect of Mg-Fe LDHs and CLDHs improved metal stabilization. Despite higher pH values, both materials were also highly effective for stabilization of As(V). After soil incubation, Mg silicates and carbonates were formed on the Mg-Fe LDHs and CLDHs surface resulting in lower Mg leaching compared to aqueous solutions (i.e., higher stability of materials). Mg-Fe Additionally, LDH/biochar composites were introduced as promising materials for remediation technologies. The results of the proposed thesis evaluated the (ad)sorption properties as well as applicability of Mg-Fe LDHs and CLDHs for water and soil remediation. Moreover, a suitable approach for testing new stabilizing materials evaluating all important (ad)sorption characteristics as well as stability of materials at different conditions was also presented.

Abstrakt

Hlavním cílem předkládané práce bylo zhodnotit adsorpční mechanismy kovů a metaloidů na podvojně vrstevnaté hydroxidy (LDHs) a směsné oxidy (CLDHs) s využitím mechanisticky/modelových přístupů, a dále popsat stabilitu a stabilizační efektivitu těchto materiálů v kontaminovaných půdách. (Ad)sorpční vlastnosti materiálů byly studovány s využitím základních adsorpčních modelů a modelů povrchové komplexace (model difuzní vrstvy). K odlišení jednotlivých (ad)sorpčních mechanismů byla využita řada analýz pevné fáze např. rentgenová difrakční analýza (identifikace materiálů/fází), elektronová mikroskopická analýza (morfologie materiálů), prvkové mapování (distribuce prvků na povrchu materiálů), infračervená spektroskopie a rentgenová fotoelektronová spektroskopie (vazebné uspořádání) a nízkoteplotní ^{57}Fe Mössbauerova spektroskopie (další strukturální změny). (Ad)sorpční procesy As(V) a Sb(V) na Mg-Fe LDHs byly rozděleny na povrchovou komplexaci (As, Sb), aniontovou výměnu (As, minoritně u Sb) a tvorbu struktur na bázi brandholzitu (Sb). V případě Mg-Fe CLDHs převládala povrchová komplexace, jelikož možný vliv inkorporace metaloidů do mezivrstevnatého prostoru během rekonstrukce materiálů byl patrný pouze při nižších koncentracích metaloidů. (Ad)sorpční mechanismy Pb(II) a Zn(II) byly ovlivněny povrchovou komplexací, (povrchovým) srážením (Zn, Pb) a izomorfní substitucí (minoritně u Zn). Stejně mechanismy byly pozorovány i v případě Mg-Fe CLDHs, avšak při vyšších koncentracích Pb(II) a Zn(II) byla významně omezena schopnost rekonstrukce materiálů. Následně byla provedena aplikace Mg-Fe LDHs and CLDHs do reálných půd se zvýšenými koncentracemi As(V), Pb(II) and Zn(II). Mg-Fe LDHs prokázaly slibnější výsledky po jejich přímé inkubaci v půdách, přestože Mg-Fe CLDHs vykazovaly vyšší efektivitu/stabilitu ve vodných roztocích. Stabilizace kovů byla významně ovlivněna pufracním efektem Mg-Fe LDHs a CLDHs, avšak i přes vyšší hodnotu pH vykazovaly oba materiály rovněž vysokou stabilizační efektivitu pro As(V). Na povrchu Mg-Fe LDHs a CLDHs byly po inkubaci v půdách pozorovány Mg silikáty a karbonáty, které měly za následek nižší uvolňování Mg ve srovnání s vodnými roztoky (tedy vyšší stabilitu materiálů). Dále byly představeny Mg-Fe LDH/biochar kompozity jako slibné materiály pro remediační technologie. Výsledky předkládané dizertační práce umožnily zhodnotit využitelnost (ad)sorpčních vlastností Mg-Fe LDHs a CLDHs a jejich využitelnost pro remediaci vod a půd. Navíc byly v práci prezentovány vhodné přístupy k testování nových stabilizačních činidel umožňující zhodnocení jak všech důležitých (ad)sorpčních vlastností, tak i stability materiálů při různých podmínkách.

Table of contents

Chapter I	General introduction	1
Chapter II	Sorption mechanisms of arsenate on Mg-Fe layered double hydroxides: A combination of adsorption modeling and solid-state analysis	35
Chapter III	Highly effective Zn(II) and Pb(II) removal from aqueous solutions using Mg-Fe layered double hydroxides: Comprehensive adsorption modeling coupled with solid state analyses	63
Chapter IV	Stability and stabilizing efficiency of Mg-Fe layered double hydroxides and mixed oxides in aqueous solutions and soils with elevated As(V), Pb(II) and Zn(II) contents	95
Chapter V	Antimonate (ad)sorption onto Mg-Fe layered double hydroxides in aqueous solutions at different pH values: Investigation of the mechanism supported by surface complexation modeling and solid-state analyses	137
Chapter VI	Biochar and its composites for metal(loid) removal from aqueous solutions	165
Chapter VII	Summary	195
References		213
Curriculum vitae & List of publications		251

Chapter I

General introduction

Content

Background of the study	3
Metals and metalloids in the environment	5
Sources and speciation of metals and metalloids	5
Chemical stabilization of metals and metalloids	7
Surface complexation	8
Ion exchange	10
Surface precipitation	10
Studing of the (ad)sorption mechanisms	12
Adsorption kinetics	12
Adsorption isotherms	15
Surface complexation modeling	18
Solid-state analyses	21
Indirect measurements	23
Layered double hydroxides and mixed oxides	25
Structure of layered double hydroxides and mixed oxides	26
(Ad)sorption of metals and metalloids	28
Factors influencing metal and metalloid (ad)sorption	30
Perspectives in the field of metal and metalloid (ad)sorption	32

Background of the study

The remediation of water and soil contaminated by metals (e.g., zinc and lead) and metalloids (e.g., arsenate, antimonate) is highly actual as metals/metalloids are priority pollutants due to their toxicity, mobility, and non-degradability in ecosystems. However, common methods of water remediation (e.g., coagulation, precipitation, reverse osmosis, or ion exchange) and soil remediation (e.g., soil excavation and dumping, soil washing/flushing, electrokinetics, or vitrification) show a lot of significant disadvantages, such as higher costs and energy demands, and are more disruptive to the natural water/soil environment (Komárek et al., 2013; Kumpiene et al., 2008). Compared to standard methods, chemical stabilization is an appropriate alternative technique offering significant advantages, being a low-cost and simple process with a high metal- and metalloid-immobilization efficiency. The chemical stabilization using solid inorganic materials is a combination of immobilizing process including adsorption (surface complexation and ion exchange) and surface precipitation (Kumpiene et al., 2008). Adsorption, as the predominant stabilizing mechanism, is the adhesion of metals/metalloids to the surface of solid materials and can be further categorized into physical (weaker binding) and chemical (stronger binding) adsorption (Liang et al., 2013). The (ad)sorption process can be evaluated with numerous empirical models, such as adsorption kinetics or isotherms (Limousin et al., 2007, Simonin et al., 2016). Nevertheless, these models cannot differentiate between individual (ad)sorption mechanisms which is crucial in terms of evaluating the immobilization efficiency of metals/metalloids using solid materials. Conversely, mechanistic models, e.g., surface complexation models (SCMs), allow the investigation of the emerging surface complexes. Moreover, the parameters obtained by SCMs (e.g., stability constants of emerging complexes) are less system-dependent and therefore transferable to other systems (Komárek et al., 2018; Koretsky, 2000). Nevertheless, the results of the SCM should be coupled with other measurements and analyses to differentiate between individual (ad)sorption mechanisms, e.g., anion exchange or surface precipitation (Sparks, 2003).

Several materials have been studied for chemical stabilization of metals/metalloids in soil and water, such as Fe/Al oxides and hydroxides (García-Sánchez et al., 2002; Hanauer et al., 2011; Komárek et al., 2013), Mn oxides (McCann et al., 2015; Michálková et al., 2016a, 2016b), biochars (Trakal et al., 2011, 2016), zeolites (Wang and Peng, 2010), or Fe(0) (Kumpiene et al., 2006; Vítková et al., 2017). Nevertheless, individual materials showed some possible disadvantages, e.g., lower stability at acidic conditions or limited efficiency for some metals or metalloids. Therefore, effective

materials that could be used for stabilization of various contaminants at different conditions need to be tested. Layered double hydroxides (LDHs) have been previously suggested as effective sorbents for metals, metalloids and non-metallic compounds in the aqueous solution (Goh et al., 2008; Liang et al., 2013). Moreover, a thermal treatment of LDHs leads to mixed oxides (CLDHs) that have a larger surface area, a higher thermal stability and stronger basic properties (Liang et al., 2013) that could even increase the (ad)sorption capacity compared to pristine LDHs. Nevertheless, most of the studies deal with Al-based LDHs that could be potentially risky for the environment since Al can be leached from LDHs and CLDHs at lower pH values (Jobbágy and Regazzoni, 2011). Therefore, Fe-based LDHs appears as potentially more appropriate materials for remediation technologies. Previously, Fe-based LDHs and CLDHs have shown a high (ad)sorption efficiency for various metals and metalloids in the aqueous solution (Caporale et al. 2011; Carja et al., 2005; Liang et al., 2009; Seida et al., 2001). Nevertheless, studies focused on advanced adsorption modeling, stability of Mg-Fe LDHs and CLDHs at various conditions and/or their application to real water and soil remain scarce.

Metals and metalloids in the environment

Sources and speciation of metals and metalloids

Metals and metalloids occur naturally in the Earth's crust in non-bioavailable forms for the plant uptake. However, natural processes and changes of the soil pH can cause their leaching to ground water and increase their bioavailability as well (Santona et al., 2006). Furthermore, metals and metalloids originating from anthropogenic activities (mining, industrial processes, pesticides or phosphate fertilizers) are usually more mobile and (bio)available (Bolan et al., 2014; Lamb et al., 2009; Singh et al., 2015). The speciation and the mobility of metals and metalloids are influenced by soil reactions (e.g., acid/base, precipitation/dissolution, oxidation/reduction, sorption or ion exchange) that are strongly dependent on the pH/Eh values, temperature, moisture, etc. (Hashim et al., 2011). The speciation and sources of chosen metals and metalloids are given in Table 1.1. The mobility of metals is strongly influenced by the pH values in the environment. In general, the mobility of Zn(II) and Pb(II) increase with decreasing pH values where both metals exist as metal cations. At natural conditions, Pb(II) predominantly forms stable inorganic compounds (chlorides, carbonates, sulphates or phosphates) or organic complexes (humates, fulvates). Soil organic matter (SOM) predominantly immobilizes Pb(II) in soils *via* surface complexation, ion exchange or surface precipitation. Since SOM is dissolved at higher pH values, leaching of Pb(II) could be observed at these conditions (Vítková et al., 2017). Similarly, Zn(II) can be also complexed with various inorganic and organic compounds. Moreover, adsorption, surface precipitation or coprecipitation of Zn(II) by hydrous Fe/Mn oxides also occurs in natural environments (Bolan et al., 2014; Hashim et al., 2011). However, Zn(II) immobilization could be decreased by the presence of Pb(II) resulting in the competition for sorption sites (Cao et al., 2004; Kumpiene et al., 2008). Contrarily, anions, e.g., As(V), can complex with Zn(II) on the surface of solid materials (Gräfe et al., 2004). Arsenic predominantly occurs as As(V) or As(III) at natural conditions. While arsenate is a soft acid forming complexes with sulphides, arsenite is a hard acid that complexes with oxides and/or nitrogen. Although As(V) is the most stable form of As at natural conditions, As(III) can be found in anaerobic conditions, such as in groundwater. Arsenic is extremely mobile at pH > 6.5 under aerobic and anaerobic conditions as well (Mohan and Pitman, 2007; Singh et al., 2015). At natural conditions, As(V) is strongly bound to Fe oxides and hydroxides at acidic conditions; contrarily, As(III) is water soluble and can be adsorbed or co-precipitated with metal sulphides (Hashim et al., 2011). Similarly, Sb can be found as Sb(V) (aerobic conditions) and Sb(III) (anaerobic conditions). Nevertheless, Sb(V) predominates at natural conditions

(Cai et al., 2015). Antimony is immobilized *via* adsorption onto Fe, Al and Mn oxides and hydroxides in soils (Leusz et al., 2006).

Table 1.1 Speciation and sources of Pb, Zn, As and Sb (Bolan et al., 2014; Hashim et al., 2011; Komárek et al., 2013; Singh et al., 2015; Fillela et al., 2002a).

Metal(loid)	Oxidation states and speciation	Natural sources	Anthropogenic sources
Pb	<ul style="list-style-type: none"> • ox.st.: 0, II • higher pH: complexation • lower pH: Pb(II) 	presence in the Earth's crust	mining and smelting, combustion of fossil fuels
Zn	<ul style="list-style-type: none"> • ox.st.: 0, II • pH > 7-7.5: Zn(OH)₂ • pH < 7-7.5: Zn(II) 	essential element	mining and smelting
As	<ul style="list-style-type: none"> • ox.st.: -III, 0, III, V • aerobic c.: As(V)⁻ • anaerobic c.: As(III)⁻ 	As-enriched minerals (pyrite ores)	mining and smelting, industrial processes
Sb	<ul style="list-style-type: none"> • ox.st.: -III, 0, III, V • aerobic c.: Sb(V) • anaerobic c.: Sb(III) 	Sb minerals (sulphides, oxides)	mining, waste incineration, spent ammunition

Chemical stabilization of metals and metalloids

Chemical stabilization reduces the bioavailability, bioaccessibility and the transport of metals and metalloids in soil and water environments (Komárek et al., 2013; Kumpiene et al., 2008). The process of chemical stabilization using solid materials consists of several transport and stabilizing (“sorption”) processes. Individual processes (Fig. 1.1) are divided into: transport of metal and metalloids from the solution to the surface of the solid material (1), transport through the liquid film attached to the surface of the solid material, i.e., film diffusion (2) and interactions of metals or metalloids with the surface, i.e., (ad)sorption (3). In the case of porous materials, metal and metalloids slowly diffuse into the pores (4) by the mean of interparticle diffusion followed by the (ad)sorption processes (Aharoni and Sparks, 1991; Gupta and Bhattacharyya, 2011).

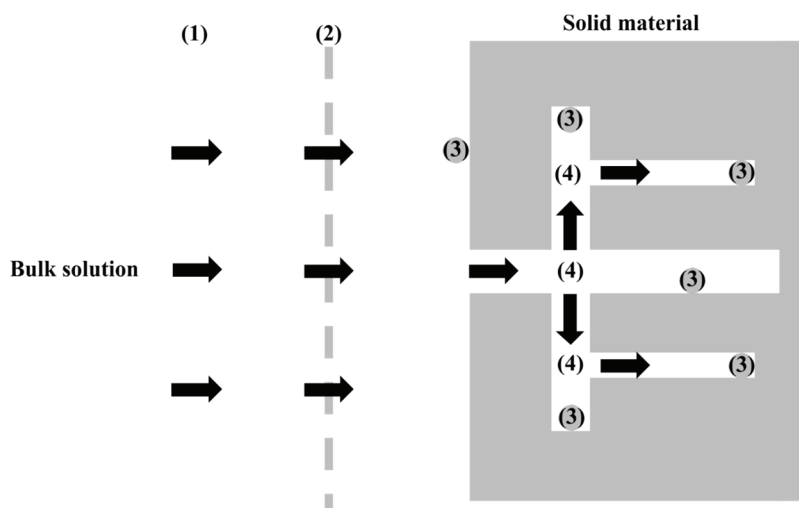


Fig. 1.1. Transport (1, 2, 4) and (ad)sorption processes (3) of metals and metalloids during chemical stabilization using solid materials; adapted according to Aharoni and Sparks (1991).

On the surface of the solid material, metals or metalloids are stabilized by various processes including adsorption that means a two-dimensional accumulation at the surface of solid materials (e.g., surface complexation and ion exchange) and/or surface complexation that means a three-dimensional accumulation (Smith, 1999). Individual processes are influenced by pH, metal/metalloid concentrations, temperature, redox potential and individual properties of solid materials (Komárek et al., 2013; Kumpiene

et al., 2008). The adsorption mechanism can be further divided into physical and chemical adsorption. Differences between these processes are given in Fig. 1.2.

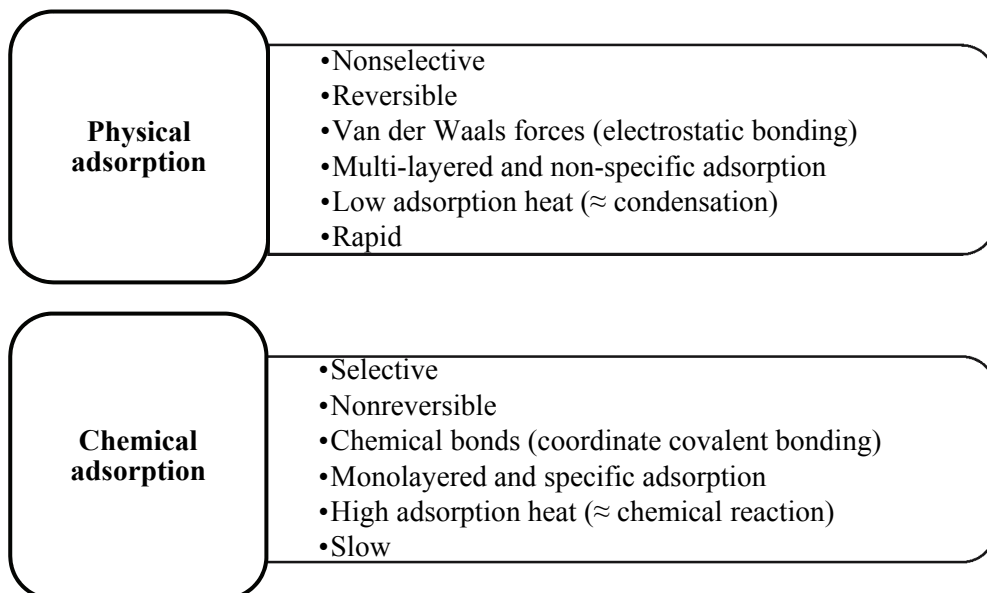


Fig. 1.2. Differences between physical and chemical adsorption (Atkins, de Paula, 2010; Sparks, 2003; Thommes et al., 2015).

Surface complexation

Surface complexation is the interaction between metal or metalloid ions in the solution and the surface functional groups resulting in a formation of stable molecular entity (Sparks et al., 2003). Surface complexes are further divided into outer-sphere complexes (corresponding to physical adsorption) and inner-sphere complexes (corresponding to chemical adsorption). Schematic representation of the most common surface complexes and surface precipitates is shown in Fig. 1.3. In the case of outer-sphere complexes, water molecule is present between the metal or metalloid ion and the surface functional groups. Conversely, no water molecules occur between these groups in inner-sphere complexes.

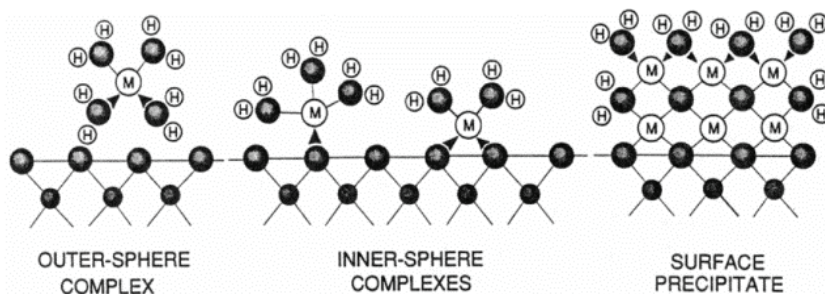


Fig. 1.3. The scheme of outer/inner-sphere complexes and surface precipitates; adapted from Brown (1990).

Inner-sphere complexes can be further divided into monodentate, i.e., binding to one oxygen, and bidentate, i.e., binding to two oxygens (Goldberg et al., 2014; Sparks, 2003; Sposito, 1989). In bidentate inner-sphere complexation, the metal or metalloid ion is bound to one type of the surface functional group, i.e., mononuclear, or to two different surface functional groups, i.e., binuclear (Sparks, 2003). The most common types of inner-sphere surface complexes are shown in Fig. 1.4.

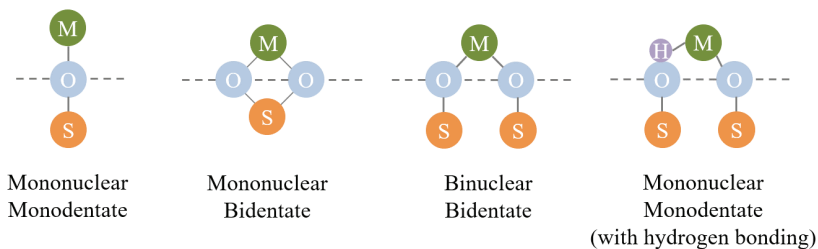


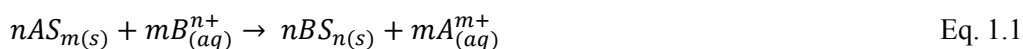
Fig. 1.4. The most common types of inner-sphere surface complexes (M = adsorbed metal or metalloid; O = oxygen; S = crystallographically-bound group on the surface; dashed lines = surface); adapted according to Maurice (2009).

Moreover, surface complexation can be further divided by a polyhedral approach describing the molecular configurations of emerging surface complexes on the surface of solid materials, i.e., a single corner monodentate mononuclear complex (one oxygen is shared with two octahedrons), a double corner bidentate binuclear complex (two nearest oxygens are shared with an octahedron and two other octahedrons), an edge bidentate mononuclear complex (two nearest oxygens are shared with two octahedrons) and face tridentate mononuclear complex (three nearest oxygens are shared with two octahedrons) (Charlet and Manceau, 1992). The formation of outer-sphere complexes is a rapid process occurring on the surface of solid materials that have a different charge compared to the metal or metalloid ion that should be adsorbed. The formation of outer-

sphere complexes is suggested if the adsorption process is dependent on the ionic strength. Nevertheless, the co-presence of both complexes is commonly observed in adsorption studies (Sparks, 2003).

Ion exchange

Ion exchange is a special type of the adsorption process and corresponds to the formation of outer-sphere complexes. Ion exchange means a replacement of exchangeable ion on the surface of the solid material by another ion from the bulk solution. The ion exchange process can be expressed by the following simple reaction:



where A and B represent exchangeable cations (or anions) with valences of m and n (negative for anions) in the solution (aq) or on the surface (S) of individual exchangers $ASm(s)$ and $BSn(s)$ with the surface S (Smith, 1999). The process of ion exchange is relatively rapid, stoichiometric and selective. Since the electroneutrality of the surface needs to be maintained, the charge deficit is balanced by ions with the same charge or by appropriate amounts of ions with lower charges. The selectivity and the rate of ion exchange is influenced by the Coulomb's law, i.e., higher selectivity towards ions with higher polarization. Cations with smaller hydrated radius occurring in the same group and at the same valence state will be preferentially exchanged. In the case of different valence states, ions with higher values will be preferred. In the case of anions, the polarization is higher for larger ones (Sparks, 2003). The maximal amount of the exchangeable ions is called the ion exchange capacity that is divided into the cation exchange capacity (CEC) and the anion exchange capacity (AEC). The CEC and AEC are influenced by the pH values, i.e., the increasing CEC by the increasing pH values caused by deprotonation of surface functional groups and; conversely, increasing AEC by decreasing pH values caused by the protonation of functional groups (Bolan et al., 2014; Sparks, 2003). To identify ion exchange by empirical models (e.g., adsorption isotherms), the concentration of the metal or metalloid ions in the solution needs to be the same order of magnitude or higher than the exchangeable ion (Limousin, 2007).

Surface precipitation

Surface precipitation relates to the sorption process of various metals and metalloids onto solid materials. In general, surface complexation, i.e., the formation of outer/inner-sphere complexes, occurs at a lower surface coverage, whereas surface precipitates are

formed at a higher surface coverage. Surface precipitation is the formation of new phases on the surface of solid materials below the saturation limit of the appropriate phase in the bulk solution (i.e., by the mean of homogenous precipitation). The atomic structure of emerging surface precipitates is similar to the standard precipitates; nevertheless, they are not identical (Smith, 1999). Another type of the surface precipitation is the formation of surface co-precipitates that consist of the metal and/or metalloid ions in the solution and ions released from the material by its partial dissolution. Nevertheless, the ionic radius of these ions needs to be similar and the dissolution of the mineral is the rate limiting step of the process. The type of surface precipitates is dependent on both metal/metalloid ions and the solid material. In general, the surface precipitation begins as a local oversaturation of metal and/or metalloid ions on the surface of the solid material resulting in the formation of micronuclei of precipitates and; subsequently, exponential grown of surface precipitates occurs (McBride, 1994). Based on the thermodynamics, surface precipitation is favoured by: a) a lowering of the nucleation energy by sterically similar sites on the solid surface; b) activity of emerging complexes that is lower than 1; c) a lowering of the solubility of surface precipitates by the lower dielectric constant near the surface compared to the bulk solution (Sparks, 2003). The formation of surface precipitates significantly reduces the metals and/or metalloid content in the solution and; moreover, aging of these surface precipitates leads to the formation of stable phases (Sparks, 2003).

Studying of the (ad)sorption mechanisms

The (ad)sorption process can be described by various models that are further divided into three main categories, i.e., empirical models (e.g., kinetics and isotherms), thermodynamically-based surface speciation models (e.g., surface complexation modeling) and semi-empirical models that means a combination of these two types of modeling approaches for heterogenous natural systems. Nevertheless, the result of these models needs to be coupled with appropriate spectroscopic and microscopic techniques to confirm the results obtained from the modeling and; moreover, to identify other mechanisms, i.e., anion exchange and/or surface precipitation, that can occur simultaneously with the surface complexation (Sparks, 2003). Moreover, other indirect measurements, e.g., point of zero charge or ionic-strength dependency, are also useful to provide more information about the (ad)sorption mechanism (Goldberg et al., 2007).

Adsorption kinetics

Adsorption kinetics enable to determine the rate of the adsorption and the time that is necessary to attain the equilibrium (Gupta and Bhattacharyya, 2011). Adsorption kinetics of metals and metalloids is commonly a biphasic process, i.e., the initial rapid adsorption (outer-sphere complexation) and subsequent slower reaching of the equilibrium (inner-sphere complexation) (Goldberg et al., 2007; Limousin et al., 2007). However, the adsorption process could be also influenced by the diffusion of metals and metalloids as well as by their desorption. Based on the rate-limiting step (the slowest), the adsorption process can be divided into diffusion-controlled process (limited by the diffusion) and adsorption-controlled process (limited by the adsorption) (Gupta and Bhattacharyya, 2011; Simonin, 2016). In general, the kinetic process can be affected by the experimental conditions, e.g., the diffusion-controlled process can be eliminated by the rapid stirring. However, some process cannot be sufficiently solved by this simple solution, since the effect of the diffusion is typical for solid materials with micropores or smaller particles that significantly increases the diffusion effect (Sparks, 2003). In general, the rate of the adsorption process for two reactants can be expressed by a differential equation:

$$\frac{dq_t}{dt} = k \cdot [A]^a \cdot [B]^b \quad \text{Eq. 1.2}$$

where k represents the rate coefficient, a and b mean the order of the reaction according to individual species A (metal or metalloid) and B (solid material). Based on the

literature, adsorption of metals and metalloids onto solid materials is commonly expressed by the pseudo-first order kinetics (PFO) or pseudo-second order kinetics (PSO). The pseudo kinetic order states that the concentration of one reactant is negligible, i.e., the reactant is unchanged during the process or is in the great excess (Gaya, 2014).

The PFO is the earliest kinetic model (Lagergren, 1898). In general, the pseudo-first order kinetics means that the whole adsorption process is reversible and depends only on the concentration of the metal or metalloid. This model has been previously used for the diffusion-controlled processes and/or if the physical adsorption was the predominant mechanism. In general, the PFO provides a reasonable fit only for the initial time stages of the kinetic process (approx. 30 min) since the subsequent slow attending of the equilibrium (denoted to chemical adsorption) cannot be well captured by the PFO. Therefore, the adsorption capacity established by the PFO may not correspond to the real adsorption capacity of the material (Ho and McKay, 1998, 1999). The pseudo-first kinetic order is represented by:

$$\frac{dq_t}{dt} = k_1 \cdot (q_e - q_t) \quad \text{Eq. 1.3}$$

The integrated form of the equation for the boundary conditions $t = 0$ to $t = t$ and $q_t = 0$ to $q_t = q_t$ is represented by:

$$q_t = q_e \cdot (1 - e^{-k_1 \cdot t}) \quad \text{Eq. 1.4}$$

where q_t and q_e (mg g^{-1}) describe the adsorbed amount at time t (min) and at the equilibrium. The constant k_1 (min^{-1}) means the rate coefficient of the pseudo-first order kinetics that depends on the initial concentration of metal or metalloid and decreases with their increasing concentration in the bulk solution (Fabrianto et al., 2008).

Compared to the PFO, the PSO is suitable for processes controlled by chemical adsorption, i.e., the process with the share/exchange of electrons between the solid material and the adsorbed metal or metalloid species (Ho and McKay, 1999). The rate of the kinetic process described by the PSO is dependent on the adsorption capacity of the solid material that should be proportional to the number of active sites on the material surface. However, the capacity is also influenced by the initial metal/metalloid concentration (Ho and McKay, 1998). The pseudo second-order is represented by:

$$\frac{dq_t}{dt} = k_1 \cdot (q_e - q_t)^2 \quad \text{Eq. 1.5}$$

The integrated form of the equation for the boundary conditions $t = 0$ to $t = t$ and $q_t = 0$ to $q_t = q_t$ is represented by:

$$q_t = q_e \cdot \frac{k_2 \cdot q_e \cdot t}{1 + k_2 \cdot q_e \cdot t} \quad \text{Eq. 1.6}$$

where q_t and q_e (mg/g) correspond to the adsorbed amount at time t (min) and at the equilibrium. The constant k_2 [$\text{g} \cdot (\text{mg} \cdot \text{min})^{-1}$] means the rate coefficient of the pseudo-second order kinetics that is also dependent on the initial metal or metalloid concentration as mentioned by the PFO. In general, the rate at which the metals or metalloids are adsorbed onto the surface of the solid material is determined by the value of the kinetic rate coefficient (Gupta and Bhattacharyya, 2011). Faster kinetic processes are represented by higher values of these coefficients (Peng et al., 2014, Sun et al., 2015a).

In general, the PFO has been established as the most suitable kinetic model to describe the rate of metal and metalloid adsorption (Gupta and Bhattacharyya, 2011; Ho, 2006). Nevertheless, the results of various studies focused on the PFO and PSO modeling have been revised by Simonin (2016). In these studies, the experimental data at the equilibrium as well as after attaining the equilibrium were used which systematically favoured the PSO compared to the PFO. Moreover, the linear forms of the PFO and PSO equations have been also widely used which significantly influenced the obtained results and; frequently, favours the PSO fitting, i.e., higher correlation coefficients for the PSO were observed. Finally, it has been mentioned that the overall adsorption mechanism should not be established by the mean of kinetic models since the good fit of the PFO or PSO may not ensure that the individual rate limiting steps controlled the adsorption process (Simonin, 2016).

Other kinetic models, e.g., the Elovich model, intra-particle diffusion model and liquid film diffusion model, have been used to describe the rate of the adsorption process. The Elovich model can be used for the solid materials with energetically heterogeneous surface and for systems that are influenced by the desorption and/or interaction between adsorbed species. The Elovich equation (Low, 1960) is represented by:

$$\frac{dq_t}{dt} = \alpha \cdot e^{-\beta q_t} \quad \text{Eq. 1.7}$$

The integrated form of the equation for the boundary conditions $t = 0$ to $t = t$ and $q_t = 0$ to $q_t = q_t$ is represented by:

$$q_t = \beta \cdot \ln(\alpha \cdot \beta \cdot t) \quad \text{Eq. 1.8}$$

where q_t (mg g^{-1}) correspond to the adsorbed amount at time t (min). The Elovich coefficients α ($\text{g mg}^{-1} \text{min}^{-2}$) and β ($\text{g mg}^{-1} \text{min}^{-1}$) represent the initial adsorption rate and desorption rate, respectively. Nevertheless, this model is suitable only for the data that are far from the equilibrium, i.e., at the initial adsorption stage, since the effect of the desorption is neglected at $t \rightarrow \infty$ (Gupta and Bhattacharyya, 2011). For the porous materials, the intra-particle diffusion model that takes account the transport of metals or metalloids into the porous structure of the adsorbent can be used. The intra-particle diffusion model (Weber and Morris, 1963) is represented by:

$$q_t = k_i \cdot t^{0.5} \quad \text{Eq. 1.9}$$

where q_t (mg g^{-1}) correspond to the adsorbed amount at time t (min) and k_i represents the intra-particle diffusion rate ($\text{mg g}^{-1} \text{min}^{-0.5}$). The straight plot means that the adsorption process is controlled by the intra-particle diffusion; contrarily, a multi-linear plot shows that more mechanisms influenced the adsorption process (Gupta and Bhattacharyya, 2011; Fierro et al., 2008). Besides the intra-particle diffusion, the liquid film diffusion can also influence the adsorption rate. The liquid film diffusion model (Boyd, 1947) is represented by:

$$\ln(-F) = -k_{fd} \cdot t \quad \text{Eq. 1.10}$$

where F (q_t/q_e) corresponds to fractional attainment of equilibrium and k_{fd} (min^{-1}) represents the film diffusion rate coefficient. Nevertheless, the intra-particle diffusion model and the liquid film diffusion model have been used rarely assuming that the adsorption rate is less affected by the transport than the binding of metals or metalloids on the surface (Gupta and Bhattacharyya, 2011).

Adsorption isotherms

Adsorption isotherm is the relationship between the equilibrium concentration of metals or metalloids in the solution and the adsorbed amount at constant temperature (Sparks, 2003). Adsorption equilibrium is the time in which a dynamic balance between metals or metalloid concentration in the solution and the concentration on the surface

of the solid material exists (Foo and Hameed, 2010). Generally, adsorption isotherms are divided into four main types (Fig. 1.5): a line of zero-origin isotherm (C-type), a convex isotherm (L- or H-type) and a sigmoidal isotherm (S-type) (Giles et al., 1974). A C-type isotherm means that the ratio between the equilibrium concentration in the solution and the adsorbed amount on the solid material (denoted as a partition coefficient K_D) remain the same by the increasing initial concentration of metals or metalloids. This isotherm type can be used as an approximation for very low initial concentrations, i.e., before the saturation of adsorption sites that is characteristic by a nonlinear shape of the isotherm. The L-type isotherm means that the ratio between the equilibrium concentration in the solution and the adsorbed amount on the surface of the solid material decreases by the increasing initial concentration of metals or metalloids. This isotherm type can be further divided into the isotherm with a strict asymptotic plateau (i.e., materials with limited adsorption sites at given conditions) and the isotherm without a plateau (i.e., materials with unlimited adsorption sites at given conditions). The H-type isotherm represents a special type of the L-type isotherm with a high initial slope suggesting a high affinity of metals or metalloids for the surface of the solid material. Such shape of the isotherm is often representative of the formation of inner-sphere complexes. The S-type isotherm means energetically different adsorption sites on the surface of the solid material or the influence of different adsorption processes on the removal mechanism (e.g., surface precipitation or ion exchange). In general, the S-type isotherm reaches the plateau at low initial metal or metalloid concentrations; however, the adsorbed amount significantly increases at higher initial concentrations (Limousin et al., 2007; Sparks, 2003).

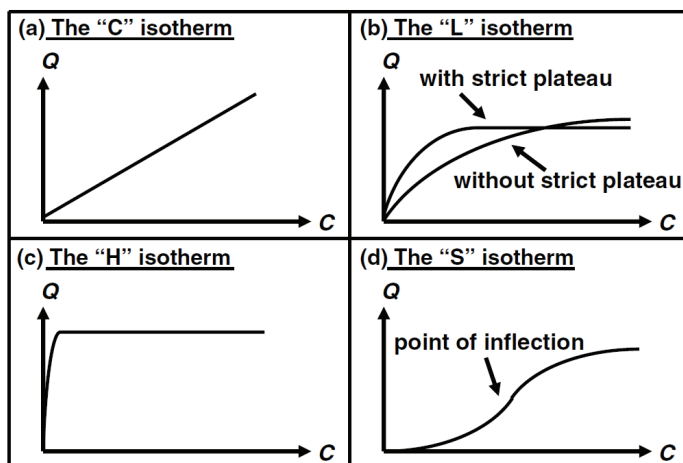


Fig. 1.5. The most common types of adsorption isotherms; adapted from Giles et al. (1974).

Various empirical models have been used to describe the adsorption isotherms. In general, models can be divided into two main categories, i.e., two parameter models (e.g., Langmuir model, Freundlich model, Temkin model, Dubinin-Radushkevich model) and three parameter models (e.g., Brunauer-Emmet-Teller model, Sips model). Among these adsorption isotherms, the Langmuir and Freundlich models are the most widely used empirical models to study metal and metalloid adsorption (Foo and Hameed, 2010; Limousin et al., 2007). However, adsorption isotherms should not be used to describe the adsorption mechanism without molecular investigations (e.g., spectroscopic techniques or identification of emerging solid phases) since adsorption isotherms are not able to sufficiently differentiate between individual (ad)sorption mechanisms (than commonly occur simultaneously) as well as between physical and chemical adsorption (Sparks, 2003). Moreover, these models are applicable only for the given system (i.e., chosen conditions and materials) since the application of the results to other systems leads to significant errors (Goldberg et al., 2007). It needs to be mentioned that many adsorption studies also used linear regression to evaluate the fitting using adsorption isotherm models which lead to the bias of the adsorption data producing different outcomes, altering the error structure and/or violation of the error variance; therefore, the non-linear form of individual adsorption isotherm models should be used (Foo and Hameed, 2010).

The Langmuir model was originally developed to describe gas adsorption onto a planar surface. The Langmuir isotherm assumes with the monolayer adsorption onto a fixed number of energetically equal adsorption sites (i.e., with constant enthalpies and activation energies of adsorption) that possess equal affinity for metals or metalloids in the solution. Moreover, no interactions between adsorbed species occurs. Therefore, this model should not be used for more complex heterogenous systems (Foo and Hameed, 2010; Langmuir, 1918; Sparks, 2003). The Langmuir equation (Langmuir, 1918) is represented by:

$$q_e = q_{MAX} \frac{K_L \cdot c_e}{1 + K_L \cdot c_e} \quad \text{Eq. 1.11}$$

where c_e and q_e correspond to the equilibrium concentration in the solution (mg L^{-1}) and the adsorbed amount at the equilibrium (mg g^{-1}), respectively. Parameters q_{MAX} and K_L mean the maximum adsorption capacity (mg g^{-1}) and the Langmuir constant related to the affinity to the adsorbate (L mg^{-1}) (Foo and Hameed, 2010; Limousin et al., 2007). The Langmuir constant can be further used to calculate a separation factor R_L (Webber and Chakkravorti, 1974) that is represented by:

$$R_L = \frac{1}{1+K_L \cdot c_0} \quad \text{Eq. 1.12}$$

where K_L and c_0 correspond to the Langmuir constant (L mg^{-1}) and initial metal or metalloid concentrations (mg L^{-1}). In general, the basic adsorption mechanism is suggested by the R_L value, i.e., irreversible adsorption ($R_L = 0$), favourable adsorption ($0 < R_L < 1$), linear adsorption ($R_L = 1$) and unfavourable adsorption ($R_L > 1$) (Foo and Hameed, 2010). Among the standard Langmuir isotherm, the modified equation can be used for the system with more than one adsorption site of a given energy. The modified Langmuir isotherm for two adsorption sites is represented by:

$$q_e = q_{MAX,1} \frac{K_{L,1} \cdot c_e}{1+K_{L,1} \cdot c_e} + q_{MAX,2} \frac{K_{L,2} \cdot c_e}{1+K_{L,2} \cdot c_e} \quad \text{Eq. 1.13}$$

where 1 and 2 represent adsorption sites of high and low activation energy. Nevertheless, if the adsorption process is influenced by ion exchange, special multispecies isotherms should be used (Limousin, 2007; Sparks, 2003).

The Freundlich model was the first to describe the non-ideal, reversible and multilayer adsorption onto gas-solid interface. This model assumes a heterogeneous surface with a non-uniform distribution of enthalpies and activation energies of adsorption, i.e., the adsorbed amount is the sum of adsorption onto all sites (stronger binding sites are occupied first). The main disadvantage of this model is a lack of fundamental thermodynamic basis. Nevertheless, it has been widely used in heterogeneous systems including metal and metalloid adsorption (Foo and Hameed, 2010). The Freundlich equation (Freundlich, 1906) is represented by:

$$q_e = K_F \cdot (c_e)^{\frac{1}{n}} \quad \text{Eq. 1.14}$$

where c_e and q_e correspond to the equilibrium concentration in the solution (mg L^{-1}) and the adsorbed amount at equilibrium (mg g^{-1}), respectively. Parameters K_F and n are the Freundlich constant [$(\text{mg g}^{-1}) (\text{L mg}^{-1})^{1/n}$] and the dimensionless constant describing the adsorption process. Values of n are commonly in the range from 1 to 10 that means favourable adsorption (Foo and Hameed, 2010; Sparks, 2003).

Surface complexation modeling

Surface complexation models (SCMs) provide a molecular description of metal and metalloid adsorption reactions onto solid materials using an equilibrium approach. The

SCMs are based on thermodynamics and define the emerging surface species, equilibrium constants, chemical reactions and mass/charge balances as a function of the pH value, ionic strength and solute concentration. Compared to empirical models (e.g., adsorption isotherms), the SCMs are applicable over variable experimental conditions and; therefore, provide a more mechanistic approach to study the adsorption process (Goldberg et al., 2007; Hayes et al., 1991). The SCMs are based on the electric double-layer theory that describes the ion distribution near the charged surface of the solid material. The Gouy-Chapman model (Gouy, 1910; Chapman, 1913) assumes the existence of a diffuse cloud in which cations and anions exist and that is located near the charged surface of the solid material. The opposite ions are concentrated near the surface and exponentially decreases with the distance until the equal number of ions with the same and opposite charges are observed. Moreover, only electrostatic interaction with the surface exists. The charge on the surface of the solid material is compensated with the ions of the opposite charge and; therefore, the electrically neutral system exists. The diffuse layer parameters (e.g., surface charge, surface potential and the thickness of the layer) depend on the type of the solid material. However, real systems show much more interactions between individual ions and the surface than is assumed by this simple model (Sparks, 2003). The Stern model is a modification of the Gouy-Chapman model (Stern, 1924). The Stern model assumes that a Stern layer between the charged surface and the diffuse layer exists and; moreover, inner-sphere complexes are formed in this layer. The charge at the surface is compensated by the charge of ions in the solution that are distributed between the Stern layer and the diffuse layer. Nevertheless, surface complexation models have been developed to sufficiently describe the ion adsorption onto more complex surfaces (Goldberg, 1992; Sparks, 2003).

The most widely used 2-pK SCMs are the constant capacitance model (CCM; Stumm et al., 1980), the diffuse layer model (DLM; Dzombak and Morel, 1990) and triple layer model (TLM; Davis et al., 1978). The surface charge is a result of protonation/dissociation reactions and surface complexation reactions on the surface hydroxyl groups (Goldberg, 1992). The scheme of the solid-liquid interface described by these models is given in Fig 1.6. In general, the CCM and the DLM describe the formation of inner-sphere complexes located in a single surface o-plane. Moreover, the diffuse layer in the DLM includes the ions attracted to the charged surface but remaining in the bulk fluid phase. Finally, the TLM describes the formation of inner-sphere surface complexes (the o-plane) and outer-sphere surface complexes (the β -plane between the surface plane and the diffuse layer) (Goldberg et al., 2007).

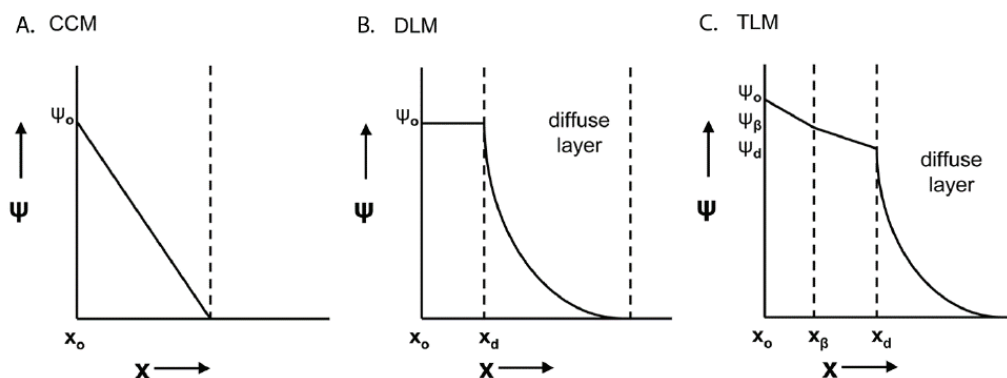


Fig. 1.6. The scheme of the solid-liquid interface described by the CCM, the DLM, the TLM (ψ is to the surface potential (V) and x is the surface charge density ($C\ m^{-2}$) in the individual planes, respectively); adapted from Goldberg et al. (2007).

Individual SCMs contain adjustable parameters that can be experimentally determined for the studied solid material (Table 1.2). The surface protolysis constants (K^+ and K^-), the total number of surface sites (N_t) and the electrolyte surface-binding constants (K_{AN} and K_{CAT}) are commonly determined by acid-base titrations. The values of the capacitance C_1 (inner-layer capacitance) and C_2 (outer-layer capacitance) can be obtained by the linear extrapolation of the potentiometric titration. To eliminate possible variability and uncertainty, the value of C_1 is commonly optimized to fit experimental titration data and the value of C_2 is fixed as $0.2\ F\ m^{-2}$ (Goldberg, 2014; Hayes et al., 1991). In general, the TLM shows better fitting of the titration data over the wide range of ionic strengths and at the constant ionic strength as well. Contrarily, the CCM is limited to the high and constant ionic strength. Finally, the DLM shows a worse fit of the titration data, but the simplicity of this model makes it more attractive than the CCM and TLM (Hayes et al., 1991; Komárek et al., 2015; Komárek et al., 2018).

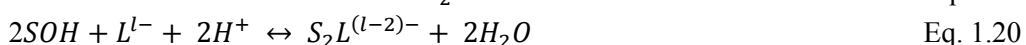
Table 1.2 Parameters of the CCM, the DLM and the TLM model (Hayes et al., 1991).

Parameters		CCM	DLM	TLM
The surface protolysis constants	K^+, K^-	√	√	√
The total number of surface sites	N_t	√	√	√
The capacitance parameter	C_1	√		√
The capacitance parameter	C_2			√
Electrolyte surface-binding constants	K_{AN}, K_{CAT}			√

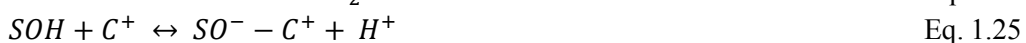
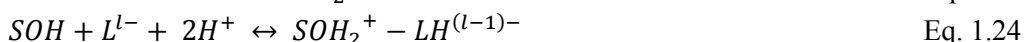
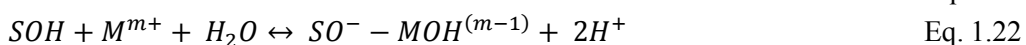
The surface of the solid material described by the 2-pK SCMs follows several chemical reactions. The surface functional groups (SOH; S represents the mineral surface and OH the reactive hydroxyl group) could be protonated or deprotonated as expressed by chemical reactions:



where SOH_2^+ and SO^- are protonated and deprotonated surface groups, respectively. The formation of inner-sphere complexes for the CCM, DLM and TLM is expressed by chemical reactions:



where M and L mean the cation of charge $m+$ and anionic ligand of charge $l-$, respectively. Moreover, surface complexes can be monodentate (S) and/or bidentate ($2S$). The formation of outer-sphere complexes for the TLM can be expressed by chemical reactions:



where C^+ and A^- is the cation and anion of the background electrolyte, respectively. (Goldberg, 1992; Goldberg, 2007). Moreover, the charge balance and mass balance for the surface functional group SOH, i.e., the sum of all surface species for the specific site type, in the SCM should be considered (Goldberg, 2007).

Solid-state analyses

Various solid-state analyses can be used to evaluate the (ad)sorption mechanisms of metals and metalloids onto solid materials as well as possible metal/metalloid

precipitation (Sparks, 2003). Moreover, the individual surface complexes established by the SCMs could be differentiated by appropriate spectroscopic techniques. The most commonly used methods are: X-ray absorption spectroscopy (XAS), Fourier-transform infrared spectroscopy (FTIR) and X-ray photoelectron spectroscopy (XPS). The X-ray absorption spectroscopy (XAS) provides structural details (geometry) of emerging surface complexes. The technique is further divided into X-ray absorption near edge structure (XANES) and extended X-ray absorption fine structure (EXAFS). The XANES describes the oxidation state of the adsorbed species and the coordination number and; therefore, provides the information about the local environment. Contrarily, the EXAFS gives more quantitative information since the average distance and the number/identity of atom in the first coordination shells around the atom are obtained. The EXAFS thus shows the type of emerging complexes and possible surface precipitates (Goldberg, 2007; Koretsky, 2000). Fourier transform infrared spectroscopy (FTIR) can provide information about interactions on the surface of solid materials, i.e., differentiate between inner- and outer-sphere complexes (Goldberg, 2007). In general, FTIR enables to identify the presence of characteristic functional groups in the structure of solid materials. A vibrational spectrum that is formed by a set of absorption or scattering peaks as a function of the energy is recorded. The vibrational spectrum is dependent on the interatomic forces in the molecule or crystal. Therefore, positions, symmetries, relative intensities and any changes of the observed peaks in the spectrum provide useful information about the structure of the material (Kloprogge and Frost, 2010). X-ray photoelectron spectroscopy (XPS) uses monoenergetic soft X-rays to describe interactions with atom near the surface of solid materials using the photoelectric effect, i.e., photoemission of core and valence electrons. Each atomic specie has its specific binding energy and; therefore, the comparison with known values can be provided and the surface ion composition can be identified (Gier and Johns, 2000). Based on the position of the peaks and their shifts, the presence of the bonds between the metals or metalloids and the specific surface sites can be provided and; additionally, the adsorption mechanism, i.e., formation of outer- and inner-complexes, can be evaluated (Komárek et al., 2015; Lu et al., 2015; Trakal et al., 2014a; Vithanage et al., 2013).

Surface precipitation is a common sorption process that can occur together with the surface complexation and; therefore, suitable methods for its identification are needed. Surface precipitates can be identified by spectroscopic techniques (mentioned above), X-ray powder diffraction (XRD) and/or microscopic analyses, i.e., scanning electron microscope/transmission electron microscope (SEM/TEM). Powder X-ray diffraction (XRD) is the major method for the structural characterization of different solid

materials. To identify the structure of the solid material as well as surface precipitates, the position of the peaks in the diffractogram and their intensity, shape and breadth as well as changes of the cell parameters are studied. Nevertheless, the intensity of peaks is directly proportional to the concentration of the studied solid phase (Klug and Alexander, 1954). Moreover, the intensity is also influenced by the nature of the solid phase. In general, broader reflections correspond to amorphous phases (without any regular interior arrangement of atoms) and sharper reflections to crystalline phases (atoms arranged in a periodic pattern in three dimensions) (Cullity, 1878; Jaiswal et al., 2014; Sparks, 2003). Scanning electron microscopy (SEM) and transmission electron microscopy (TEM) can identify morphological characteristics of the solid materials. Moreover, electron microscopes can be coupled with energy-dispersive X-ray fluorescence spectroscopy (EDX), which provides quantitative information (i.e., elemental composition) and qualitative information (i.e., distribution of elements). The elemental distribution is provided by X-ray maps which are produced by characteristic X-rays from the given element (generated by electrons) in the sample. The elemental mapping obtained from SEM and TEM measurements differ by the spatial resolutions which is about 1 μm (SEM) and 2 to 100 nm (TEM), respectively. Moreover, elemental maps can also provide quantitative information about the sample (Friel and Lyman, 2006). Nevertheless, the main disadvantage is that these methods are not able to distinguish between individual species (only elemental concentration are obtained) and the weight percentage (wt%) of individual elements need to be higher than 1% to be detectable (Sparks, 2003).

Indirect measurements

The (ad)sorption mechanism can be also supported by some indirect measurements, i.e., by the point of zero charge of the solid material (pH_{PZC}) or ionic-strength dependency. In general, the surface functional groups could be protonated or deprotonated; nevertheless, the charge on the surface of the solid material depends on the pH value in the solution. The pH_{PZC} means that the number of negatively and positively charged surface groups are equal. At the pH values higher than pH_{PZC} , negatively charged groups predominate; conversely, the opposite effect is observed at the pH values lower than pH_{PZC} (Šrůček and Zeman, 2004). The charge on the surface of the solid material could influence the (ad)sorption mechanism of metals and metalloids since electrostatic interactions take place between the ions with different charge, i.e., outer-sphere complexation occurs at $\text{pH} < \text{pH}_{\text{PZC}}$ for metalloids and at $\text{pH} > \text{pH}_{\text{PZC}}$ for metals (Koretsky, 2000). Moreover, the shift of pH_{PZC} of the material after the (ad)sorption process could be assigned to the formation of inner-sphere complexes;

however, the formation of outer-sphere complexes by the interaction of metals or metalloids *via* strong hydrogen bonds cannot exclude. Therefore, this value provides only a small insight to the possible (ad)sorption mechanisms (Goldberg, 2007). The ionic-strength dependency is commonly used to differentiate between inner- and outer-sphere complexes. The ionic-strength independency means that inner-sphere complexes are preferably formed. Conversely, decreasing (ad)sorption by increasing ionic strength of the background electrolyte means the formation of outer-sphere complexes (Hayes and Leckie, 1987; Hayes et al., 1988). However, increasing (ad)sorption by increasing ionic strength could be also assigned to the formation of inner-sphere complexes (McBride, 1997). It needs to be mentioned that the ionic-strength dependency is also influenced by the type of the electrolyte and this generalization is mainly applicable only for NaNO₃ (Goldberg, 2007).

Layered double hydroxides and mixed oxides

Layered double hydroxides (LDHs) were discovered at the end of the 19th century. To this date, more than 43 species distributed between 9 groups have been described (Mills et al., 2012). Layered double hydroxides are natural or synthetically prepared layered materials with many applications (Fig. 1.7) including catalysis, photochemistry and environmental or biomedical scientific uses (Cavani et al., 1991; Goh et al., 2008; Liang et al., 2013). Nevertheless, their use as adsorbents is still limited. In general, LDHs or CLDHs (thermally treated LDHs; mixed oxides) are mainly produced as plastic additives, flame retardants and PVC stabilizers at the industrial scale (Chubar et al., 2017). The most important advantages of these materials are their special structure, unique properties and a relatively simple and economical synthesis. Layered double hydroxides have been presented as potentially perspective materials for metal and metalloid removal at a larger scale; however, there is still a lack of comprehensive studies describing the real potential of these materials in remediation technologies (Chubar et al., 2017; Goh et al., 2008; Liang et al., 2013).

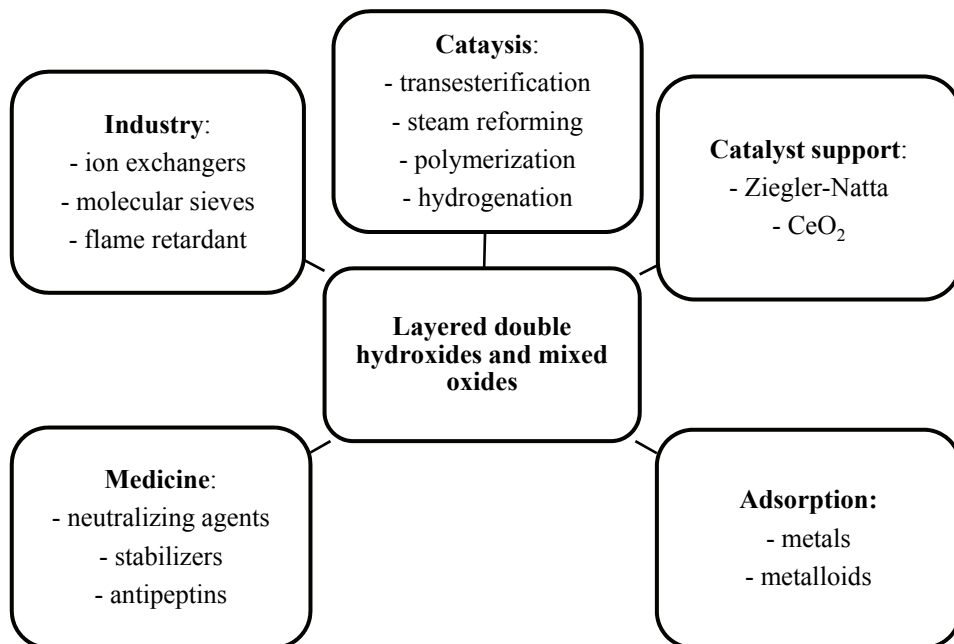


Fig. 1.7. The use of LDHs and CLDHs (Cavani et al., 1991; Goh et al., 2008, Liang et al., 2013).

Structure of layered double hydroxides and mixed oxides

The structure of LDHs consist of $Mg(OH)_6$ octahedral units that share edges in order to build $Mg(OH)_2$ brucite-like layers which are stacked on themselves and held together by hydrogen bonds. Layers are positively charged and formed by divalent and trivalent metal cations. The positive charge of layers is compensated by anions intercalated in the interlayered region. Moreover, water molecules can be found in the free space of this region (Fig. 1.8). A general formula of LDHs is given by:



where M^{2+} a M^{3+} mean divalent and trivalent metal cations and A^{n-} represents appropriate anion (n is the valence). The positive charge of layers is generated by a substitution of divalent metal cations by trivalent metal cations. Layered double hydroxides can be formed by cations with the ionic radii close to $Mg(II)$ and $Al(III)$. Possible cations and their ionic radii are shown in Table 1.3. The ionic radii are in the range 0.65 - 0.80 Å for divalent and 0.50 - 0.69 Å for trivalent metal cations (Cavani et al., 1991).

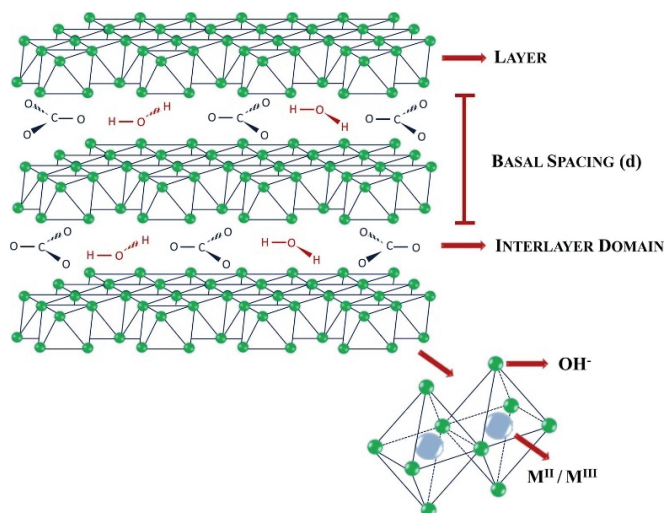


Fig. 1.8. The structure of layered double hydroxide; adapted from Benício et al. (2015).

Table 1.3 The ionic radii (Å) of divalent and trivalent metal cations possible to form LDHs (Cavani et al., 1991).

M(II)	Mg	Zn	Fe	Ca	Cu	Mn
	0.65	0.74	0.76	0.98	0.69	0.80
M(III)	Al	Fe	Ti	Ga	V	In
	0.50	0.64	0.76	0.62	0.74	0.81

The trivalent metal ratio (the symbol x) is an important parameter that describes the structure of LDHs and can be calculated by the following formula:

$$x = \frac{M^{3+}}{(M^{2+} + M^{3+})} \quad \text{Eq. 1.29}$$

The value of this parameter corresponds approximately to $0.2 \leq x \leq 0.4$ that means molar ratio of M(II) and M(III) in the structure of LDHs between 3:1 and 2:1; nevertheless, LDHs with molar ratio up to 4:1 is commonly used. The upper limit of x leads to electrostatic repulsions between neighboring trivalent cations in the layers and also between the charge-balancing anions. The lower limit of x means a collapse of the interlayered region due to a higher distance between anions in the interlayered region (de Roy, 2001). Moreover, high values of x lead to the formation of $\text{Al}(\text{OH})_3$. On the contrary, $\text{Mg}(\text{OH})_2$ is formed at low values of x . Afterwards, both hydroxides occur as secondary phases (Cavani et al., 1991).

A great variety of anions can be incorporated in the interlayered region. Moreover, these anions can be easily exchanged due to weak bonds. They are divided into five groups: halides (e.g., chloride), oxyanions (e.g., carbonate or nitrate), oxo- and polyoxometalates (e.g., dichromate), anionic complexes (e.g., ferrocyanide and ferricyanide) and organic anions (e.g., carboxylates) (de Roy, 2001). The type of the anion influences the width of the interlayered region that is represented by the basal spacing of layers calculated from XRD diffractograms. If two different basal reflections are observed, two different types of anions exist in the interlayer region (Cavani et al., 1991). Values of basal spacing of anions that commonly occur in the structure of LDHs are shown in Table 1.4.

Table 1.4 Values of basal spacing (d_{003}) of the most common interlayered anions (Cavani et al., 1991).

Type of anion	OH^-	CO_3^{2-}	Cl^-	NO_3^-
Basal spacing (Å)	7.55	7.65	7.86	8.79

The thermal treatment (calcination) of LDHs leads to mixed oxides (CLDHs) that have many advantages compared to LDHs (e.g., a larger surface area, stronger basic properties, a higher thermal stability, a smaller crystal size and a higher stability against sintering) (Liang et al., 2013). The LDHs can be also reconstructed from these materials by a rehydration. Afterwards, the intercalation of anions takes place. The whole process is called the memory effect (Cavani et al., 1991; Kang et al., 2013). The thermal treatment of LDHs is commonly held in an inert atmosphere and the structure of LDHs

changes into $(M(II)^{2+})O$ and $(M^{3+})_2O_3$. A spinel structure $(M^{2+})(M^{3+})_2O_4$ can be synthesized during higher temperatures (Yang et al., 2002). Properties of synthesized CLDHs depend on a temperature program of a furnace (e.g., a final temperature, a time and an atmosphere). The thermal treatment of is divided into several steps (Andreozzi et al., 2000; de Roy, 2001; Yang et al., 2002) that are shown for Mg-Al CO_3 at Fig. 1.8:

- Elimination of water in the interlayered region (70–190°C)
- Elimination of the OH^- groups bonded with Al(III) (190–280°C)
- Elimination of the OH^- groups bonded with Mg(II) (240–405°C) which means a collapse of the brucite-like sheets
- Elimination of CO_3^{2-} (405–580°C) resulting into transformation to the amorphous mixed oxide
- Formation of the spinel structure (600–1000°C)

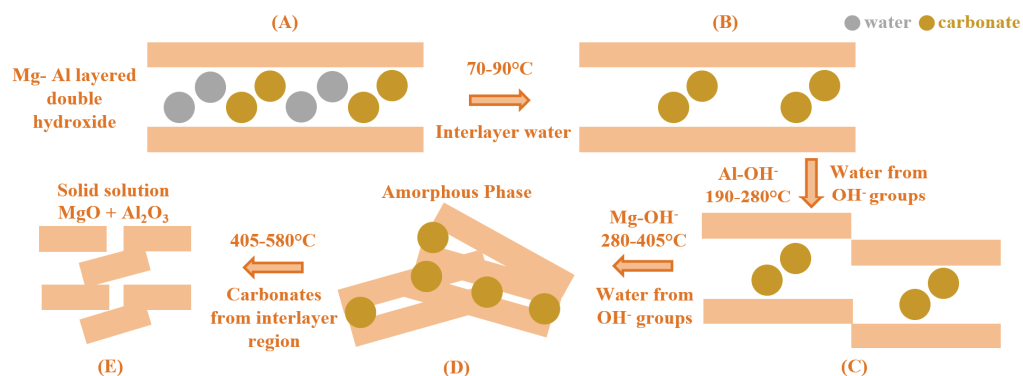


Fig. 1.9. The thermal treatment of Mg-Al CO_3 LDH; adapted according to Yang et al. (2002).

(Ad)sorption of metals and metalloids

Layered double hydroxides and mixed oxides have been used for the (ad)sorption of oxyanions (AsO_4^{3-} , PO_4^{3-}), monoatomic anions (F^- , Cl^- , Br^- , I^-) or organics, but there are only few studies focused on the (ad)sorption of metal cations (Goh et al., 2008; Liang et al., 2013). Nevertheless, studies dealing with the complex mechanistic/modelling approach are rather scarce. Generally, individual species can be stabilized by various mechanisms, i.e., surface complexation (monoatomic anions, metals, metalloids, organics), incorporation by the mean of anion exchange or during the reconstruction process (monoatomic anions, metalloids, organics), precipitation or surface precipitation (metals), isomorphic substitution (metals) and/or chelation (metals). Individual processes can occur simultaneously and may influence the whole

(ad)sorption mechanism (Liang et al., 2013). In general, the main factors influencing metal and metalloid (ad)sorption onto LDHs and CLDHs are the pH value, the temperature, the thermal treatment of LDHs, the dosage and the stability of LDHs and CLDHs.

The (ad)sorption mechanisms of metals onto LDHs and CLDHs include surface complexation, precipitation of metal hydroxides on the surface of LDHs or CLDHs (especially if the pH value is not adjusted), isomorphous substitution and chelation with functional ligands in the interlayered region (Liang et al., 2013). Surface complexation of metals onto the LDH and CLDH surface can be divided into the formation of outer-sphere complexes and inner-sphere complexes. Isomorphous substitution leads to the replacement of divalent metal cations within the lattice without any changes of the crystal structure of the material (so called diadochy). This unique mechanism enables to lock divalent metal cations in the LDH structure. Moreover, the kinetics of this process is quite rapid (Komarneni et al., 1998; Richardson and Braterman, 2009). Divalent metal cations must have the similar ionic radii as Mg(II) to be successfully incorporated (Komarneni et al., 1998; Richardson and Braterman, 2009; Sun et al., 2015a). Although the ionic radius of Zn(II) (0.74 Å) shows a higher value than ionic radii of Cu(II) (0.72 Å) and Ni(II) (0.72 Å), the affinity of metal cations decreases in the order Zn(II) > Cu(II) > Ni(II). The increasing affinity with the increasing ionic radius can be ascribed to a steric hindrance that causes a lower chance of small cations to be incorporated into the LDH structure. The substitution of Mg(II) (with a smaller ionic radius) by divalent metal cations (with larger ionic radii) can be identified by the changes in the XRD diffractogram, i.e., the decrease of the parameter a is observed. On the contrary, the lattice parameter c increases which is ascribed to changes of the original LDH structure during the isomorphous substitution (Sun et al., 2015a). Since LDHs have a buffering effect that leads to the increase of pH values, the precipitation of metals, i.e., a formation of new solid phases, can be also observed, especially if the pH is not adjusted during the (ad)sorption experiments (Fujji et al., 1992). Precipitates can occur as parts of the LDH structure (surface precipitation) or as separate phases. Other factors affecting precipitation are the composition of layers, solubility constant of metal hydroxides, sorbent stability and/or coexisting species. Finally, chelation can also influence the (ad)sorption mechanism; nevertheless, functional ligands (EDTA, DTPA, citrate, etc.) should be present in the interlayered region and; afterwards, the reaction of metal cations with these ligands without any deformation of the LDH structure takes place (Liang et al., 2013).

The (ad)sorption mechanisms of metalloids onto LDHs and CLDHs include surface complexation and anion exchange in the interlayered region. Moreover, CLDHs enable the intercalation of metalloid anions in the renewed interlayer region as the reconstruction of the original layered structure of LDHs (Kang et al., 2013). (Ad)sorption of metalloids (e.g., arsenate, antimonate) is the pH-dependent surface complexation and takes place mainly at low pH values, i.e., on the protonated surface. Anion exchange is influenced by the layer charge density and the type of anions in the interlayered region of LDHs. The layer charge density depends on the amount of trivalent metal cations in the brucite-like sheets that means the increasing charge of layers with the increasing number of trivalent cations (Goh et al., 2008). Furthermore, the effectivity of the anion exchange strongly depends on ionic radii of metalloid anions. It means that the maximal effectivity is reached when the interlayered region is large enough for the chosen type of the metalloid anion. Nevertheless, the effectivity of the anion exchange is also influenced by the competing anion in the interlayer region. Generally, HCO_3^- , CO_3^{2-} and HPO_4^{2-} have the highest interfering effects (Kiso et al., 2005; Yang et al., 2005). Moreover, the competing anions have stronger effects for LDHs than for CLDHs (Yang et al., 2005). However, the most attractive (ad)sorption mechanism is the LDH reconstruction by the mean of the memory effect that is caused by the rehydration of CLDHs and the concurrent intercalation of metalloid anions into the interlayered region (Goh et al., 2008).

Factors influencing metal and metalloid (ad)sorption

The effectivity of metal and metalloid (ad)sorption strongly depends on the point of zero charge (pH_{PZC}) of LDHs and CLDHs. Generally, pH_{PZC} of Mg-Al LDHs and Mg-Fe LDHs is between 8.7 and 12.5. As has been previously discussed, the surface is positively charged when the pH value is lower than pH_{PZC} and *vice versa*. Since metal (ad)sorption increases with increasing pH values, the buffering effect of LDHs and CLDHs spontaneously increases the pH value and improves metal (ad)sorption efficiency by precipitation of new solid phases (hydroxides or carbonates) (Kameda et al., 2005). Therefore, it is necessary to separate the influence of the different mechanisms influencing the whole (ad)sorption process. On the contrary, favourable (ad)sorption of metalloids is observed with a decreasing pH value. However, the pH value that is significantly higher than pH_{PZC} ($\text{pH} \gg \text{pH}_{\text{PZC}}$) leads to the decrease of (ad)sorption of arsenate due to competitive effects with OH^- groups (Liang et al., 2013).

The efficiency of the (ad)sorption process is also influenced by the temperature. In the case of metalloid (ad)sorption using LDHs and CLDHs, increasing (ad)sorption with

decreasing temperature, i.e., the exothermic process, was observed (Yang et al., 2005); however, opposite results were presented by Das et al. (2004). Metal (ad)sorption is commonly described as an endothermic process. In general, increasing temperature influences the interparticle diffusion that could be the rate-limiting step and thus influence the whole (ad)sorption process (Liang et al., 2013). The temperature of the thermal treatment of LDHs, i.e., the formation of CLDHs, significantly affects the (ad)sorption properties of the final material (e.g., surface area and memory effect). At lower temperatures (see Fig. 1.9), the layered structure is not completely collapsed, not all carbonates are eliminated, and the surface area does not reach the maximum value. On the contrary, at higher temperatures (over 800°C) the spinel structure disables the reconstruction of LDHs and decreases the surface area (Goh et al., 2008; Liang et al., 2013).

The optimum dosage of the solid material is a necessary factor for cost-effective applications of LDHs and CLDHs. Increased solid content results into more available surface sites, so (ad)sorption increases rapidly. However, the (ad)sorption capacity could decrease with a higher solid content due to the presence of surface sites of different binding energies. Therefore, a higher (ad)sorption capacity could be observed in the case of lower sorbent dosages while all sites are exposed for (ad)sorption and the saturation is fast. Moreover, higher sorbent dosages could lead to the decrease of available surface sites of higher energy (at the expense of a larger fraction of surface sites of lower energy). Moreover, increasing the solid content can cause aggregation and; afterwards, the diffusion affects the (ad)sorption process (Liang et al., 2013).

The stability of the sorbent is a crucial factor affecting the (ad)sorption of metals and metalloids. The stability depends on the pH value and also on the type of metal cations in brucite-like sheets of LDHs and CLDHs (Boclair and Braterman, 1999; Ferreira et al., 2006; Jobbágy and Regazzoni, 2011). Generally, the stability of LDHs and CLDHs increases with the stability of divalent metal cations in the order $Mg(II) < Mn(II) < Co(II) \cong Ni(II) < Zn(II)$ and with the stability of trivalent metal cations in order $Al(III) < Fe(III)$ (Boclair and Braterman, 1999). In the case of Mg-Al LDH, the leaching of Mg(II) is observed in the pH range from 5 to 9 and increases with the decrease of the pH value (without any leaching of Al^{3+}). However, a complete dissolution (the leaching of Al) takes place in 3 hours at pH 4 (Jobbágy and Regazzoni, 2011). The dissolution of Mg-Fe LDHs can be observed at pH 3 (Jiao et al., 2014). Therefore, the release of harmful metals must be controlled by appropriate pH values of the (ad)sorption process or by using LDHs and CLDHs that are free of toxic metals in the brucite-like sheets, e.g., Mg-Fe LDHs and CLDHs (Goh et al., 2008; Liang et al., 2013).

Perspectives in the field of metal and metalloid (ad)sorption

Surface complexation models can provide a useful tool to identify individual (ad)sorption mechanisms of metals and metalloids onto the surface of solid materials. Nevertheless, the SCM describing metal and metalloid (ad)sorption onto LDHs or CLDHs has not been presented yet. Up to now, the SCM has been used only to describe the surface charging behaviour of LDHs by the modified complexation model (Rojas Delgado et al., 2004, 2008) and the formation of LDHs by the Zn co-precipitation with $\text{Al}(\text{OH})_3$ by the diffuse layer model (Tokoro et al., 2015). In general, the formation of outer- and/or inner-sphere complexes during metal and metalloid (ad)sorption onto LDHs and CLDHs has been studied by XAS analyses (Izumi et al., 2002, 2005; Liu et al., 2006; Paikaray et al., 2013; Sommella et al., 2015; Wang et al., 2009), XPS analyses (Goh et al., 2009) or by ionic-strength dependency (Liang et al. 2009; Zhang and Hou, 2007; Zhao et al., 2011). However, metal (ad)sorption onto LDHs and CLDHs were mainly performed without pH adjustment resulting in the predominant effect of precipitation or surface precipitation of new solid phases rather than surface complexation (Liang et al., 2013).

Some studies have focused on the application of LDHs and CLDHs in soils. However, these studies are rather scarce. Moreover, the stabilization mechanism as well as the stability of materials in soil conditions have not been studied in detail. Therefore, future studies based on the application of LDHs and CLDHs in soils contaminated by metals and metalloids should be useful to evaluate the stabilizing potential of these materials in real contaminated soils. Previously, the remediation of Cr(VI) was performed by the combination of adsorption onto CLDHs and electrokinetic methods which could be a promising method for the remediation of other oxyanions (Zhang et al., 2012a). Moreover, the removal of the organic matter in alkaline soils was also studied. Strong interactions between the organic matter (anionic compounds) and LDHs enable accumulation and storage of the organic matter in these soils (Grünwald et al., 2008). Perspectives of LDHs and CLDHs in the agriculture have been also tested (Benício et al., 2015). The intercalation of N and P within LDHs was published as a new fertilizer technology that optimizes N and P supply to plants (a long-term exchanger that controls the movement and reduces the leaching of NO_3^-) (da Silva et al., 2014; Torres-Dorante et al., 2008). Moreover, agrochemicals (such as pesticides and herbicides) can be encapsulated in the LDH structure thus reduces environmental hazards of their application (Bruna et al., 2009). Finally, LDHs and CLDHs may be used for the removal of anionic species that are commonly used in the agriculture (e.g., nitrates, phosphates) by adsorption. Subsequently, the adsorbed compounds can be slowly

released back to the plants (Benício et al., 2015; Terry, 2009). Previously, Mg-Al CLDHs were compared with other amendments (sepiolite, red mud, iron grit, phosphogypsum, ferrihydrite and iron phosphate) for the reduction of As(V) bioavailability in soils and to study the influence of these amendments on the plant growth and other biological processes. In the case of CLDHs, a significant decrease of water soluble and also soil available As(V) fraction was observed. Moreover, the uptake of As(V) by plants (*Bactris campestris*) was also reduced by the application of CLDHs. However, a significant decrease in *B. campestris* dry matter is observed that is probably caused by the buffering effect of CLDHs which increased soil pH from 7.11 to 7.50 (Sun et al., 2015b). This study showed that LDHs and CLDHs can be effective stabilizing amendments in soils; however, more studies evaluating their stabilizing potential as well as the effect on plants and/or microorganisms in real conditions are necessary.

Chapter II

Sorption mechanisms of arsenate on Mg-Fe layered double hydroxides: A combination of adsorption modeling and solid-state analysis

B. Hudcová, V. Veselská, J. Filip, S. Číhalová, M. Komárek

Adapted from Chemosphere 168 (2017): 539-548

Content

Abstract	37
Introduction	38
Materials and methods	40
Materials	40
Synthesis and basic properties of the Mg-Fe LDH	40
Kinetic adsorption experiments	40
Equilibrium adsorption experiments	41
Surface complexation modeling	41
Solid state analyses	42
Results and discussion	44
Kinetic adsorption experiments	44
Equilibrium adsorption experiments	45
Surface complexation modeling	46
Solid state analyses	48
Conclusions	55
Supplementary Material	56

Abstract

Layered double hydroxides have been proposed as effective sorbents for As(V), but studies investigating adsorption mechanisms usually lack a comprehensive mechanistic/modeling approach. In this work, we propose coupling surface complexation modeling with various spectroscopic techniques. To this end, a series of batch experiments at different pH values were performed. Kinetic data were well fitted by a pseudo-second order kinetic model, and the equilibrium data were fitted by the Freundlich model. Moreover, the pH-dependent As(V) sorption data were satisfactorily fitted by a diffuse layer model, which described the formation of $>SOAsO_3H^-$ monodentate and $>(SO)_2AsO_2^-$ bidentate inner-sphere complexes (" $>S$ " represents a crystallographically-bound group on the surface). Additionally, XPS analyses confirmed an adsorption mechanism. The sorption mechanisms were affected by anion exchange, which was responsible for the formation of outer sphere complexes, as identified by XRD and FTIR analyses. Further, a homogenous distribution of As(V) was determined by HR-TEM with elemental mapping. Using low-temperature Mössbauer spectroscopy on isotope ^{57}Fe , a slight shift of the hyperfine parameters towards higher values following As(V) sorption was measured, indicating a higher degree of structural disorder. In general, mechanistic adsorption modeling coupled with solid state analyses presents a powerful approach for investigating the adsorption mechanism of As(V) on Mg-Fe LDH or other sorbents.

Introduction

Several materials have been used to remove As(V) from aqueous solutions (including soil solutions), such as Fe (hydr)oxides (Komárek et al., 2013), ferrates (Prucek et al., 2013), zeolites (Melo et al., 2012), anionic clays (Doušová et al., 2011) and/or layered double hydroxides (Goh et al., 2008). Layered double hydroxides (LDHs) are natural or synthetically prepared layered materials that can be used for various purposes, including catalysis, photochemistry, environmental or biomedical applications (Cavani et al., 2001; Fan et al., 2014). The most important advantages of LDHs are their unique structure, sorption properties and relatively simple and economical synthesis (Goh et al., 2008; Liang et al., 2013). Their unique structure facilitates various applications, e.g., intercalation of different fertilizers or agrochemicals in the structure of LDHs that can be slowly released back to the plants or intercalation of hazardous compounds *via* various mechanisms including isomorphic substitution of metals in the layers or anion exchange of As(V) in the interlayered region (Benício et al., 2015; Goh et al., 2008; Liang et al., 2013). The structure of LDHs consist of $\text{Mg}(\text{OH})_6$ octahedral units that share edges to create $\text{Mg}(\text{OH})_2$ brucite-like stacked layers held together by hydrogen bonds. The layers are positively charged and formed by divalent and trivalent metal cations. The positive charge of the layers is compensated by anions intercalated in the interlayered region. In addition, water molecules can also be present in the free space of this region (Cavani et al., 2001).

LDHs or their thermally treated products (CLDHs) have been shown to be potential sorbents for oxyanions and metal cations (Goh et al., 2008; Liang et al., 2013). However, most studies have examined the sorption of metals and metalloids on Al-based LDHs or CLDHs, which have the negative consequence of possible leaching of Al at low pH values (Boclair and Braterman, 1999; Jobbágy and Regazzoni, 2011). Therefore, Fe-based LDHs and CLDHs may be more appropriate (Caporale et al., 2011; Carja et al., 2005; Kang et al., 2013; Peng et al., 2014). The adsorption of As(V) onto Mg-Fe LDHs and CLDHs has been already described by several authors (Kang et al., 2013; Peng et al., 2014; Paikaray et al., 2013; Türk et al., 2009, with the main focus on the sorption mechanism of As(V) on CLDHs by structural reconstruction meaning incorporation of As(V) as the interlayered anion in the contact of CLDHs with aqueous solutions (Cavani et al., 2001; Goh et al., 2008). However, research based on the sorption of As(V) on LDHs to include adsorption via bonding with surface hydroxyl groups and anion exchange in the interlayered region remains limited, while the authors are mainly focused on the detailed adsorption mechanism of As(V) on Mg-Fe CLDHs (Kang et al., 2013; Peng et al., 2014; Huang et al., 2015).

Although the adsorption rate, efficiency and capacity are commonly described by kinetic and equilibrium adsorption experiments (Liang et al., 2013), advanced spectroscopic methods are used to determine the adsorption mechanisms of As(V) on Mg-Fe LDHs and CLDHs, including SEM/EDX, TEM, XRD, FTIR, XPS (Kang et al., 2013; Park and Kim, 2011; Peng et al., 2014) and/or XAS (Izumi et al., 2005; Paikaray et al., 2013). However, the adsorption mechanisms of oxyanions and metal cations on LDHs by a coupled surface complexation modeling/spectroscopic approach have not yet been examined. Thermodynamically based surface complexation models (SCMs) are used to describe metal and/or metalloid adsorption onto different solid materials as a function of pH, ionic strength and solute concentration (Komárek et al., 2015; Reich and Koretsky, 2011; Tonkin et al., 2004; Hayes et al., 1991; Veselská et al., 2016). Generally, As(V) sorption on Fe-based materials is strongly influenced by pH, i.e., decreasing As(V) sorption as a result of increasing pH (Dzombak and Morel, 1990). Therefore, a detailed study dealing with the pH-dependent sorption of As(V) on Mg-Fe LDH is needed. There are few studies based on the application of the SCM for LDHs, including the surface-charging behavior of LDHs described by the modified multisite complexation model (MUSIC) (Rojas Delgado et al., 2004, 2008) and the coprecipitation of Zn on aluminum hydroxide that measures the formation of LDHs using the diffuse layered model (DLM) (Tokoro et al., 2015).

The aim of this study is to investigate the adsorption mechanisms of As(V) onto Mg-Fe LDHs using a combination of SCMs and detailed analyses of the solid phases (XRD, SEM/EDX, HR-TEM with elemental mapping, FTIR-ATR, XPS and low-temperature ^{57}Fe Mössbauer spectroscopy). Additionally, the determination of the equilibrium time, reaction rates, adsorption capacity and other spectroscopic parameters were obtained.

Materials and methods

Materials

All chemical reagents used in this study were of analytical grade and used directly without any purification or treatment. All solutions were prepared using deionized water (18.2 M Ω). The pH value of the adsorption experiments was adjusted using HNO₃ and NaOH (0.001 M, 0.01 M, 0.1 M).

Synthesis and basic properties of the Mg-Fe LDH

The Mg-Fe LDH was prepared using the co-precipitation method described in Seida et al. (2001). The detailed synthesis is given in Supplementary Material. The pHPZC of the material was determined by the immersion technique (Fiol and Villaescusa, 2009). Finally, the specific surface area of the adsorbent was measured by N₂ adsorption at 77 K (BET analysis) using an ASAP 2050 (Micrometrics Instrument Corporation, USA).

Kinetic adsorption experiments

The kinetic adsorption experiments were performed in individual batches containing 10⁻⁴ M As(V) prepared by dissolution of Na₂HAsO₄·7H₂O in 0.01 M NaNO₃ as the background electrolyte. The solid/liquid ratio in all experiments was 1 g L⁻¹ and the pH values (5.5 and 8.5) were controlled using 1 M and 0.1 M HNO₃ during the whole experiment. The given experimental conditions were chosen according to Michálková et al. (2016a). The slightly acidic conditions (pH 5.5) are characteristic pH values for soils that are investigated in subsequent works. On the other hand, slightly alkaline conditions (pH 8.5) limit As(V) sorption (Dzombak, Morel, 1990; Michálková et al., 2016a). Moreover, lower pH causes leaching of Mg(II) from the LDH structure (Liang et al., 2013). The adsorbent was then added to the solution and the mixture was stirred (550 rpm) using a magnetic stirrer at specific time intervals (i.e., 1, 3, 5, 10, 15, 20, 30, 60, 90 and 120 min). The samples were filtered using a 0.45 μ m membrane and the As (limit of detection: 0.01121 mg L⁻¹), Fe (limit of detection: 0.00036 mg L⁻¹) and Mg (limit of detection: 0.00024 mg L⁻¹) concentrations were determined using ICP-OES (Agilent Technologies 700 Series). The adsorption efficiency of As(V) (in %) on Mg-Fe LDH was calculated as the concentration difference between the initial and final As concentrations.

Equilibrium adsorption experiments

The equilibrium adsorption experiments were also performed in individual batches at specific pH values (i.e., 5.5, 6.5 and 7.5). The solid/liquid ratio in all experiments was 1 g L^{-1} and equilibrium was reached after 120 min, in accord with the results of the kinetic experiments. The initial As(V) concentration for the equilibrium adsorption experiments ranged from 1 to 450 mg L^{-1} . The experiments were performed in an orbital shaker (GFL 3005; 250 rpm) at constant pH values. The samples were then filtered (cellulose acetate membrane; $0.45 \text{ }\mu\text{m}$) and analyzed by ICP-OES. To obtain the samples for the solid-state analyses, the initial concentration of As(V) was set to 500 mg L^{-1} . The liquid sample (10 mL) was filtered ($0.45 \text{ }\mu\text{m}$) and analyzed using ICP-OES. The entire solution was subsequently filtered using a vacuum pump and the sample was dried at room temperature.

Surface complexation modeling

Acid-base potentiometric titrations were performed in triplicates to characterize the protonation behavior of the Mg-Fe LDH surface (Jolstera et al., 2010; Turner and Fein, 2006). The titration procedure is described in detail Supplementary Material. The adsorption edge experiments were conducted under atmospheric conditions at total As(V) concentrations of 10^{-5} and 10^{-4} M and at different solution pH values (ranging from 5.5 to 12) and ionic strengths (0.001, 0.01, and 0.1 M NaNO_3 as the background electrolyte). A set of individual batches was prepared with a 25 mL volume of the solution containing As(V) and the background electrolyte. Mg-Fe LDH (1 g L^{-1}) was then added to the solution and the slurry was pre-equilibrated with constant stirring (250 rpm) at room temperature for 24 h. The pH value was then held constant for 120 min for each individual batch using 0.1 to 1 M HNO_3 and NaOH, starting at a pH value of 5.5 in the first batch and increasing in steps of ~ 1 pH for each subsequent batch until pH 12 was reached. Finally, the samples were filtered using $0.45 \text{ }\mu\text{m}$ filters and analyzed by ICP-OES. The adsorption edge data were used to calibrate the two-pK DLM and the surface complexation constants were obtained using the software FITEQL 4.0 (Herbelin and Westall, 1999) with the default thermodynamic data for aqueous species from Visual MINTEQ (Gustafsson, 2013) (Table 2.1). Visual MINTEQ 3.0 was used to calculate surface complexation model predictions for the studied systems (Goldberg et al., 2007). More information is available in Supplementary Material.

Table 2.1 Reaction stoichiometries and stability constants for formation of aqueous and solid species (taken from the Visual MINTEQ 3.1 database) during adsorption edge experiments. Stability constants describing As(V) inner-sphere complexation using DLM are present as average values (optimized in FITEQL 4.0).

Reactions in solution	Log Stability Constant
$\text{H}_2\text{O} \rightleftharpoons \text{H}^+ + \text{OH}^-$	-13.99
$\text{Na}^+ + \text{NO}_3^- \rightleftharpoons \text{NaNO}_3$	-0.55
$\text{Na}^+ + \text{OH}^- \rightleftharpoons \text{NaOH}$	-13.90
$6\text{H}^+ + 2\text{AsO}_4^{3-} \rightleftharpoons \text{As}_2\text{O}_5 + 3\text{H}_2\text{O}$	34.69
$\text{H}^+ + \text{AsO}_4^{3-} \rightleftharpoons \text{HAsO}_4^{2-}$	11.80
$2\text{H}^+ + \text{AsO}_4^{3-} \rightleftharpoons \text{H}_2\text{AsO}_4^-$	18.79
$3\text{H}^+ + \text{AsO}_4^{3-} \rightleftharpoons \text{H}_3\text{AsO}_4$	21.09
<hr/>	
Reactions on the LDH-solution interface	
$>\text{SOH} + \text{H}^+ \rightleftharpoons >\text{SOH}_2^+$	3.56
$>\text{SOH} \rightleftharpoons >\text{SO}^- + \text{H}^+$	-5.33
Formation of monodentate complexes	
<i>10⁻⁴ M As(V)</i>	
$>\text{SOH} + \text{AsO}_4^{3-} + \text{H}^+ \rightleftharpoons >\text{SOAsO}_3^{2-} + \text{H}_2\text{O}$	25.74
$>\text{SOH} + \text{AsO}_4^{3-} + 2\text{H}^+ \rightleftharpoons >\text{SOAsO}_3\text{H}^- + \text{H}_2\text{O}$	31.14
$>\text{SOH} + \text{AsO}_4^{3-} + 3\text{H}^+ \rightleftharpoons >\text{SOAsO}_3\text{H}_2 + \text{H}_2\text{O}$	35.00
<i>10⁻⁵ M As(V)</i>	
$>\text{SOH} + \text{AsO}_4^{3-} + \text{H}^+ \rightleftharpoons >\text{SOAsO}_3^{2-} + \text{H}_2\text{O}$	26.56
$>\text{SOH} + \text{AsO}_4^{3-} + 2\text{H}^+ \rightleftharpoons >\text{SOAsO}_3\text{H}^- + \text{H}_2\text{O}$	33.36
$>\text{SOH} + \text{AsO}_4^{3-} + 3\text{H}^+ \rightleftharpoons >\text{SOAsO}_3\text{H}_2 + \text{H}_2\text{O}$	36.67
Formation of bidentate complexes	
<i>10⁻⁴ M As(V)</i>	
$2>\text{SOH} + \text{AsO}_4^{3-} + 2\text{H}^+ \rightleftharpoons (>\text{SO})_2\text{AsO}_2^- + 2\text{H}_2\text{O}$	32.69
$2>\text{SOH} + \text{AsO}_4^{3-} + 3\text{H}^+ \rightleftharpoons (>\text{SO})_2\text{AsO}_2\text{H} + 2\text{H}_2\text{O}$	37.76
<i>10⁻⁵ M As(V)</i>	
$2>\text{SOH} + \text{AsO}_4^{3-} + 2\text{H}^+ \rightleftharpoons (>\text{SO})_2\text{AsO}_2^- + 2\text{H}_2\text{O}$	34.87
$2>\text{SOH} + \text{AsO}_4^{3-} + 3\text{H}^+ \rightleftharpoons (>\text{SO})_2\text{AsO}_2\text{H} + 2\text{H}_2\text{O}$	38.05
<hr/>	
Site density: 47.5 sites nm ⁻²	
Specific surface area: 40.1 m ² g ⁻¹	
<hr/>	

Solid state analyses

The structural characterization of the solid phase before (Mg-Fe LDH) and after As(V) sorption was performed by X-ray diffraction analysis (XRD) using a PANalytical X'Pert Pro diffractometer with an X'Celerator detector (CuK_α radiation, 40 kV, 30 mA, a measuring step 0.02° s⁻¹ in the range 10 to 80° 2Θ). The morphology and chemical composition of the materials were analyzed using a scanning electron microscope (SEM; Tescan Inc., USA) and energy dispersive X-ray spectroscopy (EDX; Bruker

Quantax, USA). Characteristic functional groups were described using Fourier transform infrared spectroscopy in attenuated total reflection mode using diamond crystal (FTIR-ATR; Nicolet 6700). The surface analysis was performed by X-ray photoelectron spectroscopy (XPS; Omicron Nanotechnology, Ltd) and the Casa XPS program, which was used to deconvolute the spectra. High-resolution transmission electron microscopy images (HRTEM) were obtained using a HRTEM TITAN 60-300 microscope with an X-FEG type emission gun operating at 80 kV. Elemental mappings were obtained by STEM-Energy Dispersive X-ray Spectroscopy (EDS) with an acquisition time of 20 min. ^{57}Fe Mössbauer spectra were collected in transmission geometry (constant acceleration mode) with a $^{57}\text{Co}(\text{Rh})$ radioactive source (1.85 GBq) at 5 K. The values of the hyperfine parameters (e.g., isomer shifts) were calibrated against a metallic iron ($\alpha\text{-Fe}$) foil at room temperature. The spectra were fitted by Lorentz functions using the CONFIT2000 software (Žák and Jirásková, 2006). The experimental error is $\pm 0.02 \text{ mm s}^{-1}$ for the hyperfine parameters.

Results and discussion

Kinetic adsorption experiments

Kinetic adsorption experiments provide information on the equilibrium time, the adsorption rate and additional parameters that describe the adsorption process (Gupta and Bhattacharyya, 2011; Limousin et al., 2007; Simonin, 2016). The adsorption efficiency of As(V) removal by Mg-Fe LDH at pH values 5.5 and 8.5 was 99% and 98%, respectively. The adsorption data (Fig. 2.1A) were modeled by pseudo-first and pseudo-second order kinetics (see Supplementary Material) (Gupta and Bhattacharyya, 2011; Simonin, 2016). Experimental values of the adsorbed amount at equilibrium ($q_{e(exp)}$), the calculated parameters (q_e , k_1 and k_2) and the correlation coefficients (R^2) for both models are given in Supplementary Table S2.1. As seen, the experimental data are described better by the pseudo-second order kinetic model and the experimental values of the adsorbed amount at equilibrium correspond to the modeled values. Based on the newest results described by Simonin (2016), the experimental data were also modelled without data after reaching the equilibrium ($t = 20$ min; data not shown). Identically, this process led to the improvement of R^2 established by the pseudo-first order kinetics. On other hand, pseudo-second order kinetics still better described the experimental data. The rate coefficients (k_1 , k_2) permit determination of the rate at which the metals and/or metalloids adsorb onto the surface of a solid material (Gupta and Bhattacharyya, 2011). Higher values of the rate coefficients were obtained for the data at pH 5.5 as a result of a faster kinetic process (Peng et al., 2014). In general, higher pH values result for the desorption of As(V) from Fe-based solid materials that is caused by the change in the surface charge from positive to negative as pH increases above pH_{PZC} (Dzombak and Morel, 1990). The adsorption of As(V) on Mg-Fe LDH was also influenced by the high value of pH_{PZC} (about 10) for the material (see Supplementary Fig. S2.1). The surface becomes positively charged as the pH value decreases below the pH_{PZC} value (Bohn et al., 2015).

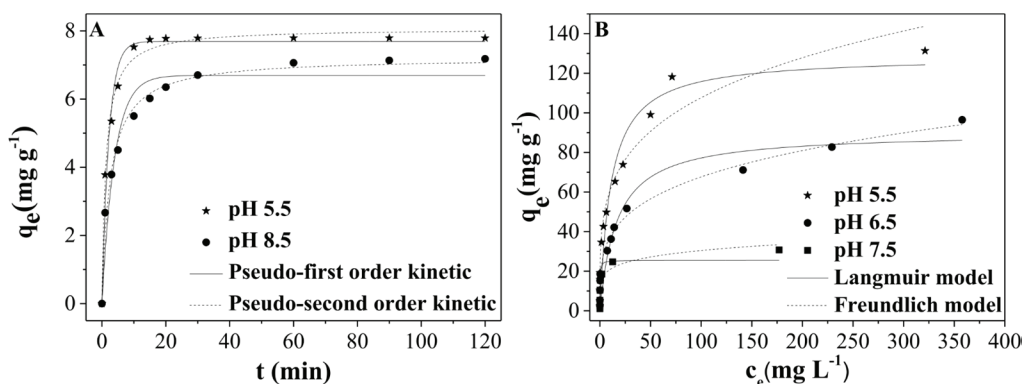


Fig. 2.1. Adsorption kinetics fitted by the non-linear form of pseudo-first and pseudo-second order kinetic models (A) and adsorption isotherms fitted by the non-linear form of the Langmuir and Freundlich model (B) of As(V) on Mg-Fe LDH at different pH values. Data (B) presented are means ($n = 3$). Maximum SD is ± 2.3 mg g⁻¹.

Equilibrium adsorption experiments

Equilibrium adsorption experiments give the basic adsorption mechanism, the adsorbed amount and additional parameters that describe the adsorption process (Foo and Hameed, 2010; Limousin et al., 2007). The adsorption equilibrium data of As(V) on Mg-Fe LDH at pH 5.5, 6.5 and 7.5 are given in Fig. 2.1B. All measured isotherms exhibited a convex shape, and the Langmuir and Freundlich equations were chosen as appropriate models (see Supplementary Material) (Foo and Hameed, 2010). The calculated parameters (i.e., q_{max} , K_L , K_F , and n) and the correlation coefficients (R^2) of both models are given in Supplementary Table S2.2. The highest values of R^2 were obtained by the Freundlich model. This model describes a non-ideal and reversible adsorption process on a heterogeneous surface without the formation of a monolayer, whereas the Langmuir model describes a monolayer adsorption at a fixed number of identical and equivalent sites (Foo and Hameed, 2010; Limousin et al., 2007). Higher R^2 values for both models were calculated for the data measured at lower pH values. The q_{max} values provided by the Langmuir model were slightly undervalued according to the experimental values of the adsorbed amount ($q_{max(exp)}$). Although experimental data were better fitted by the Freundlich model, $q_{(max)}$ established by the Langmuir model was used for comparison of As(V) adsorption on different LDHs (Table 2.2). In this study, the highest value of q_{max} (i.e., 129 mg g⁻¹) was observed for the data measured at pH 5.5 from the kinetic experiments. However, the highest affinity to the adsorbate described by K_L was obtained for the experimental data measured at pH 7.5. In general, affinity is evaluated by the initial slope, which was very high for these materials

(Limousin et al., 2007). The Freundlich model provides an evaluation of the adsorption process by the parameter n . All experimental data exhibited n values ranging from 1 to 10, indicating a positive adsorption process, which suggests that the adsorbate concentration is higher than in the bulk solution (Tan, 2010). Based on the modeled experimental data, higher concentrations of As(V) on the surface of Mg-Fe LDH were observed until the bulk solution concentration reached 25, 73 and 116 mg L⁻¹ at pH 7.5, 6.5 and 5.5, respectively.

Table 2.2 A comparison of $q_{(max)}$ established by the Langmuir model for As(V) sorption on different LDHs.

Type of the LDH	Initial pH	q_{max} (mg g ⁻¹)	Reference
Mg-Al	natural	33	Lazaridis et al. (2002)
Mg-Al	7	105	Kiso et al. (2005)
Li-Al	5	24	Liu et al. (2006)
Mg-Al	6	130	Violante et al. (2009)
Zn-Fe	7	97	Lu et al. (2015)
Mg-Fe	6	195	Caporale et al. (2011)
Mg-Al	7	126	Huang et al. (2015)
Mg-Fe	5.5 (controlled)	129	This study

Surface complexation modeling

Adsorption of As(V) on Mg-Fe LDH has been described using the DLM. The results indicate that the model works better for lower loading concentrations of As(V). First, surface reactions were used to include simple monodentate inner-sphere complexes. The average DLM stability constants for three different monodentate complexes (Table 2.1) can describe the pH-dependent As(V) adsorption on Mg-Fe LDH well below pH \sim 8 at higher As(V) concentrations (Fig. 2.2). An improvement in the DLM fit was observed with decreasing As(V) concentration since the DLM simulations describe the As(V) adsorption along a wider pH region (pH 5 – 10) at an As(V) concentration of 10⁻⁵ M. Nevertheless, the DLM does not correctly capture the measured data at higher pH values ranging from 8.5 to 12 and 10.5 to 12 at As(V) concentrations of 10⁻⁴ M and 10⁻⁵ M, respectively (Fig. 2.2). A possible explanation for these discrepancies is the formation of outer-sphere complexes that could not be described by the DLM. In general, As(V) adsorption decreases with increasing ionic strength, whereas the difference between the highest and the lowest ionic strength is more significant at 10⁻⁴ M As(V). However, the ionic strength dependence of As(V) adsorption is correctly captured by the simple DLM only for >SOAsO₃H⁻ and >SOAsO₃H₂ complexes. The results of DLM simulations for >SOAsO₃²⁻ also predict a decrease in adsorption with

decreasing ionic strength. According to the adsorption edge positions relative to the experimental data, the DLM best describes the formation of $>\text{SOAsO}_3\text{H}_2$ at 10^{-4} M As(V) and $>\text{SOAsO}_3\text{H}^-$ at 10^{-5} M As(V).

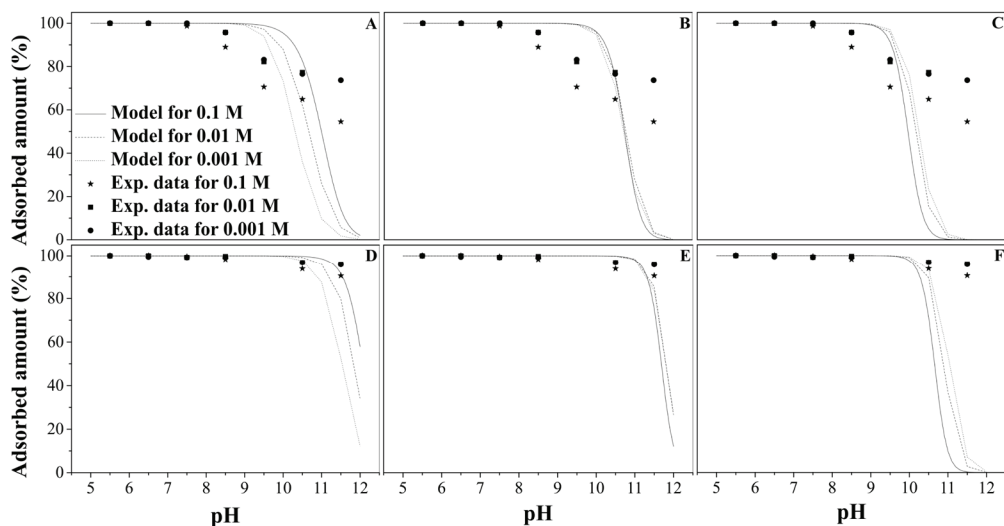


Fig. 2.2. Adsorption of monodentate inner-sphere complexes $>\text{SOAsO}_3^{2-}$ (A, D), $>\text{SOAsO}_3\text{H}^-$ (B, E) and $>\text{SOAsO}_3\text{H}_2$ (C, F) on Mg-Fe LDH at 10^{-4} (A-C) and 10^{-5} M (D-F) As(V).

Previously, the presence of monodentate mononuclear complexes was confirmed on Mg-Al LDHs using XPS by the stoichiometric ratio of the surface hydroxyl groups between the material before and after As(V) sorption (Goh et al., 2009). However, prior XAS spectroscopic studies performed on different LDHs (Izumi et al., 2005; Liu et al., 2006; Paikaray et al., 2013; Wang et al., 2009) indicated either the preferential formation of inner-sphere bidentate complexes (Goh et al., 2009; Paikaray et al., 2013) or outer-sphere complexes (Goh et al., 2009, 2010; Wang et al., 2009). Moreover, the simultaneous presence of both inner-and outer-sphere surface complexes has been also observed during on LDHs synthesized by the coprecipitation of individual metals with As(V) with the preferential formation of inner-sphere bidentate binuclear complexes (Sommella et al., 2015). To confirm the XAS spectroscopic observations, additional reactions involving the formation of bidentate surface complexes have been examined (Table 2.1). The DLM simulations for bidentate As(V) complexes did not significantly improve the fitting of the adsorption edges for 10^{-4} M As(V) compared with the monodentate complexes (Fig. 2.3). A satisfactory fit for the experimental data was observed for $>(\text{SO})_2\text{AsO}_2^-$ at 10^{-5} M As(V). Accordingly, the DLM with either the monodentate complex $>\text{SOAsO}_3\text{H}^-$ or bidentate complex $>(\text{SO})_2\text{AsO}_2^-$ can sufficiently

describe the pH-dependent As(V) adsorption on Mg-Fe layered double hydroxides from pH 5.5 to pH 11.5. As mentioned before, regarding the discrepancies between the model and the measured data above pH 11.5, the formation of outer-sphere complexes, which cannot be described by the DLM, are possible. Moreover, the adsorption of As(V) on the LDHs is affected by the type of interlayered anions, which have a strong influence on the formation of outer sphere complexes by way of anion exchange (Goh et al., 2010). However, carbonates are the most probable interlayered anions in Mg-Fe LDH (Seida et al., 2001) and due to their high affinity, adsorption is the most favourable mechanism (Violante et al., 2009). Otherwise, the effect of anion exchange is also expected (Huang et al., 2015).

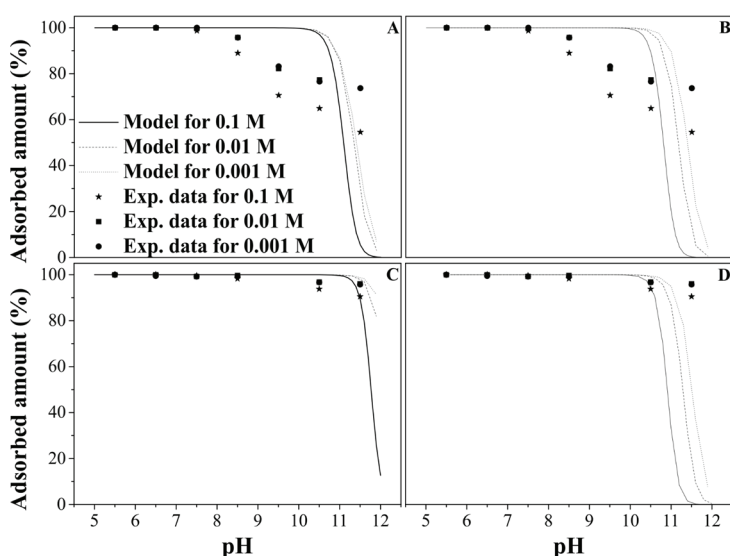


Fig. 2.3. Adsorption of bidentate inner-sphere complexes $>(\text{SO})_2\text{AsO}_2^-$ (A, C) and $>(\text{SO})_2\text{AsO}_2\text{H}$ (B, D) on Mg-Fe LDH at 10^{-4} (A-B) and 10^{-5} M (C-D) As(V).

Solid state analyses

The solid phase analyses of Mg-Fe LDH and Mg-Fe LDH after As(V) sorption (Mg-Fe LDH-As) were performed using various techniques including XRD, SEM/EDX, HR-TEM with elemental mapping, FTIR-ATR, XPS and low-temperature $^{57}\text{Mö}$ ssbauer spectroscopy. Mg-Fe LDH-As exhibited a relatively large amount of As(V) adsorbed (159 mg g^{-1}), which is comparable to other studies on LDHs (see Table 2.2 or Goh et al., 2008) and higher than commonly used Fe-based materials that is mostly lower than 60 mg g^{-1} (Micháľková et al., 2016a).

The XRD patterns of Mg-Fe LDH and Mg-Fe LDH-As are shown in Supplementary Fig. S2.3. The diffractogram of Mg-Fe LDH exhibited characteristic patterns for an LDH structure (Kang et al., 2013; Kuśtrowski et al., 2005) (see also Supplementary Material). All diffraction peaks shifted to lower values of 2Θ in the diffractogram of Mg-Fe LDH-As and no additional diffraction peaks appeared. However, a noticeable decrease of intensities of the reflections and a higher background occurred. Similar diffractograms following As(V) sorption were also observed in Kang et al. (2013) and Huang et al. (2015). The decreasing intensity of the reflections could be assigned to the leaching of Mg during the sorption process (Supplementary Fig. S2.4), especially since Mg leaching is strongly influenced by the pH. Generally, the leaching of Mg is observed in the pH range from 5 to 9 and increases with decreasing pH. Otherwise, the structure of the LDH remains stable. At lower pH values, dissolution occurs (Jobbágy and Regazzoni, 2011). The intensity of the reflections could also be caused by the decreasing crystallinity of the material as a result of the As(V) sorption process. To characterize this process further, the basal spacing of layers d_{003} and the cell parameters a and c were calculated (Supplementary Table S2.3). The cell parameters a and c correspond to the rhombohedral structure of LDHs and represent the average cation–cation distance and three times the basal spacing, respectively. The values of these parameters can be calculated from the positions of the (003), (006) and (110) diffraction lines (Evans and Slade, 2006; Klemkaite et al., 2011; Paikaray et al., 2013). Parameter a was calculated from the (110) diffraction line:

$$a=2d_{110} \quad (1)$$

Parameter c was calculated from the (003) and (006) diffraction lines:

$$c=3/2(d_{003} + 2d_{006}) \quad (2)$$

The value of parameter a did not change after the sorption of As(V). However, the basal spacing of the layers and parameter c increased. Generally, the basal spacing depends on the type of anion; and parameter c is a function of the average charge of the metal cations, the nature of the interlayer anions, a degree of hydration and general electrostatic interactions between the positive brucite-like sheets and the interlayer region (Cavani et al., 2001). The increase of both parameters has been assigned to the influence of anion exchange (Goh et al., 2010; Huang et al., 2015; Kang et al., 2013). As an interlayered anion, the affinity of CO_3^{2-} is higher than the affinity of AsO_4^{3-} (Miyata, 1983; Palmer et al., 2009; Sato, 1993; Violante et al., 2009). However, minor differences of these parameters can also be affected by structural changes of the

material after the sorption of As(V). Therefore, the sorption of As(V) on Mg-Fe LDH was likely influenced by both processes (i.e., adsorption and anion exchange) (Paikaray et al., 2013).

The SEM images of Mg-Fe LDH and Mg-Fe LDH-As showed slightly different particle sizes (Supplementary Fig. S2.5A-B). The distribution was probably caused by the sieving procedure (particles under 250 μm) during the preparation of the material. In general, LDHs prepared by the co-precipitation method at low supersaturation show agglomerated and irregular sheets that lie on top of one another (Cochechi et al., 2010). However, no obvious changes between individual materials have been found. Therefore, the chemical composition of the materials using the EDX analysis was measured (Supplementary Table S2.4). The EDX analysis of both materials identified C, O, Mg and Fe. However, the total amount of these elements differed after the sorption of As(V). First, the amount of Mg decreased. This result is attributed to the leaching of Mg during the sorption process, which is also consistent with the results from the XRD analysis. Of course, the decrease of Mg results in a percentage increase of Fe that was not leached during the sorption of As(V). A significant amount of As (13.7%) was observed in the EDX spectrum following sorption, and the same amount of As (14.0%) was found for Mg-Al LDH (Goh et al., 2009). However, we note that a smaller amount of As (8.1%) was described in (Huang et al., 2015). The morphological details of the samples were also studied by TEM (Supplementary Fig. S2.5C-D). The TEM image of Mg-Fe LDH showed characteristic hexagonal shape morphology of individual sheets (Abellán et al., 2015). Compared with the material before As(V) sorption, Mg-Fe LDH-As possessed a smoother surface (Yue et al., 2016). To identify the distribution of individual elements after As(V) sorption, elemental mapping of Mg, Fe, O and As was performed (Fig. 2.4A-E) and showed a homogenous distribution of all these elements. The similar distribution of As(V) could be assigned to anion exchange, as has been presented in previous studies based on Cr(VI) sorption on Mg-Al and Zn-Al LDHs (Yan et al., 2015a; Yu et al., 2012; Yue et al., 2016). The image containing Fe, As and O (Fig. 2.4F) indicate a slightly higher Fe content in the outer part of the aggregates relative to the other elements. The chemical composition of the marked mapped area is shown in Fig. 2.4G.

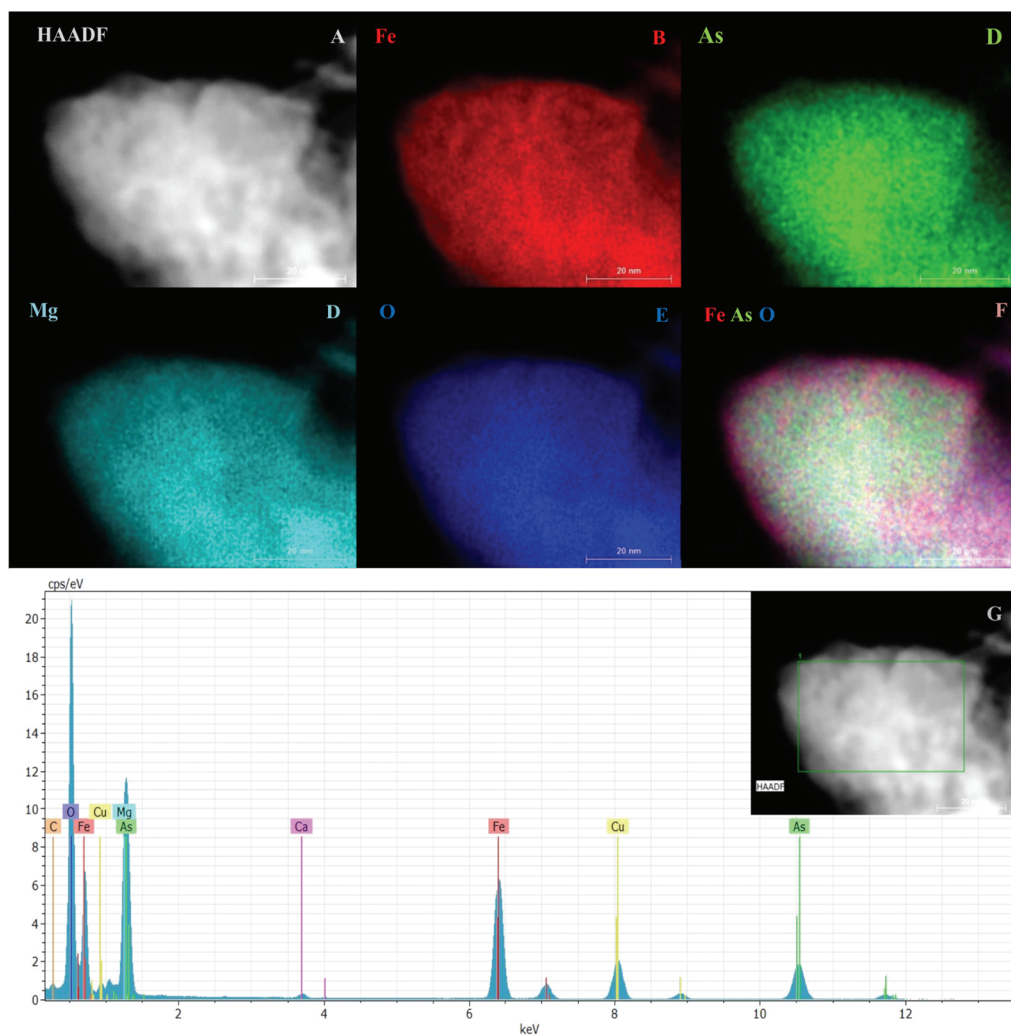


Fig. 2.4. Elemental mapping (A-F) and the chemical composition of the marked mapped area (G) of Mg-Fe LDH-As.

The FTIR-ATR spectra of both samples are given in Supplementary Fig. S2.6. As seen, the Mg-Fe LDH spectrum has characteristic bands corresponding to important binding arrangements (Cavani et al., 2001; Goh et al., 2008; Kang et al., 2013) (see also Supplementary Material). Mg-Fe LDH-As showed a lower intensity of signals, which is likely caused by structural changes of the material after As(V) sorption. Therefore, the measurement was performed at a different number of scans (i.e., 65 scans for Mg-Fe LDH and 750 scans for Mg-Fe LDH-As). Based on these properties, the intensity of the Mg-Fe LDH-As spectrum was even lower than that shown in Supplementary Fig. S2.6. Some changes in the Mg-Fe LDH-As spectrum are visible. The shift of the band

corresponding to the stretching vibration of hydroxyl groups from 3444 cm^{-1} to 3205 cm^{-1} could be a result of stronger and shorter hydrogen bonds with the oxygen atoms of the arsenate groups (Sumin de Portilla, 1974). The presence of stronger hydrogen bonds during the sorption of As(V) on hematite was observed by (Blanchard et al., 2012) and outer-sphere complexes were deemed to be the most favorable adsorption configuration. Moreover, the formation of outer-sphere complexes was assigned to the influence of an anion exchange mechanism for the As(V) sorption on the LDHs (Goh et al., 2010), which was confirmed by a decrease of the band corresponding to carbonates (Huang et al., 2015; Park and Kim, 2011). Finally, a new peak at 785 cm^{-1} in the Mg-Fe LDH-As spectrum indicates the formation of As-O bonds (Park and Kim, 2011).

The Mg 2s, Mg 2p, Fe 2p, C 1s and O 1s peaks appeared in the XPS spectrum of both samples (Supplementary Fig. S2.7). Additionally, peaks corresponding to As 3s (209.8 eV), As $3p_{1/2}$ (149.1 eV), As $3p_{3/2}$ (144.3 eV) and As 3d (45.2 eV) were identified after the sorption of As(V), a proof of effective adsorption onto the Mg-Fe LDH surface (Goh et al., 2009; Kang et al., 2013; Paikaray et al., 2013; Yoshida et al., 2015). A decreasing intensity of the Mg 2s and Mg 2p peaks following As(V) adsorption corresponds to the partial leaching of Mg during the sorption process, which is consistent with the XRD and EDX analysis. The intensity of the Fe 2p peak increased and a spectral shift to lower binding energy was observed, indicating a strong interaction between As(V) and Fe (Goh et al., 2009). Further, both contributions from Fe 2p (i.e., Fe $2p_{1/2}$ and Fe $2p_{3/2}$) correspond to Fe(III) (Hadnadjev et al., 2008; Han et al., 2013; Paikaray et al., 2013). The C 1s peak is composed of two contributions. The larger contribution at lower binding energies reflects atmospheric CO_2 and the smaller contribution at higher binding energies corresponds to CO_3^{2-} . The intensity of both peaks decreased significantly after the adsorption of As(V) on Mg-Fe LDH. The decreasing intensity of the peak corresponding to carbonates is assigned to the partial replacement of the interlayered CO_3^{2-} by As(V), as was described in Huang et al. (2015), and corresponds with the results from the XRD and FTIR-ATR analyses. A decreasing intensity and different shape of the O 1s peak was observed as a result of changes to the oxygen compounds on the Mg-Fe LDH-As surface (Goh et al., 2009; Kang et al., 2013). Based on the peaks in the XPS spectra, the surface stoichiometry of the samples was calculated (Supplementary Table S2.5).

The deconvolution of the O 1s peak of Mg-Fe LDH and Mg-Fe LDH-As is given in Fig. 2.5.A and Fig. 2.5B, respectively. The O 1s peak of Mg-Fe LDH was deconvoluted into three components corresponding to the M-O bond (529.6 eV), the M-OH bond

(531.2 eV) and carbonates (533.6 eV). However, the contributions of Mg and Fe oxides and hydroxides for the O 1s peak cannot be clearly separated (Kang et al., 2013; Leftheriotis et al., 2003). The O 1s spectrum of Mg-Fe LDH-As was deconvoluted into four components corresponding to the M-O bond (530.3 eV), the As-O bond (531.1 eV), the M-OH bond (532.0 eV) and chemically or physically adsorbed water (532.9 eV) (Kang et al., 2013; Zhang et al., 2010). Generally, the binding energies of carbonates and water are often overlapped in the O 1s peak. Therefore, an appropriate contribution for the deconvolution was chosen by the intensity of the C 1s in the XPS spectrum of Mg-Fe LDH and Mg-Fe LDH-As. As mentioned before, the intensity of the C 1s in the Mg-Fe LDH-As spectrum was very low; thus water was chosen as an appropriate contribution for the deconvolution procedure. The XPS results indicate that chemical adsorption is preferable, which is consistent with the results from the adsorption modeling (Sections *Equilibrium adsorption experiments* and *Surface complexation modeling*).

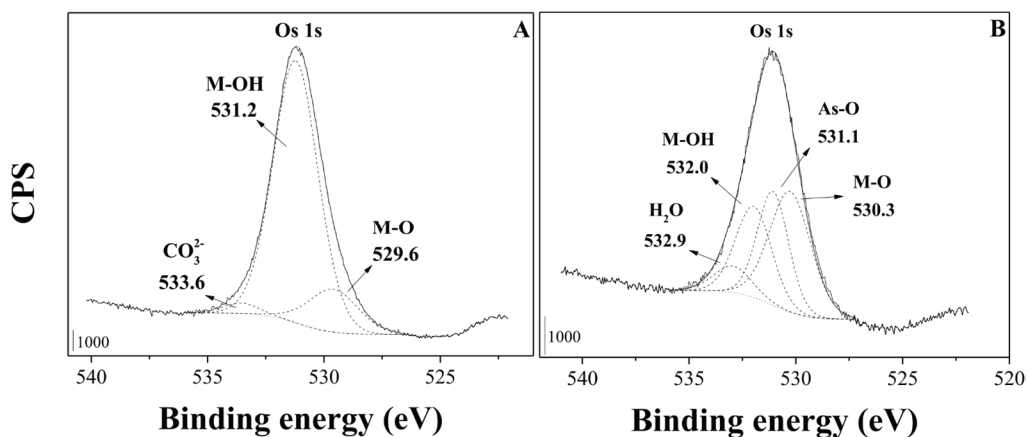


Fig. 2.5. Deconvolution of the O 1s peak of Mg-Fe LDH (A) and Mg-Fe LDH-As (B).

The low-temperature Mössbauer spectra on isotope ⁵⁷Fe measured before and after As(V) sorption are almost identical (Supplementary Fig. S2.8). The doublet-form (i.e., one doublet for Fe(III) in the case of sample Mg-Fe LDH and two doublets for Fe(III) and Fe(II) in the case of sample Mg-Fe LDH-As) of the spectra indicates paramagnetic (or superparamagnetic) ordering of both materials at a temperature of 5 K, which is consistent with an LDH structure. The slight asymmetry of the Fe(III)-doublets suggests that LDH phase is somehow textured in both samples. This result corresponds to the TEM observations. The slight shift of the hyperfine parameters (i.e., isomer shift, quadrupole splitting, line width; see Supplementary Table S2.6) toward higher values for Mg-Fe LDH-As could indicate a higher degree of structural disorder compared with

Mg-Fe LDH. This observation could be linked with the partial leaching of Mg, leading to an increased number of vacancies and overall structural disorder of the LDH. From the Mg-Fe LDH-As spectrum, 6% of the Fe atoms appear to be in the Fe(II) valence state. However, there was no indication of newly formed ferric oxides/hydroxides upon As(V) sorption on the LDH.

Conclusions

The Mg-Fe LDH synthesized by the co-precipitation method showed a promising As(V) sorption efficiency. The adsorption processes were successfully described by adsorption modeling; specifically, the adsorption kinetics by the pseudo-second order model and the equilibrium data by the Freundlich model. For further insight into the sorption mechanism, a diffuse layer model was constructed to describe the pH-dependency of As(V) sorption. The best fit was obtained for $>SOAsO_3H^-$ monodentate and $>(SO)_2AsO_2^-$ bidentate inner-sphere complexes. Notably, adsorption modeling was supported by various solid-state analyses. XPS analysis confirmed that the main sorption mechanism was chemical adsorption. The influence of anion exchange, which contributed to the formation of the outer-sphere complexes, was proposed according to XRD and the FTIR analyses. Moreover, elemental mapping by HR-TEM showed a homogenous distribution of As(V), indicating the possible influence of anion exchange. A higher degree of structural disorder of the material following As(V) sorption was established by the slight shift of hyperfine parameters to higher values as determined by low-temperature Mössbauer spectroscopy on isotope ^{57}Fe . In conclusion, adsorption modeling coupled with solid state analyses effectively describe the adsorption mechanism of As(V) on Mg-Fe LDH. For this reason, we recommend this comprehensive approach for further studies on metal/metalloid adsorption onto synthetic materials.

Supplementary Material

Materials and methods

Synthesis and basic properties of the Mg-Fe LDH

First, $\text{MgCl}_2 \cdot 6\text{H}_2\text{O}$ (30.50 g) and $\text{FeCl}_3 \cdot 6\text{H}_2\text{O}$ (9.05 g) were dissolved in 200 mL of deionized water and stirred vigorously. Second, the solution was titrated to pH 13.3 with 2.5 M KOH and stirred for 24 h at room temperature. The mixture was then filtered (cellulose; basic weight: 84 g/m²) and washed with demineralized water to remove residual chemicals (e.g., Cl⁻). Subsequently, the wet solid sample was dried at 393 K for 12 hours. The dried sample was then milled and sieved (< 250 μm) (Seida et al., 2001). The yield of the single synthesis was 12 g and the synthesis procedure was repeated in triplicates. All solid samples were mixed and the representative sample for further measurements was chosen by the quartering.

Acid-base potentiometric titration

The titration of the LDH-H⁺ system was performed in triplicates in suspension with a Mg-Fe LDH concentration of 12.5 g L⁻¹ (0.5 g of solid phase in 40 mL of 0.1 M NaNO₃ background electrolyte) according to (Jolstera et al., 2010). First, the suspension was titrated to pH 12 by adding 0.1 M NaOH under constant stirring and a N₂ atmosphere using an automatic TitroLine® *alpha plus* Titration Unit (Schott, Germany). The solution was then titrated to pH 6 using 0.1 M HNO₃. Titration data were used to optimize the adjustable model parameters (including surface protonation constants and the total number of surface sites) using the program ProtoFit 2.1 (Turner and Fein, 2006) and are presented in Supplementary Fig. S2.1.

Adsorption edge experiments

The surface complexation constants for As(V) were obtained using FITEQL 4.0 (Herbelin and Westall, 1999) and the reactions in Table 2.1. The values of the surface protonation constants and the total number of surface sites were obtained from the titration data (Table 2.1). Then, the average stability constant for a given reaction stoichiometry was included in the thermodynamic database program of Visual MINTEQ 3.1 (Gustafsson, 2013) to obtain the final DLM for As(V) adsorption onto the LDHs. For this study, the DLM was tested to provide a good fit to the experimental adsorption data. Although the DLM only enables a description of the formation of the

inner-sphere complexes, this model was chosen because of its simplicity since it requires a minimum number of adjustable model parameters (Goldberg et al., 2007). The goodness of fit of each calculated edge to the experimental data was assessed using the WSOS/DF ratio.

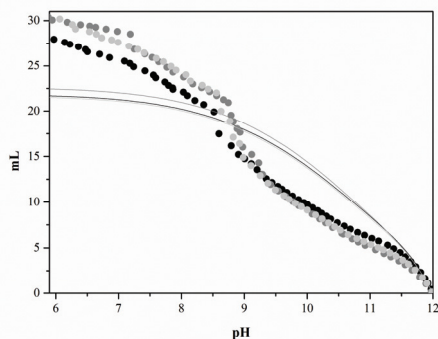


Fig. S2.1. Potentiometric titration data and DLM model for Mg-Fe LDH at ionic strength of 0.1 M NaNO_3 .

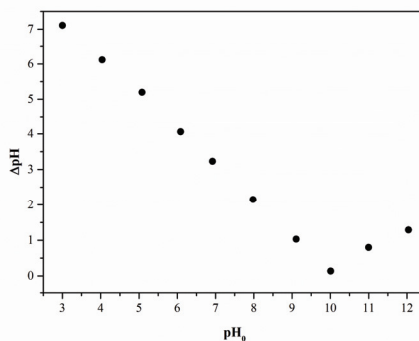


Fig. S2.2. pH_{PZC} of Mg-Fe LDH determined by the immersion technique.

Results and discussion

Kinetic adsorption experiments

The pseudo-first order kinetics is represented by:

$$q_t = q_e(1 - e^{-k_1 t}) \quad \text{Eq. S2.1}$$

where q_t and q_e (mg g^{-1}) describe the adsorbed amount at time t (min) and at the equilibrium time, respectively, and the constant k_1 (min^{-1}) is the pseudo-first order rate coefficient. The pseudo-second order kinetics is given by:

$$q_t = k_2 q_e^2 t / (1 + k_2 q_e t) \quad \text{Eq. S2.2}$$

where q_t and q_e (mg g^{-1}) correspond to the adsorbed amount at time t (min) and at the equilibrium time, respectively, and the constant k_2 [$\text{g} (\text{mg min})^{-1}$] is the pseudo-second order rate coefficient (Gupta and Bhattacharyya, 2011; Simonin et al., 2016).

Table S2.1 Parameters of the non-linear modeling using the pseudo-first and pseudo-second order kinetic for adsorption of As(V) on Mg-Fe LDH.

		pH 5.5	pH 8.5
Pseudo-first order	$q_{e(exp)}$ (mg g ⁻¹)	7.79	7.18
	q_e (mg g ⁻¹)	7.69	6.69
	k_1 (min ⁻¹)	0.46	0.25
	R^2	0.97	0.93
Pseudo-second order	q_e (mg g ⁻¹)	8.07	7.22
	k_2 [g (mg min) ⁻¹]	0.10	0.05
	R^2	0.99	0.99

Equilibrium adsorption experiments

The non-linear form of the Langmuir equation is given by:

$$q_e = q_{max} K_L c_e / (1 + K_L c_e) \quad \text{Eq. S2.3}$$

where c_e and q_e correspond to the equilibrium concentration in the solution (mg L⁻¹) and the adsorbed amount at equilibrium (mg g⁻¹), respectively. The parameters q_{max} and K_L are the maximum adsorption capacity (mg g⁻¹) and the Langmuir constant related to the affinity to the adsorbate (L mg⁻¹), respectively. The non-linear form of the Freundlich equation is given by:

$$q_e = K_F c_e^{1/n} \quad \text{Eq. S2.4}$$

where c_e and q_e correspond to the equilibrium concentration in the solution (mg L⁻¹) and the adsorbed amount at equilibrium (mg g⁻¹), respectively. The parameters K_F and n are the Freundlich constant [(mg g⁻¹)(L mg⁻¹)^{1/n}] and a dimensionless constant that describes the influence of the surface heterogeneity on the adsorption process, respectively (Foo and Hameed, 2010).

Table S2.2 Parameters of the non-linear modeling using the Langmuir and Freundlich model for adsorption of As(V) on Mg-Fe LDH.

		pH 5.5	pH 6.5	pH 7.5
Langmuir model	$q_{max(exp)}$ (mg g ⁻¹)	131	96.4	30.8
	q_{max} (mg g ⁻¹)	129	90.1	25.5
	K_L (L mg ⁻¹)	0.10	0.06	5.02
	R^2	0.92	0.91	0.86
Freundlich model	n (-)	4.04	3.87	6.10
	K_F [(mg g ⁻¹)(L mg ⁻¹) ^{1/n}]	34.4	20.6	14.3
	R^2	0.97	0.99	0.90

Solid state analyses

Reflections on the basal planes, characterized by sharp and symmetric peaks, were observed at low and high values of 2Θ (11.42, 22.87, 59.48 and 60.78) and belonged to the Miller indexes (003), (006), (110) and (013). However, reflections on the non-basal planes, characterized by broad and asymmetric peaks, were found in the middle of the 2Θ values (34.05, 38.52 and 45.55) and belonged to the Miller indexes (009), (015) and (018). Reflections corresponding to the Miller indexes (110) and (013) are known to result from a highly crystalline structure (Kang et al., 2013; Kuśtrowski et al., 2005).

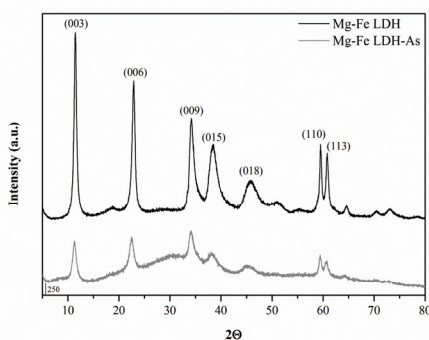
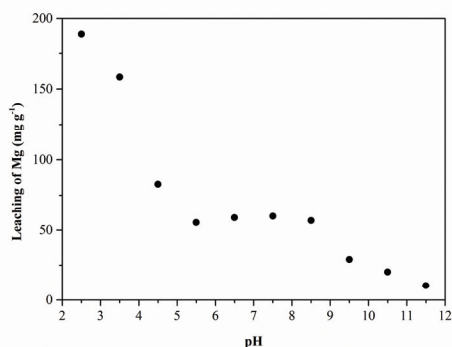
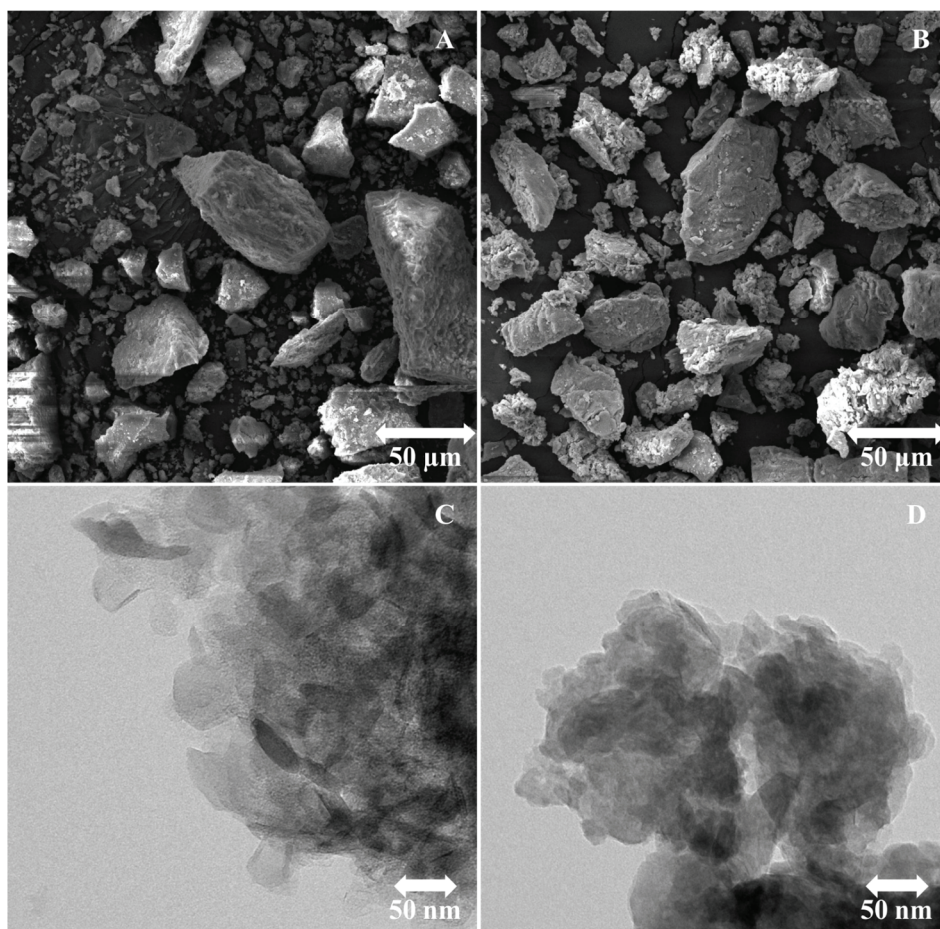
**Fig. S2.3.** XRD patterns of Mg-Fe LDH and Mg-Fe LDH-As**Fig. S2.4.** Leaching of Mg during the sorption of As ($c_0 = 10^{-4}$ M) at different pH values (in 0.01 M NaNO₃ for 120 min).

Table S2.3 The basal spacing of layers and the cell parameters calculated from diffractograms of Mg-Fe LDH and Mg-Fe LDH-As.

Material	d_{003} (Å)	d_{006} (Å)	d_{009} (Å)	d_{010} (Å)	a (Å)	c (Å)
Mg-Fe LDH	7.748	3.888	2.633	1.554	3.108	23.24
Mg-Fe LDH-As	7.826	3.947	2.947	1.556	3.111	23.48

Table S2.4 The EDX analysis of Mg-Fe LDH and Mg-Fe LDH-As.

%	Mg-Fe LDH	Mg-Fe LDH-As
C	18.42	13.59
O	59.25	47.27
Mg	15.58	10.64
Fe	6.67	15.07
As	-	13.73

**Fig. S2.5.** SEM (A, B) and TEM images (C, D) of Mg-Fe LDH (A, C) and Mg-Fe LDH-As (B, D).

The broad band at 3444 cm^{-1} corresponds to the stretching vibration of hydroxyl groups in the brucite-like layers. The bending vibration of water occurs at 1637 cm^{-1} . The absorption band of CO_3^{2-} in the interlayered region is observed at 1361 and 643 cm^{-1} . Finally, the region at approximately 535 cm^{-1} indicates the vibrations of M-O and/or M-OH (Cavani et al., 2001; Goh et al., 2008; Kang et al., 2013).

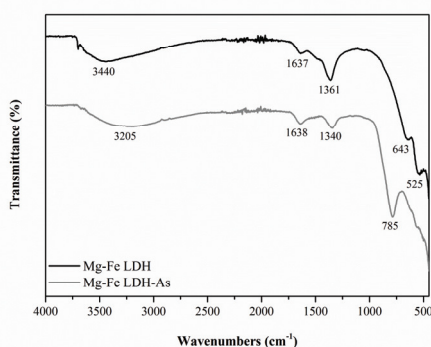


Fig. S2.6. FTIR-ATR spectra of Mg-Fe LDH and Mg-Fe LDH-As.

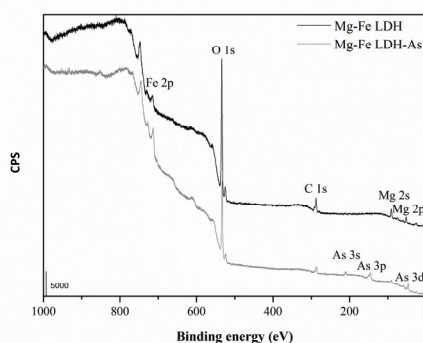


Fig. S2.7. The XPS spectra of Mg-Fe LDH and Mg-Fe LDH-As.

Table S2.5 The surface stoichiometry (%) of Mg-Fe LDH and Mg-Fe LDH-As.

	Mg-Fe LDH	Mg-Fe LDH-As
Fe 2p	1.4	4.0
Mg 2s	35.9	15.5
O 1s	45.5	55.8
C 1s	17.2	18.1
As 3p	-	6.6

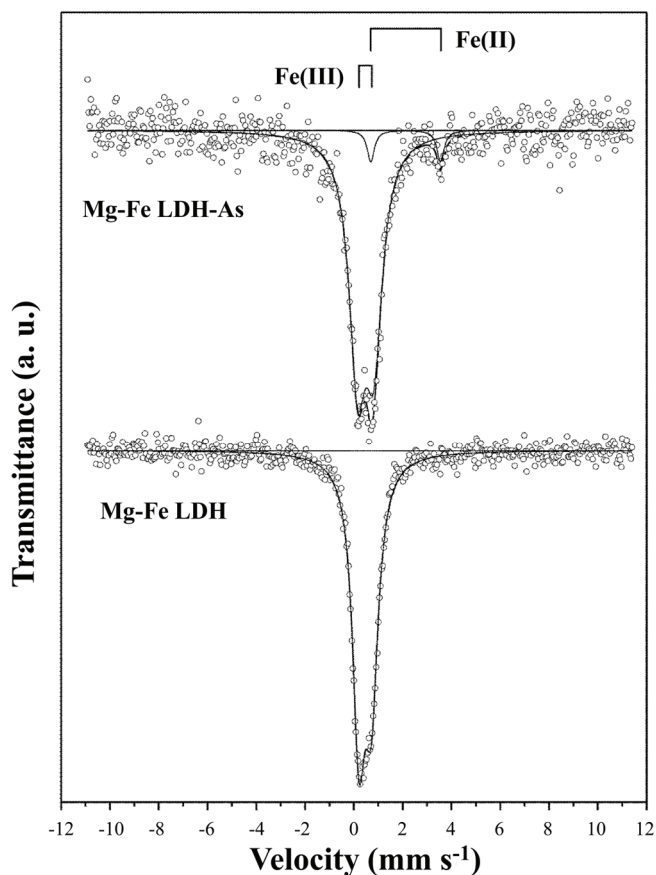


Fig. S2.8. Low-temperature Mössbauer spectra on isotope ^{57}Fe of Mg-Fe LDH and Mg-Fe LDH-As.

Table S2.6 Low-temperature (5 K) ^{57}Fe Mössbauer hyperfine parameters for Mg-Fe LDH and Mg-Fe LDH-As.

Sample	δ (mm s $^{-1}$)	ΔE_Q (mm s $^{-1}$)	RA (%)	Assignment
Mg-Fe LDH	0.46	0.52	100	Fe(III)
Mg-Fe LDH-As	0.48	0.67	94	Fe(III)
	2.12	2.86	6	Fe(II)

Notations: δ – isomer shift (± 0.02 mm s $^{-1}$), ΔE_Q – quadrupole splitting (± 0.02 mm s $^{-1}$) and RA – relative area in the spectrum ($\pm 3\%$).

Chapter III

Highly effective Zn(II) and Pb(II) removal from aqueous solutions using Mg-Fe layered double hydroxides: Comprehensive adsorption modeling coupled with solid state analyses

B. Hudcová, V. Veselská, J. Filip, S. Číhalová, M. Komárek

Adapted from Journal of Cleaner Production 171 (2018): 944-953

Content

Abstract	65
Introduction	66
Materials and methods	68
Materials	68
Synthesis and characterization of Mg-Fe LDHs with different Mg/Fe molar ratios	68
Kinetic and equilibrium adsorption experiments	68
Surface complexation modeling	68
Solid state analyses after Zn(II) and Pb(II) sorption	69
Results and discussion	70
Characterization of materials	70
Kinetic and equilibrium adsorption experiments	70
Surface complexation modeling	73
Solid state analyses of Mg-Fe LDH samples after Zn(II) and Pb(II) sorption	76
Conclusions	83
Supplementary Material	84

Abstract

Comprehensive mechanistic and modeling approaches are needed to effectively evaluate sorption of metal ions from aqueous solutions. However, such a complex study using layered double hydroxides has not yet been presented. Therefore, adsorption modeling was performed coupled with solid state analyses describing the mode of zinc and lead removal by magnesium-iron layered double hydroxides, and an excellent removal efficiency for both metal ions was observed. The maximal adsorbed concentration, as established by the Langmuir model, increased with the increasing magnesium/iron molar ratio. The pH-dependent sorption was fitted by the diffuse layer model, which described the formation of monodentate inner-sphere complexes, indicating strong binding between metal ions and the layered double hydroxides surface. Based on the solid state analyses of materials with high surface concentrations of zinc (1.44 mmol g^{-1}) and lead (1.65 mmol g^{-1}), respectively, the whole sorption mechanism was also influenced by other processes, i.e., precipitation (lead) and surface accumulation/precipitation/isomorphic substitution (zinc). Transmission electron microscopy-based elemental mapping showed a heterogeneous distribution of zinc and lead on the surface of particles. Low-temperature Mössbauer spectra were nearly identical for the studied materials before/after zinc and lead sorption indicating no structural changes in incorporated iron. Generally, we suggest that these layered double hydroxides are highly effective sorbents for metal ions from aqueous solutions. Furthermore, we propose a comprehensive mechanistic/modeling approach as a powerful tool for describing the mechanism of metal ions binding on layered double hydroxides in contaminated waters.

Introduction

Layered double hydroxides (LDHs) have been proposed as universal low-cost sorbents that can effectively remove various contaminants from real drinking/waste/ground water samples contaminated by oxyanions, e.g., AsO_3^{3-} (Jiang et al., 2015), AsO_4^{3-} (Ha et al., 2016), CrO_4^{2-} (Zhang et al., 2012b), PO_4^{3-} (Drenkova-Tuhtan et al., 2013), SO_4^{2-} (Sepehr et al., 2014), boron species, e.g., H_3BO_3 and/or $\text{B}(\text{OH})_4^-$ (Kameda et al., 2017), monoatomic anions, e.g., Br^- (Echigo et al., 2007) and F^- (Elhalil et al., 2016), organics (Teixeira et al., 2014) and metal ions, e.g., Zn^{2+} (Zhang et al., 2012b). However, there are a lack of comprehensive studies based on sorption of metal ions including accessible and powerful approaches. Therefore, we propose mechanistic adsorption modeling coupled with solid state analyses for predicting the reactions on the LDH surface during the sorption process. Layered double hydroxides (LDHs) are layered materials with positively charged brucite-like layers consisting of octahedrally coordinated divalent and trivalent metal cations. The positive charge of the layers is compensated by intercalated anions. The interlayered region also contains water molecules. A general formula for the LDH structure is given by $[\text{M}_{1-x}\text{M}_x^{3+}(\text{OH})_2]^{x+}[\text{A}_{x/n}^{n-} \cdot y\text{H}_2\text{O}]^{x-}$, where M^{2+} and M^{3+} mean divalent (e.g., Mg^{2+} or Zn^{2+}) and trivalent cations (e.g., Fe^{3+} or Al^{3+}) and A^{n-} corresponds to appropriate n-valence anions (e.g., CO_3^{2-} or NO_3^-). The symbol x describes the trivalent metal ratio $\text{M}^{3+}/(\text{M}^{2+}+\text{M}^{3+})$ (Cavani et al., 1991; Liang et al., 2013). Generally, the sorption mechanism for metal ions by LDHs intercalated with inorganic anions is performed by adsorption through bonding with surface hydroxyl groups (surface complexation), isomorphic substitution, and precipitation of metal hydroxides and/or carbonates on the surface of the LDHs (Liang et al., 2013). The sorption mechanism has been described previously by various techniques including SEM/EDX, TEM, XRD, FTIR, XPS (Sun et al., 2015a; Xiao et al., 2015; Liang et al., 2009; Park et al., 2007) and/or EXAFS (Izumi et al., 2005; Izumi et al., 2002). However, the emphasis was mainly put on Mg-Al LDHs and their thermal thermally products (CLDHs) (Liang et al., 2013) that contain potentially risky Al(III). Moreover, the production of CLDHs is more expensive due to the thermal treatment. There are just a few studies (Izumi et al., 2005; Izumi et al., 2002; Liang et al., 2009; Seida et al., 2001) that focused on metal ions sorption by Mg-Fe LDHs and CLDHs as more environmental friendly materials. Moreover, there are a lack of studies dealing with the effect of different M(II)/M(III) molar ratios on the removal efficiency.

Generally, the mobility and speciation of metals is strongly influenced by the pH value controlling their leaching (desorption) at lower pH values and the precipitation of metal hydroxides and/or carbonates at higher pH values (Hashim et al., 2011). Most of the

sorption studies of metal ions on LDHs were performed without pH adjustment resulting in preferential metal precipitation caused by the buffering effect of the LDHs (Fujji et al., 1992; González et al., 2015; Seida et al., 2001). To differentiate between precipitation and adsorption, the pH during the sorption process needs to be adjusted. Moreover, pH-dependent sorption enables the development of surface complexation models (SCMs) that describe the binding of metal ions onto solid materials depending on the pH, ionic strength and sorbate concentration (Komárek et al., 2015; Veselská et al., 2016). An SCM has been successfully optimized in our previous studies based on As(V) sorption on Mg-Fe LDH (Hudcová et al., 2017). However, an SCM describing metal ions sorption on LDHs or CLDHs has not been performed at all.

The aim of this study is to describe the sorption mechanisms and competition of Zn(II) and Pb(II) on Mg-Fe LDHs by complex adsorption modeling coupled with the solid-state analyses (XRD, SEM/EDX, FTIR-ATR, XPS, HR-TEM with elemental mapping and low-temperature ^{57}Fe Mössbauer spectroscopy). Both metals reflect contrasting geochemical behavior although they commonly occur together in contaminated water and soil due to industrial activities (Ettler et al., 2006), while the presence of Pb(II) can decrease the sorption efficiency of Zn(II) (Kumpiene et al., 2008). The basic adsorption mechanism of Zn(II) and Pb(II) was described by adsorption kinetic and equilibrium experiments. Moreover, the effect of different Mg/Fe molar ratios on adsorption properties was also studied. Finally, the pH-dependent equilibrium data were described by the diffuse layer model (DLM).

Materials and methods

Materials

All chemical reagents were analytical grade without any purification or treatment. All solutions were prepared using deionized water (18.2 M Ω). HNO₃ and NaOH solutions (0.001, 0.01 and 0.1 M) were used to adjust the pH value during sorption experiments.

Synthesis and characterization of Mg-Fe LDHs with different Mg/Fe molar ratios

The Mg-Fe LDHs with different Mg/Fe molar ratios were synthesized by the coprecipitation method described in Seida et al. (2001). The synthesis procedure is given in detail in the Supplementary Material. The structural characterization of synthesized materials was determined by X-ray diffraction analysis (XRD) using a PANalytical X'Pert PRO diffractometer with an X'Celerator detector (CuK α radiation, 40 kV, 30 mA, a measuring step 0.02° s⁻¹ in the range 10 to 80° 2 Θ). The chemical composition of material was measured using ICP-OES (Agilent Technologies 720 Series) after dissolution in 0.1 M HNO₃. The pHPZC of material was determined by the immersion technique described by Fiol and Villaescusa (2009). The specific surface area was determined by N₂ adsorption at 77 K (BET analysis) using an ASAP 2050 (Micrometrics Instrument Corporation, USA).

Kinetic and equilibrium adsorption experiments

Kinetic experiments were performed in individual batches using single- and multi-metal solutions with Zn(II) and Pb(II) concentrations of 0.1 mM according to our previous studies (Hudcová et al., 2017). The detailed experimental conditions are given in the Supplementary Material. The equilibrium adsorption experiments were performed in individual batches according to our previous studies (Hudcová et al., 2017) at initial Zn(II) and Pb(II) concentrations ranging from 0.03 to 3 mM and at pH 5.5. Detailed experimental conditions are given in the Supplementary Material.

Surface complexation modeling

The characterization of the protonation behavior of the Mg-Fe LDH-4 surface (surface protonation constants and the total number of surface sites) was performed by acid-base potentiometric titrations (Rojas Delgado et al., 2004; Turner and Fein, 2006). The

details of the titration of the LDH-H⁺ system and the modeled titration data are given in the Supplementary Material (Fig. S3.1). The adsorption edge experiments of Zn(II) and Pb(II) on Mg-Fe LDH-4 were conducted according to our previous studies (Hudcová et al., 2017) and detailed experimental conditions are given in the Supplementary Material. The adsorption edge data were used to calibrate the two-pK DLM describing the formation of inner-sphere complexes (Goldberg et al., 2007; Gustafsson, 2013; Herbelin and Westall, 1999). The goodness-of-fit $V(Y)$ of the DLM to the experimental data was assessed according to Heinrich et al. (2008) and Reich et al. (2010) and is generally considered to be reasonable if it is between 1 and 20 (at 95% confidence interval). More information is available in the Supplementary Material. All established constants are given in Table S3.1.

Solid state analyses after Zn(II) and Pb(II) sorption

The solid samples before (Mg-Fe LDH-4) and after Zn(II) and Pb(II) sorption (Mg-Fe LDH-Zn and Mg-Fe LDH-Pb) were characterized by a robust combination of the following techniques: XRD analysis (see Section *Synthesis and characterization of Mg-Fe LDHs with different Mg/Fe molar ratios*) was performed to identify the structures of all materials and the possible formation of new phases. A scanning electron microscope (SEM; Tescan, Inc., USA) and energy dispersive X-ray spectroscopy (EDX; Bruker Quantax, USA) were used to study the morphology and the chemical composition of the materials. Material morphology was visualized by high-resolution transmission electron microscopy (HR-TEM; TITAN 60-300 microscope with an X-FEG type emission gun operating at 80 kV). The distribution of individual elements after Zn(II) and Pb(II) sorption was studied by elemental mapping performed by the STEM-Energy Dispersive X-ray Spectroscopy (EDX) with an acquisition time of 20 min. Fourier transform infrared spectroscopy in attenuated total reflection mode using a diamond crystal (FTIR-ATR; Nicolet 6700) enabled the establishment of characteristic functional groups. The surfaces of materials, including the surface stoichiometry, was described using X-ray photoelectron spectroscopy (XPS; Omicron Nanotechnology, Ltd). The spectra were deconvoluted using the Casa XPS program. The low-temperature (5 K) transmission ⁵⁷Fe Mössbauer spectra were collected with constant acceleration mode using an MS96 spectrometer equipped with a ⁵⁷Co(Rh) radioactive source (1.85 GBq). The values of the hyperfine parameters (e.g., isomer shifts) were calibrated against a metallic iron (α -Fe) foil at room temperature. The spectra were fitted by Lorentz functions using the CONFIT2000 software (Žák and Jirásková, 2006).

Results and discussion

Characterization of materials

Diffraction patterns of synthesized Mg-Fe LDHs with different Mg/Fe molar ratios exhibited characteristic patterns for the LDH structure, i.e., sharp and symmetric peaks at low and high values of 2θ and broad and asymmetric peaks in the middle of the 2θ values (see Fig. S3.2). Reflections corresponding to Miller indexes (110) and (013) suggested a highly crystalline structure of the as-prepared materials. Moreover, the increasing Mg/Fe molar ratio led to the increasing intensity of all reflections, except for the reflection corresponding to Miller index (015), which is caused by the increasing crystallinity of materials (Kang et al., 2013; Seida and Nakano, 2000). However, some changes in the relative intensity of particular diffraction peaks in the diffraction pattern of Mg-Fe LDH-3 also occurred resulting in increasing intensity of the reflection corresponding to Miller index (015). This effect could be assigned to some structural disorder in the material (Cavani et al., 1991). Moreover, a small peak at 18.81° in the diffraction patterns of Mg-Fe LDH-3 and Mg-Fe LDH-4, respectively, meant the formation of $\text{Mg}(\text{OH})_2$ during the synthesis, i.e., not all $\text{Mg}(\text{II})$ was incorporated into the structure of the synthesized LDHs. The basal spacing of layers d_{003} and cell parameters a and c calculated from the (003), (006) and (110) diffraction peaks (Evans and Slade, 2006; Klemkaite et al., 2011) are given in Table S3.2. The values of all cell parameters increased due to the increasing Mg/Fe molar ratio as was described in Kang et al. (2013). However, the Mg-Fe LDH-3 showed higher values of the cell parameters than Mg-Fe LDH-4. As has been mentioned before, this effect was probably caused by some structural disorder of the Mg-Fe LDH-3.

The general properties of synthesized Mg-Fe LDHs with different Mg/Fe molar ratios are given in Table S3.3. The Mg/Fe molar ratios in all materials determined by acid dissolution were slightly overestimated, which was probably caused by the synthesis procedure as has been mentioned by the XRD analyses (i.e., dissolution of redundant Mg). The pH_{ZPC} of all materials was similar. The specific surface area decreased with the increasing Mg/Fe molar ratio corresponding to the increasing crystallinity of the materials as was described by the XRD analyses.

Kinetic and equilibrium adsorption experiments

Adsorption kinetics enable the determination of the removal rate and the adsorption efficiency of $\text{Zn}(\text{II})$ and $\text{Pb}(\text{II})$ on LDHs (González et al., 2015; Liang et al., 2009; Sun

et al., 2015a). The removal efficiency for Zn(II) and Pb(II) is given in Fig. S3.3. The excellent removal efficiency (100%) for both metal ions (ad)sorbed on all materials was observed in the experiments without pH control (Fig. S3.3A-B). The change of pH during kinetic experiments is shown in Fig. S3.3C-D. The pH value increased from the initial pH of 5.5 to the final pH of approximately 8.5-9.5, which was also observed by González et al. (2015), indicating a strong buffering effect for Mg-Fe LDHs (Seida et al., 2001). Therefore, these sorption processes were mainly affected by precipitation of carbonates and/or hydroxides as was confirmed by the oversaturation of such species using the program Visual MINTEQ 3.1. To avoid these artefacts, the removal efficiency at controlled pH 5.5 was determined (Fig. S3.3E-F). Based on these results, the removal efficiency for Zn(II) strongly depended on the Mg/Fe molar ratio, i.e., Mg-Fe LDH-2 (60%) < Mg-Fe LDH-3 (63%) < Mg-Fe LDH-4 (77%). However, the removal efficiency for Pb(II) was nearly the same for all materials, i.e., 97% for Mg-Fe LDH-2, 93% for Mg-Fe LDH-3 and 98% for Mg-Fe LDH-4. Subsequently, kinetic data at pH 5.5 (not influenced by precipitation) (Fig. 3.1A-B) were modeled by the non-linear form of pseudo-first and pseudo-second order kinetics (Gupta and Bhattacharyya, 2011; Simonin, 2016). Based on the results described by Simonin (2016), only the experimental data near the equilibrium ($t = 20$ min) were modeled. The use of such experimental data results in a significant improvement of the pseudo-first order kinetics that is commonly undervalued in comparison with pseudo-second order kinetics. Experimental values of the adsorbed amount at equilibrium ($q_{e(exp)}$), calculated parameters (q_e , k_1 and k_2) and correlation coefficients (R^2) are given in Table S3.4. The experimental data of Zn(II) and Pb(II) adsorption on Mg-Fe LDH-2 were better fitted by the pseudo-second order kinetics that are commonly used for kinetic data of metal ions sorption on LDHs and CLDHs (González et al., 2015; Xiao et al., 2015; Zhao et al., 2011). However, the correlation coefficients for both models of Zn(II) and Pb(II) adsorption on Mg-Fe LDHs with higher Mg/Fe molar ratios were equal. The adsorbed amount at equilibrium (q_e) for both metal ions on all materials increased with increasing molar ratios. The rate coefficients (k_1 and k_2) for Zn(II) were significantly lower for data describing sorption on Mg-Fe LDH-3. Similar values were observed for Mg-Fe LDH-2 and Mg-Fe LDH-4. It is important to note that k_1 and k_2 describing Pb(II) sorption were strongly influenced by the Mg/Fe molar ratio, i.e., they increased with increasing Mg/Fe molar ratios. Generally, the increasing rate coefficients indicate a faster removal process (Sun et al., 2015a). Based on these results, Mg-Fe LDHs with higher Mg/Fe molar ratios seem to be more effective sorbents for Zn(II) and Pb(II) from aqueous solutions. Additionally, the co-adsorption of Zn(II) and Pb(II) on Mg-Fe LDH-4 is given in Fig. 3.1C and the calculated parameters are in Table S3.5. The adsorption efficiency, i.e., 72% for Zn(II) and 93% for Pb(II), slightly decreased

compared to individual kinetic experiments. The experimental data describing Zn(II) sorption were better fitted by pseudo-second order kinetics. However, the correlation coefficients for both models describing Pb(II) sorption were equal. The rate coefficients for both models significantly decrease for Zn(II). Conversely, minor differences in rate coefficients for Pb(II) sorption were observed. The decreasing Zn(II) sorption on Mg-Fe LDH-4 due to the co-presence of Pb(II) was also described by Kumpiene et al. (2008).

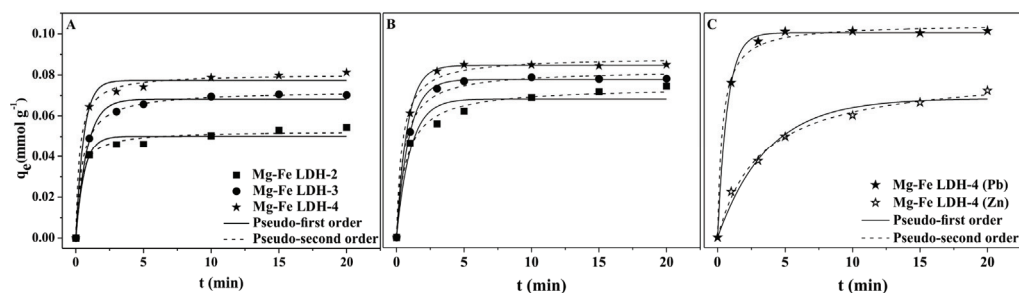


Fig. 3.1. Adsorption kinetics of Zn(II) (A) and Pb(II) (B) on Mg-Fe LDH with different Mg/Fe molar ratios and co-adsorption of Zn(II) and Pb(II) on Mg-Fe LDH-4 (C) at pH 5.5 fitted by the nonlinear form of pseudo-first and pseudo-second order kinetic models.

The basic adsorption mechanism is commonly described by the equilibrium adsorption data (Fig. 3.2.A-B) that can be modeled by several models, e.g., the Langmuir model (monolayer adsorption) and/or the Freundlich model (adsorption on a heterogeneous surface without the formation of a monolayer) (Foo and Hameed, 2010; Limousin et al., 2007). The precipitation of Zn(II) and Pb(II) compounds during equilibrium adsorption experiments at pH 5.5 was excluded by the program Visual MINTEQ 3.1. The maximal adsorbed amounts (q_{max}), Langmuir constants (K_L), Freundlich constants (K_F), parameters n and the correlation coefficients for both models are given in Table S3.6. The sorption of Zn(II) and Pb(II) on all materials (except for Zn(II) sorption on Mg-Fe LDH-4) were better fitted by the Langmuir model. The maximal adsorbed amount (q_{max}) for both metal ions increased with increasing Mg/Fe molar ratio and higher values were observed for Pb(II). Moreover, the affinity of Pb(II) described by K_L (Limousin et al., 2007) was significantly higher than the affinity of Zn(II).

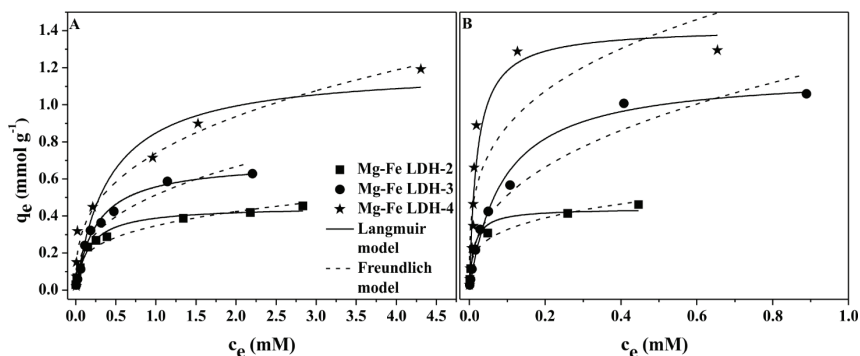


Fig. 3.2. Adsorption isotherms of Zn(II) (A) and Pb(II) (B) on Mg-Fe LDHs with different Mg/Fe molar ratios fitted by the non-linear form of the Langmuir and Freundlich model. Data presented are means ($n = 3$). Maximum SD is ± 0.06 mmol g^{-1} .

Surface complexation modeling

The pH-dependent sorption of Zn(II) and Pb(II) on Mg-Fe LDH-4 at different ionic strengths is given in Fig. 3.3. Generally, the pH-dependent sorption of Zn(II) and Pb(II) on LDHs is divided into several regions due to the charge of the LDH surface and predominant Zn(II) and Pb(II) species at the given pH value, i.e., the sorption was influenced by several mechanisms. At lower pH values ($\text{pH} < 4$), the possible dissolution of LDHs occurred (see Fig. S3.4 or Jobbágy and Regazzoni, 2011). Subsequently, increasing pH resulted in increasing sorption that was assigned to the surface properties of Mg-Fe LDH. The surface was positively charged at $\text{pH} < \text{pH}_{\text{PZC}}$ (see Table S3.3). Therefore, the surface of Mg-Fe LDH-4 was positively charged at $\text{pH} < 10$ (protonation reaction) and negatively charged at $\text{pH} > 10$ (dissociation of functional groups). The high sorption efficiency of Zn(II) and Pb(II) also occurred at lower pH values, i.e., on the positively charged surface of Mg-Fe LDH, indicating predominantly chemical adsorption. Other mechanisms may also influence the sorption process of metal ions on LDHs. In the case of Pb(II) sorption on LDHs, the effect of surface-induced precipitation has been previously observed in Liang et al. (2009) and Park et al. (2007). The surface-induced precipitation of metal hydroxides, e.g., $\text{Pb}_3(\text{CO}_3)_2(\text{OH})_2$, occurs at lower pH values than in pure aqueous solutions and it is caused by the high pH on the surface of LDHs (similar to pH_{PZC}) (Zhang and Hou, 2007). Due to similar properties, Zn(II) sorption was probably also influenced by these mechanisms.

The formation of inner-sphere complexes, i.e., chemical binding, and outer-sphere complexes, i.e., electrostatic binding, corresponds to the charge of the LDH surface at a given pH, as has been discussed above. Generally, XAS studies have been used to differentiate between these complexes. However, previous XAS studies based on Zn(II) and LDH interactions have been mainly focused on the formation of Zn-based LDHs during sorption of Zn(II) on different materials, e.g., kaolinite (Nachtegaal and Sparks, 2004) or pyrophyllite (Ford and Sparks, 2000), at higher pH values. Identically, the XAS studies based on Pb(II) and LDH interactions are also limited (Izumi et al., 2005; Izumi et al., 2002). Such sorption processes have been mainly provided without pH control, which means the predominant effect was the surface-induced precipitation as has been mentioned above. Few studies have been focused on the sorption experiments at different ionic strength that can also differentiate between inner-sphere and outer-sphere complexes. However, this approach cannot differentiate between the individual types of these complexes. In the case of Pb(II) sorption on Mg-Al LDHs, the predominant formation of outer-sphere complexes has been observed (Zhang et al., 2007; Zhao et al., 2011). On the other hand, Mg-Fe LDH showed the preferable formation of inner-sphere complexes according to Liang et al. (2009). As shown in Fig. 3.3, the Zn(II) and Pb(II) sorption on Mg-Fe LDH was not influenced by the ionic strength indicating the formation of inner-sphere complexes. Therefore, the data describing pH-dependent Pb(II) adsorption fit well with the DLM. In the case of Zn(II), the model slightly overestimates adsorption at $\text{pH} > 6$ and underestimates it at $\text{pH} < 4$. In general, the DLM works better for lower adsorbate concentrations, which is consistent with our previous results for As(V) adsorption on Mg-Fe LDH (Hudcová et al. 2017). In contrast to As(V), less ionic strength dependence for Zn(II) and Pb(II) adsorption was observed indicating the formation of inner-sphere complexes on the Mg-Fe LDH surfaces. For both metal ions, pH-dependent adsorption could be best described by the formation of simple monodentate inner-sphere complexes optimized within the pH range 6-10 (Table S3.1, Fig. 3.3A-B, E-F). The DLM simulations for bidentate complexes did not improve the fitting of the adsorption edges for either Zn(II) or for Pb(II) compared with the monodentate ones (Fig. 3.3C-D, G-H). In general, the DLM can be used as a successful tool for prediction of Zn(II) and Pb(II) adsorption onto Mg-Fe DLMs when considering them as potential materials for water remediation.

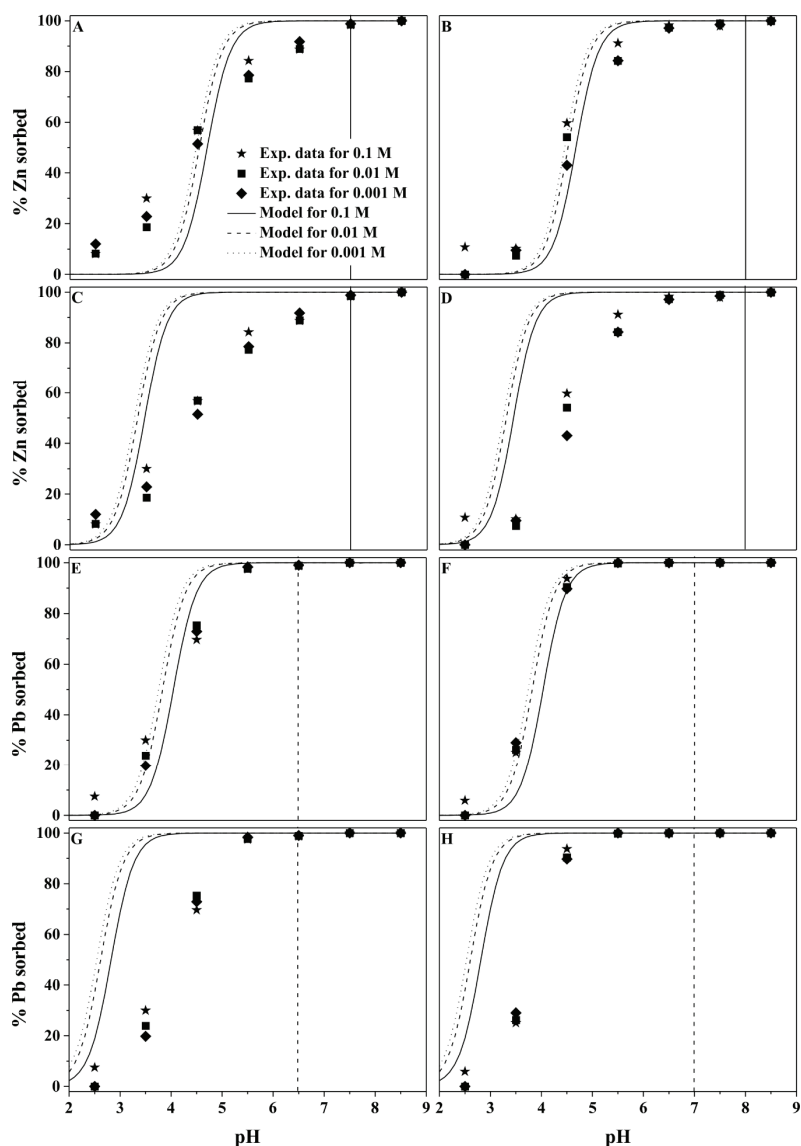


Fig. 3.3. Adsorption of monodentate (A-B, E-F) and bidentate (C-D, G-H) inner-sphere complexes of Zn(II) (A-D) and Pb(II) (E-H) on Mg-Fe LDH at metal concentrations of 10^{-4} (A,C,E,G) and 10^{-5} M (B,D,F,H) and with 0.1 M (asterisk), 0.01 M (square) and 0.001 M (diamond) NaNO_3 . Symbols represent experimental data; DLM adsorption edges are represented by solid, dashed and dotted lines at 0.1, 0.01 and 0.001 M NaNO_3 , respectively. Vertical lines indicate hydrozincite (solid lines) and hydrocerussite (dashed lines) supersaturation for aqueous Zn(II) and Pb(II) concentration of 10^{-4} and 10^{-5} M in the absence of adsorption.

Solid state analyses of Mg-Fe LDH samples after Zn(II) and Pb(II) sorption

The detailed characterization of Mg-Fe LDH-4, Mg-Fe LDH-Zn and Mg-Fe LDH-Pb samples was performed using a combination of XRD, SEM/EDX, FTIR-ATR, XPS, HR-TEM with elemental mapping and low-temperature ^{57}Fe Mössbauer spectroscopy. The (ad)sorbed amounts of Zn(II) and Pb(II) on Mg-Fe LDH-4 reached 1.44 and 1.65 mmol g^{-1} , respectively. As mentioned previously, the sorption processes at pH 5.5 should not be affected by precipitation. However, high initial concentrations of Zn(II) and Pb(II) could also affect the sorption mechanism. First, the precipitation of Zn(II) at the given conditions was not confirmed by Visual MINTEQ 3.1. Contrarily, the saturation index of hydrocerussite (SI = 0.017) confirmed its possible formation during Pb(II) sorption (apparent equilibrium at initial concentration higher than 493 mg L^{-1}). A comparison of the (ad)sorbed amount of Zn(II) and Pb(II) on different LDHs incorporated with inorganic anions is given in Table S3.7. However, these results are mainly affected by the precipitation of carbonates and/or hydroxides since these sorption processes are without pH control.

The XRD diffractograms of Mg-Fe LDH-4, Mg-Fe LDH-Zn and Mg-Fe LDH-Pb are given in Fig. 3.4. The characteristic peaks for the LDH structure were observed in all the diffractograms. The intensities of these peaks decreased after Zn(II) and Pb(II) sorption and this decrease was more pronounced for Mg-Fe LDH-Pb. Generally, decreasing intensities in diffractograms after Pb(II) adsorption originated from the slight decomposition of Mg-Fe LDH-4 after the sorption process (Liang et al., 2009; Park et al., 2007; Zhang and Hou, 2007; Zhao et al., 2011). Moreover, the new peaks observed after Pb(II) sorption were assigned to the precipitation of hydrocerussite (in accordance with Visual MINTEQ 3.1 modeling) and cerussite (Liang et al., 2009; Yang et al., 2016). Moreover, as mentioned previously, surface-induced precipitation during Pb(II) sorption on LDHs also occurred. Precipitation of carbonates was supported by the presence of atmospheric CO_2 and interlayer carbonates in the structure of Mg-Fe LDH-4 as well (Liang et al., 2009). As has already been mentioned, interlayered carbonates could be

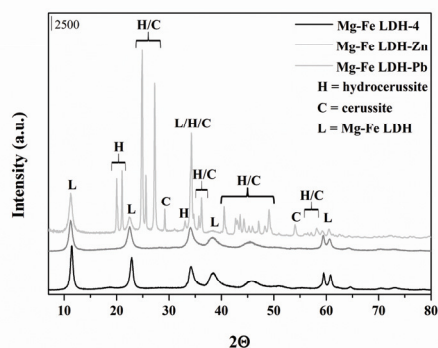


Fig. 3.4. XRD patterns of Mg-Fe LDH-4, Mg-Fe LDH-Zn and Mg-Fe LDH-Pb.

available for precipitation with Pb(II) leading to the decomposition of the LDHs and such behavior has also been previously observed by Park et al. (2007). The influence of Pb(II) adsorption on the whole sorption mechanism was also expected, whereas Pb(II) surface complexation on LDHs is expected at $\text{pH} < 6$ (Yang et al., 2016). Contrarily, the diffractogram of Mg-Fe LDH-Zn showed no additional peaks of crystalline phases. Therefore, the removal of Zn(II) was mainly influenced by adsorption (surface complexation), precipitation of amorphous phases and/or isomorphic substitution (Xiao et al., 2015).

For further description of the adsorption mechanism, the cell parameters a and c were calculated for all Mg-Fe LDH samples. The cell parameter c slightly increased after Zn(II) and Pb(II) sorption (see Table S3.2). Generally, increasing cell parameter c means the influence of mechanisms other than adsorption, e.g., isomorphic substitution (Sun et al., 2015a; Xiao et al., 2015). However, the isomorphic substitution of Pb(II) is not expected due to a significantly higher ionic radius of Pb(II) (1.19 Å) compared to Mg(II) (0.65 Å) indicating a steric hindrance for isomorphic substitution (Liang et al., 2013; Sun et al., 2015a). Conversely, the ionic radius of Zn(II) (0.74 Å) is much closer to the ionic radius of Mg(II). Therefore, isomorphic substitution could also affect the removal of Zn(II) by Mg-Fe LDHs (Komarneni et al., 1998; Richardson and Braterman, 2009; Sun et al., 2015a).

The SEM/EDX analyses of Mg-Fe LDH-4, Mg-Fe LDH-Zn and Mg-Fe LDH-Pb are given in Fig. 3.5. The Mg-Fe LDH-4 surface was significantly smoother compared to the surface of Mg-Fe LDH-Zn and Mg-Fe LDH-Pb. Based on the XRD results, the Pb(II) sorption was also influenced by the precipitation of (hydro)cerussite with characteristic hexagonal plates indicating a crystalline structure. The EDX analysis showed a high amount of Pb(II) (59%) on the Mg-Fe LDH-Pb surface resulting in decreased concentrations of the other elements. On the other hand, some new amorphous phases were also observed on the Mg-Fe LDH-Zn surface. Based on the XRD results, precipitation of crystalline Zn phases was excluded. Therefore, the mechanism was assigned to the possible precipitation of amorphous Zn oxides/hydroxides or to the accumulation of Zn(II) on the surface of Mg-Fe LDH via the formation of the Zn-O-Zn bond described in Xiao et al. (2015). Moreover, possible multilayer adsorption of Zn(II) on Mg-Fe LDH-4 was also confirmed by adsorption modeling (see Section *Kinetic and equilibrium adsorption experiments*).

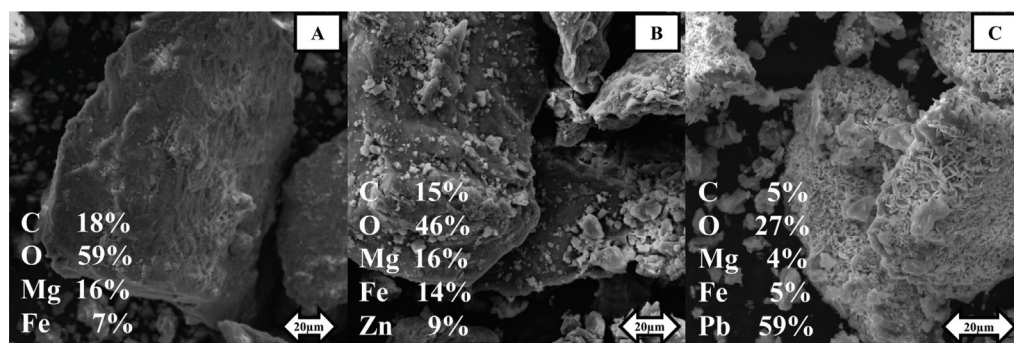


Fig. 3.5. SEM images of Mg-Fe LDH-4 (A), Mg-Fe LDH-Zn (B) and Mg-Fe LDH-Pb (C).

The FTIR-ATR spectra of Mg-Fe LDH-4, Mg-Fe LDH-Zn and Mg-Fe LDH-Pb are given in Fig. S3.5. The Mg-Fe LDH-4 spectrum shows the characteristic bands corresponding to important binding arrangements (see Supplementary Material). The Mg-Fe LDH-Zn and Mg-Fe LDH-Pb spectra exhibited all the characteristic adsorption bands. However, the Mg-Fe LDH-Zn and Mg-Fe LDH-Pb showed lower intensity for individual signals. Therefore, the measurement was performed with a different number of scans, i.e., 65 scans for Mg-Fe LDH-4 and 750 scans for Mg-Fe LDH-Zn and Mg-Fe LDH-Pb. Based on these properties, the intensity of the spectra after Zn(II) and Pb(II) sorption were even lower than that shown in Fig. S3.5. The precipitation of carbonates during Pb(II) sorption was confirmed by the increasing intensity of the CO_3^{2-} absorption band (Liang et al., 2009). Moreover, the precipitation of (hydro)cerrusite was confirmed by the newly formed band at 838 cm^{-1} (Sternlieb et al., 2010). The Zn(II) sorption led to the formation of a new band at 551 cm^{-1} corresponding to the Zn-O bond (Alias and Mohamad, 2013), which could also be assigned to the precipitation of amorphous Zn oxides/hydroxides as previously discussed. However, this broad peak could be composed of other contributions, e.g., Zn-O-Zn at approximately 540 cm^{-1} (Arakha et al., 2015; Singh et al., 2007). The accumulation of Zn on the Mg-Fe LDH surface via the formation of Zn-O-Zn bond has also been discussed above.

The XPS spectra of Mg-Fe LDH-4, Mg-Fe LDH-Zn and Mg-Fe LDH-Pb are given in Fig. 3.6A and the surface stoichiometry is given in Table S3.8. All XPS spectra include Mg 2s, Mg 2p, Fe 2p, C 1s and O 1s peaks. Moreover, the peaks corresponding to Zn 2p and Pb 4f were identified after the sorption of Zn(II) and Pb(II), indicating proof of effective sorption onto the Mg-Fe LDH-4 surface. A symmetric Mg 2p peak (49.2 eV) of the Mg-Fe LDH-4 spectrum has position typical for $\text{Mg}(\text{OH})_2$ indicating octahedral coordinated Mg(II) in the LDH structure (Carja et al., 2012). The intensity of this peak

decreased after Zn(II). Moreover, this peak showed two contributions, i.e., a larger contribution (71%) at higher binding energies (49.5 eV) reflected from Mg(II) in the brucite-like layers and a smaller contribution (29%) at lower binding energies (48.1 eV). This small peak was not observed prior to Zn(II) sorption and significantly decreased after Ar⁺ sputtering corresponding to the removal of the adsorbed species from the surface (Zhao et al., 2012). The intensity of the Mg 2p peak after Pb(II) sorption was even lower and was caused by a low surface concentration of Mg(II). The broad Fe 2p peaks, i.e., the Fe 2p_{1/2} and Fe 2p_{3/2}, correspond to Fe(III) and indicate a variety of possible contributions (e.g., Fe-O, Fe-OH, etc.) (Biesinger et al., 2011). The intensity of this peak was similar for Mg-Fe LDH-4 and Mg-Fe LDH-Zn. After Pb(II) sorption, the intensity significantly decreased caused by the low surface concentration of Fe(III). The C 1s peak decreased after sorption of both metal ions. However, the amount of C on the surface significantly increased after Pb(II) sorption, which could be assigned to the precipitation of (hydro)cerussite on the surface of Mg-Fe LDH as confirmed by previous analyses.

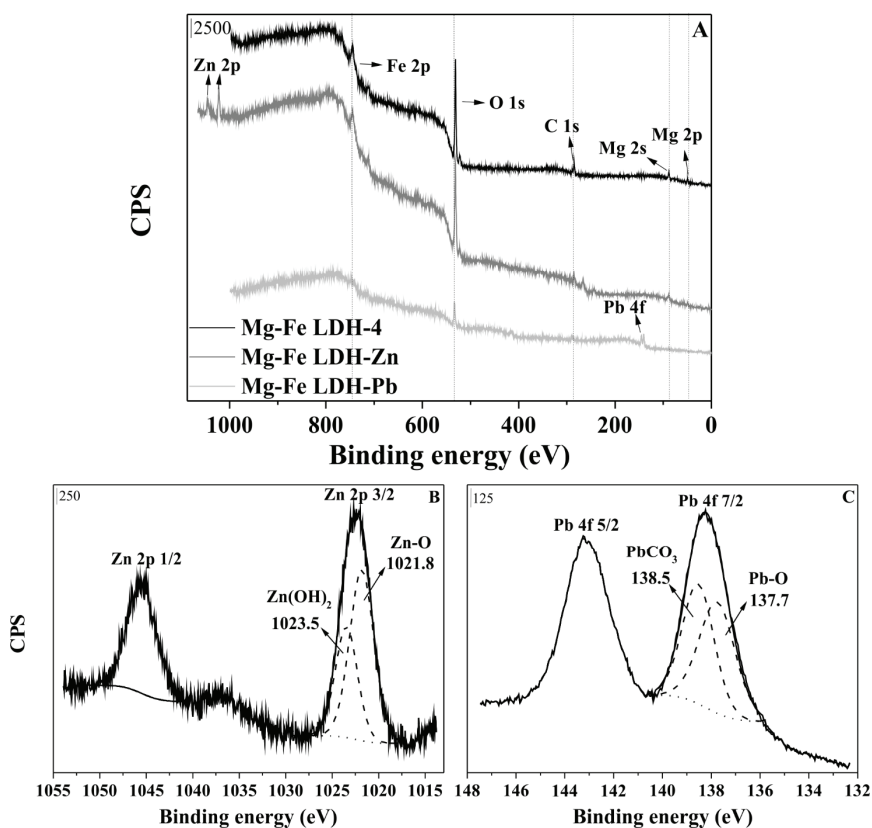


Fig. 3.6. XPS spectra of Mg-Fe LDH-4, Mg-Fe LDH-Zn and Mg-Fe LDH-Pb (A) and deconvolution of the Zn 2p (B) and Pb 4f peak (C).

The intensity of the O 1s peak in the Mg-Fe LDH-4 and Mg-Fe LDH-Zn spectra was similar. However, this peak significantly decreased after Pb(II) sorption. Generally, this broad peak consists of several contributions, i.e., the M-O bond at lower binding energies (approximately 529 - 530 eV), M-OH and/or M-CO₃ bonds (approximately 531 - 533 eV) at middle binding energies and water at higher binding energies (approximately 535 eV) (Alexander et al., 2000; Baltrusaitis et al., 2012). To identify the sorption mechanism, deconvolution of the Zn 2p and Pb 4f peaks was performed. The Zn 2p peak (Fig. 3.6B) consisted of two contributions, i.e., Zn 2p_{1/2} at approximately 1045 eV and Zn 2p_{3/2} at approximately 1022 eV. Moreover, the Zn 2p_{3/2} peak was deconvoluted into two contributions. First, the Zn-O bond occurred at 1021.8 eV (approximately 63%) identifying a Zn-O-Mg and Zn-O-Fe bond. Additionally, the contribution at 1023.5 eV (approximately 37%) was assigned to Zn(OH)₂ indicating the formation of Zn-O-Zn and/or precipitation of amorphous Zn oxides/hydroxides. The formation of the Zn-O-Zn bond has been described by Xiao et al. (2015) and is a result of Zn(II) accumulation on the Mg-Fe LDH-4 surface after its saturation (i.e., all adsorption sites are occupied). Finally, the Pb 4f peak (Fig. 3.6C) also consisted of two contributions, i.e., Pb 4f_{5/2} at approximately 145.3 eV and Pb 4f_{7/2} at approximately 140.2 eV. The Pb 4f_{7/2} peak was also deconvoluted into two contributions, i.e., the Pb-O bond at 137.7 eV (51%) and Pb(OH)₂/PbCO₃ at 138.5 eV (49%). The formation of the Pb-O bond could be assigned to surface complexation reactions and the second contribution confirmed surface-induced precipitation of Pb(II). Additionally, the shift of Mg 2p, Fe 2p_{3/2} and O 1s peaks (data not shown), i.e., changes in binding energies, after Zn(II) and Pb(II) sorption, indicated changes in the local bonding environments and the chemical states of Mg, Fe and Mg that was assigned to the formation of inner-sphere complexes (Zhang and Hou, 2007). The XPS results confirmed that the mechanism of Zn(II) and Pb(II) immobilization on Mg-Fe LDH is a combination of chemical adsorption and surface-induced precipitation.

To shed light on the distribution of Zn(II) and Pb(II) on the surface of Mg-Fe LDH particles, elemental mapping of Mg, Fe, O, Zn and Pb was performed (Fig. 3.7). For Mg-Fe LDH-Zn, the image containing Fe, Zn and O (Fig. 3.7A) shows a heterogeneous distribution for Zn(II). Despite highly concentrated places, Zn(II) was also distributed on the whole LDH particle (Fig. 3.7E). Therefore, the general mechanism was identified as adsorption and surface accumulation as has been confirmed by previous analyses. While the distribution of Fe(III) was also heterogeneous (located mainly in the inner part of the LDH particle), the distribution of Mg(II) was homogeneous and Mg(II) also occurred together with higher Zn(II) concentrations. The connection of Mg(II) and Zn(II) during the sorption process has also been observed by XPS analyses,

i.e., changes of the Mg 2p peak after Zn(II) sorption. For Mg-Fe LDH-Pb, a heterogeneous distribution of Pb was also observed that was mainly assigned to the precipitation of hydrocerussite as has been confirmed by previous analyses (Fig. 3.7G and Fig. 3.7K). A lower concentration of Pb(II) also occurred over the whole of the LDH particles supporting the hypothesis of Pb adsorption. Other elements, i.e., Mg, Fe and O, were homogeneously distributed over the LDH particles. The chemical composition of the marked mapped areas after Zn(II) and Pb(II) sorption are shown in Fig. 3.7F and Fig. 3.7L, respectively.

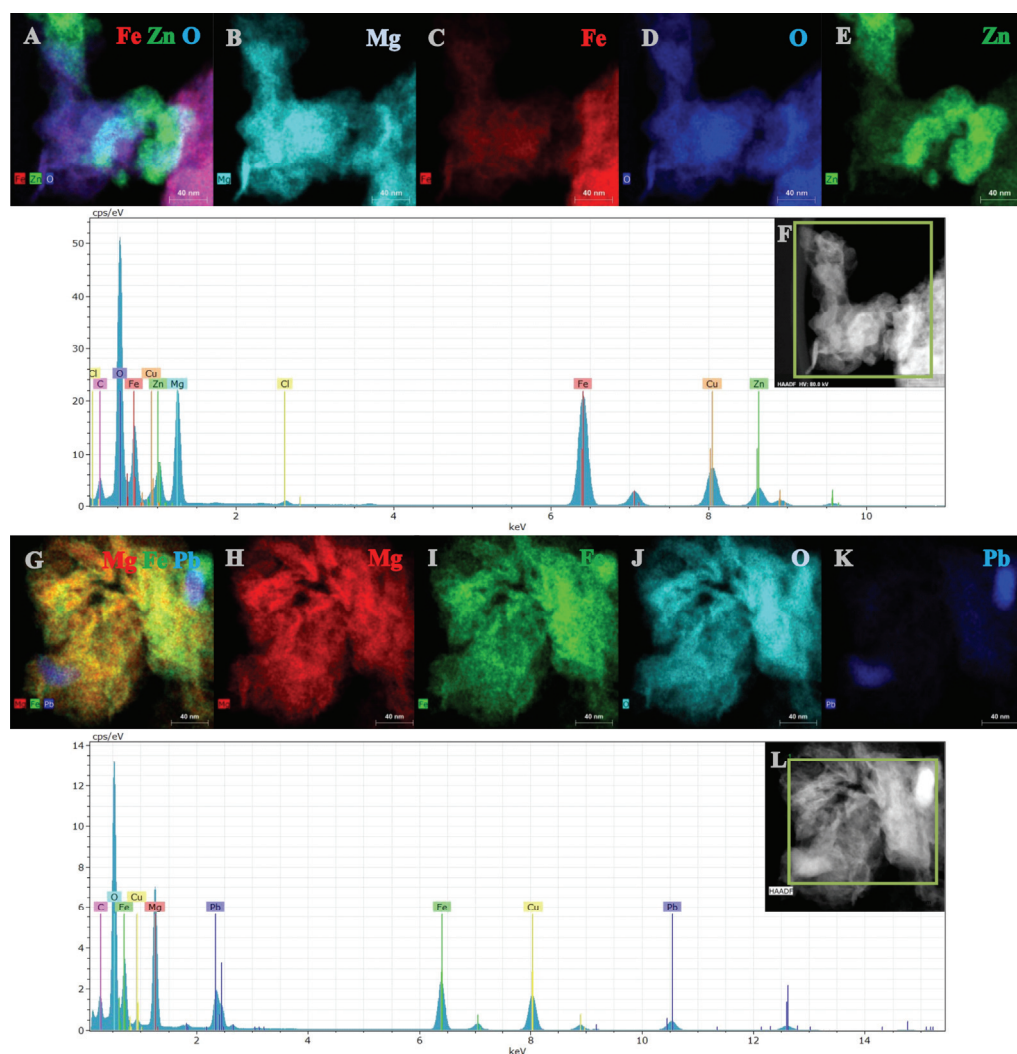


Fig. 3.7. Elemental mapping (A-E) and the chemical composition of the marked mapped area (F) of Mg-Fe LDH-Zn and elemental mapping (G-K) and the chemical composition of the marked mapped area of Mg-Fe LDH-Pb (L).

Based on Mössbauer spectroscopy measured on isotope ^{57}Fe at a temperature of 5 K (Fig. 3.8; for hyperfine parameters see Table S3.9) we can conclude that there is no formation of secondary Fe-phases, such as ferric oxides and/or oxyhydroxides, at a temperature of 5 K. There would be a sextet of magnetically split spectral components when nanocrystalline ferric precipitates have formed (see Prucek et al., 2013). Moreover, from the nearly identical spectral characteristics for the Mg-Fe LDH sample and samples with Zn and Pb (i.e., in all cases, the spectra were fit with just one doublet corresponding to Fe^{3+} in the structure of LDH), it is clear, that there are no structural changes in the LDH from the viewpoint of structurally incorporated iron. The non-symmetrical spectra of all three samples (i.e., the two spectral lines of the fitted doublet have different intensities) indicate a preferential orientation of the LDH sheets and/or preferential orientation of iron-sites in the structure of the LDH, which is a typical feature of layered materials. There is also no evidence for reduction of Fe^{3+} during the interaction of the LDH with Zn(II) or Pb(II) in aqueous solution.

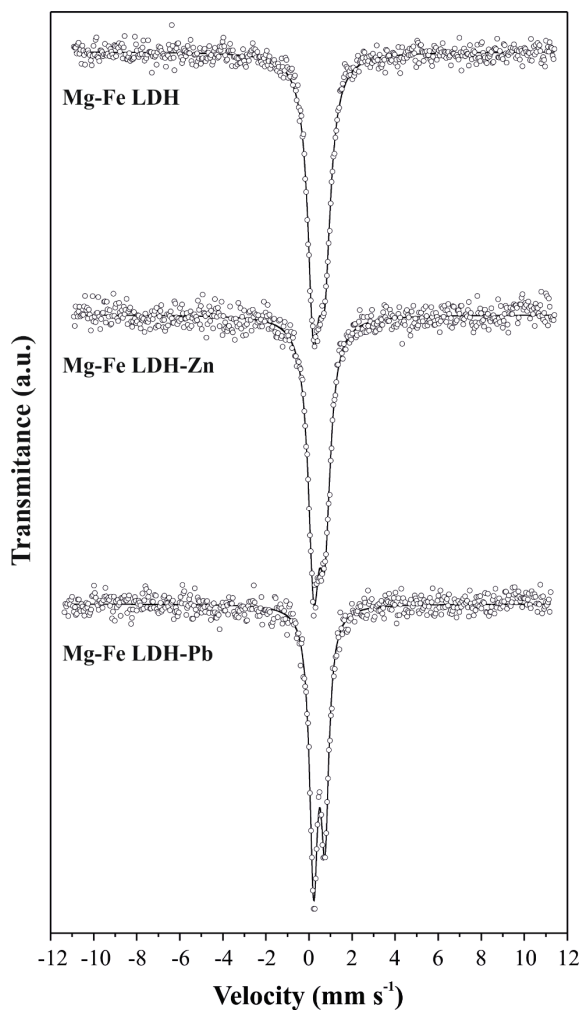


Fig. 3.8. Low-temperature ^{57}Fe Mössbauer spectra of Mg-Fe LDH-4, Mg-Fe LDH-Zn and Mg-Fe LDH-Pb.

Conclusions

Mg-Fe LDHs showed excellent removal efficiency for Zn(II) and Pb(II) from aqueous solutions without pH control, high removal efficiency at a controlled pH value (5.5) and minor changes in removal efficiency in multi-metal solutions. The maximal adsorbed amount of Zn(II) and Pb(II) increased with increasing Mg/Fe molar ratio, and thus Mg-Fe LDH with higher Mg/Fe molar ratios appeared as more promising metal ions sorbents. Based on the DLM simulations, Zn(II) and Pb(II) formed inner-sphere complexes on the Mg-Fe LDH surface indicating chemical binding via strong covalent bonds. Adsorption modeling was coupled with solid state analyses showing that the whole sorption mechanism of Zn(II) and Pb(II) was influenced by several processes, i.e., surface precipitation/complexation (Pb) and surface complexation/accumulation/precipitation of amorphous phases/isomorphic substitution (Zn). Such a comprehensive mechanistic/modeling approach describing metal ions sorption on LDHs is the first of its type and it showed Mg-Fe LDHs performed as universal sorbents usable in metal contaminated waters under variable experimental conditions.

Supplementary Material

Materials and methods

Synthesis of Mg-Fe LDHs with different molar ratios

Mg-Fe LDHs with different Mg/Fe molar ratios were synthesized by dissolution of $\text{MgCl}_2 \cdot 6\text{H}_2\text{O}$ (0.15 mol) and $\text{FeCl}_3 \cdot 6\text{H}_2\text{O}$ (0.075 mol – Mg-Fe LDH-2, 0.05 mol – Mg-Fe LDH-3, 0.0375 mol – Mg-Fe LDH-4) in deionized water (200 mL). The solutions were vigorously stirred and titrated with 2.5 M KOH to pH 13.3. The mixture was kept for 24 hours at room temperature. Subsequently, vacuum filtration (cellulose filtration paper; basic weight: 84 g m^{-2}), washing (to remove residual chemicals, e.g., Cl⁻) and drying of the wet samples at 393 K (12 hours) were performed. Afterwards, the solid samples were milled and sieved (below 250 μm).

Kinetic experiments

Kinetic experiments were performed in individual batches using single- and multi-metal solutions with Zn(II) and Pb(II) concentrations of 0.1 mM prepared by dissolution of $\text{Zn}(\text{NO}_3)_2 \cdot 6 \text{H}_2\text{O}$ and $\text{Pb}(\text{NO}_3)_2$ in the background electrolyte (0.01 M NaNO_3). The experiments were performed without pH control, and at a controlled pH of 5.5. The experimental conditions were obtained to discover the buffering effect of synthesized materials (Seida et al., 2001) and slightly acidic conditions were chosen due to the connection with subsequent experiments in soils (soil pH approximately 6). Moreover, the given experimental conditions decreased the possible leaching of Mg(II) from the LDH structure (Liang et al., 2013). In a typical experiment, a solid sample (1 g L^{-1}) was added to the solution, vigorously stirred (550 rpm; magnetic stirrer) and 10 mL of suspension was sampled at specific time intervals (i.e., 1, 3, 5, 10, 15, 20, 30, 60, 90 and 120 min). The samples were immediately filtered using a 0.45 μm cellulose acetate membrane. The concentrations of Zn (limit of detection: 0.0001 mg L^{-1}), Pb (limit of detection: $0.00368 \text{ mg L}^{-1}$), Mg (limit of detection: $0.00024 \text{ mg L}^{-1}$) and Fe (limit of detection: $0.00036 \text{ mg L}^{-1}$) in the solution were measured by ICP-OES. The adsorption efficiency of Zn(II) and Pb(II) (in %) on Mg-Fe LDHs was calculated as the concentration difference between the initial and final Zn and Pb concentrations.

Equilibrium experiments

The equilibrium adsorption experiments were performed in individual batches in an orbital shaker (GFL 3005; 250 rpm). The solid/liquid ratio was 1 g L^{-1} and the pH (5.5) was controlled during all experiments. The samples (10 mL) were filtered ($0.45 \text{ }\mu\text{m}$) after 120 min and analyzed using ICP-OES. Moreover, the solid-state analyses of Mg-Fe LDH-4 after Zn(II) and Pb(II) sorption were performed at the initial Zn(II) and Pb(II) concentrations of 7.7 mM and 2.4 mM (i.e., 500 mg L^{-1}), respectively. The liquid sample (10 mL) was filtered ($0.45 \text{ }\mu\text{m}$) and analyzed using ICP-OES. The filtration of the entire solution was performed using a vacuum pump and the wet solid sample was dried at 298 K.

Acid-base titrations

The titration of the LDH- H^+ system was performed in triplicate in suspension with a Mg-Fe LDH-4 concentration of 3.33 g L^{-1} (0.2 g of solid phase in 60 mL of 0.1 M NaNO_3 background electrolyte) according to a modified procedure described by Rojas Delgado et al. (2004). The suspension was titrated from an initial pH (approximately 10) to pH 3 by adding 0.2 M HNO_3 under constant stirring and a N_2 atmosphere to omit CO_2 using an automatic TitroLine® *alpha plus* Titration Unit (Schott, Germany). Titration data were used to optimize the adjustable model parameters, i.e., surface protonation constants and the total number of surface sites, using the program ProtoFit 2.1 (Turner and Fein, 2006). Titration data and the corresponding models for Mg-Fe LDH-4 are presented in Fig. S3.1.

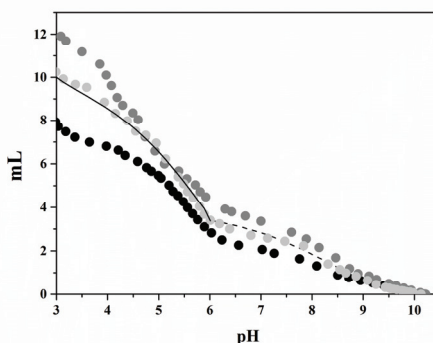


Fig. S3.1. Potentiometric titration data (circles) and DLM fit (lines) for Mg-Fe LDH-4 at ionic strength of 0.1 M NaNO_3 . Solid line represents the best fit of DLM for titration data at pH values ranging from 3 to 6; dashed line for pH range from 6 to 10. Two fits result in two datasets of model parameters, which points out to the presence of two different structural sites on the Mg-Fe LDH.

Adsorption edges

The adsorption edge experiments for Zn(II) and Pb(II) on Mg-Fe LDH-4 were conducted in individual batches at Zn(II) and Pb(II) concentrations of 0.01 and 0.1 mM at different pH values (2.5 to 8.5) in the background electrolyte (0.001, 0.01 and 0.1 M NaNO₃). The adsorbent (1 g L⁻¹) was added to the solution and the mixture was pre-equilibrated with constant stirring (250 rpm; orbital shaker) at 298 K for 24 h. Afterwards, the specific pH value (starting at 2.5 and increasing in steps of ~1) in each individual batch was manually controlled for 120 min using 0.01 to 1 M HNO₃ and NaOH. The samples were filtered (0.45 μm) and analyzed by ICP-OES.

The surface complexation constants for Zn(II) and Pb(II) on Mg-Fe LDH-4 were obtained using the software FITEQL 4.0 (Herbelin and Westall, 1999) with the default thermodynamic data for aqueous species from Visual MINTEQ 3.1 (Gustafsson, 2013). The constant values were optimized for two sets of protonation and deprotonation constants acquired from Protonfit modeling. The median stability constants for monodentate and bidentate complexes were further used to optimize DLM prediction for each adsorption edge using Visual MINTEQ 3.1.

Table S3.1 Surface properties, reactions on the LDH-solution interface and stability constants describing the Zn(II) and Pb(II) inner-sphere complexation using DLM (median values of constants optimized in FITEQL 4.0). Two sets of surface protonation and deprotonation constants were optimized in ProtoFit 2.1 in pH ranges 3-6 and 6-10, respectively.

Reaction	Log K					
	Value	I. dataset		II. dataset		
		V(Y)	(V(Y) _{min} , V(Y) _{max})	Value	V(Y)	(V(Y) _{min} , V(Y) _{max})
Surface protonation and deprotonation						
$>\text{SOH} + \text{H}^+ \rightleftharpoons >\text{SOH}_2^+$	-2.11			1.71		
$>\text{SOH} \rightleftharpoons >\text{SO}^- + \text{H}^+$	0.16			-3.14		
Formation of monodentate complexes						
$>\text{SOH} + \text{Zn}^{2+} \rightleftharpoons >\text{SOZn}^+ + \text{H}^+$	-7.64	7.1	(5.0, 11.0)	-3.86	5.5	(3.8, 8.5)
$>\text{SOH} + \text{Pb}^{2+} \rightleftharpoons >\text{SOPb}^+ + \text{H}^+$	-6.40	7.3	(5.1, 11.4)	-2.43	1.7	(1.2, 2.7)
Formation of bidentate complexes						
$>2\text{SOH} + \text{Zn}^{2+} \rightleftharpoons >(\text{SO})_2\text{Zn} + 2\text{H}^+$	-4.70	20.3	(14.2, 31.4)	-3.73	30.8	(21.6, 47.6)
$>2\text{SOH} + \text{Pb}^{2+} \rightleftharpoons >(\text{SO})_2\text{Pb} + 2\text{H}^+$	-3.27	21.9	(15.3, 33.8)	-2.29	27.5	(19.3, 42.5)
Site density (sites nm⁻²)	153.53			57.05		
Specific surface area: 40.1 m² g⁻¹						
V(Y) = parameter indicating the goodness-of-fit of the DLM to the measured adsorption edges (Heinrich et al., 2008; Reich et al., 2010)						

Results and discussion

Characterization of materials

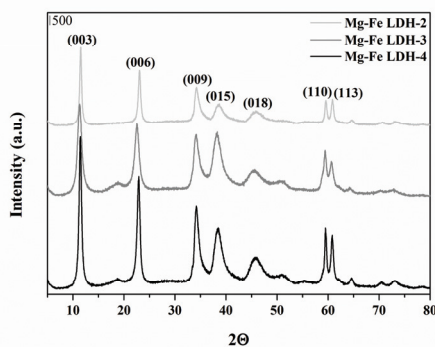


Fig. S3.2. Diffractograms of Mg-Fe LDHs with different Mg/Fe molar ratios.

Table S3.2 Basal spacing of layers and cell parameters calculated from diffractograms of Mg-Fe LDH with different Mg/Fe molar ratios, Mg-Fe LDH-Zn and Mg-Fe LDH-Pb.

Material	d_{003} (Å)	d_{006} (Å)	d_{009} (Å)	d_{010} (Å)	a (Å)*	c (Å)**
Mg-Fe LDH-2	7.672	3.860	2.629	1.550	3.100	23.09
Mg-Fe LDH-3	7.855	3.941	2.624	1.555	3.110	23.61
Mg-Fe LDH-4	7.748	3.888	2.633	1.554	3.108	23.24
Mg-Fe LDH-Zn	7.878	3.940	2.643	1.554	3.108	23.64
Mg-Fe LDH-Pb	7.828	3.954	2.633	1.561	3.122	23.60

* $a=2d_{110}$ ** $c=3/2(d_{003} + 2d_{006})$

Table S3.3 Basic characteristics of Mg-Fe LDHs with different Mg/Fe molar ratios.

	Mg-Fe LDH-2	Mg-Fe LDH-3	Mg-Fe LDH-4
Mg:Fe ratio (theoretical)	2	3	4
Mg:Fe ratio (real)	2.4	3.5	4.6
pH _{PZC}	9	10	10
S _{BET} (m ² g ⁻¹)	71.24	50.56	40.14

Kinetic and equilibrium adsorption experiments

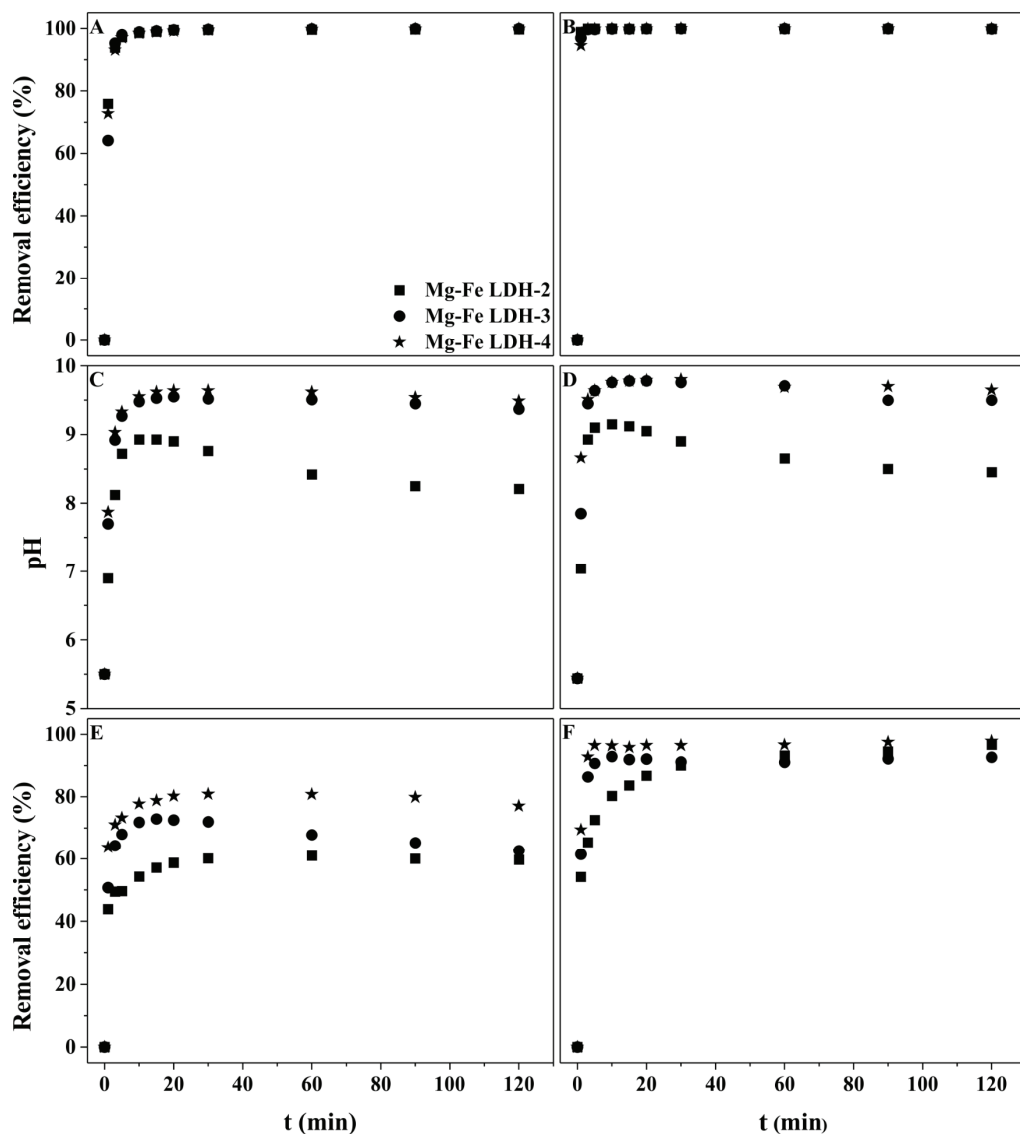


Fig. S3.3. The removal efficiency for Zn(II) (A) and Pb(II) (B) without pH control, the increase of pH during Zn(II) (C) and Pb(II) sorption without pH control and the removal efficiency for Zn(II) (E) and Pb(II) (F) at pH 5.5.

Table S3.4 Parameters of the non-linear modeling using the pseudo-first and pseudo-second order kinetics for adsorption of Zn(II) and Pb(II) on Mg-Fe LDH with different Mg/Fe molar ratios.

Model	Parameter	Mg-Fe LDH-2		Mg-Fe LDH-3		Mg-Fe LDH-4	
		Zn	Pb	Zn	Pb	Zn	Pb
	$q_{\text{max}}(\text{exp})$ (mmol g ⁻¹)	0.05	0.07	0.07	0.08	0.09	0.09
Pseudo-first order kinetics	q_e (mmol g ⁻¹)	0.05	0.07	0.07	0.08	0.08	0.09
	k_1 (min ⁻¹)	1.63	0.37	0.23	0.14	0.04	0.28
	R^2	0.97	-	-	1.00	-	-
Pseudo-second order kinetics	q_e (mmol g ⁻¹)	0.05	0.07	0.07	0.08	0.08	0.09
	k_2 [g (mmol min) ⁻¹]	55.2	15.3	3.81	23.5	3.72	28.3
	R^2	1.00	-	-	1.00	-	-

Table S3.5 Parameters of the non-linear modeling using the pseudo-first and pseudo-second order kinetics for co-adsorption of Zn(II) and Pb(II) on Mg-Fe LDH-4.

Model	Parameter	Mg-Fe LDH-4			
		Zn		Pb	
		Value	S.E.	Value	S.E.
	$q_{\max(\text{exp})}$ (mmol g ⁻¹)	0.08		0.10	
Pseudo-first order kinetics	q_e (mmol g ⁻¹)	0.07	0.00	0.10	0.00
	k_1 (min ⁻¹)	0.27	0.04	1.40	0.06
	R^2	0.98	-	1.00	-
Pseudo-second order kinetics	q_e (mmol g ⁻¹)	0.08	0.00	0.10	0.00
	k_2 [g (mmol min) ⁻¹]	3.82	0.51	27.4	3.81
	R^2	1.00	-	1.00	-

Table S3.6 Parameters of the non-linear modeling using the Langmuir and Freundlich model for adsorption of Zn(II) and Pb(II) on Mg-Fe LDH with different Mg/Fe molar ratios.

Model	Parameters	Mg-Fe LDH-2			Mg-Fe LDH-3			Mg-Fe LDH-4			
		Zn	Pb	Pb	Zn	Pb	Pb	Zn	Pb	Pb	
		Value	S.E.	Value	S.E.	Value	S.E.	Value	S.E.	Value	S.E.
	$q_{\max(\text{exp})}$ (mmol g ⁻¹)	0.46	0.05	0.46	0.04	0.63	0.06	1.06	0.05	1.19	0.05
Langmuir model	q_{\max} (mmol g ⁻¹)	0.45	0.02	0.44	0.02	0.70	0.03	1.17	0.05	1.20	0.17
	K_L (L mmol ⁻¹)	6.08	0.97	82.5	20.3	3.94	0.43	11.5	1.46	2.41	1.35
	R^2	0.98	-	0.96	-	0.99	-	0.99	-	0.90	-
Freundlich model	n (-)	3.47	0.34	3.91	0.53	2.68	0.32	2.65	0.27	2.93	0.30
	K_F^*	0.35	0.01	0.59	0.05	0.51	0.03	1.22	0.08	0.74	0.04
	R^2	0.96	-	0.95	-	0.94	-	0.95	-	0.97	-

* [(mmol g⁻¹)(L mmol⁻¹)^{1/n}]

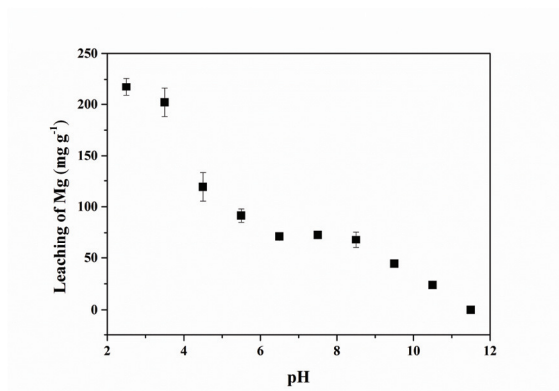


Fig. S3.4. Leaching of Mg at different pH values after 120 min. Data presented are means of Mg leaching in 0.1, 0.01 and 0.001 M electrolyte ($n = 3$).

Table S3.7 A comparison of the (ad)sorbed amount (q_{MAX}) of Zn(II) and Pb(II) on different LDHs.

	Type of LDH (anion)	Initial pH	Solid/liquid (g L ⁻¹)	q_{MAX} (mmol g ⁻¹)	Reference
Zn	Mg-Fe (CO ₃ ²⁻)	5.5*	1	1.44	This study
	Mg-Al (CO ₃ ²⁻)	4.7	2	4.76	Komarneni et al. (1998)
	Mg-Al (CO ₃ ²⁻)	5	10	1.20	Fujji et al. (1992)
	Mg-Al (Cl ⁻)	5	10	1.02	Fujji et al. (1992)
Pb	Mg-Fe (CO ₃ ²⁻)	5.5*	1	1.65	This study
	Mg-Al (Cl ⁻)	5.7	0.2	0.33	Zhao et al. (2011)
	Mg-Al (Cl ⁻)	3 - 5.5	1	0.86	Liang et al. (2010)
	Mg-Fe (Cl ⁻)	3 - 5.5	1	2.03	Liang et al. (2009)
	Mg-Al (Cl ⁻)	6	2.5	0.53	Zhang and Hou (2007)
	Mg-Al (Cl ⁻)	5	10	0.97	Fujji et al. (1992)
	Mg-Al (CO ₃ ²⁻)	5	10	0.96	Fujji et al. (1992)
	Mg-Al (Cl ⁻)	5	1.7	0.63	González et al. (2015)

* controlled

Solid state analyses after Zn(II) and Pb(II) sorption

The Mg-Fe LDH-4 spectrum shows characteristic bands corresponding to important binding arrangements (Fig. S3.5.), i.e., the stretching vibration of hydroxyl groups in the brucite-like layers (broad band at 3444 cm^{-1}), the bending vibration of water (1637 cm^{-1}), the absorption band of CO_3^{2-} in the interlayered region (1361 and 643 cm^{-1}) and vibrations of M-O and/or M-OH (region at approximately 550 cm^{-1}) (Cavani et al., 1991; Kang et al., 2013).

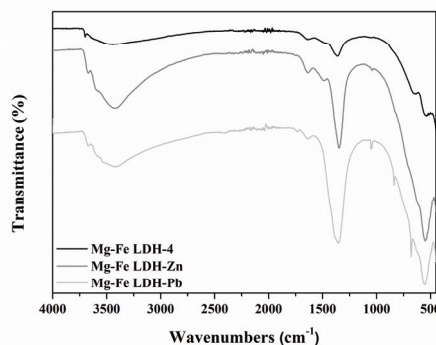


Fig. S3.5. FTIR-ATR of Mg-Fe LDH-4, Mg-Fe LDH-Zn and Mg-Fe LDH-Pb.

Table S3.8 Surface stoichiometry (%) of Mg-Fe LDH-4, Mg-Fe LDH-Zn and Mg-Fe LDH-Pb.

	Mg-Fe LDH-4	Mg-Fe LDH-Zn	Mg-Fe LDH-Pb
Fe 2p	1.40	1.70	2.30
Mg 2s	35.9	34.9	14.1
O 1s	45.5	44.6	56.1
C 1s	17.2	16.1	24.2
Zn 2p	-	2.70	-
Pb 4d	-	-	3.30

Table S3.9 Low-temperature (5 K) ^{57}Fe Mössbauer hyperfine parameters for Mg-Fe LDH-4, Mg-Fe LDH-Zn and Mg-Fe LDH-Pb.

Sample	δ (mm s $^{-1}$)	ΔE_Q (mm s $^{-1}$)	RA (%)	Assignment
Mg-Fe LDH-4	0.46	0.52	100	Fe^{3+} in LDH
Mg-Fe LDH-Zn	0.48	0.52	100	Fe^{3+} in LDH
Mg-Fe LDH-Pb	0.48	0.52	100	Fe^{3+} in LDH

Notations: δ – isomer shift ($\pm 0.02\text{ mm s}^{-1}$), ΔE_Q – quadrupole splitting ($\pm 0.02\text{ mm s}^{-1}$) and RA – relative area in the spectrum ($\pm 3\%$)

Chapter IV

Stability and stabilizing efficiency of Mg-Fe layered double hydroxides and mixed oxides in aqueous solutions and soils with elevated As(V), Pb(II) and Zn(II) contents

B. Hudcová, M. Vítková, P. Ouředníček, M. Komárek

Adapted from Science of the Total Environment 648 (2019): 1511-1519

Content

Abstract	97
Introduction	98
Materials and methods	100
Soil characterization	100
Synthesis and characterization	100
Sorption mechanisms in aqueous solutions	101
Stability of materials in deionized water and soil solutions	101
pH-static leaching experiments	102
Incubation batch experiments	102
Statistical analysis	103
Results and discussion	104
Synthesis and characterization	104
Sorption mechanisms in aqueous solutions	105
Stability of the studied materials	107
pH-static leaching experiments	109
Incubation experiments	110
Perspectives for chemical stabilization	116
Conclusions	118
Supplementary Material	119

Abstract

Although the mechanisms of metal(loid) removal from aqueous solutions using LDHs (layered double hydroxides) and mixed oxides (thermally treated LDHs; CLDHs) have been studied, research dealing with their stability, stabilizing efficiency and remediation potential for contaminated soils remains scarce. We present a complex study investigating the stabilizing efficiency of Mg-Fe LDHs and CLDHs at different conditions, including aqueous solutions and real soils with highly elevated As(V), Pb(II) and Zn(II) concentrations. All studied materials showed excellent (ad)sorption efficiency for As(V), Pb(II) and Zn(II) in aqueous solutions. Additionally, the reconstruction ability of CLDHs at different conditions that could improve their adsorption properties was also evaluated, and the dependence on time, pH and the concentrations of metal(loid)s was shown. In general, CLDHs showed higher stability and stabilizing efficiency in aqueous and soil solutions; however, LDHs were more efficient in contaminated soils. Furthermore, solid state analyses coupled with geochemical modeling showed the formation of new phases corresponding to Mg-carbonates/silicates on the surfaces of LDH/CLDH after their incubation in soils. Both LDHs and CLDHs significantly decreased the bioavailable/labile fraction of As(V) and Zn(II) in the studied soils. In general, our work shows Mg-Fe LDHs and CLDHs as prospective materials for water and soil remediation.

Introduction

Different oxides and/or hydroxides have already been used for chemical stabilization of As(V), Pb(II) and Zn(II) in soils, e.g., Fe/Al oxides/hydroxides (García-Sánchez et al., 2002; Hanauer et al., 2011), Mn oxides (McCann et al., 2015; Michálková et al., 2016a, 2016b) or Fe(0) (Kumpiene et al., 2006; Tiberg et al., 2016). Nevertheless, complex studies dealing with long-term stability/stabilizing efficiency and possible transformations of such materials in soil conditions are still needed to evaluate the potential release of risk elements back to soils. Moreover, the universality of soil amendments is crucial in terms of stabilization efficiency for various metal(loid)s. In this context, layered double hydroxides (LDHs) and mixed oxides (thermal thermally LDHs; CLDHs) have been previously proposed as excellent sorbents for As(V), Pb(II) and Zn(II) in aqueous solutions. Moreover, CLDHs have shown even higher sorption efficiency for such contaminants compared to pristine LDHs, and this enables their incorporation *via* reconstruction of the original LDH structure (Goh et al., 2008; Liang et al., 2013).

Although the sorption of As(V) and metals from aqueous solutions has been studied intensively, research dealing with the stability and stabilizing efficiency of LDHs and CLDHs in real contaminated soils remains scarce (Goh et al., 2008; Liang et al., 2013). Generally, the main disadvantage of LDHs and CLDHs is the possible Mg(II) leaching from the LDH structure that commonly occurs at pH values from 4 to 9 (Jobbágy and Regazzoni, 2011). However, the information about Mg(II) release is often omitted in sorption studies using LDHs and CLDHs. Therefore, stability testing combining both solution and solid-state investigations is an important step in the assessment of the materials as potential amendments for soils. Up to now, only a few studies have dealt with stabilization of metal(loid)s in real/spiked soils using LDHs and CLDHs (Sun et al., 2015b; Zhang et al., 2012a; Zhou et al., 2017). Some studies have focused on incorporation of different fertilizers or agrochemicals, e.g., nitrate and/or phosphate (Everaert et al., 2016; Torres-Dorante et al., 2008), in the LDH structure to enable their slow release and their uptake by plants. Therefore, a complex study dealing with stability and/or stabilizing efficiency of LDHs and CLDHs and their influence on soil properties is needed. To the best of our knowledge, possible transformations of LDHs and CLDHs in soils, e.g., reconstruction of CLDHs or formation of new phases, have not been studied.

The objective of this study is a complex characterization of the behaviors Mg-Fe LDHs and CLDHs at different experimental conditions including (ad)sorption experiments in

aqueous As(V), Pb(II) and Zn(II) solutions, stability testing of materials using deionized water and real soil solutions contaminated with As(V), Pb(II) and Zn(II), the influence of pH on metal(loid)s leaching from amended soils and the stability and stabilizing efficiency of materials in real contaminated soils. The sorption mechanisms and phase transformations of materials were investigated using a combination of solid state analyses and geochemical modeling.

Materials and methods

Soil characterization

The stability, stabilization efficiency and transformations of LDH, CLDH-450 and CLDH-550 were studied in two contrasting soil types with elevated metal(loid) contents. Both soils originated from the Czech Republic and were collected from the superficial layer (0-20 cm), air dried, homogenized and sieved (2 mm stainless sieve). Soil enriched with As(V) (As-soil) was collected in a forest area with naturally occurring As-bearing minerals (Smolotely, Příbram), e.g., arseniosiderite, bariopharmacosiderite, yukonite, and Fe (hydr)oxides with variable As₂O₅ contents (Drahota et al., 2018). Soil contaminated mainly with Pb(II) and Zn(II) (Zn-soil) was collected from a river alluvium contaminated by the smelting industry (Trhové Dušníky, Příbram). The detailed characteristics of the soils used in this study (Table S4.1) were determined according to Michálková et al. (2016b).

Synthesis and characterization

The synthesis of Mg-Fe LDH with a Mg/Fe molar ratio of 4 (denoted further as LDH) was performed according to our previous studies (Hudcová et al., 2017, 2018; Seida et al., 2001). Mixed oxides were obtained by the calcining synthesis of Mg-Fe LDH in a muffle furnace at 450°C and 550°C (CLDH-450 and CLDH-550) with a temperature rate of 5°C min⁻¹, and the final temperature was maintained for 8 hours. The structural characterization of all synthesized materials was performed by X-ray diffraction analysis (XRD) using a PANalytical X'Pert Pro diffractometer with an X'Celerator detector (CuK_α radiation, 40 kV, 30 mA, and measuring step of 0.02° s⁻¹ in the range from 10° to 80° 2 Θ), and the identification of all phases was performed using PANalytical X'Pert HighScore Plus software (version 3) and the ICDD PDF-2 database (2003). The specific surface area, pore size and pore distribution were determined using the BET (*Brunauer-Emmett-Teller*) and BJH (*Barrett-Joyner-Halenda*) methods by N₂ adsorption at -196°C using ASAP 2050 (Micrometrics Instrument Corporation, USA). The pH_{H20} of all materials was measured in suspensions (1:5 w/v) of given material and deionized water (ISO 10390:2005) with an inoLab pH meter (pH 7310, WTW, Germany) equipped with a combined pH electrode (SenTix 41, WTW, Germany). Finally, the pH_{PZC} of all materials was determined by the immersion technique (Fiol and Villaescusa, 2009).

Sorption mechanisms in aqueous solutions

Adsorption properties of CLDH-450 and CLDH-550 were studied by kinetic and equilibrium experiments using the same procedure and conditions as described for pristine LDH in our previous studies where the basic adsorption properties of LDHs were also evaluated (Hudcová et al., 2017, 2018). More specifically, kinetic and equilibrium experiments were performed in individual batches using As(V) ($\text{Na}_2\text{HAsO}_4 \cdot 7\text{H}_2\text{O}$; Sigma-Aldrich Co., USA), Pb(II) ($\text{Pb}(\text{NO}_3)_2$; *Lach-Ner, Ltd., Czech Republic*) and Zn(II) ($\text{Zn}(\text{NO}_3)_2 \cdot 6\text{H}_2\text{O}$; *Lach-Ner, Ltd.*) solutions at concentrations of 0.1 mM (kinetic experiments) and 0.01 to 3 mM (equilibrium experiments) at pH 5.5 for 120 min. All experiments were performed in 0.01 M NaNO_3 (*Lach-Ner, Ltd.*) as the background electrolyte. The pH value was maintained using 1-0.01 M HNO_3 (PENTA, Ltd., Czech Republic) and NaOH (PENTA, Ltd.). Concentrations of individual elements in the solutions were determined by ICP OES (Agilent Technologies 720 Series).

The reconstruction abilities of CLDH-450 and CLDH-550 were determined by XRD. The morphology of CLDHs after As(V), Pb(II) and Zn(II) sorption was studied by scanning electron microscopy (SEM; Tescan Inc., USA) coupled with energy dispersive X-ray spectroscopy (EDX; Bruker Quantax, USA), and the surfaces of materials were described using X-ray photoelectron spectroscopy (XPS; Omicron Nanotechnology, Ltd). The XPS spectra were deconvoluted using the Casa XPS program. Detailed information is given in the Supplementary Material.

Stability of materials in deionized water and soil solutions

The stability of LDH, CLDH-450 and CLDH-550 was tested in deionized water and soil solutions (1 g L^{-1}). The soil solutions were prepared as follows: the As-soil and Zn-soil were first maintained at ~70% of the water holding capacity (WHC) for 14 days, then dried at room temperature and extracted in deionized water (1:5 w/v). For stability testing, the samples were leached (in duplicates), collected at given time intervals from 10 minutes to 28 days, and then filtrated ($0.2 \mu\text{m}$ acetate membrane), and the pH value was measured. The liquid and solid analyses were determined using ICP OES, XRD and SEM/EDX analyses.

pH-static leaching experiments

The influence of the pH value on the leachability of metal(loid)s from soils amended with LDH, CLDH-450 and CLDH-550 was tested by pH-static leaching experiments at pH 3.5, 5.5, and 7.5 (manually adjusted using NaOH and HNO₃) and without pH adjustments (CEN/TS 14997, 2006). The detailed procedure is given in the Supplementary Material. At the end of the experiment, the pH and Eh values were measured. The Eh was determined using a digital multimeter (Multi 3420, WTW, Germany) equipped with a combined IDS electrode (SenTix ORP 900, WTW, Germany). Afterwards, all samples were centrifuged (3000 rpm, 20 min) and filtered using a 0.2- μ m acetate membrane. The content of elements was determined by ICP OES, and the dissolved organic carbon (DOC) was measured using the carbon analyzer TOC-L CPH (Shimadzu, Japan).

Incubation batch experiments

The stabilizing efficiency, stability and transformations of LDH and CLDH-450, in real contaminated soils were studied using incubation batch experiments. The mixed oxide CLDH-450 was selected according to better sorption properties and the reconstruction ability compared to CLDH-550. Two types of experiments using As-soil and Zn-soil were performed. First, LDH and CLDH-450 (1% w/w) were individually mixed with each soil type, and 100 g samples of these mixtures were placed into plastic pots. Second, materials were placed into two-layered sealed polypropylene pouches, and 99 g of each soil was placed on these pouches. The setup of the experiment is given in Fig. S4.1. All experiments were performed in separate pots for time intervals of 1, 3, 5 and 10 weeks including a control variant (without amendments). Detailed information (including liquid/solid analyses) is given in the Supplementary Material. In addition, the analytical results were coupled with the PHREEQC-3 hydrogeochemical code (Parkhurst and Appelo, 2013) to determine the potential precipitation of selected secondary phases. The T&H.dat database (containing major and trace elements as well as fulvic/humic acids) was used for all the calculations. According to Borůvka and Vácha (2006), the DOC was entered into the code as fulvate (FA) (70%) and humate (HA) (30%). Moreover, the pH_{H2O}, pH_{KCl} and simple/sequential extractions of the non-amended and amended As-soil (Wenzel et al., 2001) and Zn-soil (Rauret et al., 2000; Quevauviller, 1998) after 10 weeks were determined.

Statistical analysis

The results of pH-static leaching experiments and incubation batch experiments were statistically treated using the software Statistica 13 (StatSoft Inc., USA). The significant differences between non-amended/amended soils and individual amendments were evaluated. Since preliminary data analyses showed a non-normal distribution, the nonparametric test (Mann-Whitney U test) at a significance level of $\alpha = 0.05$ was used.

Results and Discussion

Synthesis and characterization

Diffraction patterns of LDH, CLDH-450 and CLDH-550 are given in Fig. 4.1. The diffraction pattern of LDH showed all characteristic peaks corresponding to the crystalline LDH structure of layered double hydroxides as previously described (Hudcová et al., 2017, 2018). After thermal treatment, the layered structure of LDHs collapsed, and Mg-Fe mixed oxides were formed, which resulted in the reduction of peaks in the diffraction patterns (Kuśtrowski et al., 2005; Millange et al., 2000). Peaks in the diffraction pattern of CLDH-450 and CLDH-550 corresponded to the formation of mixed cubic MgO-like oxides (periclase). Commonly, mixed oxides are described as the solid solution of Me(II) (e.g., Mg) and Me(III) (e.g., Fe) with Me(III) dispersed in the MgO lattice (Kuśtrowski et al., 2005). The higher temperature of the thermal treatment led to the increase of sharpness and intensity of all peaks that corresponded to the increasing crystallinity of CLDH-550 (Millange et al., 2000). Moreover, the broad peak at 35.5° was assigned to the formation of spinel MgFe_2O_4 as has been discussed by Hájek et al. (2017).

The specific surface area and porosity of LDH, CLDH-450 and CLDH-550 are given in Table S4.2 and N_2 adsorption-desorption isotherms in Fig. S4.2. Detailed information about N_2 adsorption-desorption isotherms is given in the Supplementary Material (Teixeira et al., 2014; Thommes et al., 2015; Vulic et al., 2012). The specific surface area of both mixed oxides significantly increased in comparison to LDH. However, lower specific surface area was observed for CLDH-550, which corresponded to the increasing crystallinity of this material (changes in the internal arrangement caused by the crystallization process) as was discussed above and by Kovanda et al. (2003). In general, the porous structure of CLDHs is developed during the thermal treatment by the destruction of brucite-like layers as shown by XRD analyses and discussed by Zhang et al. (2012c).

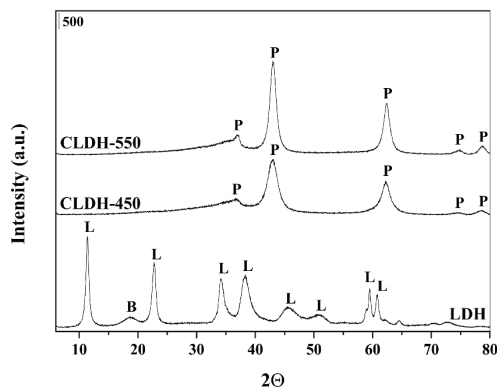


Fig. 4.1. XRD diffraction patterns of LDH, CLDH-450 and CLDH-550 (B: brucite; L: layered double hydroxide; P: periclase).

All materials showed high pH (9.8–11.4) in water (Table S4.2) that corresponded to high pH on the LDH/CLDH surface. Moreover, LDHs and CLDHs showed a strong buffering effect as was previously discussed by Zhang and Hou (2007). The pH_{PZC} of newly synthesized LDH ($\text{pH}_{\text{PZC}} = 10$) corresponded to our previous studies (Hudcová et al., 2017, 2018). However, both CLDHs showed even higher values ($\text{pH}_{\text{PZC}} = 12.5$) in comparison to LDHs and other CLDHs (Goh et al., 2008). In general, the high pH_{PZC} of LDHs is attributed to the positive charge of basal sites by the substitution of Mg(II) by Fe(III) during the synthesis. The positive charge is compensated by interlayered CO_3^{2-} . Nevertheless, the pH_{PZC} of CLDHs showed even higher values that can correspond to the absence of interlayer CO_3^{2-} compensating thus the positive charge; therefore, the surface of CLDHs becomes more positive (Fang et al., 2015; Hu et al., 2017a, 2017b; Isaacs-Paez et al., 2014).

Sorption mechanisms in aqueous solutions

Kinetic and equilibrium adsorption data describing the adsorption of As(V), Pb(II) and Zn(II) on CLDH-450 and CLDH-550 at a controlled pH of 5.5 are given in Fig. S4.3A-C and Fig. S4.3D-F, respectively. The kinetic data were modeled by pseudo-first and pseudo-second order kinetics (Table S4.3) and equilibrium data by the Langmuir and Freundlich models (Table S4.4), respectively (Foo and Hameed, 2010; Simonin, 2016). The correlation coefficients of pseudo-first and pseudo-second order kinetics describing the adsorption of all studied metal(loid)s on CLDH-450 and metals on CLDH-550 were similar. However, the adsorption of As(V) on CLDH-550 was better described by pseudo-second order kinetics. These results are in accordance with our previous studies with LDHs (Hudcová et al., 2017, 2018). Equilibrium data describing the As(V) sorption on CLDHs was better fit by the Freundlich model, while Pb(II) and Zn(II) sorption on both CLDHs was better fit by the Langmuir model. The appropriate models describe As(V) and Pb(II) sorption in accordance with pristine LDHs. However, Zn(II) sorption on LDHs was better fit by the Freundlich model (Hudcová et al., 2017, 2018). More detailed information is given in the Supplementary Material. In general, both CLDHs showed high adsorption rates for all contaminants. In comparison to pristine LDHs, CLDH-450 and CLDH-550 showed higher Zn(II) adsorption efficiency. However, Mg-Fe LDHs appeared as comparable sorbents of As(V) and Pb(II) as Mg-Fe CLDHs, although other studies showed CLDHs as significantly more efficient materials for (ad)sorption of metal(loid)s (Sun et al., 2015a).

Although the XRD diffractograms of CLDH-450 after being stirred in deionized water and in the background electrolyte showed characteristic peaks for the LDH structure (Fig. S4.4), i.e., successful reconstruction under the given conditions, lower intensity and sharpness of all peaks indicated lower crystallinity of the reconstructed materials compared to pristine LDHs. However, CLDH-550 remained the same before and after the experiment, which corresponded to the findings of previous studies (Evans and Slade, 2006), i.e., decreasing reconstruction ability of CLDHs synthesized at higher temperatures (500°–600°C). In general, the temperature of the thermal treatment has a strong effect on the reconstruction ability of CLDHs since the increasing temperature (over 500°C) leads to the formation of stable spinel (the solid-state diffusion of divalent cation (Mg) into tetrahedral positions). The formation of spinel blocks completed reconstruction of the original LDH structure. However, these results are contradictory to Hájek et al. (2017), where such CLDHs were synthesized with successful reconstruction in less than 30 min in demineralized water. As our experiments were performed at a controlled pH of 5.5, lower than the natural pH of CLDHs (see Table S4.2), we conclude that the decreasing pH blocked the complete reconstruction of CLDH-550. Moreover, a strong influence of the initial metal(loid) concentrations on the reconstruction of CLDH-450 was also observed (Fig. S4.5), i.e., a decreasing ability of CLDH-450 to reconstruct the original LDH structure with increasing initial As(V), Pb(II) and Zn(II) concentration. Detailed information is given in the Supplementary Material. Therefore, we suggest that the reconstruction depends on several key factors including time, pH value and concentrations of metal(loid)s. However, the reconstruction could influence the As(V) and Zn(II) sorption *via* incorporation of As(V) into interlayered regions and isomorphic substitution of Mg(II) in layers by Zn(II). The (ad)sorbed amounts at the highest initial metal(loid) concentrations is presented in Table 4.1.

Table 4.1 (Ad)sorbed amounts of As(V), Pb(II) and Zn(II) on LDH, CLDH-450 and CLDH-550.

Material	(Ad)sorbed amount (mmol g ⁻¹)		
	As	Pb	Zn
LDH	1.72 ^a	1.65 ^b	1.44 ^b
CLDH-450	2.01±0.10	1.87±0.04	1.18±0.06
CLDH-550	1.21±0.08	1.37±0.08	1.03±0.13
Precipitation ^a	excluded	(hydro)cerussite	excluded

^aHudcová et al. (2017); ^bHudcová et al. (2018); ^cpredicted by Visual MINTEQ 3.1 (initial concentration 500 mg L⁻¹; pH 5.5; background electrolyte 0.01 M NaNO₃)

The SEM images (Fig. S4.6) and the XPS spectra (Fig. S4.7) of CLDH-450 and CLDH-550 before and after As(V), Pb(II) and Zn(II) sorption showed minor changes when

compared to pristine LDHs, suggesting a similar morphology and sorption mechanisms (Hudcová et al., 2017, 2018). Since these results are consistent with our previous studies using LDHs, detailed information is given in the Supplementary Material. The EDX results (Fig. S4.6) and the surface stoichiometry (Table S4.5) corresponded to the (ad)sorbed amounts on individual materials (Table 4.1). In general, the overall mechanisms of As(V), Pb(II) and Zn(II) sorption on CLDHs were affected by adsorption/incorporation (As), adsorption/surface-induced precipitation (Pb) and adsorption/surface-induced precipitation/isomorphous substitution (Zn), following the previously discussed sorption mechanisms on pristine LDHs (Hudcová et al., 2017, 2018).

Stability of the studied materials

The stability of the studied materials was evaluated through Mg(II) and Fe(III) leaching from the structure and/or surface of LDHs and both CLDHs. The Mg(II) leaching from the LDH, CLDH-450 and CLDH-550 structures in deionized water and soil solutions is shown in Fig. S4.8 and Fig. 4.2, respectively. In general, a lower amount of Mg(II) was released from both CLDHs compared to LDH. A slight release of Mg(II) from the LDH structure was observed in deionized water when finally equilibrated after 240 hours. Since Fe(III) leaching was not observed, the possible destruction of the LDH structure was excluded (Jobbágy and Regazzoni, 2011). In contrast, an even smaller amount of Mg(II) was released from CLDH-450 and CLDH-550 structures, and it subsequently decreased and was equilibrated after 96 hours. Moreover, the stability of materials in soil solutions was also tested (Fig. 4.2). The Mg(II) leaching from LDH and both CLDHs in soil solutions showed a similar shape to that in the deionized water. However, the amount of Mg(II) leached from the LDH structure reached equilibrium within 8–24 hours. Since the soil solutions also contain other elements (i.e., Fe, Al, Zn, Pb, As), the effect of LDHs and CLDHs on their stabilization was also evaluated. Based on the results, the amount of As, Pb, and Zn from soil solutions significantly decreased using LDH and both CLDHs, which confirmed the high stabilization efficiency (within less than 7 hours for the latter ones). The pH value in deionized water increased to 10–11 for LDH and both CLDHs, while the increase from the initial pH of 6.9 (As-soil) and 6.4 (Zn-soil) to 8.8–8.9 for LDH, 9.1–9.8 for CLDH-450 and 9.7–9.8 for CLDH-550 in the soil solutions were observed.

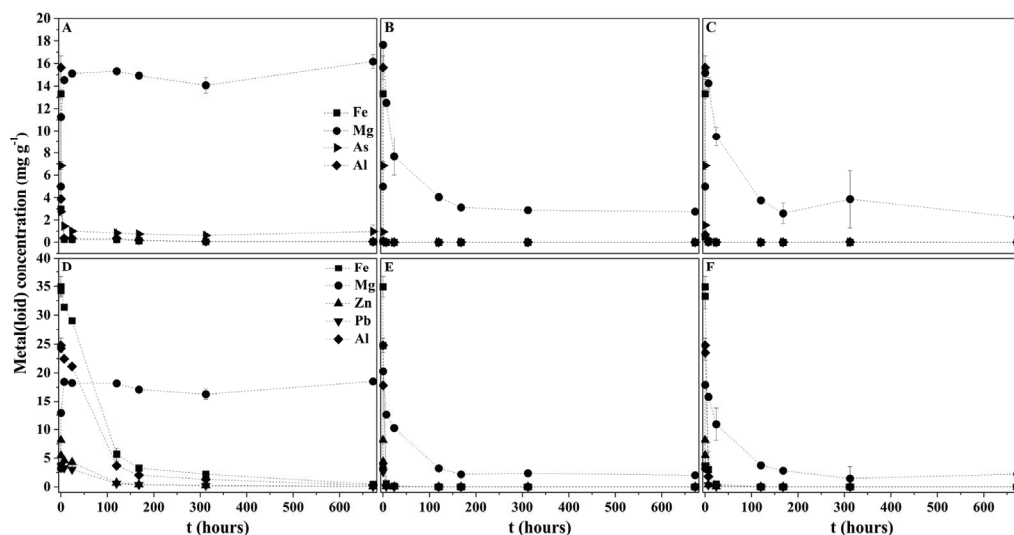


Fig. 4.2. Stability and sorption efficiency of LDH (A, D), CLDH-450 (B, E) and CLDH-550 (C, F) in As-soil solutions (A-C) and Zn-soil solutions (D-F). Data presented are means and standard deviations ($n = 2$).

The solid state XRD analyses of the residues (Fig. 4.3) showed characteristic peaks for the LDH structure without any formation of new phases, and successful reconstructions of CLDH-450 and CLDH-550 were observed. The sharpness and intensity of all peaks corresponding to the LDH structure increased in comparison to Fig. S4.4, which confirmed our hypothesis that time as well as the pH value have strong effects on the structure, i.e., the crystallinity, of reconstructed LDHs. The SEM/EDX results (Fig. S4.9) showed significant changes in the morphology of all materials, which were probably caused by the aging in alkaline conditions. Moreover, a plate-like morphology was observed (especially in the case of CLDHs) that was in agreement with the LDH structure (Delorme et al., 2006). Based on the results from the liquid/solid state analyses, the reconstruction was assigned to the dissolution-recrystallization process. Both CLDHs (i.e., Mg and Fe in tetrahedral sites) were rehydrated, and the newly emerged Mg and Fe hydroxides formed single positively charged sheets (i.e., Mg and Fe in octahedral sites) with shared edges. Finally, anions (especially carbonates) and water entered the interlayered region, and the LDH structure was recovered (Millange et al., 2000). As mentioned in Section *Sorption mechanisms in aqueous solutions*, the reconstruction could also influence the metal(loid) stabilization. However, Pb(II) and Zn(II) were more likely stabilized by precipitation as a result of high pH. In contrast, all materials showed extremely high affinity for the As(V) even at high pH values, confirming that LDHs and CLDHs are highly effective As(V) sorbents in aqueous (including soil) solutions.

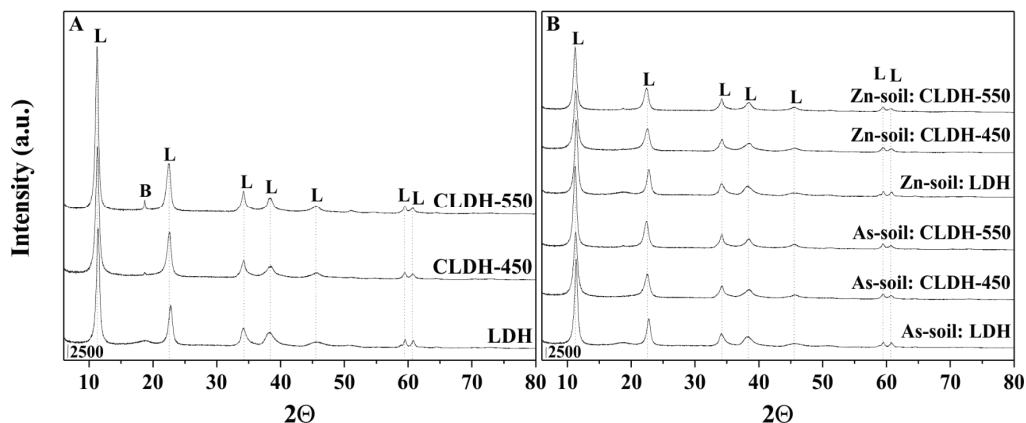


Fig. 4.3. XRD diffractograms of LDH, CLDH-450 and CLDH-550 after stability tests in deionized water (A), As-soil solutions and Zn-soil solutions (B) (B: brucite; L: layered double hydroxide).

pH-static leaching experiments

The results of pH-static leaching experiments are given in Fig. S4.10, and the pe-pH values measured during experiments without pH adjustments (i.e., at natural pH) are shown in Fig. S4.10A. The natural pH (5–6) significantly increased for soils amended with LDH (7–8) < CLDH-450 and CLDH-550 (8.4–8.7). The pH increase was caused by a stronger buffering effect of LDHs and CLDHs than the neutralization capacity of the soils, as has been demonstrated in aqueous solutions (see Section *Sorption mechanisms in aqueous solutions* and *Stability of the studied materials*) and in soils (Sun et al., 2015b). The increasing pH value led to a corresponding decrease in the pe values (Vítková et al., 2017). Based on the pe-pH diagram, oxidizing conditions prevailed in all batches. The stability of LDH and CLDHs was evaluated by the Mg(II) leaching (Fig. S4.11). The Mg(II) leaching increased with decreasing pH values, which is in accordance with the behavior of LDHs in aqueous solutions (Hudcová et al., 2017). The lowest Mg(II) leaching was observed in batches at the natural pH. In comparison to soils amended with both CLDHs, significantly lower Mg(II) leaching was observed from soils amended with LDH, indicating a higher stability of LDHs incubated in soils compared to after their direct application to deionized water/soil solutions (see Section *Stability of the studied materials*).

All materials (LDH, CLDH-450 and CLDH-550) significantly decreased the As(V) leachability (Fig. S4.10B) over the whole pH range, both at low and high pH values,

which indicates a high affinity of LDHs and CLDHs towards As(V), as was also observed in soil solutions (see Section *Stability of the studied materials*). The decrease in the As(V) leachability from amended soils was significantly different at pH 5.5, 7.5 and the natural pH (i.e., without pH control). At pH 3.5 and 5.5, the As(V) leachability was more efficiently decreased in soils amended with LDH than with both CLDHs. The opposite effect was observed at pH 7.5 and at the natural pH. Moreover, CLDH-450 was more efficient than CLDH-550. In general, the DOC concentration (Fig. S4.10C) increased with increasing pH values as we previously discussed (Micháľková et al., 2016b). Nevertheless, the DOC significantly decreased after the addition of LDHs and CLDHs at pH 7.5 and at the natural pH. However, the influence of individual materials on the DOC leaching was statistically insignificant (except for pH 5.5).

The Pb(II) leachability (Fig. S4.10D) increased with increasing pH values that correlate with the dissolution of the soil organic matter (SOM). In comparison to the non-amended soils, a significant decrease in the Pb(II) leachability from amended soils was observed at pH 5.5 and 7.5, following a decrease in the sequence of CLDH-550 > CLDH-450 > LDH and LDH > CLDH-450 > CLDH-550, respectively. However, the Pb(II) leachability in amended soils at the natural pH slightly increased, which correlated with higher DOC leaching at the natural pH (see below). The Zn(II) leaching behavior was different from that for Pb(II), i.e., increasing leachability with decreasing pH values (Fig. S4.10E). This contrasting behavior has been discussed previously (Ettler et al., 2015; Vítková et al., 2017). Significant differences in the Zn(II) leachability from non-amended and amended soils were observed at pH 5.5, 7.5 and at the natural pH. More specifically, all amendments significantly decreased Zn(II) leachability at higher pH values (pH 7.5 and natural pH), i.e., LDH > CLDH-450 > CLDH-550. However, Zn(II) leachability from amended soils increased at pH 5.5 (Fig. S4.10E). In comparison to the As-soil, a higher DOC leaching from the non-amended Zn-soils was observed even at pH 5.5 (Fig. S4.10F) that was connected to a higher TOC in this soil type (see Table S4.1). All amendments significantly decreased the DOC concentration at pH 5.5 (except using LDH) and 7.5. However, the experiments at the natural pH resulted in an increase in the DOC concentration.

Incubation batch experiments

Incubation experiments represent an important step towards potential application of the LDHs and CLDHs in real soil conditions (Fig. 4.4). As expected, the pH values of amended soils significantly increased after 10 weeks of the experiment in comparison to the non-amended soils (see Table S4.6 and Fig. S4.12), which corresponds to the

results presented in Section *Stability of the studied materials and pH-static leaching experiments*. The Mg(II) leaching from both soils amended with LDH and CLDH-450 increased over time (Fig. 4.4A, D). A lower leaching of Mg(II) was observed from the amended As-soil in comparison to the amended Zn-soil. A significantly higher amount (nearly 2 times) was leached from CLDH-450 than from LDH, showing higher stability of LDHs in the soil conditions, which corresponds to the results of the pH-static leaching experiments (see Section *pH-static leaching experiments*). In contrast, the excess Mg in the CLDH solutions resulted in oversaturation with respect to several Mg-phases as predicted by the PHREEQC calculations (Table S4.7). In particular, Ca-Mg carbonates and Mg carbonate-hydrates were likely to precipitate in the Zn-soil treated with CLDH, which was mainly related to the high pH values (8.4–8.9) observed within the studied time frame. The saturation index values for artinite ($\text{Mg}_2(\text{CO}_3)(\text{OH})_2 \cdot 3\text{H}_2\text{O}$) and nesquehonite ($\text{MgCO}_3 \cdot 3\text{H}_2\text{O}$) showed strong correlation with pH for all the samples at all time intervals ($R^2 > 0.97$). The model results show the important role of carbonates and indicate the long-term behavior and stability of the amendment in soils. Generally, the DOC increased with the increasing pH values, as mentioned in Section *pH-static leaching experiments*, and decreased over time (Fig. 4.4B, E). The DOC was more apparent for CLDH-450 in both soils. As in the pH-static leaching experiments, higher DOC concentrations were observed in the case of Zn-soil. The concentration of Si(IV) decreased in both amended soils in comparison to the non-amended soil (Fig. 4.4C, F), which could be attributed to possible precipitation of newly formed Si-phases. Moreover, geochemical modeling predicted sepiolite ($\text{Mg}_4(\text{Si}_6\text{O}_{15})(\text{OH})_2 \cdot 6\text{H}_2\text{O}$) as the main phase controlling the Si behavior, showing positive saturation indices for both soils amended with CLDH (Table S4.7). Furthermore, the precipitation of sepiolite was confirmed by XRD (see later in the text).

The As(V) concentration in the soil solutions of the non-amended As-soils increased over time (Fig. 4.4G). A significant decrease in the As(V) concentration was observed in soils amended with LDH at all time intervals. Moreover, the As(V) stabilizing potential of LDH increased over time, i.e., 33% after 3 weeks; 51% after 5 weeks; and 50% after 10 weeks, compared with the the non-amended soil leachates. Moreover, the ability of LDH to decrease the As(V) concentration remained the same even if the initial As(V) concentration increased. Surprisingly, in contrast with previous results (see Section *Stability of the studied materials and pH-static leaching experiments*), the As(V) stabilizing efficiency of CLDH-450 resulted in significantly different As(V) concentrations in amended soils only after 1 and 5 weeks of the experiment with the lowest effectivity after 10 weeks (14%), showing the decreasing ability of this material to stabilize As(V) in soil conditions with increasing time. Additionally, no As-rich

mineral phases were predicted by the PHREEQC calculations. Although Vítková et al. (2017) predicted scorodite ($\text{FeAsO}_4 \cdot 2\text{H}_2\text{O}$) to precipitate in As-rich solutions, this phase was not seen in our leachates. This observation may be related to prevailing adsorption rather than precipitation. Based on these results, we suggest LDHs as more promising amendments for As(V) stabilization in real extremely contaminated soils.

The Zn(II) concentration in the soil solutions of the non-amended Zn-soil increased over time (Fig. 4.4H). However, the Pb(II) concentration is not shown as all the values were below the limit of detection. A significant decrease in Zn(II) concentration was observed in soils amended with LDH and CLDH-450 at all time intervals. The Zn(II) stabilizing potential of LDH and CLDH-450 after 10 weeks reached 99% and 100% compared with the non-amended soil, respectively, showing strong Zn(II) stabilizing efficiency of these materials that corresponded to sorption effectivities of these materials in aqueous solutions (see Section *Sorption mechanisms in aqueous solutions, Stability of the studied materials and pH-static leaching experiments*). Based on the modeling results (Table S4.7), smithsonite (ZnCO_3) or Zn carbonate-hydrate ($\text{ZnCO}_3 \cdot \text{H}_2\text{O}$) could be the solubility-controlling phases for Zn, yielding saturation index values within the interval $<-1; 1>$. However, this was probably not the main immobilizing mechanism for Zn, since similar predictions were determined for control and LDH-treated soils. Since the stabilization of metals, i.e., Pb(II) and Zn(II), using LDHs and CLDHs in real contaminated soils has not yet been studied, these results are crucial in terms of novel remediation techniques.

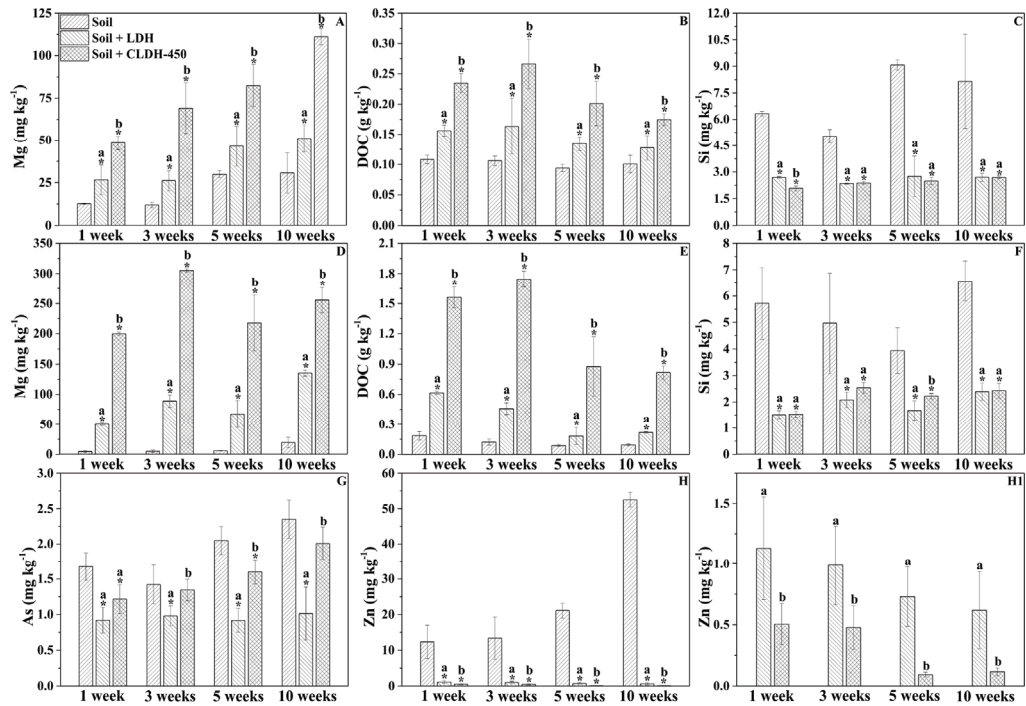


Fig. 4.4. Mg(II) (A), DOC (B), Si(IV) (C) and As(V) (G) in As-soil solutions and Mg(II) (D), DOC (E), Si(IV) (F) and Zn(II) (H) in Zn-soil solutions after 1, 3, 5 and 10 weeks of incubation batch experiments. Statistical tests were performed separately for every single time interval to compare the non-amended and amended soils (the data with the asterisk means significantly different values) and individual amendments (the data with the different letter means significantly different values) ($\alpha < 0.05$; $n = 4$).

Additionally, As(V), Pb(II) and Zn(II) fractionation after 10 weeks (i.e., at the end of the experiment) is given in Table S4.8. The most labile As(V) fraction (non-specifically sorbed) significantly decreased in soils amended with LDH and CLDH-450 by 51% and 37%, respectively, compared with the control soil. Pb(II) fractionation established by both the simple and sequential extractions showed similar values for non-amended and amended soils, since Pb(II) is predominantly bonded to the SOM. However, a different behavior was determined for Zn(II), which is commonly found in soils in labile forms (Ettler et al., 2015). Based on the sequential extraction, a slight decrease of the exchangeable (plant-available) fraction was observed in soils amended with LDH and CLDH-450 by 17% and 11%, respectively, compared with the control soil. However, the first step using acetic acid caused elevated Mg(II) leaching and a slight Fe(III) leaching from the LDH structure, indicating a partial destruction of the LDH/CLDH structure (Jobbágy and Regazzoni, 2011). However, milder conditions of

the simple extraction using CaCl_2 resulted in a complete stabilization of the most labile Zn(II) fraction and thus appeared as more appropriate for the evaluation of the most harmful fraction of Zn(II) at higher pH values caused by the buffering effect of LDHs and CLDHs.

The XRD diffractograms of LDH and CLDH-450 (placed into pouches) after incubation batch experiments showed the characteristic peaks for the LDH structure (Fig. 4.5), corresponding to previous XRD analyses (see Section *Sorption mechanisms in aqueous solutions* and *Stability of the studied materials*), indicating successful reconstruction of CLDH-450 in the soil conditions at given time intervals. Moreover, formation of new phases was also observed (mainly on the LDH surface) after the incubation of materials in both soils. These phases were identified as magnesium carbonate (lansfordite, $\text{MgCO}_3 \cdot 5\text{H}_2\text{O}$) and hydrated magnesium silicate (sepiolite, $\text{Mg}_4\text{Si}_6\text{O}_{15} \cdot 6\text{H}_2\text{O}$). These minerals commonly occur in alkaline soils in the excess of free Mg(II) ions (Abtahi, 1985; Carrow et al., 2001; Ropp, 2013). Moreover, natural sepiolite has been previously evaluated as an effective sorbent for metals (Hu et al., 2017c); therefore, its formation on the surface of LDHs and CLDHs could positively influence the stabilization of metals in studied soils. The Mg(II) leaching as well as the increase in the pH values in amended soils have been discussed previously, and the possible formation of such phases has been confirmed. The lowest Mg(II) leaching was observed in soils amended with LDH after 5 and 10 weeks, as was confirmed by the highest intensity of peaks corresponding to lansfordite and/or sepiolite in the XRD diffractograms. However, Mg(II) leaching increased in soils amended with CLDH-450, resulting in a very low intensity of such peaks (or even no precipitation). Additionally, SEM/EDX analyses were performed (Fig. 4.6) and confirmed the formation of new phases on the LDH and CLDH surfaces. Additionally, the plate-like morphology observed for LDH particles was more apparent for LDHs incubated in the Zn-soil for a longer time, i.e., 5 and 10 weeks. Nevertheless, some morphological changes, such as development of a porous structure, were observed in the case of CLDH-450.

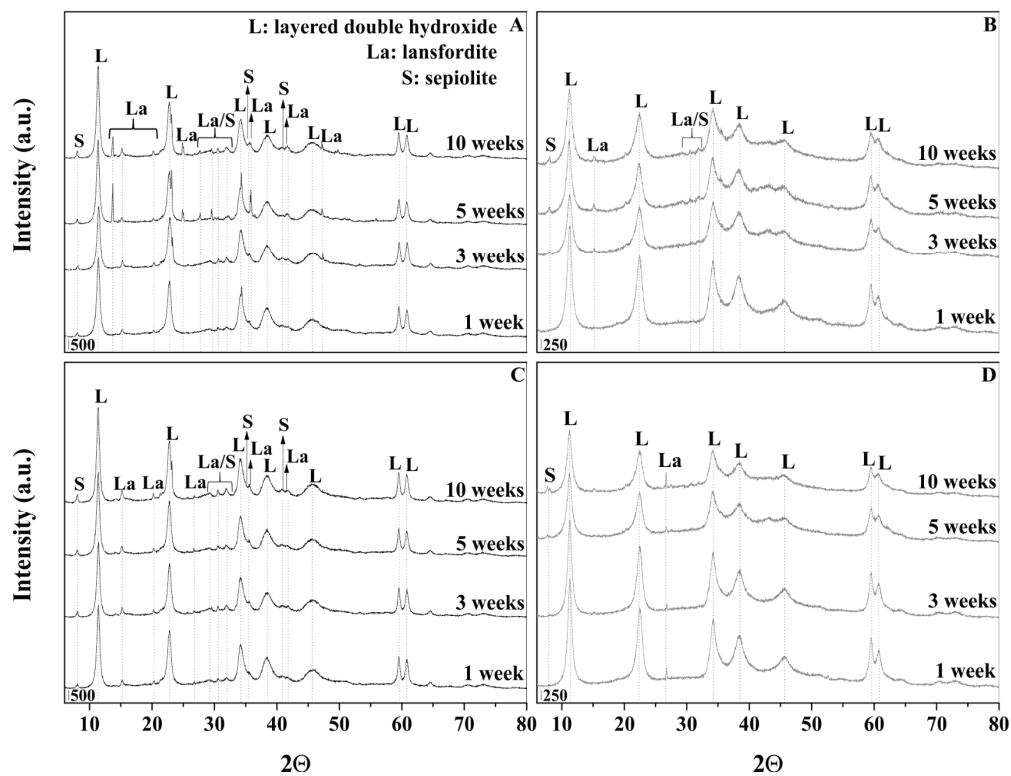


Fig. 4.5. XRD diffractograms of Mg-Fe LDH (A, C) and CLDH-450 (B, D) after 1, 3, 5 and 10 weeks of incubation batch experiments in As-soil (A, B) and Zn-soil (C, D) (L: layered double hydroxide; La: lansfordite; S: sepiolite).

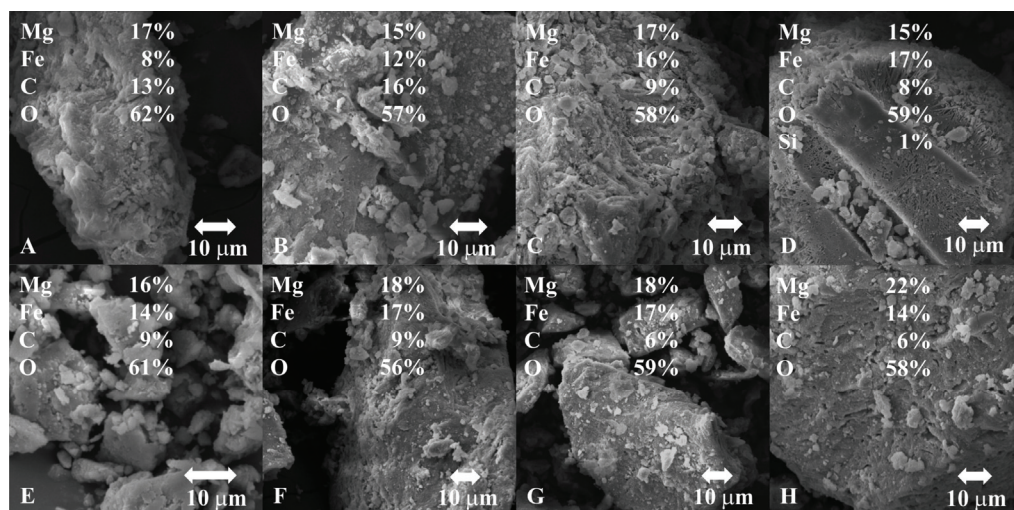


Fig. 4.6. SEM images of Mg-Fe LDH (A-D) and CLDH-450 (E-H) after 1 week (A-B, E-F) and 10 weeks (C-D, G-H) of incubation batch experiments in As-soil (A, E, C, G) and Zn-soil (B, F, D, H).

Perspectives for chemical stabilization

Although LDHs and CLDHs appeared as highly effective sorbents for metal(loid)s in aqueous (including soil) solutions (see Section *Sorption mechanisms in aqueous solutions* and *Stability of the studied materials*) and in real contaminated soils (see Section *pH-static leaching experiments* and *Incubation experiments*), potential side effects need to be solved before their use in direct remediation. In general, pristine LDHs showed higher stability after their direct application into soils, since CLDHs were more promising in aqueous (including soil) solutions. In addition to the stability of materials in soil conditions, the stabilization of the most labile and potentially bioavailable metal(loid)s fraction as well as actual pH are crucial factors affecting the use of the new amendments in real soils. Previously, the adsorption of humic and fulvic acids on the positively charged surface of LDHs/CLDHs has been studied and resulted into improved metal stabilization due to their prevailing negative charge (Chang et al., 2017; Fang et al., 2015, 2018); therefore, their presence in soils with LDHs/CLDHs could improve the overall stabilizing efficiency of the metals. Contrarily, the adsorption of negatively charged species (e.g., chromate, arsenate) could be decreased (Hu et al., 2017d). Moreover, it will also be necessary to evaluate the effect of low-molecular-weight organic acids on the stability of LDHs/CLDHs in soils in future studies, since these acids are exuded by plant roots and can influence the long-term stability and behavior of amendments in soils in general (Vítková et al., 2015). The presence of such

acids could play an important role in the release of nutrients, e.g., Zn(II), which could be completely immobilized in amended soils (see Table S4.8). The possible Zn(II) deficiency together with the increasing pH caused by the buffering effect of LDHs/CLDHs (see Table S4.6 and Fig. S4.12) could also be potential drawbacks that may influence plants and/or (micro)organisms (Broadley et al., 2007; Sun et al., 2015b). In general, we recommend using pristine LDHs in soil remediation technologies rather than CLDHs; however, further studies dealing with the abovementioned problems are needed.

Conclusions

Mg-Fe LDH and CLDH showed excellent sorption efficiency for As(V), Pb(II) and Zn(II); however, these materials exhibited different stabilities at different conditions. In general, the reconstruction of CLDH was strongly influenced by time, pH and concentrations of metal(loid)s. Although CLDHs showed a higher stability and stabilizing efficiency in aqueous solutions, LDHs were more efficient amendments in soils. The solid-state analyses coupled with geochemical modeling after incubation of LDHs/CLDHs in soils showed the formation of new phases (Mg-carbonates/silicates) on the LDH/CLDH surface. In general, LDHs and CLDHs were able to significantly decrease the most labile and potentially bioavailable fraction of the studied metal(loid)s. Such a comprehensive study based on the stability/stabilizing efficiency of LDHs/CLDHs in aqueous solutions and in real contaminated soils shows LDHs/CLDHs as promising amendments in soils highly contaminated with metal(loid)s. We recommend using pristine LDHs in remediation technologies due to their higher stability and stabilizing efficiency in real contaminated soils.

Supplementary Material

Materials and methods

Table S4.1 Basic physico-chemical characteristics of the studied soils.

	As-soil	Zn-soil
pH _{H2O}	6.12 ± 0.00	5.55 ± 0.01
pH _{KCl}	4.87 ± 0.01	4.85 ± 0.00
TOC ^a (%)	1.16 ± 0.14	2.15 ± 0.05
Texture ^b	loamy sand	sandy loam
Pseudo total metal concentration (mg kg⁻¹) (n = 3)		
As	15910 ± 1094	413 ± 9
Pb	118 ± 35	4357 ± 75
Zn	213 ± 9	4107 ± 179
Fe	57853 ± 3610	36884 ± 482
Mg	12457 ± 655	3006 ± 106

^aTOC = total organic carbon according to Michálková et al. (2016b)

Sorption mechanisms in aqueous solutions

The reconstruction ability and sorption properties of CLDH-450 and CLDH-550 under given conditions were evaluated here. The samples of CLDH-450 and CLDH-550 for the solid-state analyses were prepared by stirring individual materials in deionized water and in 0.01 M NaNO₃ for 2 hours at pH 5.5 (corresponding to conditions during equilibrium experiments). The (ad)sorption of As(V), Pb(II) and Zn(II) at initial concentrations ranging from 5 - 500 mg L⁻¹ (i.e., 0.07, 0.02, 0.08 to 6.7, 2.4 and 7.7 mM) were performed on CLDH-450 and CLDH-550. The solid residues were obtained by filtration (cellulose filtration paper) using a vacuum pump and further drying at room temperature.

pH-static leaching experiments

The influence of the pH value on the leachability of metal(loid)s from soils amended with LDH and CLDH-450 was tested by pH-static leaching experiments. As-soil and Zn-soil were mixed with each material (1% w/w) and maintained at ~70% of the WHC for 8 weeks. A control variant without amendments was also included. All soil samples were dried at room temperature, and 1.5 g samples were weighed into 50-mL centrifuge tubes. Subsequently, 15 mL of deionized water was added, and the suspensions were leached for 48 hours at pH 3.5, 5.5, and 7.5 (manually adjusted using NaOH and HNO₃) and without pH control, i.e., not adjusted (termed the natural pH of the material). All experiments were performed in triplicate.

Incubation batch experiments

The mixture of LDH and CLDH-450 with soils was evaluated for the stability and stabilizing efficiency of the materials in soils. The materials were inserted into pouches placed in the soils to obtain solid residue samples of LDH and CLDH-450 for XRD and SEM/EDX analyses to evaluate possible transformations of the materials and/or formation of secondary phases. In both experimental setups, silica sand (CAS Nr. 14808-60-7, Sklopísek Střelec, a.s.) was placed approx. 3 cm from the bottom of each pot, representing an inert layer. The soil solutions were collected at predefined time intervals using the rhizon samplers (mean pore volume size 0.15 μm ; Rhizosphere Research Products, Netherlands) that were placed directly on the surface of the sand layer. The experimental setup is given in Fig. S4.1. All experiments were performed in separate pots in duplicate for specific time intervals, and a control variant was provided for both soils under the same experimental conditions. During the experiment, all pots were watered with deionized water to maintain 70% of the WHC for the whole experiment. Before sampling, additional watering was needed. At each time-step, the soil solutions were filtered using 0.2- μm acetate membranes, and the pH and Eh values were measured. The

contents of individual elements were determined using ICP-OES, the concentration of anions using Dionex ICS-2000 ion chromatography (Dionex, USA) and the DOC using the carbon analyzer TOC-L CPH (all analyses were performed in duplicate). The identification and morphology of LDH and CLDH-450 were established by XRD and SEM-EDX, respectively.

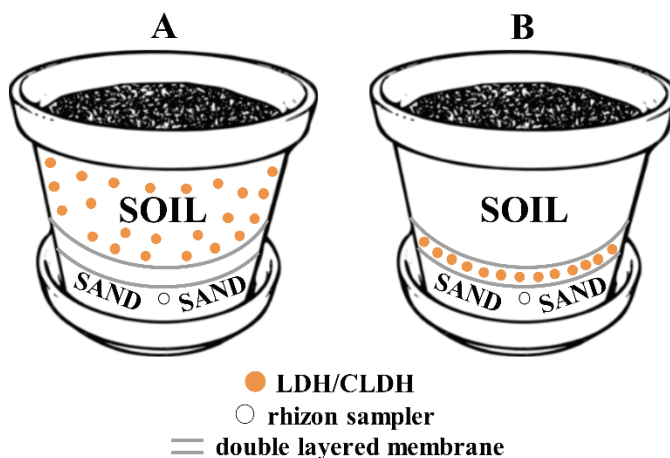


Fig. S4.1. The setup of incubation batch experiments using mixture of LDH/CLDH with soils (A) and LDH/CLDH in pouches below the soils (B).

Results and discussion*Synthesis and characterization*

The N₂ adsorption-desorption isotherm (Fig. S4.2) showed the same shape for all materials, Type IV with hysteresis loop Type H3, indicating no well-defined mesoporous structure of all materials. According to the IUPAC classification, these properties are typical for clays, i.e., mesoporous materials with plate-like aggregates and nonuniform slit-shaped pores (Thommes et al., 2015). The average pore size established by BET and BJH methods and the mesopore distribution based on adsorption and desorption branch are given in Table S4.2 and Fig. S4.2, respectively. The adsorption branch corresponds better to the actual pore size, as this branch is not influenced by the nature of the adsorbent (Vulic et al., 2012). Although larger mesopores (over 10 nm) predominated, a fraction of smaller pores (approx. 2-4 nm) was also observed. The pore size of CLDH-450 decreased in comparison to LDH and CLDH-550. However, the pore volume increased with the increasing temperature of the thermal treatment. Moreover, the thermal treatment also resulted in increasing amounts of micropores that corresponded to a higher specific surface area of CLDH-450 and CLDH-550 in comparison to pristine LDHs (Teixeira et al., 2014).

Table S4.2 Basic properties of LDH, CLDH-450 and CLDH-550.

	LDH	CLDH-450	CLDH-550
S _{BET} (m ² g ⁻¹)	54.80	111.57	92.80
Pore size (nm)	17.81 ^a	15.30 ^a	19.57 ^a
	16.26 ^b	13.26 ^b	17.89 ^b
	12.33 ^c	11.60 ^c	15.96 ^c
V _{pores} (cm ³ g ⁻¹)	0.28 ^d	0.46 ^d	0.50 ^d
	0.29 ^e	0.48 ^e	0.53 ^e
V _{micro} (mm ³ g ⁻¹)	4.30 ^f	12.00 ^f	15.60 ^f
pH _{H2O}	9.76 ± 0.00	9.82 ± 0.00	11.40 ± 0.01
pH _{PZC}	10	12.5	12.5

^aAverage pore diameter - adsorption (BET analysis); ^bAverage pore diameter - adsorption; ^cAverage pore diameter - desorption (BJH method); ^dCumulative pore volume - adsorption (BJH method); ^eCumulative pore volume - desorption (BJH method); ^fMicropore volume (t-plot method)

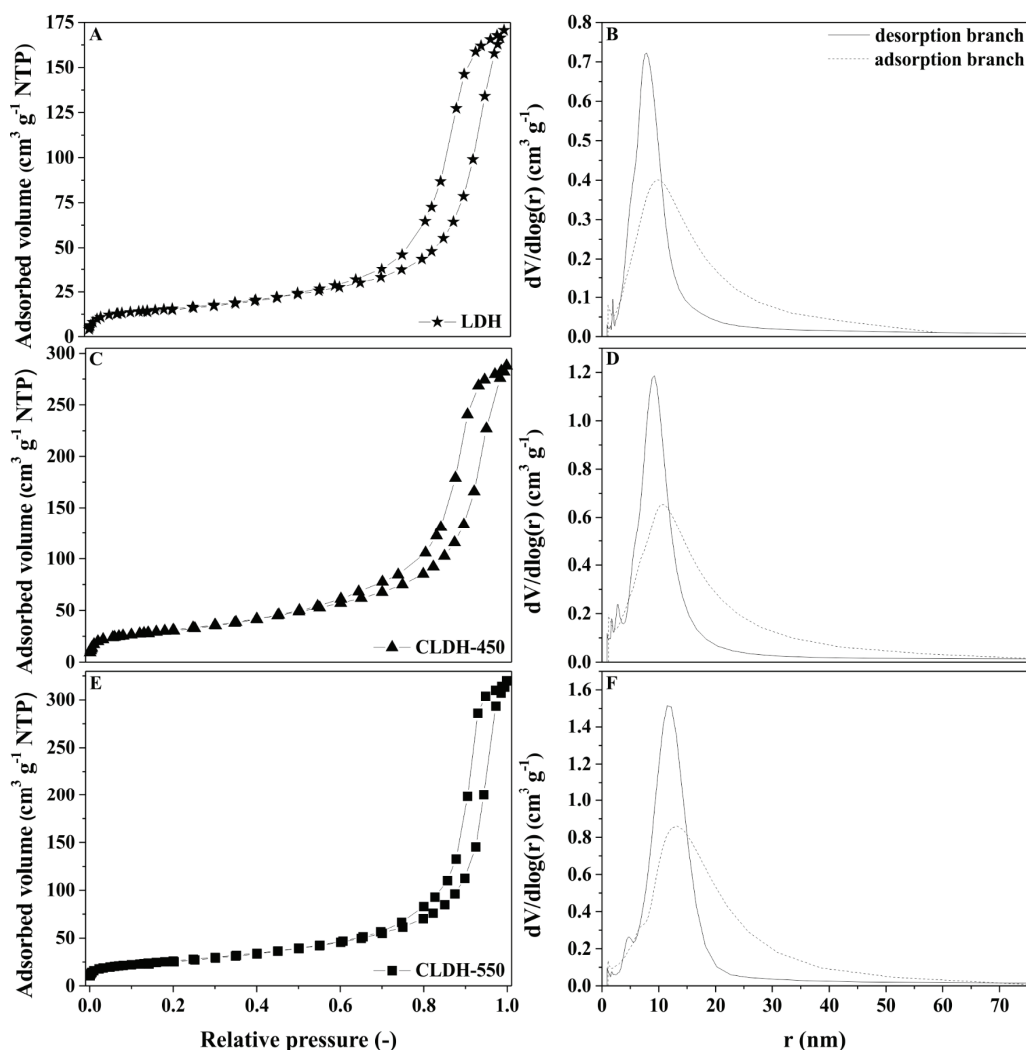


Fig. S4.2. N_2 adsorption-desorption isotherms (A, C, E) and pore size distribution (B, D, F) of LDH (A-B), CLDH-450 (C-D) and CLDH-550 (E-F).

Sorption mechanisms in aqueous solutions

Kinetic data describing adsorption of As(V), Pb(II) and Zn(II) on CLDH-450 and CLDH-550 at controlled pH 5.5 are given in Fig. S4.3A-C. Saturation indices of potential secondary carbonates and/or hydroxides were calculated using the program Visual MINTEQ 3.1 in order to confirm that there was no precipitation under the given conditions. All materials showed high adsorption rates for all contaminants, resulting in equilibrium times less than 20 min for As(V), 10 min for Pb(II) and 15 min for Zn(II).

The data were modeled by pseudo-first order and pseudo-second order kinetics and the adsorption efficiency, experimental values of the adsorbed amount at equilibrium ($q_{e(exp)}$), calculated parameters (q_e , k_1 and k_2) and correlation coefficients (R^2) are given in Table S4.3. The rate coefficients (k_1 and k_2) evaluating the removal rate (with higher rate coefficients meaning faster removal) showed the highest values for data describing Pb(II) adsorption on CLDH-450 in comparison to other metal(loid)s adsorbed on this material and on CLDH-550 as well. The adsorption efficiency of all studied metal(loid)s on CLDH-450 and CLDH-550 were nearly 100%, meaning that the Zn(II) adsorption was improved in comparison to pristine LDHs (Hudcová et al., 2018). Although CLDH-450 showed higher rate coefficients for As(V) and Pb(II), LDHs showed higher rate coefficients for Zn(II) adsorption (in comparison to both CLDHs) and Pb(II) adsorption (in comparison to CLDH-550). Finally, the rate coefficients were similar for data describing As(V) adsorption on LDHs and CLDH-550 (Hudcová et al., 2017, 2018).

Equilibrium adsorption data for As(V), Pb(II) and Zn(II) on CLDH-450 and CLDH-550 at controlled pH 5.5 fitted by the Langmuir and Freundlich models are given in Fig. S4.3D-F and the maximal adsorbed amounts (q_{max}), Langmuir constants (K_L), Freundlich constants (K_F), parameters n and the correlation coefficients for both models are presented in Table S4.4. Again, potential precipitation was checked under the given conditions and excluded using the speciation modeling in the Visual MINTEQ 3.1. However, previous findings on LDHs showed that the surface-induced precipitation could also influence the whole sorption mechanism of Pb(II) and/or Zn(II) (Hudcová et al., 2018). In comparison to pristine LDHs and CLDH-550, CLDH-450 showed the highest adsorbed amount (q_{max}) of Pb(II) and Zn(II). The q_{max} of As(V) on LDHs and CLDH-450 was similar. However, CLDH-550 showed a similar adsorbed amount of Pb(II) and lower adsorbed amount of As(V) and Zn(II) in comparison to pristine LDHs (Hudcová et al., 2017, 2018). In contrast, the affinity of Pb(II) and Zn(II) described by K_L showed the highest values for CLDH-550 in comparison to pristine LDH and CLDH-450 (Hudcová et al., 2017, 2018). The affinity of As(V) was slightly higher for pristine LDHs (Hudcová et al., 2017).

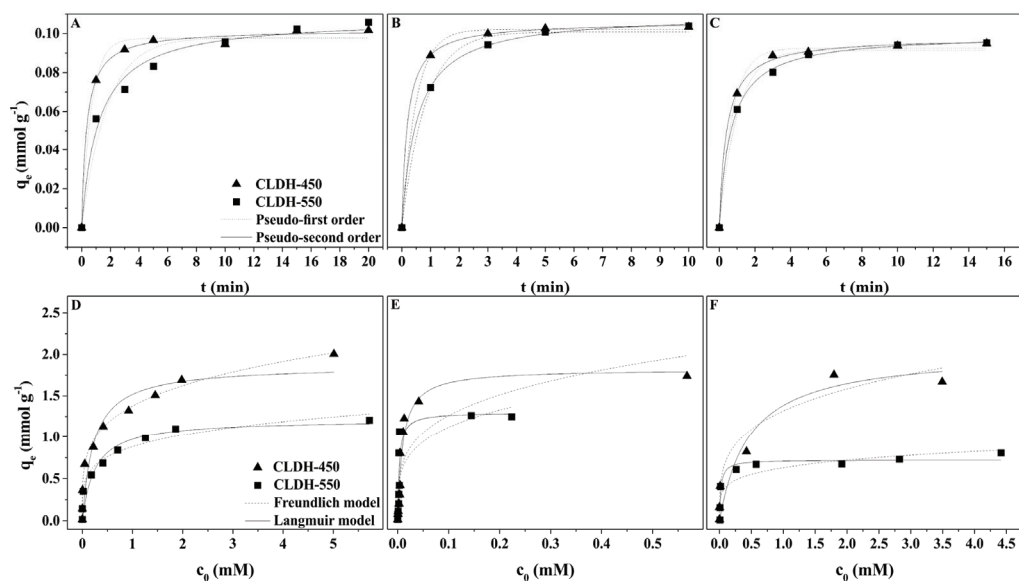


Fig. S4.3. Adsorption kinetics of As(V) (A), Pb(II) (B) and Zn(II) (C) on CLDH-450 and CLDH-550 fitted by the nonlinear form of pseudo-first and pseudo-second order kinetics and adsorption isotherms of As(V) (D), Pb(II) (E) and Zn(II) (F) on CLDH-450 and CLDH-550 fitted by the non-linear form of the Langmuir and Freundlich model.

Table S4.3 Parameters of the non-linear modeling using pseudo-first and pseudo-second order kinetics for adsorption of As(V), Pb(II) and Zn(II) on CLDH-450 and CLDH-550.

Model	Mg-Fe CLDH-450			Mg-Fe CLDH-550			
	Parameter	As	Pb	Zn	As	Pb	Zn
	Ads. efficiency (%)	100	100	98	100	100	98
	$q_{\max(\text{exp})}$ (mmol g ⁻¹)	0.10	0.10	0.10	0.11	0.11	0.10
Pseudo-first order kinetic	q_e (mmol g ⁻¹)	0.10±0.00	0.10±0.00	0.09±0.00	0.10±0.01	0.10±0.00	0.09±0.00
	k_1 (min ⁻¹)	1.48±0.18	2.03±0.12	1.36±0.09	0.58±0.14	1.23±0.11	1.01±0.14
	R^2	0.99	1.00	1.00	0.94	1.00	0.99
Pseudo-second order kinetic	q_e (mmol g ⁻¹)	0.10±0.00	0.11±0.00	0.10±0.00	0.11±0.00	0.11±0.00	0.10±0.00
	k_2 [g (mmol min) ⁻¹]	28.7±4.09	49.4±2.66	25.6±2.16	7.89±1.75	17.5±0.85	15.5±0.99
	R^2	1.00	1.00	1.00	0.98	1.00	1.00

^aAdsorption efficiency was calculated as the difference between the initial and final metal(loid)s concentrations

Table S4.4 Parameters of the non-linear modeling using the Langmuir and Freundlich model for adsorption of As(V), Pb(II) and Zn(II) on CLDH-450 and CLDH-550

Model	Parameter	Mg-Fe CLDH-450			Mg-Fe CLDH-550		
		As	Pb	Zn	As	Pb	Zn
Langmuir model	$q_{\max(\text{exp})}$ (mmol g ⁻¹)	2.01	1.74	1.67	1.21	1.25	0.81
	q_{\max} (mmol g ⁻¹)	1.87±0.17	1.82±0.13	2.04±0.31	1.21±0.11	1.30±0.15	0.72±0.04
	K_L (L mmol ⁻¹)	4.36±1.82	100±20.1	2.10±1.22	4.05±1.60	316±108	47.0±17.5
	R^2	0.90	0.94	0.92	0.91	0.84	0.91
Freundlich model	n (-)	4.21±0.18	3.83±0.72	3.75±0.80	4.69±0.41	4.05±0.90	5.17±1.31
	K_F^*	1.38±0.02	2.30±0.39	1.32±0.09	0.88±0.02	1.98±0.40	0.63±0.05
	R^2	1.00	0.73	0.94	0.98	0.72	0.80

*[(mmol g⁻¹)(L mmol⁻¹)^{1/n}]

Additionally, diffractograms of CLDH-450 after As(V), Pb(II) and Zn(II) sorption at different initial concentrations are given in Fig. S4.5. In particular, at the lowest As(V), Pb(II) and Zn(II) concentrations, the reconstruction of CLDH-450 occurred without any formation of new phases, e.g., oxides/hydroxides/carbonates. In general, the reconstruction was limited by the increasing metal(loid)s concentrations (Fig. S4.5A-C). After As(V) sorption, all observed peaks corresponded to periclase, with intensity decreasing with increasing As(V) concentrations (Fig. S4.5A). Moreover, a higher background was observed. The increasing Pb(II) concentrations led to a surface-induced precipitation of (hydro)cerussite ($\text{Pb}_3(\text{CO}_3)_2(\text{OH})_2$) on the CLDH surface that occurred at lower pH values than in pure aqueous solutions (Fig. S4.5B). Moreover, the preferable precipitation at higher initial Pb(II) concentrations (up to 50 mg L^{-1}) also made the reconstruction impossible. The diffractograms of CLDH-450 after Zn(II) sorption showed peaks corresponding to the LDH structure as well as peaks corresponding to periclase. However, some additional peaks occurring at an initial Zn(II) concentration of 50 mg L^{-1} were assigned to the formation of zincite (ZnO) (Fig. S4.5C). In the case of CLDH-550, only diffractograms after As(V), Pb(II) and Zn(II) sorption at the highest initial concentrations are given (Fig. S4.5D-E). The diffractograms after As(V) and Zn(II) sorption showed peaks corresponding to periclase/spinel without reconstruction of the LDH structure. Finally, the diffractogram after Pb(II) sorption confirmed the surface-induced precipitation without any reconstruction.

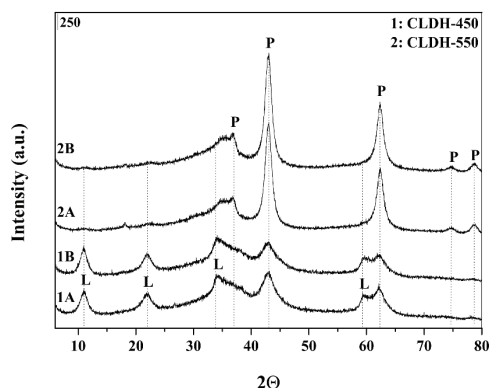


Fig. S4.4. XRD diffractograms of CLDH-450 (1A, 1B) and CLDH-550 (2A, 2B) after being stirred in deionized water (1A, 2A) and in the background electrolyte (1B, 2B) after 2 hours at pH 5.5 (L: layered double hydroxide; P: periclase).

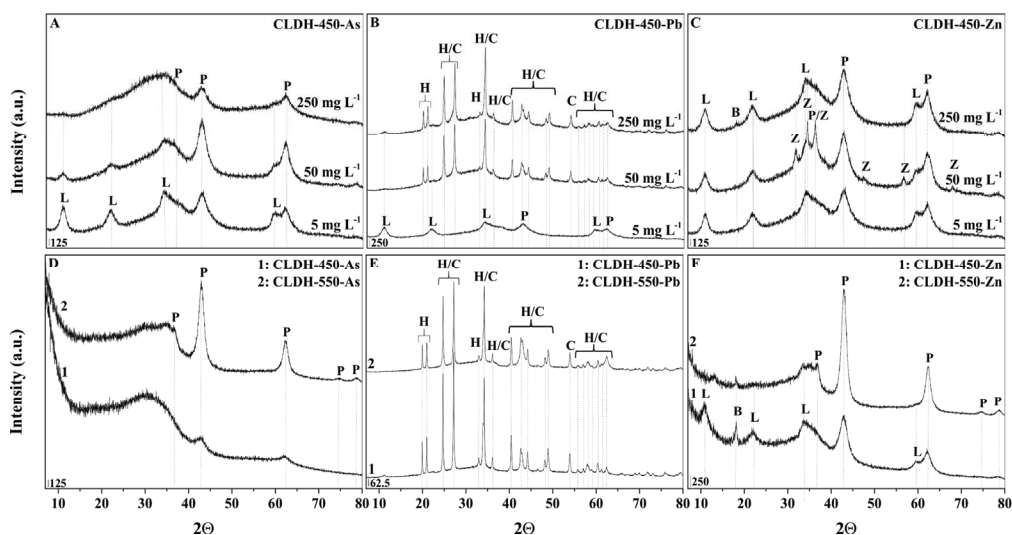


Fig. S4.5. XRD diffractograms of CLDH-450 after As(V) (A), Pb(II) (B) and Zn(II) (C) sorption at different initial As/Pb/Zn concentrations (5–250 mg L⁻¹) and XRD diffractograms of CLDH-450 and CLDH-550 after As(V) (D), Pb(II) (E) and Zn(II) (F) sorption at initial As/Pb/Zn concentrations of 500 mg L⁻¹ (B: brucite; C: cerussite; H: hydrocerussite L: layered double hydroxides; P: periclaise; Z: zincite).

The SEM images of CLDH-450 and CLDH-550 before and after As(V), Pb(II) and Zn(II) sorption are given in Fig. S4.6. In comparison to the smooth surface of LDHs (Hudcová et al., 2018), agglomerates were observed on the CLDH-450 and CLDH-550 surface and probably formed during the thermal treatment process. After As(V) sorption, the agglomerates on the surface of both CLDHs disappeared. However, precipitation/agglomeration was observed after Pb(II) and Zn(II) sorption on both CLDHs, which corresponded to our previous studies based on LDHs, with the Pb(II) precipitation of crystalline (hydro)cerussite with characteristic hexagonal plates and the precipitation of amorphous Zn oxides/hydroxides or to the accumulation of Zn(II) on the CLDHs surface (Hudcová et al., 2018).

The EDX showed more As(V) on the CLDH-450 surface (22%) in comparison to pristine LDH (14%) (Hudcová et al., 2017). However, a lower As(V) amount (11%) was observed on the CLDH-550 surface. Moreover, the surface of CLDH-450 showed the highest concentration of Pb(II) (64%) in comparison to pristine LDH (59%) and CLDH-550 (33%) as well. However, the amount of Zn(II) on the studied materials decreased in the order of LDH (9%) > CLDH-450 (6%) > CLDH-550 (3%) (Hudcová et al., 2018).

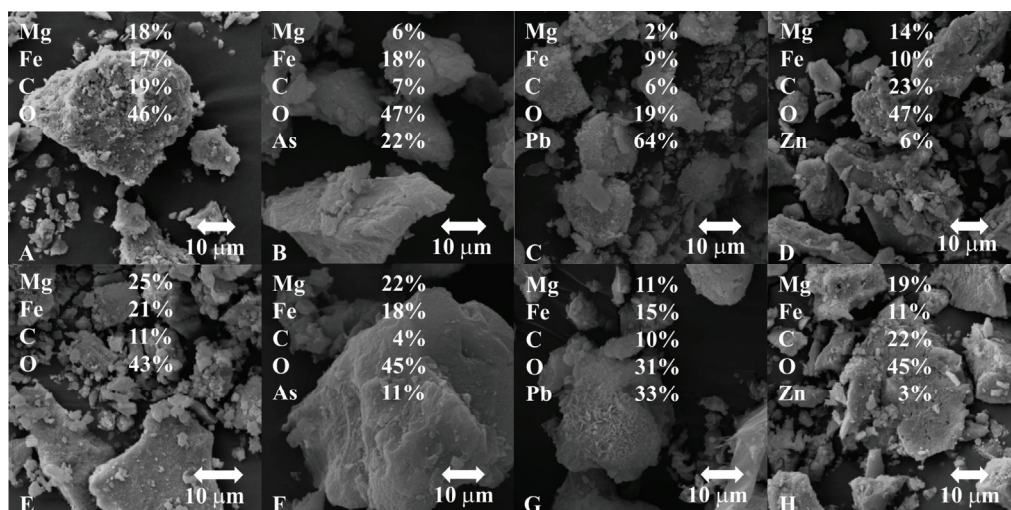


Fig. S4.6. SEM images of CLDH-450 (A) and CLDH-550 (E) before and after As(V) (B, F), Pb(II) (C, G) and Zn(II) (D, H) sorption with corresponding weight % based on EDX.

The XPS spectra and the surface stoichiometry of CLDH-450 and CLDH-550 before and after As(V), Pb(II) and Zn(II) sorption are given in Fig. S4.7 and Table S4.5, respectively. The structure of both CLDHs was confirmed by the symmetric Mg 2p peak at approx. 50.5 eV and the Fe 2p peak at approx. 710.5 eV, suggesting the formation of metal oxides (Fig. S4.7A). However, the broad Fe 2p peak also contained the contribution (less intensive) corresponding to Fe hydroxides at approx. 713.0 eV. The C 1s peak at approx. 285.0 eV indicated an adventitious carbon on the surface of both CLDHs. The O 1s peak represented several contributions: metal oxides at approx. 530.0 eV, metal hydroxides/hydroxyl groups at approx. 532.0 eV and carbonates/adsorbed water at approx. 534 eV. After As(V), Pb(II) and Zn(II) sorption, new peaks appeared: As 3s/3p/3d, Pb 4f and Zn 2p. The deconvolution of individual peaks enabled us to investigate the sorption mechanisms of metal(loid)s on CLDHs. The As 3d peak (Fig. S4.7B-C) consisted of two contributions corresponding to As(V) at approx. 45.7-46.1 eV (approx. 83-85%) and As(III) at 44.7-44.9 eV (approx. 15-17%). The reduction of As(V) was caused by the X-rays, which was confirmed by the increasing intensity of this less intensive peak after Ar⁺ sputtering (data not shown). Therefore, we suggested that As(V) was not reduced on the CLDHs surface during the sorption process and was effectively adsorbed on the surface of both CLDHs. The Pb(II) sorption mechanism was proven by the deconvolution of the Pb 4f_{7/2} peak (Fig. S4.7D-E). This peak consisted of two contributions, Pb oxides (138.1 eV/46.3% for CLDH-450 and 138.6 eV/34.2% for CLDH-550) and Pb hydroxides/carbonates (139.0

eV/53.7% for CLDH-450 and 139.2 eV/65.8% for CLDH-550). After Ar^+ sputtering, the peak corresponding to Pb hydroxides/carbonates significantly decreased in the spectra of both CLDHs (data not shown). The deconvolution of the Zn $2p_{3/2}$ peak (Fig. S4.7F-G) also showed two contributions, Zn oxides (1022.4 eV/72.1% for CLDH-450 and 1022.1 eV/71.9% for CLDH-550) and Zn hydroxides (1024.0 eV/27.9% for CLDH-450 and 1023.4 eV/18.9% for CLDH-550). Additionally, a small peak corresponding to Zn carbonates occurred in the spectrum of CLDH-550 (1020.6 eV/9.2%). In contrast to the spectra after Pb(II) sorption, the peak corresponding to Zn oxides significantly decreased after Ar^+ sputtering (data not shown). Generally, we concluded that Pb(II) and Zn(II) on the surface of both CLDHs followed similar sorption mechanisms, i.e., surface complexation (adsorption) and surface-induced precipitation; however, the Ar^+ sputtering showed contrasting behavior of the individual sorbed species.

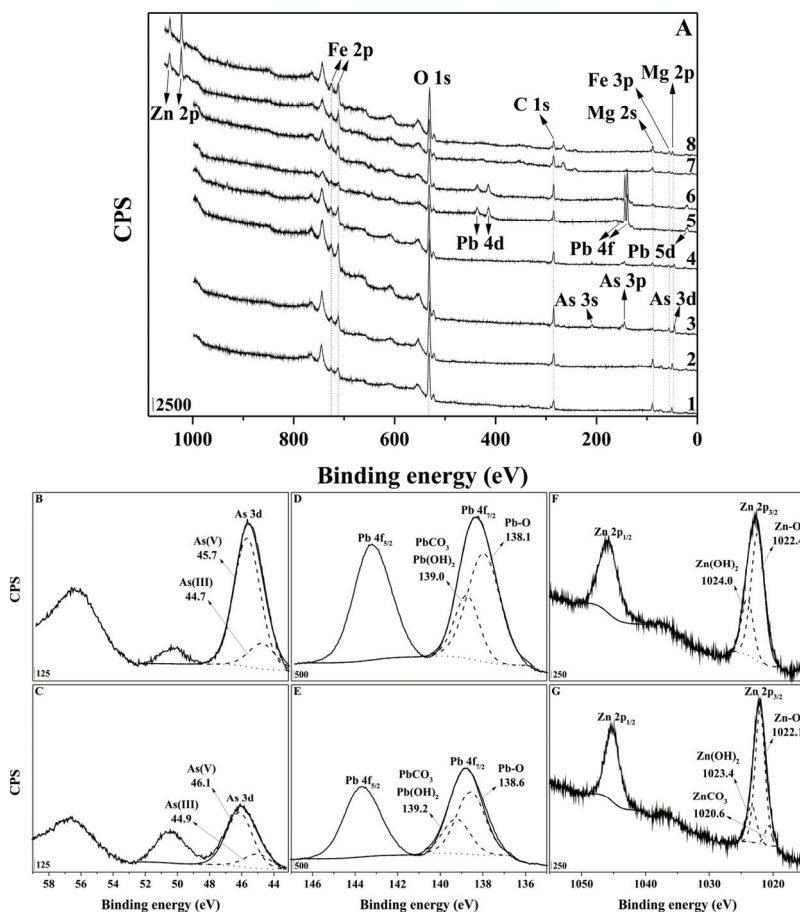
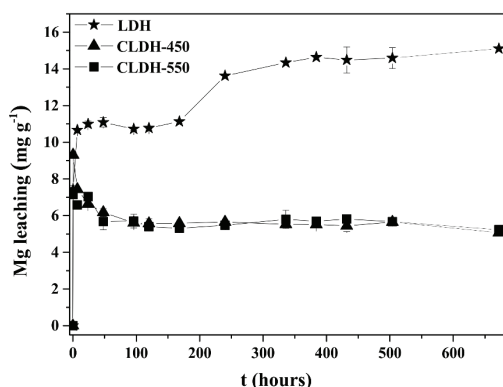
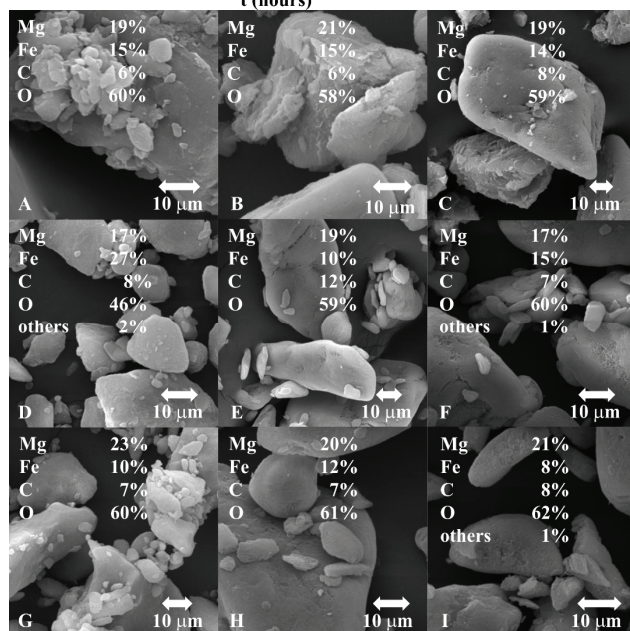


Fig. S4.7. XPS spectra of CLDH-450 and CLDH-550 before and after As(V), Pb(II) and Zn(II) sorption (A: wide scan; B-G: deconvolution of individual peaks).

Table S4.5 Surface stoichiometry (%) of CLDH-450 and CLDH-550 before and after As(V), Pb(II) and Zn(II) sorption.

	Fe 2p	Mg 2s	O 1s	C 1s	As 3p	Pb 4d	Zn 2p
CLDH-450	1.5	42.9	35.8	19.8	-	-	-
CLDH-550	1.8	42.3	33.7	22.1	-	-	-
CLDH-450-As	4.0	9.9	46.5	32.9	6.6	-	-
CLDH-550-As	3.2	21.7	41.1	30.3	3.8	-	-
CLDH-450-Pb	1.9	5.8	36.2	47.1	-	8.9	-
CLDH-550-Pb	2.5	19.0	36.6	36.6	-	5.3	-
CLDH-450-Zn	2.3	42.0	28.1	24.6	-	-	3.0
CLDH-550-Zn	2.8	46.7	32.8	15.4	-	-	2.3

Stability of the studied materials**Fig. S4.8.** Mg(II) leaching from the LDH, CLDH-450 and CLDH-550 structures in deionized water in deionized water (n = 2).**Fig. S4.9.** SEM images of LDH (A, D, G), CLDH-450 (B, E, H) and CLDH-550 (C, F, I) after stability tests in deionized water (A-C), As-soil solutions (D-F) and Zn-soil solutions (G-I) with corresponding weight % based on EDX.

pH-static leaching experiments

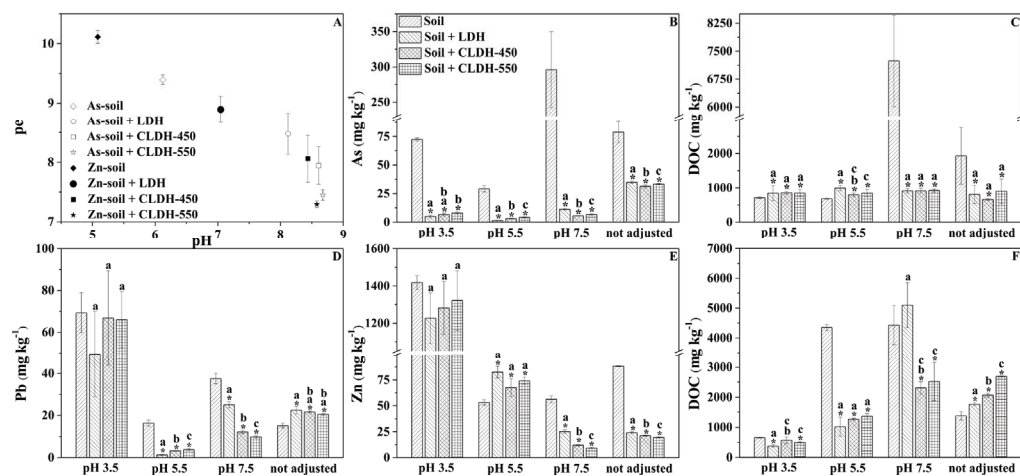


Fig. S4.10. The pe-pH diagram (A) and concentrations of As(V) (B) and DOC (C) in soil solutions of non-amended and amended As-soil and concentrations of Pb(II) (D), Zn(II) (E) and DOC (F) in soil solutions of non-amended and amended Zn-soil at pH 3.5, 5.5, 7.5 and without pH control (not adjusted). Statistical tests were performed separately for every single pH value to compare the non-amended and amended soils (the data with the asterisk means significantly different values) and individual amendments (the data with the different letter means significantly different values) ($\alpha < 0.05$; $n = 3$).

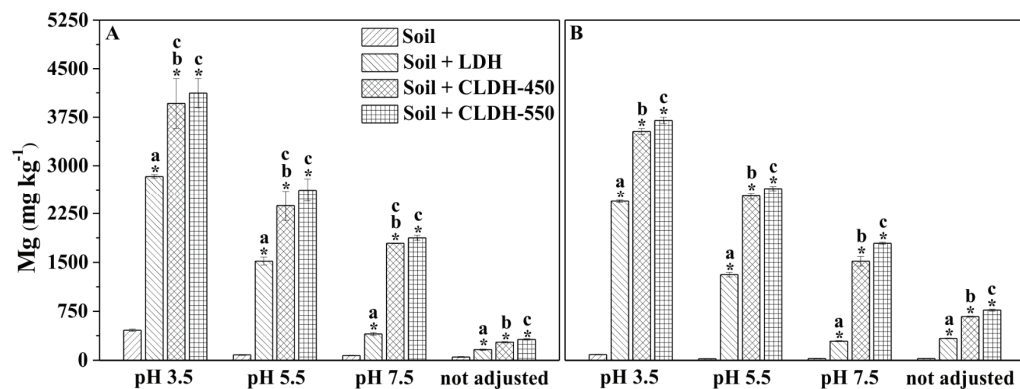


Fig. S4.11. Concentrations of Mg in soil solutions of non-amended and amended As-soil (A) and in soil solutions of non-amended and amended Zn-soil at pH 3.5, 5.5, 7.5 and without pH control (not adjusted). Statistical tests were performed separately for every single pH value to compare the non-amended and amended soils (the data with the asterisk means significantly different values) and individual amendments (the data with the different letter means significantly different values) ($\alpha < 0.05$; $n = 3$).

Incubation experiments

Table S4.6 The pH values of non-amended and amended As-soils and Zn-soils after 10 weeks of incubation batch experiments (n = 3).

		Soil	Soil + LDH	Soil + CLDH-450
As-soil	pH _{H2O}	6.00 ± 0.11	8.28 ± 0.07	8.86 ± 0.00
	pH _{KCl}	4.86 ± 0.03	7.76 ± 0.17	8.38 ± 0.07
Zn-soil	pH _{H2O}	5.52 ± 0.04	7.77 ± 0.17	9.20 ± 0.00
	pH _{KCl}	5.00 ± 0.02	7.64 ± 0.03	8.99 ± 0.00

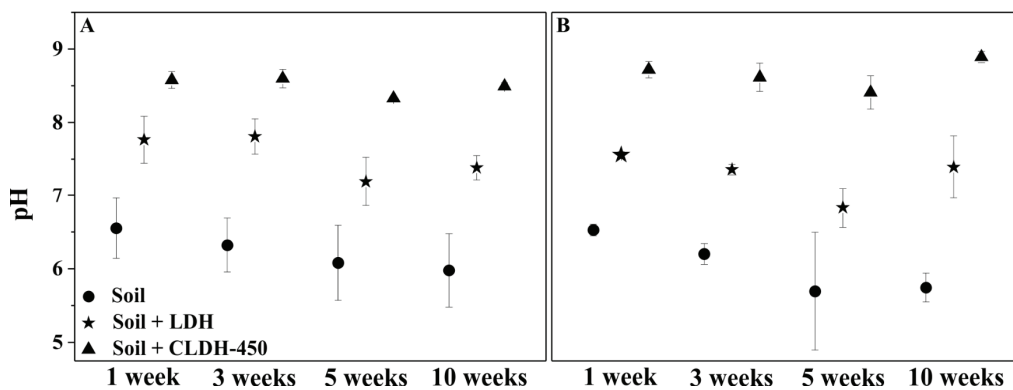
**Fig. S4.12.** The pH values of As-soil solutions (A) and Zn-soil solutions (B) after 1, 3, 5 and 10 weeks of incubation batch experiments (n = 4).

Table S4.7 Saturation indices of selected solubility-controlling phases calculated by PHREEQC-3 in the leachates of incubation batch experiments.

As-soil		pH	Calcite $CaCO_3$	Magnesite $MgCO_3$	Nesquehonite $MgCO_3 \cdot 3H_2O$	Sepiolite $Mg_4(Si_6O_{13})(OH)_2 \cdot 6H_2O$	Talc $Mg_3Si_4O_{10}(OH)_2$		
1 week	Soil	6.55	-1.15	-1.81	-4.22	-7.87	-7.63		
	Soil + LDH	7.77	0.46	0.21	-2.20	-3.55	-0.95		
	Soil + CLDH	8.58	1.33	1.33	-1.08	-0.28	4.02		
3 weeks	Soil	6.32	-1.55	-2.20	-4.61	-9.10	-9.42		
	Soil + LDH	7.81	0.30	0.10	-2.31	-3.55	-0.92		
	Soil + CLDH	8.60	1.32	1.49	-0.92	0.24	4.77		
5 weeks	Soil	6.08	-1.68	-2.32	-4.73	-8.71	-8.96		
	Soil + LDH	7.20	-0.19	-0.46	-2.87	-5.42	-3.76		
	Soil + CLDH	8.33	1.05	1.18	-1.23	-0.63	3.44		
10 weeks	Soil	5.98	-1.80	-2.46	-4.87	-9.22	-9.70		
	Soil + LDH	7.39	-0.02	-0.27	-2.68	-4.60	-2.53		
	Soil + CLDH	8.50	1.11	1.35	-1.06	0.34	4.89		
Zn-soil		pH	Calcite $CaCO_3$	Magnesite $MgCO_3$	Nesquehonite $MgCO_3 \cdot 3H_2O$	Sepiolite $Mg_4(Si_6O_{13})(OH)_2 \cdot 6H_2O$	Artinite $Mg_2(CO_3)(OH)_2 \cdot 3H_2O$	Smithsonite $ZnCO_3$	ZnCO ₃ ·H ₂ O
1 week	Soil	6.53	-1.06	-2.00	-4.41	-8.94	-10.33	-0.17	0.09
	Soil + LDH	7.56	0.42	0.66	-1.75	-4.74	-4.71	-0.39	-0.13
	Soil + CLDH	8.72	1.80	2.52	0.11	0.50	-0.19	-1.98	-1.72
3 weeks	Soil	6.20	-1.72	-2.66	-5.06	-10.35	-11.60	-0.75	-0.49
	Soil + LDH	7.36	0.23	0.54	-1.86	-4.66	-4.99	-0.46	-0.20
	Soil + CLDH	8.62	1.93	2.62	0.21	1.07	-0.15	-2.03	-1.77
5 weeks	Soil	5.70	-2.60	-3.59	-6.00	-12.59	-13.51	-1.52	-1.27
	Soil + LDH	6.83	-0.75	-0.52	-2.93	-7.24	-7.21	-1.11	-0.85
	Soil + CLDH	8.41	1.48	2.17	-0.24	0.03	-1.05	-2.30	-2.04
10 weeks	Soil	5.74	-2.25	-3.06	-5.47	-10.88	-12.46	-1.11	-0.85
	Soil + LDH	7.39	0.04	0.35	-2.06	-4.06	-4.98	-0.76	-0.50
	Soil + CLDH	8.89	1.80	2.55	0.14	1.96	0.30	-2.59	-2.33

SI > 0, i.e., supersaturation of the leachates with respect to the solid phase is indicated in bold
-1 < SI < 1, i.e., saturation close to zero is highlighted with grey background

Table S4.8 Fractionation of As(V) in non-amended and amended As-soil and Pb(II) and Zn(II) in non-amended and amended Zn-soil established by simple and sequential extractions after 10 weeks of incubation batch experiments ($n = 3$).

Fractionation of As (mg kg^{-1}) established sequential extraction (Wenzel et al., 2001)					
	FA ^a	FB ^a	FC ^a	FD ^a	Residual
As					
As-soil	43 ± 2	880 ± 56	9486 ± 1010	3916 ± 182	1585
As-soil + LDH	21 ± 2	764 ± 43	9739 ± 906	4056 ± 292	1330
As-soil + CLDH-450	27 ± 2	744 ± 45	8818 ± 789	3602 ± 379	2719
Fractionation of Pb and Zn (mg kg^{-1}) established sequential extraction (Rauret et al., 2000)					
	FA ^b	FB ^b	FC ^b	Residual	
Pb					
Zn-soil	294 ± 50	4089 ± 148	284 ± 11	< DL	
Zn-soil + LDH	282 ± 40	3738 ± 184	255 ± 21	< DL	
Zn-soil + CLDH-450	261 ± 19	3892 ± 307	243 ± 9	< DL	
Zn					
Zn-soil	2693 ± 70	1353 ± 36	448 ± 34	< DL	
Zn-soil + LDH	2250 ± 65	1491 ± 129	434 ± 32	< DL	
Zn-soil + CLDH-450	2391 ± 265	1447 ± 30	407 ± 28	< DL	
Bio-available fractionation of Zn (mg kg^{-1}) established simple extraction (Quevauviller, 1998)					
Zn					
Zn-soil	478 ± 12				
Zn-soil + LDH	1.81 ± 0.13				
Zn-soil + CLDH-450	0.21 ± 0.15				

FA^a = non-specifically sorbed, FB^a = specifically sorbed, FC^a = bound to amorphous oxides, FD^a = bound to well-crystallized oxides, FA^b = exchangeable, FB^b = reducible, FC^b = oxidizable
< DL = below the limit of detection

Chapter V

Antimonate (ad)sorption onto Mg-Fe layered double hydroxides in aqueous solutions at different pH values: Investigation of the mechanism supported by surface complexation modeling and solid-state analyses

B. Hudcová, M. Erben, M. Vítková, M. Komárek

Manuscript submitted to Applied Surface Science

Content

Abstract	139
Introduction	140
Materials and methods	142
Materials	142
Kinetic and equilibrium adsorption experiments	142
Surface complexation modeling	143
Spectroscopic and microscopic analyses	144
Results and discussion	146
Kinetic and equilibrium adsorption experiments	146
Surface complexation modeling	148
Spectroscopic and microscopic analyses	150
Conclusions	159
Supplementary Material	160

Abstract

In this study, the importance of Sb behavior under different pH conditions has been addressed with respect to its stabilization in aqueous solutions using Mg-Fe layered double hydroxides (LDHs). The Sb(V) adsorption onto Mg-Fe LDHs was performed at different initial Sb(V) concentrations and pH values (pH 5.5, 6.5 and 7.5). The removal rate and the maximal adsorbed amount increased with decreasing pH values. Moreover, the surface complexation modeling (SCM) predicted preferable formation of monodentate mononuclear complexes on the Mg-Fe LDH surface. Spectroscopic (X-ray diffraction analysis, Fourier transform infrared spectroscopy, X-ray photoelectron spectroscopy) and microscopic (scanning electron microscopy and energy-dispersive X-ray spectroscopy) techniques were used to further specify the adsorption mechanisms. The influence of chemical adsorption, surface-induced precipitation of brandholzite, formation of brandholzite-like phases and/or anion exchange was observed. Moreover, Sb(V) was nonhomogeneously distributed on the Mg-Fe LDH surface at all pH values. The surface complexation modeling supported by solid-state analyses provided a strong tool to investigate the binding arrangements of Sb(V) on the Mg-Fe LDH surface. Such a complex mechanistic/modeling approach has not previously been presented and enables prediction of the Sb(V) adsorption behavior onto Mg-Fe LDHs under different conditions, evaluating their possible use in actual applications.

Introduction

Antimony is a priority pollutant in water and soil environments due to its high toxicity and mobility (Filella et al., 2002a, 2002b). The behavior of Sb is strongly influenced by the pH value and redox potential. In general, Sb primarily occurs in two oxidation states, i.e., Sb(III) or Sb(V). Nevertheless, Sb(V) predominates under natural conditions (Ardau et al., 2016; Cai et al., 2015). In the environment, Sb(V) is commonly adsorbed onto Fe, Mn or Al oxides. However, natural materials often provide only limited adsorption capacity (De Gisi et al., 2016; Deng et al., 2017) and Sb(V) could be easily desorbed at higher pH values (Vithanage et al., 2013). Since Sb(V) concentrations in water and soil environments are increasing, novel effective adsorbents are being tested (Lu et al., 2015). Moreover, complex studies dealing with the adsorption mechanism of Sb on individual adsorbents are still limited (Ardau et al., 2016; Cai et al., 2015; Vithanage et al., 2013). Recently, layered double hydroxides (LDHs) have been used as promising sorbents for various metalloids and nonmetallic species, e.g., antimonate/antimonite (Constantino et al., 2018; Kameda et al., 2015), arsenate/arsenite (Hudcová et al., 2017; Jiang et al., 2015), selenate/selenite (Constantino et al., 2017), molybdate (Ardau et al., 2012), borate (Kameda et al., 2017), sulfate (Kameda et al., 2012) and phosphate (Luengo et al., 2017). However, reports of complex mechanistic/modeling approaches dealing with the adsorption mechanism of Sb(V) on LDHs under variable conditions remain scarce although it is crucial to predict the future application of LDHs in remediation technologies (Hudcová et al., 2017).

In our previous studies, we presented As(V) and metal adsorption onto carbonate-intercalated Mg-Fe LDHs (Hudcová et al., 2017, 2018). Nevertheless, studies dealing with Sb(V) adsorption onto LDHs have been focused only on basic adsorption models (kinetics and isotherms) and/or limited spectroscopic/microscopic techniques (XRD, EDX, XPS). Moreover, attention was mainly paid to Al-based and/or Zn-based LDHs, e.g., Mg-Al (Dore and Frau, 2018; Constantino et al., 2018; Kameda et al., 2011, 2012, 2015; Lee et al., 2018a, 2018b), Mg-Al-Fe (Kameda et al., 2012), Zn-Fe (Lu et al., 2015) and Zn-Al (Ardau et al., 2016). However, these materials could be potentially dangerous for water ecosystems since LDHs could be partially decomposed under acidic conditions (Jobbágy and Regazzoni, 2011). Compared to empirical models (e.g., the Langmuir and Freundlich models), thermodynamically based surface complexation models (SCM) provide more-mechanistic approaches and specify the binding of contaminants onto solid materials under different conditions such as pH values, ionic strengths and contaminant concentrations (Goldberg et al., 2007, 2014; Komárek et al., 2015). Several SCMs exist, i.e., the constant capacitance model (CCM), diffuse layer

model (DLM) and the triple layer model (TLM), with the DLM being the most commonly used due to its simplicity and applicability for various systems (Hayes et al., 1991). Nevertheless, the DLM describes only the formation of inner-sphere complexes, i.e., chemical adsorption, and is not able to capture the formation of outer-sphere complexes, i.e., physical adsorption (Vithanage et al., 2013). However, the number of studies dealing with the SCM investigating Sb(V) adsorption onto solid materials is still limited (Vithanage et al., 2013, 2015) although the SCM can predict Sb(V) behavior in the environment as well as possible risks based on experimental conditions (Filella et al., 2002a, 2002b). Experiments describing the effect of different pH values on the structure of LDHs after Sb(V) adsorption as well as the characteristics of adsorbed Sb(V) species and associated SCM have not been performed in detail.

The objective of the present study is to investigate Sb(V) adsorption mechanisms on Mg-Fe layered double hydroxides using surface complexation modeling coupled with various spectroscopic/microscopic techniques. The basic adsorption properties (e.g., the removal rate or maximal adsorbed amount) were described by adsorption kinetics and isotherms. Moreover, the equilibrium data at different pH values, ionic strengths and Sb(V) concentrations were fitted by the DLM. Modeling of Sb(V) adsorption onto Mg-Fe LDH at different pH values and initial Sb(V) concentrations was supported by XRD, SEM/EDX (including mapping), FTIR-ATR and XPS.

Materials and methods

Materials

All experiments were performed using deionized water (18.2 M Ω) and chemical reagents of analytical grade (without any treatment or purification). The constant pH values during all experiments were maintained by the addition of HNO₃ and NaOH at concentrations of 0.01–1 M. Mg-Fe layered double hydroxides (denoted further as LDH; Mg/Fe = 4) prepared by the coprecipitation method according to our previous studies (Hudcová et al., 2017, 2018; Seida et al., 2001) were used as adsorbents in all experiments. The synthesis was repeated (10 times). Solid samples from individual syntheses were mixed and a representative sample was chosen by quartation.

Kinetic and equilibrium adsorption experiments

Kinetic and equilibrium adsorption experiments were performed according to our previous studies (Hudcová et al., 2017, 2018). In general, solutions for kinetic adsorption experiments were prepared by dissolution of KSb(OH)₆ in the background electrolyte (0.01 M KNO₃) to obtain an Sb(V) concentration of 0.1 mM (12.2 mg L⁻¹). The solid/liquid ratio in all experiments was 1 g L⁻¹. Kinetic adsorption experiments were performed at pH 5.5, 6.5 and 7.5 to study the effect of different pH values on the Sb(V) removal process. Individual batches were mixed using a magnetic stirrer (550 rpm). At given time intervals (1-120 min), 10 mL of the suspension was sampled, filtered (cellulose acetate membrane, 0.45 μ m pore size) and subsequently analyzed by ICP-OES (Agilent Technologies 700 Series). The kinetic adsorption data were modeled by the nonlinear form of the pseudo-first and pseudo-second order kinetics (Gupta and Bhattacharyya, 2011). For the modeling purposes, only the experimental data near the equilibrium were chosen according to Simonin (2016).

Solutions for equilibrium adsorption experiments were prepared using the same chemical reagents, with Sb(V) concentrations ranging from 1 to 500 mg L⁻¹. Individual batches with the solutions at given concentrations and the solid/liquid ratio (1 g L⁻¹) were mixed using an orbital shaker (GFL 3005; 250 rpm) for 120 min, sampled, filtered and analyzed as described previously for kinetic experiments. The experiments at the highest Sb(V) concentrations were performed in duplicate. The equilibrium adsorption data were modeled by the nonlinear form of the Langmuir and Freundlich model (Foo and Hameed, 2010). The distribution coefficient was calculated according to Wang and Gao (2006).

Selected samples after the adsorption experiments at low initial Sb(V) concentration (12 mg L^{-1} ; the maximal adsorption efficiency) and at high initial Sb(V) concentration (500 mg L^{-1} ; the maximal adsorbed amount) were prepared for the solid-state analyses. The suspension was filtered using a vacuum pump and the wet solid residue was dried at room temperature.

Surface complexation modeling

The equilibrium adsorption experiments at different pH values (i.e., adsorption edges) were performed according to our previous studies (Hudcová et al., 2017, 2018). In general, the adsorption edges were performed at Sb(V) concentrations of 0.1 mM and 0.01 mM in KNO_3 as the background electrolyte at concentrations of 0.1 M, 0.01 M and 0.001 M. The solid/liquid ratio was 1 g L^{-1} and pH values ranged from 4.5 to 10.5. All suspensions were stirred for 24 hours without pH adjustment (orbital shaker; 250 rpm). After this period, the suspensions were manually adjusted to the given pH values using HNO_3 and NaOH for 120 min. Afterwards, the suspensions were sampled, filtered and analyzed as described in Section *Kinetic and equilibrium adsorption experiments*.

The surface complexation constants for Sb(V) adsorption on LDHs (Table 5.1) were obtained using FITEQL 4.0 (2-pK DLM; Herbelin and Westall, 1999). All necessary constants for investigation of the 2-pK DLM model including the stability constant for aqueous species (Visual MINTEQ 3.1; Gustafsson, 2013), the specific surface area of Mg-Fe LDHs (Hudcová et al., 2017), the surface protonation/deprotonation constants of the Mg-Fe LDH surface and the total number of surface sites of Mg-Fe LDHs (Protofit; Hudcová et al., 2017) are also given in Table 5.1. The average values of the surface complexation constants describing the formation of monodentate mononuclear and bidentate binuclear surface complexes were used in the surface complexation model (Visual MINTEQ 3.1; Gustafsson, 2013). The goodness-of-fit $V(Y)$ for the formation of monodentate mononuclear and bidentate binuclear surface complexes on the Mg-Fe LDH surface to the measured adsorption edges were determined according to Heinrich et al. (2008) and Reich et al. (2010). In general, values of the $V(Y)$ between 1 and 20 indicate a reasonable fit of the experimental data (at the 95% confidence interval).

Table 5.1 The stability constants for aqueous species (Visual MINTEQ 3.1 database), surface properties of Mg-Fe LDHs, reactions on the Mg-Fe LDH-solution interface (Prototit) and the average stability constants describing formation of Sb(V) inner-sphere complexes on Mg-Fe LDHs (optimized in FITEQL 4.0).

Reactions in solution	Log Stability Constant	
$\text{H}_2\text{O} \rightleftharpoons \text{H}^+ + \text{OH}^-$	-13.99	
$\text{K}^+ + \text{NO}_3^- \rightleftharpoons \text{KNO}_3$	-0.19	
$\text{K}^+ + \text{OH}^- \rightleftharpoons \text{KOH}$	-13.76	
$\text{Sb}(\text{OH})_6^- + \text{H}^+ \rightleftharpoons \text{Sb}(\text{OH})_5^0 + \text{H}_2\text{O}$	2.85 ^a	
Protonation and deprotonation of the LDH surface		
$>\text{SOH} + \text{H}^+ \rightleftharpoons >\text{SOH}_2^+$	3.56	
$>\text{SOH} \rightleftharpoons >\text{SO}^- + \text{H}^+$	-5.33	
Emerging Sb(V) complexes on the LDH surface	V(Y) (V(Y) _{min} , V(Y) _{max}) ^b	
Formation of monodentate mononuclear complexes		
<i>10⁻⁴ M Sb(V)</i>		
$>\text{SOH} + \text{Sb}(\text{OH})_6^- \rightleftharpoons >\text{SOSb}(\text{OH})_5^- + \text{H}_2\text{O}$	5.08	1.74 (1.22, 2.69)
<i>10⁻⁵ M Sb(V)</i>		
$>\text{SOH} + \text{Sb}(\text{OH})_6^- \rightleftharpoons >\text{SOSb}(\text{OH})_5^- + \text{H}_2\text{O}$	8.61	0.05 (0.04, 0.08)
Formation of bidentate binuclear complexes		
<i>10⁻⁴ M Sb(V)</i>		
$2>\text{SOH} + \text{Sb}(\text{OH})_6^- \rightleftharpoons (>\text{SO})_2\text{Sb}(\text{OH})_4^- + 2 \text{H}_2\text{O}$	7.70	38.94 (27.27, 60.18)
<i>10⁻⁵ M Sb(V)</i>		
$2>\text{SOH} + \text{Sb}(\text{OH})_6^- \rightleftharpoons (>\text{SO})_2\text{Sb}(\text{OH})_4^- + 2 \text{H}_2\text{O}$	11.41	0.07 (0.05, 0.11)
Site density: 47.45 ^c sites nm ⁻²		
Specific surface area: 40.14 ^c m ² g ⁻¹		
pH _{PZC} : 10 ^c		

^a according to Accornero et al. (2008); ^b V(Y) = parameter indicating the goodness-of-fit of the DLM to the measured adsorption edges (Heinrich et al., 2008; Reich et al., 2010); ^c according to Hudcová et al. (2017)

Spectroscopic and microscopic techniques

The adsorption mechanisms of Sb(V) on the LDH before and after Sb(V) adsorption at different initial Sb(V) concentrations, i.e., 12 mg L⁻¹ and 500 mg L⁻¹, and pH values, i.e., pH 5.5 (LDH-Sb-5.5), pH 6.5 (LDH-Sb-6.5) and pH 7.5 (LDH-Sb-7.5) were characterized by a combination of spectroscopic and microscopic techniques. The structure of materials was identified by X-ray diffraction analysis (XRD) using a PANalytical X'Pert Pro diffractometer with an X'Celerator detector (Cu K_α radiation, 40 kV, 30 mA, a measuring step 0.02° s⁻¹ in the range 10-80 2θ) using PANalytical X'Pert HighScore Plus software (version 3) and the ICDD PDF-2 database (2003). The morphology and chemical composition were studied by scanning electron microscopy

(SEM; *TESCAN VEGA 3 XMU*) and energy-dispersive X-ray spectroscopy (EDX; *QUANTAX 200*). Moreover, the distribution of individual elements after Sb(V) adsorption at the highest adsorbed amount was performed. Characteristic functional groups were determined by Fourier transform infrared spectroscopy in attenuated total reflection mode using a diamond crystal (FTIR-ATR; *Nicolet 6700*). The binding arrangements on the surface and the surface stoichiometry were studied using X-ray photoelectron spectroscopy (XPS; *Omicron Nanotechnology, Ltd*), and deconvolution of the spectra using the *Casa XPS* program.

Results and discussion

Kinetic and equilibrium adsorption experiments

The removal rate of metals, metalloids and nonmetallic species on different solid materials is commonly described by adsorption kinetics (Simonin et al., 2016). For Sb(V) adsorption onto LDHs, the most used models are the pseudo-first order and pseudo-second order kinetics (Dore, Frau, 2018; Kameda et al., 2015, Lee et al., 2018a, 2018b, Lu et al., 2015). Adsorption kinetic data describing Sb(V) adsorption onto Mg-Fe LDHs at different pH values are given in Fig. 5.1A. The Sb(V) removal efficiency increased with decreasing pH values caused by the decreasing negative charge of the LDH surface (Hu et al., 2017; Hudcová et al., 2017). The experimental adsorbed amount ($q_{e(exp)}$), modeled parameters, i.e., adsorbed amount (q_e) and rate coefficients (k_1 , k_2) and coefficient of determination (R^2) are given in Table S5.1. The pseudo-first and pseudo-second order kinetics showed a similar fit at all pH values. The similar fit for both models using different LDH types was also discussed by Lee et al. (2018a, 2018b). In contrast, a slightly better fit using pseudo-second order kinetics was observed by Lu et al. (2015). Kameda et al. (2011) and Dore and Frau (2018) tested individually pseudo-second and pseudo-first order kinetics, respectively, showing a reasonable fit for the experimental data. Nevertheless, the adsorbed amount at all pH values corresponded better to the modeled adsorbed amounts using pseudo-first order kinetics; therefore, we suggest that pseudo-first order kinetics described better the Sb(V) adsorption onto Mg-Fe LDHs. The modeled rate coefficients (k_1 , k_2) increased by decreasing pH values, i.e., pH 7.5 < pH 6.5 < pH 5.5, which meant the Sb(V) removal was faster at lower pH values. Compared to As(V) adsorption on the same LDH type, the rate coefficients k_1 and k_2 were lower by 1 and 2 orders of magnitude, respectively (Hudcová et al., 2017). The faster As(V) adsorption compared to Sb(V) was also discussed by Lee et al. (2018a, 2018b) and Lu et al. (2015), but in contrast with Kameda et al. (2015).

The basic adsorption characteristics, including the maximal adsorbed amount and the affinity of adsorbate towards the sorbent, are commonly described by adsorption isotherms (Foo and Hameed, 2010). The adsorption isotherms of Sb(V) on Mg-Fe LDHs at different pH values fitted by the Langmuir and Freundlich models are given in Fig. 5.1B, and the acquired parameters including the experimental adsorbed amounts (q_{exp}), the maximal adsorbed amount (q_{max}), Langmuir constant (K_L), Freundlich constant (K_F) and the parameter n are given in Table S5.2. The experimental data at all pH values corresponded to the L-type isotherm (Limousin et al., 2007). Adsorption data

at lower pH values, i.e., pH 5.5 and 6.5, provided a reasonable fit using the Freundlich model, i.e., favorable multilayered adsorption onto heterogeneous adsorption sites. In contrast, the adsorption data at pH 7.5 were better fitted by the Langmuir model, i.e., theoretically favoring monolayered adsorption onto homogenous adsorption sites (Lee et al., 2018b). Nevertheless, minor differences between the coefficient of determination of both models were observed at pH 5.5. The similarity in coefficient of determination for the Langmuir and Freundlich models were also discussed by Lee et al. (2018a, 2018b). The maximal adsorbed amount increased by decreasing pH values corresponding to the adsorption kinetic results. Concerning the Freundlich model, the values of the parameter n were between 1 and 10 meaning a favorable adsorption process (Hudcová et al., 2017). Generally, values greater than 1 imply surface heterogeneity (Jeppu and Clement, 2012). The influence of different pH values and the equilibrium concentrations on the affinity of Mg-Fe LDH towards Sb(V), i.e., the values of the distribution coefficient K_D , are given in Fig. S5.1. Based on the shape of the curve, the distribution coefficients decreased with increasing adsorbed amounts at individual pH values and equilibrated at 0.14 L g^{-1} at pH 5.5, 0.04 L g^{-1} at pH 6.5 and 0.02 L g^{-1} at pH 7.5. The decrease in the distribution coefficients with increasing adsorbed amounts could be attributed to the presence of adsorption sites of different affinity on the Mg-Fe LDH surface, which also would confirm the surface heterogeneity mentioned above. At a low surface coverage, the adsorption sites of high affinity are predominantly occupied. After their saturation, adsorption onto low-affinity sites begins, resulting in the decrease in K_D (Undabeytia et al., 2002; Yoshitake, 2012). Moreover, the decrease in K_D by increasing pH values has been observed previously after Tc(VII) adsorption onto LDHs (Wang and Gao, 2006) and As(V) adsorption onto goethite (Jeppu and Clement, 2012).

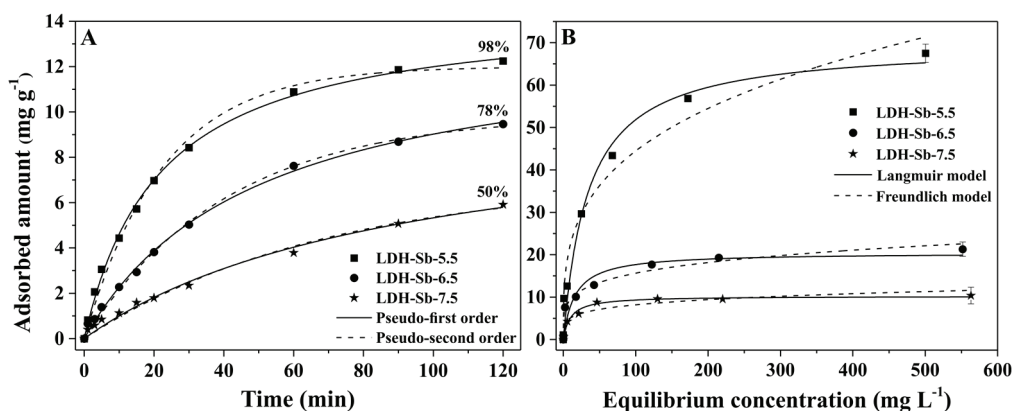


Fig. 5.1. Adsorption kinetic data of Sb(V) using Mg-Fe LDHs at different pH values (A) modeled by the nonlinear form of the pseudo-first order (solid line) and pseudo-second order (dashed line), and adsorption equilibrium data at different pH values (B) modeled by the nonlinear form of the Langmuir (solid line) and Freundlich (dashed line) models. Data at the highest adsorbed amounts are means and standard deviations ($n = 2$).

Surface complexation modeling

The pH-dependent adsorption (adsorption edges) of Sb(V) onto Mg-Fe LDHs at different initial Sb(V) concentrations and ionic strengths is given in Fig. 5.2. In general, adsorption edges at higher initial Sb(V) concentrations can be divided into three main regions, i.e., high Sb(V) adsorption ($\approx 100\%$) at $\text{pH} \leq 5.5$, decreasing Sb(V) adsorption within the pH range 6.5-7.5 and low adsorption (0-10%) at $\text{pH} \geq 8.5$. At lower initial Sb(V) concentrations, only two regions were observed, i.e., high Sb(V) adsorption ($\approx 100\%$) at $\text{pH} \leq 6.5$ and lower Sb(V) adsorption ($\approx 90\%$) at $\text{pH} \geq 7.5$. In general, the decreasing Sb(V) adsorption with increasing pH values has been observed previously during Sb(V) adsorption onto different Fe-based materials, i.e., goethite (Guo et al., 2014), ferrihydrite (Qi and Pichler, 2016), Fe-Zr bimetal oxides (Li et al., 2012) and Fe-rich soils (Vithanage et al., 2013), and clay minerals, i.e., kaolinite (Rakshit et al., 2015). Surprisingly, higher pH dependency was observed for Sb(V) compared with As(V) adsorption onto the same LDH type showing different behavior of individual metalloids that could correspond to their different structural ordering (Doušová et al., 2018; Hudcová et al., 2017). In contrast, pH-independent Sb(V) adsorption was observed using Zn-Fe LDHs (Lu et al., 2015) that could be influenced by the different LDH type or by surface-induced precipitation at high Sb(V) concentrations or at a low solid/liquid ratio (Vithanage et al., 2013). In general, the measured adsorption edges showed ionic strength independency, except a slight ionic strength dependency at

higher initial Sb(V) concentrations at $\text{pH} \geq 9.5$ (i.e., near the pH_{PZC} of Mg-Fe LDHs; Hudcová et al., 2017). Nevertheless, we suggest the formation of inner-sphere complexes as the predominant adsorption mechanism (Hudcová et al., 2017). In general, the LDH surface is negatively charged at $\text{pH} > \text{pH}_{\text{PZC}}$, which is approximately 10 (see Table 5.1); nevertheless, we observed increasing adsorption with the increase in ionic strength. This could be attributed to the increase in the LDH surface potential, i.e., the surface becomes less negative at higher ionic strengths (He et al., 1997). Based on the adsorption edges, the data were further fitted by the DLM, predicting the formation of inner-sphere complexes, i.e. chemical adsorption. The average stability constants for emerging monodentate mononuclear and bidentate binuclear complexes are given in Table 5.1. Based on the goodness-of-fit, the adsorption edges at both initial Sb(V) concentrations corresponded better to the formation of monodentate mononuclear inner-sphere complexes. Although the Sb(V) adsorption mechanism on LDHs using the SCM has not been studied yet, the formation of inner-sphere complexes has been previously suggested by the results of adsorption isotherms, activation energy calculations (Constantino et al., 2018; Kameda et al., 2015; Mitsunobu et al. 2008) or XPS analyses (Lee et al., 2018b; Lu et al., 2015). Nevertheless, the SCM has been previously used to model Sb(V) adsorption edges on different solid materials showing the preferable formation of monodentate inner-sphere complexes on the surface of Fe-rich sands and gibbsite (Cai et al., 2015; Rakshit et al., 2015), bidentate inner-sphere complexes on the surface of goethite, kaolinite, ferrihydrite and titanium oxide (Guo et al., 2014; Martínez-Lladó et al., 2008; Saeidnia et al., 2016; Yan et al., 2017) and the copresence of both complexes on the surface of biochar, Fe-rich soils, kaolinite and quartz (Rakshit et al., 2015; Vithanage et al., 2013, 2015). Nevertheless, the modeled curve for the measured adsorption edges at higher initial Sb(V) concentrations slightly underestimated the experimental values at $\text{pH} \geq 8.5$ (especially at higher ionic strengths). In contrast, the modeled curve at lower initial Sb(V) concentrations slightly overestimated the experimental values in the pH range of 6.5-9.5 and underestimated them at $\text{pH} \geq 10.5$. Since the DLM did not fit well the adsorption edges at higher pH values, we suggest that another process could influence the overall Sb(V) adsorption mechanism on Mg-Fe LDHs at higher pH values, e.g., outer-sphere complexation (physical adsorption) and/or precipitation of newly formed solid phases (Vithanage et al., 2013, 2015).

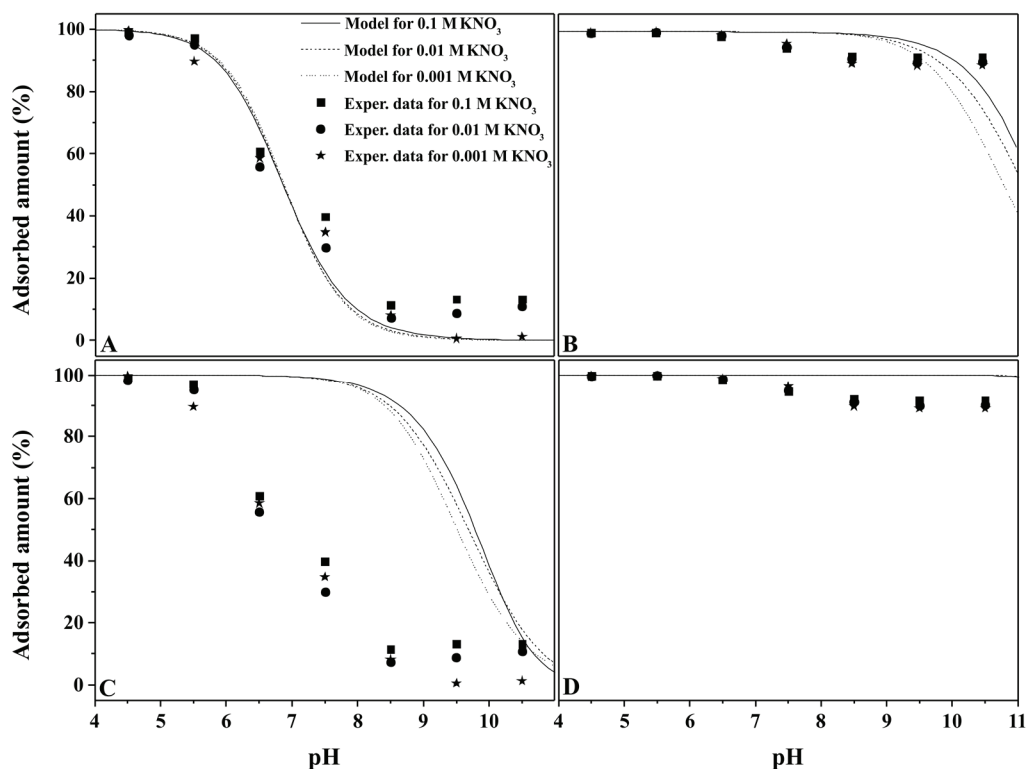


Fig. 5.2. Adsorption of monodentate mononuclear complexes (A, B) and bidentate binuclear complexes (C, D) on the LDH surface at initial Sb(V) concentrations of 0.1 mM (A, C) and 0.01 mM (B, D). Experimental data are represented by symbols and individual models by solid, dashed and dotted lines for 0.1 M, 0.01 M and 0.001 M KNO_3 , respectively.

Spectroscopic and microscopic techniques

Transformations according to XRD analyses

Diffraction patterns of Mg-Fe LDH before and after Sb(V) adsorption at different initial Sb(V) concentrations and pH values are given in Fig. 5.3, and the calculated parameters are listed in Table S5.3. All diffraction patterns showed characteristic peaks for the LDH structure (PDF-2 card: 00-014-0293). Moreover, the presence of brucite (PDF-2 card: 01-076-0667) in the diffraction pattern of LDH before Sb(V) adsorption was detected. Brucite was formed during the LDH synthesis and was identified by the new broad peak at 18.88° and the growth of LDH peaks at 38.35° , 51.20° and 58.02° (Hudcová et al., 2019). The diffraction patterns of LDH after Sb(V) adsorption at lower initial Sb(V) concentrations (12 mg L^{-1} ; corresponding to the adsorbed amounts given in Table S5.1)

at all pH values (Fig. 5.3A) showed minor changes compared to pristine LDHs. Nevertheless, the main brucite peaks at 18.88° disappeared and other brucite peaks significantly decreased. This phenomenon corresponded to the washing of residual $\text{Mg}(\text{OH})_2$ from the LDH surface during adsorption experiments and resulted in the increase in $\text{Mg}(\text{II})$ in the solution (Hudcová et al., 2017). Compared to our previous studies, the position and intensity of individual LDH peaks at lower $\text{Sb}(\text{V})$ initial concentrations remained the same as before the experiment excluding the partial decomposition of Mg-Fe LDHs and/or precipitation of new phases (Hudcová et al., 2017, 2018). The basal spacing of layers d_{003} (thickness of the LDH interlayered region) and cell parameters a (the average cation-cation distance in the LDH layers) and c (the overall LDH structure including the interlayer region) (Cavani et al., 2001; Hudcová et al., 2017) remained the same at pH 7.5 and 6.5. A slight increase in the basal spacing d_{003} and parameter c was observed at pH 5.5, which could be attributed to a partial rearrangement in the interlayered region of the studied carbonate-intercalated Mg-Fe LDHs. Such changes suggested possible anion exchange or other mechanisms at this pH value. Nevertheless, these minor changes confirmed that $\text{Sb}(\text{V})$ was predominantly adsorbed on the Mg-Fe LDH surface. Moreover, anion exchange of interlayer anions by $\text{Sb}(\text{V})$ using carbonate-intercalated LDHs has been previously excluded by Dore and Frau (2018) and Kameda et al. (2011, 2012). In general, anions with high charge density (e.g., carbonates) have a higher affinity for the LDH interlayer region; therefore, anion exchange is not expected compared to LDHs intercalated with nitrates, chlorides and/or sulfates (Kameda et al., 2011). In contrast, anion exchange has been confirmed in our previous study focused on $\text{As}(\text{V})$ adsorption onto the same LDH type. Nevertheless, the changes in diffractograms and individual parameters were more pronounced in that study than in the case of the LDH diffractogram after $\text{Sb}(\text{V})$ adsorption. A higher influence of anion exchange in the case of $\text{As}(\text{V})$ adsorption could be explained by the different affinities as well as the ionic size of individual metalloids since the effective ionic radius of $\text{Sb}(\text{V})$ (0.60 \AA) is larger than that of $\text{As}(\text{V})$ (0.46 \AA).

The diffractograms of LDHs after $\text{Sb}(\text{V})$ adsorption at higher initial $\text{Sb}(\text{V})$ concentrations (500 mg L^{-1} , corresponding to the maximal adsorbed amounts given in Table S5.2) at all pH values (Fig. 5.3B) showed all the peaks corresponding to the LDH structure. However, the intensity of individual LDH peaks slightly decreased with decreasing pH values compared to the LDHs before $\text{Sb}(\text{V})$ adsorption, i.e., $\text{LDH} \approx \text{LDH-Sb-7.5} > \text{LDH-Sb-6.5} > \text{LDH-Sb-5.5}$. The broad peak at $18\text{-}19^\circ$ corresponding to brucite in the diffractogram of LDH before $\text{Sb}(\text{V})$ adsorption showed significant changes after $\text{Sb}(\text{V})$ adsorption and. Additionally, other brucite peaks significantly decreased. These changes were identified as the formation of new phases, i.e.,

precipitation of crystalline brandholzite (PDF-2 card 01-073-0596) at pH 7.5 and formation of brandholzite-like phases on/in the structure of LDHs at pH 6.5 and 5.5. At pH 7.5, new sharp peaks appeared at 18.24°, 19.30° and 26.61° suggesting the surface-induced precipitation of brandholzite. In contrast, only the broad peak at 19.30° (without the formation of other brandholzite peaks) was observed at pH 6.5 and 5.5, which excluded the surface-induced precipitation of brandholzite as the prevailing mechanism (despite a greater adsorbed amount of Sb(V) compared to pH 7.5; see Fig. 5.1 and Table S5.2). In general, brandholzite is a layered mineral composed of $\{[\text{Sb}(\text{OH})_6]_9\}^{9-}$ (first layer; $\text{Sb}(\text{OH})_6$ octahedra) and $\{[\text{Sb}(\text{OH})_6]_3[\text{Mg}(\text{H}_2\text{O})_6]_6\}^{9+}$ (second layer; $\text{Sb}(\text{OH})_6/\text{Mg}(\text{H}_2\text{O})_6$ octahedra) connected by hydrogen bonds (Friedrich et al., 2000). The formation of brandholzite-like phases after Sb(V) adsorption using different LDHs has been previously discussed by Ardaul et al. (2016), Dore and Frau (2018) and Kameda et al. (2011, 2012, 2015). Identical to the case of lower Sb(V) initial concentrations, the highest basal spacing d_{003} and c was observed at pH 5.5 suggesting a possible Sb(V) intercalation. Moreover, the possible influence of anion exchange at this pH value and initial Sb(V) concentration could be supported by the decreasing intensities of individual peaks corresponding to the LDH structure following our previous findings after As(V) adsorption onto the same LDH type (Hudcová et al., 2017). Except the possible minor influence by the anion exchange at pH 5.5, the adsorption mechanism at pH 6.5 and 5.5 was predominantly composed from the formation of negatively charged monolayered surface complexes (see Section *Surface complexation modeling*; Table 5.1). Afterwards, adsorption occurred of positively charged Mg(II), which is commonly leached from the surface/structure of LDHs during adsorption experiments (Hudcová et al., 2017, 2018), resulting in the formation of individual layers corresponding to the brandholzite-like phases. As mentioned above, the surface-induced precipitation of brandholzite was the prevailing mechanism at pH 7.5 since brandholzite is formed at near-neutral pH values in natural environments with elevated Sb(V) and Mg(II) concentrations (Majzlan et al., 2016).

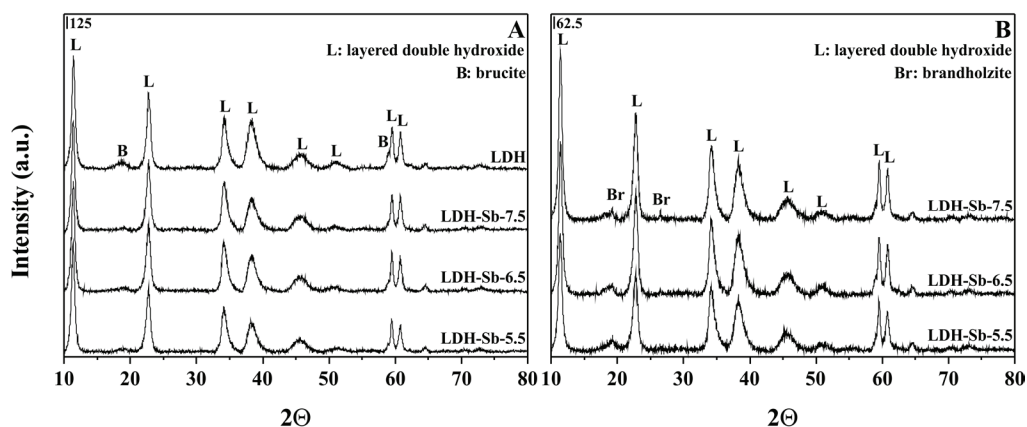


Fig. 5.3. Diffractograms of LDH before Sb(V) adsorption (A; top diffractogram) and LDH-Sb-7.5, LDH-Sb-6.5, LDH-Sb-5.5 at initial concentrations of 12 mg L^{-1} (A) and 500 mg L^{-1} (B).

Microscopic investigations

The SEM images of LDH before and after Sb(V) adsorption at different initial Sb(V) concentrations and pH values are shown in Fig. S5.2 and Fig. 5.4, respectively, and the EDX results are given in Table S5.4. The morphology of LDHs corresponded to our previous studies (Hudcová et al., 2017, 2018, 2019). After Sb(V) adsorption, aggregation of LDH particles at both initial Sb(V) concentrations and all studied pH values was observed. Moreover, Sb(V) was nonhomogeneously distributed on the LDH surface preferring adsorption on smaller particles based on the EDX results. The Sb(V) coverage increased with decreasing pH values following the results in Sections *Kinetic and equilibrium adsorption experiments* and *Surface complexation modeling*. Compared to the EDX results of Mg(II) after adsorption experiments in our previous studies (Hudcová et al., 2017, 2018, 2019), Mg(II) leaching was significantly reduced (especially at higher Sb(V) concentrations) at all pH values suggesting its stabilization on negatively charged Sb(V) complexes on the LDH surface following the XRD results. At pH 7.5 and higher initial Sb(V) concentrations (Fig. 5.4D), the hexagonal-shaped precipitates were formed on the LDH surface containing approx. 47% of Sb(V), i.e., a characteristic wt.% for crystalline brandholzite (Majzlan et al., 2016; Sejkora et al., 2010), confirming its surface-induced precipitation on the LDH surface as demonstrated by XRD analyses. In contrast, precipitation of brandholzite was not observed at the higher initial Sb(V) concentration at pH 6.5 and 5.5 or at the lower initial Sb(V) concentration at any of the studied pH values. Therefore, the decrease in free Mg(II) in the solution was attributed to its adsorption on the negatively charged

Sb(V) monodentate complexes and the formation of brandholzite-like phases as also suggested by XRD analyses.

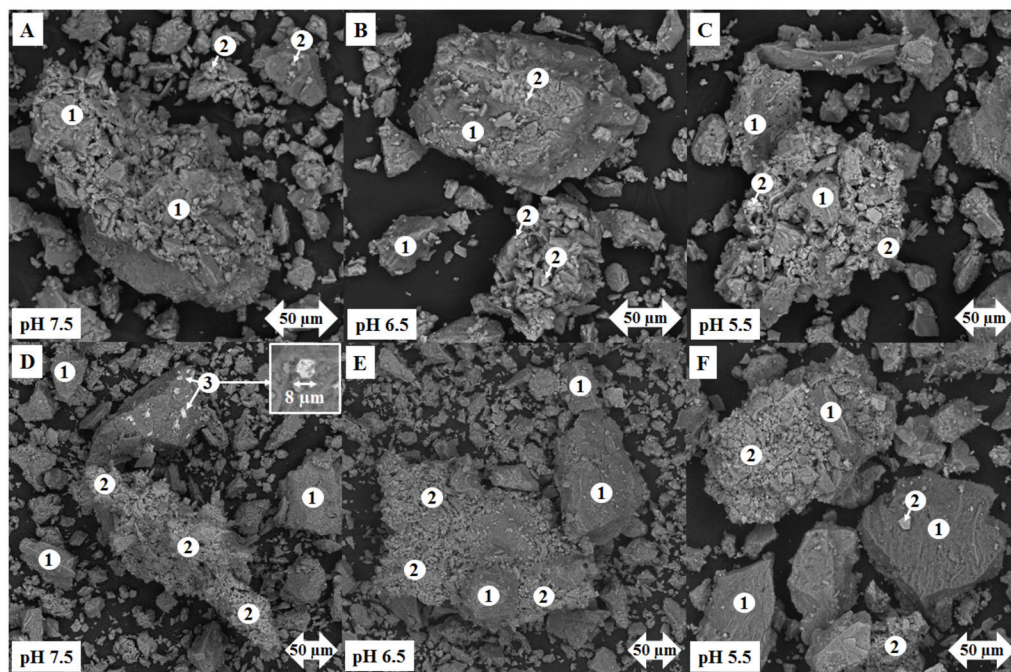


Fig. 5.4. SEM images of LDH-Sb-7.5 (A, D), LDH-Sb-6.5 (B, E), LDH-Sb-5.5 (C, F) at initial concentrations of 12 mg L⁻¹ (A-C) and 500 mg L⁻¹ (D-F).

The distribution of individual elements on the surface of Mg-Fe LDH at the highest Sb(V) coverage (see Table S5.2 and Table S5.4), i.e., initial Sb(V) concentrations of 500 mg L⁻¹ and pH 5.5, is shown in Fig. 5.5. The local excess of Mg(II) and/or Fe(III) in the LDH structure was attributed to structural defects originated from the LDH synthesis. As discussed previously (see Table S5.4), Sb(V) showed a nonhomogeneous distribution on the LDH surface that could be due to the single or multilayered adsorption. Moreover, Sb(V) was predominantly adsorbed on smaller particles or occasionally on the larger ones. Nevertheless, a small amount of Sb(V) was also observed inside the particles following a possible anion exchange at pH 5.5.

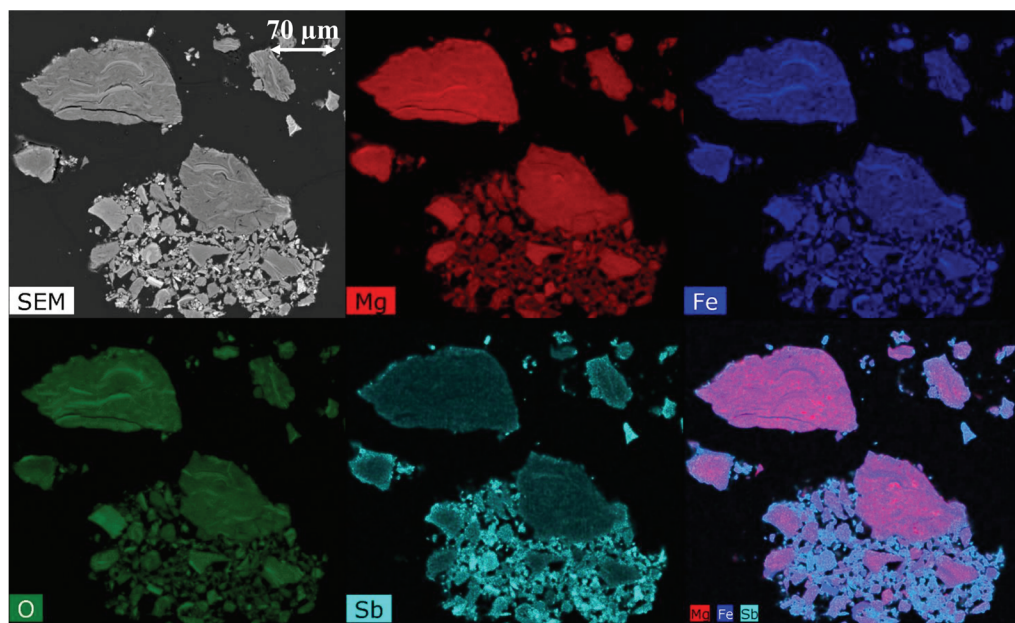


Fig. 5.5. Elemental mapping of LDH-Sb-5.5 at an initial Sb(V) concentration of 500 mg L⁻¹.

Spectroscopic analyses

The FTIR-ATR spectra of LDH before and after Sb(V) adsorption at the initial Sb(V) concentration of 500 mg L⁻¹ and different pH values are given in Fig. 5.6. The spectra showed all characteristic bands corresponding to the LDH structure, i.e., the stretching vibration of hydroxyl groups (3454 – 3409 cm⁻¹), the bending vibration of water (1633–1642 cm⁻¹), the absorption band of carbonates (1361 – 1353 cm⁻¹ and 659 – 654 cm⁻¹) and the absorption bands of metal oxide/hydroxide groups (approx. 550 cm⁻¹) (Hudcová et al., 2017, 2018). After Sb(V) adsorption, significant changes in individual peaks were observed. The shift of the stretching vibration of hydroxyl groups to lower frequencies corresponded to the formation of stronger hydrogen bonds that were assigned to new interactions between hydroxyl groups on the LDH surface and Sb(V) (McComb et al., 2007). Moreover, the shift increased with increasing Sb(V) coverage, i.e., by decreasing pH values. This shift could be attributed to the formation of the Fe-O-Sb bond, i.e., inner-sphere complexation of Sb(V) on the LDH surface (McComb et al., 2007; Vithanage et al., 2013) confirming the results of adsorption modeling (see Section *Surface complexation modeling*). However, changes of hydroxyl groups could also be attributed to the formation of brandholzite-like phases (pH 6.5 and 5.5) or surface-induced precipitation of brandholzite (pH 7.5) as discussed for XRD and SEM/EDX analyses. Nevertheless, the most significant shift at pH 5.5 could also be

influenced by the anion exchange following the XRD results. This mechanism could also be considered due to the significant decrease in the carbonate absorption band intensity at this pH value, suggesting changes in the interlayer region, i.e., the anion exchange of carbonates by Sb(V). Similar changes have been previously observed during As(V) adsorption onto the same LDH type (Hudcová et al., 2017). The bands due to Sb–O stretching could be expected in the region $620\text{--}750\text{ cm}^{-1}$ (Bahfenne and Frost, 2010), which coincides with the absorption by carbonates. Thus, the broadened shoulder observed at $\sim 712\text{ cm}^{-1}$, the intensity of which increases with decreasing pH, was assigned to the stretching mode of adsorbed Sb(V) species (Frost et al., 2009; McComb et al., 2007; Vithanage et al., 2013; 2015). Similarly, the most significant changes were observed at the highest Sb(V) coverage, i.e., pH 5.5.

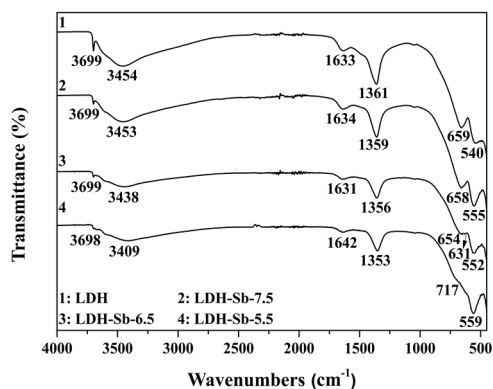


Fig. 5.6. FTIR-ATR spectra of LDH before Sb(V) adsorption and LDH-Sb-7.5, LDH-Sb-6.5, LDH-Sb-5.5 at an initial Sb(V) concentration of 500 mg L^{-1} .

The XPS spectra of LDH before and after Sb(V) adsorption at an initial Sb(V) concentration of 500 mg L^{-1} and different pH values are shown in Fig. S5.3 and the calculated surface stoichiometry is given in Table S5.5. The XPS spectra of all materials included Fe 2p, Mg 2s, Mg 2p, O 1s and C 1s peaks confirms the structure of Mg-Fe LDHs. Moreover, new peaks corresponding to Sb 3p and Sb 3d occurred after Sb(V) adsorption at all pH values. The amount of Sb(V) on the LDH surface increased with decreasing pH values corresponding to results discussed above and in Sections *Kinetic and equilibrium adsorption experiments* and *Surface complexation modeling*. Moreover, significant changes in individual peaks after Sb(V) adsorption were observed (Fig. S5.4). The Fe 2p peak after Sb(V) adsorption at all pH values increased and shifted to higher binding energies that meant formation of strong bonds between Fe(III) and Sb(V), i.e., inner-sphere complexation on the LDH surface that corresponded to the results of adsorption modeling (Sections *Surface complexation modeling*). A similar shift has been previously observed after As(V) adsorption on LDHs (Goh et al., 2009; Hudcová et al., 2017). Surprisingly, and in contrast to our previous adsorption studies using the same LDH type (Hudcová et al., 2017, 2018), the increase in and spectral shift of Mg 2s and Mg 2p peaks after Sb(V) adsorption at all

pH values were observed. As shown by previous instrumental techniques, the Mg(II) leaching during Sb(V) adsorption was reduced compared to the same LDH type after As(V), Zn(II) and Pb(II) adsorption, thus confirming the formation of brandholzite-like phases (at lower pH values) or surface-induced precipitation of brandholzite (at higher pH values) on the LDH surface. In general, the Mg 2p peak consisted of two contributions, i.e., M-O (higher binding energies) and Mg-OH (lower binding energies) bonds. After Sb(V) adsorption, changes in individual contributions were observed (especially at pH 5.5), i.e., for LDH (Mg-O: 76.4%; Mg-OH: 23.6%), LDH-Sb-7.5 (Mg-O: 76.7%; Mg-OH: 23.3%), LDH-Sb-6.5 (Mg-O: 70.9%; Mg-OH: 29.1%) and LDH-Sb-5.5 (Mg-O: 82.5%; Mg-OH: 17.5%). These changes in Mg(II) binding arrangements confirmed the formation of brandholzite-like phases or brandholzite surface-induced precipitation on the LDH surface as discussed above.

Additionally, the deconvolution of O 1s spectra was performed (Fig. 5.7). The O 1s peak at all pH values consisted of several contributions, i.e., M-O (531.5-531.8 eV), M-OH (533.1-533.2 eV), carbonates (534.3-534.2 eV) and water (535.4-535.5 eV) (Hudcová et al., 2017, 2018). Moreover, the Sb 3d peak occurred in this region after Sb(V) adsorption and consisted of two contributions, i.e., Sb 3d_{5/2} (lower binding energies) and Sb 3d_{3/2} (higher binding energies). Since the Sb 3d_{5/2} peak overlapped the O 1s peak, the deconvolution (intensity of individual peaks and their binding energy) was provided according to the Sb 3d_{3/2} peak in the ratio 2:3 following the spin-orbit splitting (Watts and Wolsethholme, 2003). The broad Sb 3d_{3/2} peak consisted of Sb(V) (higher intensity) and Sb(III) (lower intensity) and therefore these contributions were also used for the deconvolution of the O 1s and Sb 3d_{5/2} peaks. Nevertheless, reduction of Sb(V) during adsorption on Mg-Fe LDHs was excluded since it was caused by the X-rays during XPS measurements. This effect was confirmed by the increase in the peaks corresponding to Sb(III) after Ar⁺ sputtering following our previous XPS results after As(V) adsorption (Hudcová et al., 2019). Moreover, reduction caused by Ar⁺ sputtering using Fe oxides has also been discussed by Fondell et al. (2018). Nevertheless, the decrease in the Mg-OH contributions to the O 1s peak after Sb(V) adsorption was also observed following the changes in the Mg 2p peak discussed above, i.e., the decrease in the Mg-OH peak by the increasing Sb(V) coverage. In contrast, only minor changes were observed for Mg-O based on the O 1s peak. Nevertheless, the Mg(II) contributions to the O 1s peak after Sb(V) adsorption could be influenced by the deconvolution process compared to the deconvolution of Mg 2p without any other contributions as discussed above.

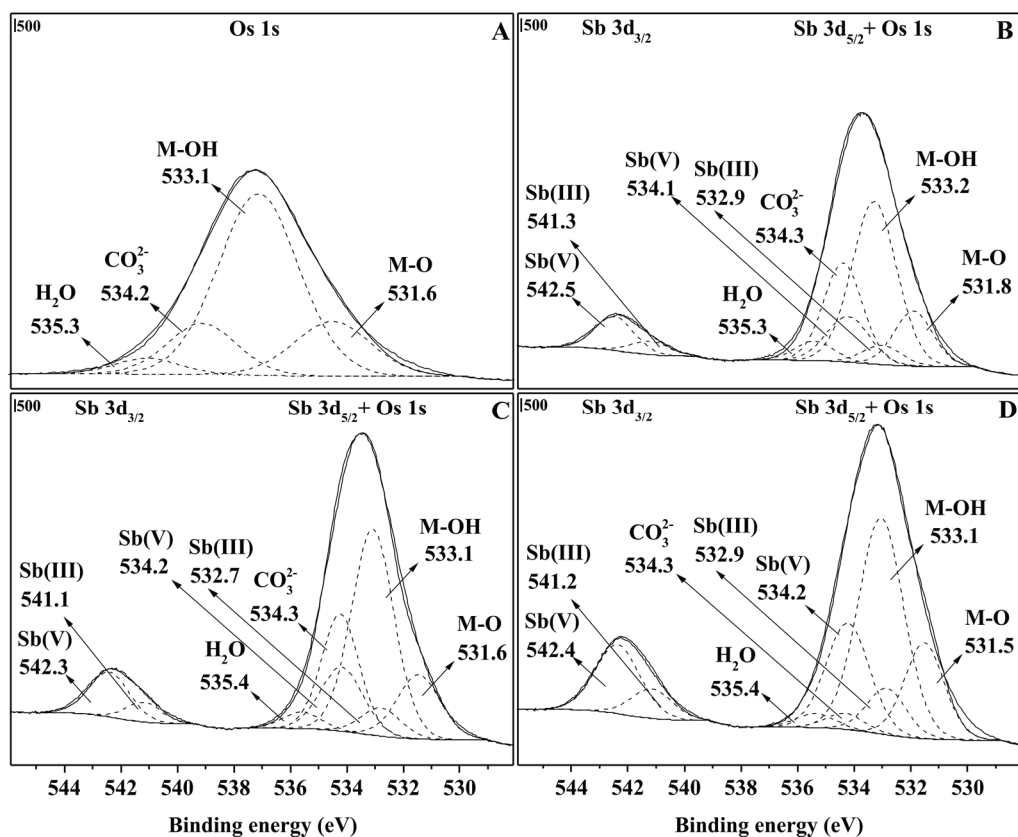


Fig. 5.7. XPS deconvolution of the Sb 3d and O 1s peaks of LDH before Sb(V) adsorption (A) and LDH-Sb-7.5 (B), LDH-Sb-6.5 (C), LDH-Sb-5.5 (D) at an initial concentration of 500 mg L⁻¹.

Conclusions

The Sb(V) adsorption mechanism on Mg-Fe LDHs at different initial Sb(V) concentrations and pH values was investigated by adsorption modeling coupled with various spectroscopic and microscopic techniques. Our results showed that Sb(V) adsorption onto Mg-Fe LDHs is a strongly pH-dependent process. The kinetic data were successfully described by pseudo-first order kinetics and the equilibrium data by the Freundlich model (lower pH values) and/or Langmuir model (higher pH values). In general, the adsorption rate and the adsorbed amounts increased with decreasing pH values. The preferable formation of monodentate-inner sphere complexes on the Mg-Fe LDH surface was supported by the DLM. The results of adsorption modeling were supported by solid-state analyses and indicated that the adsorption mechanism was also influenced by the surface-induced precipitation of brandholzite, the formation of brandholzite-like phases and/or anion exchange based on the initial Sb(V) concentrations and pH values. The presented mechanistic/modeling approach investigated the Sb(V) adsorption mechanism on Mg-Fe LDHs and predicted their adsorption characteristics under different experimental conditions.

Supplementary Material

Table S5.1 Parameters of the nonlinear modeling using the pseudo-first and pseudo-second order kinetics for adsorption of Sb(V) on Mg-Fe LDH at different pH values.

Parameter	Mg-Fe LDH-Sb-5.5	Mg-Fe LDH-Sb-6.5	Mg-Fe LDH-Sb-7.5
	Value	Value	Value
q_{exp} (mg g ⁻¹)	12.3	9.47	5.92
Pseudo-first order kinetics			
q_e (mg g ⁻¹)	12.0	9.89	6.99
k_1 (min ⁻¹)	0.04	0.03	0.02
R^2	0.99	0.99	0.99
Pseudo-second order kinetics			
q_e (mg g ⁻¹)	14.6	13.5	10.3
k_2 [g (mg min) ⁻¹]	0.00	0.00	0.00
R^2	0.99	0.99	0.99
	S.E.	S.E.	S.E.
	0.26	0.22	0.59
	0.00	0.00	0.00
	-	-	-
	0.24	0.42	1.02
	0.00	0.00	0.00
	-	-	-

Table S5.2 Parameters of the nonlinear modeling using the Langmuir and Freundlich models for adsorption of Sb(V) on Mg-Fe LDH at different pH values.

Parameter	Mg-Fe LDH-Sb-5.5		Mg-Fe LDH-Sb-6.5		Mg-Fe LDH-Sb-7.5	
	Value	S.E.	Value	S.E.	Value	S.E.
Langmuir model						
q_{exp} (mg g ⁻¹)	67.5	2.17	21.3	1.69	10.4	1.95
q_{max} (mg g ⁻¹)	69.8	4.27	20.5	1.77	10.2	0.33
K_L (L mg ⁻¹)	0.03	0.00	0.06	0.03	0.10	0.02
R^2	0.98	-	0.92	-	0.99	-
Freundlich model						
n (-)	3.41	0.34	4.66	0.45	4.98	1.02
K_F^*	11.5	1.78	5.82	0.62	3.25	0.68
R^2	0.98	-	0.98	-	0.91	-

* [(mg g⁻¹)(L mg⁻¹)^{1/n}]

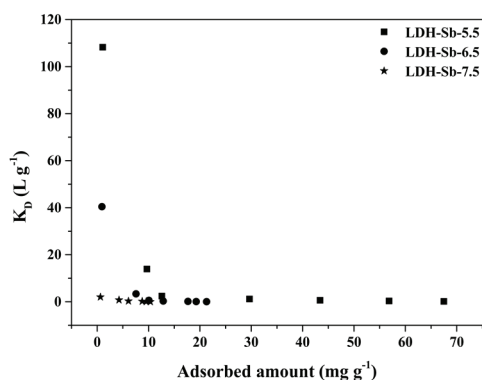


Fig. S5.1. Values of the distribution coefficient K_D as a function of the Sb(V) adsorbed amount on Mg-Fe LDH.

Table S5.3 Basal spacings and cell parameters calculated from diffractograms of LDH before Sb(V) adsorption and LDH-Sb-7.5, LDH-Sb-6.5, LDH-Sb-5.5 at initial Sb(V) concentrations of 12 mg L^{-1} and 500 mg L^{-1} .

Material	c_0^*	$d_{003} (\text{\AA})$	$d_{006} (\text{\AA})$	$d_{009} (\text{\AA})$	$d_{110} (\text{\AA})$	$a (\text{\AA})^{**}$	$c (\text{\AA})^{***}$
LDH	-	7.741	3.909	2.631	1.553	3.106	23.339
LDH-Sb-7.5	12	7.730	3.910	2.636	1.554	3.108	23.325
LDH-Sb-6.5		7.730	3.909	2.635	1.553	3.106	23.322
LDH-Sb-5.5		7.793	3.918	2.627	1.555	3.110	23.444
LDH-Sb-7.5	500	7.787	3.900	2.642	1.553	3.106	23.381
LDH-Sb-6.5		7.721	3.884	2.628	1.553	3.106	23.234
LDH-Sb-5.5		7.817	3.908	2.635	1.553	3.106	23.450

* c_0 = initial concentration (mg L^{-1})

** $a = 2d_{110}$

*** $c = 3/2(d_{003} + 2d_{006})$

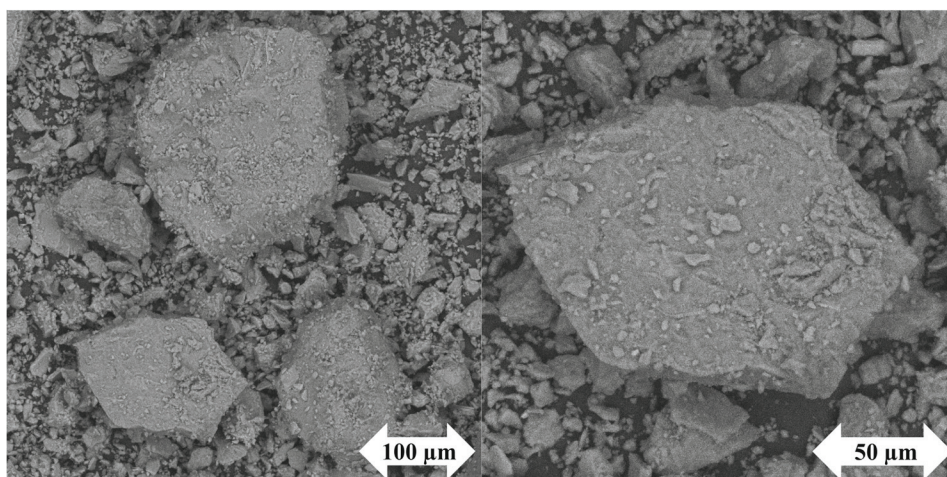


Fig. S5.2. SEM images of LDH before Sb(V) adsorption.

Table S5.4 EDX analyses (wt.%) of LDH before Sb(V) adsorption and LDH-Sb-7.5, LDH-Sb-6.5 and LDH-Sb-5.5 at initial Sb(V) concentrations of 12 mg L⁻¹ and 500 mg L⁻¹.

Material	c ₀ *	Point**	Mg	Fe	O	K	Sb
LDH-Sb-7.5	12	1	24.1±1.62	15.8±0.53	42.8±3.37	-	-
	12	2	20.6±0.54	18.7±0.39	40.2±2.23	-	0.89±0.36
	500	1	20.5±2.19	26.2±1.14	40.3±2.45	-	4.51±0.47
	500	2	21.9±0.24	16.9±1.42	42.4±1.27	0.12±0.03	3.60±0.83
	500	3	19.6±1.88	14.2±0.64	39.6±4.37	0.17±0.05	5.71±1.86
LDH-Sb-6.5	12	1	12.3±4.16	6.20±4.56	22.6±5.94	-	46.0±16.0
	12	2	22.7±1.95	18.2±0.74	39.4±0.33	-	1.34±0.26
	500	1	19.3±0.30	23.7±1.71	36.8±5.31	-	5.19±0.50
	500	2	21.6±1.11	16.6±1.14	45.6±4.63	0.23±0.05	6.77±1.12
	500	2	20.7±0.70	18.6±2.96	42.1±5.04	0.30±0.04	9.49±1.07
LDH-Sb-5.5	12	1	19.5±1.59	19.3±1.09	39.8±1.96	-	2.93±1.93
	12	2	15.8±0.79	23.3±1.37	37.2±4.88	-	9.31±1.99
	500	1	21.4±1.49	15.9±0.62	35.2±2.99	-	9.00±1.75
	500	2	16.2±1.94	15.3±1.31	33.0±1.88	0.52±0.23	22.6±5.11

* c₀ = initial concentration (mg L⁻¹) ** points corresponded to numbers given in Fig. 5.4.

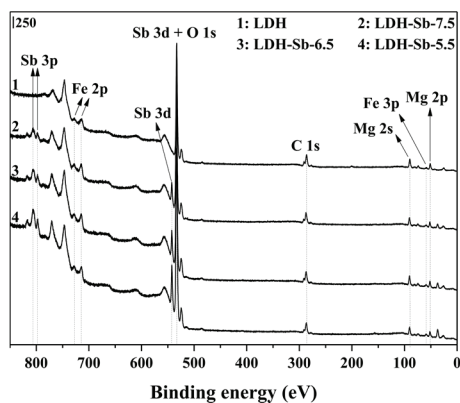


Fig. S5.3. XPS spectra of LDH before Sb(V) adsorption and LDH-Sb-7.5, LDH-Sb-6.5, LDH-Sb-5.5.

Table S5.5 Surface stoichiometry (%) of LDH before Sb(V) adsorption and LDH-Sb-7.5, LDH-Sb-6.5, LDH-Sb-5.5 according to XPS data.

	Fe 2p	Mg 2s	O 1s	C 1s	Sb 3d
Mg-Fe LDH	1.1	37.0	43.7	18.2	-
Mg-Fe LDH-Sb-7.5	1.5	32.3	47.9	16.7	1.7
Mg-Fe LDH-Sb-6.5	1.4	32.5	48.9	15.2	2.0
Mg-Fe LDH-Sb-5.5	1.5	31.4	49.2	15.6	2.4

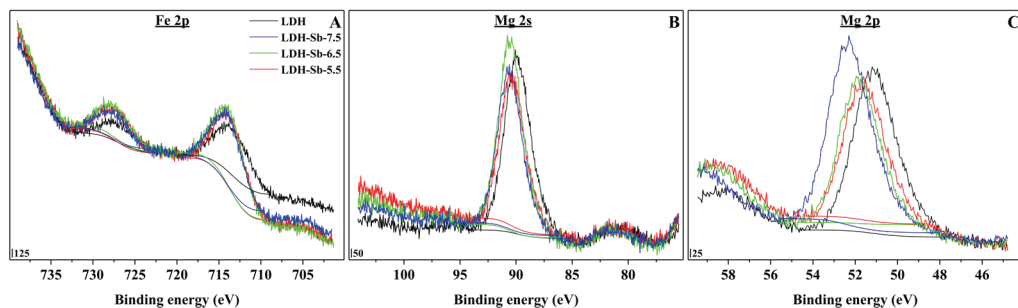


Fig. S5.4. XPS spectra of Fe 2p, Mg 2s and Mg 2p peaks of LDH before Sb(V) adsorption and LDH-Sb-7.5, LDH-Sb-6.5, LDH-Sb-5.5.

Chapter VI

Biochar and its composites for metal(loid) removal from aqueous solutions

L. Trakal, M. Vítková, B. Hudcová, L. Beesley, M. Komárek

Adapted from Ok, Y., Tsang, D., Bolan, N., Novak J. (eds.), *Biochar from Biomass and Waste* (2019): 113-141, with permission of the coauthors.

Content

Abstract	167
Metal sorption on various biochars	168
The effect of biochar characteristics	168
Optimization of metal sorption	175
Metal-sorption mechanisms	176
Biochar modifications	178
Chemical activation	178
Iron modifications	180
Layered double-hydroxide modification	185
Manganese-oxide coating	189
Engineering implications of biochar and its modifications	193

Abstract

Biochar-based materials are currently intensively studied and used as highly efficient sorbents. While “pure” biochars can exhibit important adsorption properties for some metal(loid)s, the efficiency for others can be limited. For this reason, several modifications have been developed in order to increase their efficiency, selectivity for different elements or even their stability. These composites include, for example, magnetic modification with Fe oxides, nano zero-valent Fe, layered double hydroxides and Mn oxides. This chapter aims to review the potential of these composite materials and the responsible mechanisms for metal(loid) sorption.

Metal sorption on various biochars

The conversion of surplus biomass into biosorbent biochars (BC) can be described as a “win–win” solution for the production of a new material with enhanced environmental value (Cao et al., 2009; Zheng et al., 2010) for the treatment of contaminated waters (Tan et al., 2015). Many studies have described effective removal of metals from waters using biochars originating from different organic wastes (Table 6.1). For example, the high performance of pristine biochars to remove Cd and/or Pb from aqueous solutions has been found to be within the range of one order (from 2.87 to 2872 mmol kg⁻¹) (Inyang et al., 2011; Jiang et al., 2012; Han et al., 2013; Kim et al., 2013; Xu et al., 2013a; Trakal et al., 2014a; Zama et al., 2017; Sekulić et al., 2018). Thus, it would appear that modifications to biochar-based sorbents, aimed at stimulating specific geochemical mechanisms, could enhance their efficiency.

Effect of biochar characteristics

The origin and methods of biochar preparation (pyrolysis) are ultimately greatly responsible for its final physical and chemical characteristics (Table 6.1). Thus, biochar properties significantly affect metal-sorption performance.

Firstly, the volume of micropores, which is very strongly related to the Brunauer–Emmett–Teller (BET) surface (Harvey et al., 2011), can affect metal sorption due to the effective reactive surface. This reactive surface (shown here by scanning electron microscopy (SEM) images; Fig. 6.1) shows the various surface morphology of tested biochars. Woody (high lignin) biochars show well-developed structures with high macro- and microporosity (Fig. 6.1A; Chen et al., 2011, Mohan et al., 2014a). On the other hand, poorly structurally developed biochars (Fig. 6.1B) show a limited presence of these pores. This is in agreement with the lower BET surface and lower volume of micropores in these cases (Table 6.2). The resultant metal sorption is higher for those biochars with poorly developed structures represented by lower BET surface, so the morphology of biochars is not a crucial factor affecting metal-sorption efficiency (later in Fig. 6.2).

Table 6.1 Comparison of Cd(II) and Pb(II) sorption onto different pristine biochars originated from contrasting agricultural waste materials (from selected recent studies).

Biochar origin	Temperature of pyrolysis (°C)	Maximum metal sorption		Reference
		Cd (mmol kg ⁻¹)	Pb (mmol kg ⁻¹)	
Grape stalks	600	450	2872	Trakal et al. (2014a)
<i>Canna indica</i>	500	1679	/	Cui et al. (2016)
Celery stems	500	/	1467	Zhang et al. (2017a)
Celery stems	350	/	1390	Zhang et al. (2017a)
Wheat straws	600	400	1322	Trakal et al. (2014a)
<i>Canna indica</i>	600	1246	/	Cui et al. (2016)
Sugar cane bagasse	250	/	1240	Ding et al. (2014)
<i>Alternanthera philoxeroides</i>	600	/	1240	Yang et al. (2014)
Chemically pre-treated pig manure	600	1041	1110	Kołodźńska et al. (2012)
Mechanically separated dairy cow manure	600	1050	1062	Kołodźńska et al. (2012)
Mechanically separated dairy cow manure	400	1023	1028	Kołodźńska et al. (2012)
Chicken bone	600	967.0	/	Park et al. (2015)
Chemically pre-treated pig manure	400	951.9	839.8	Kołodźńska et al. (2012)
<i>Prunus armeniaca</i>	500	941.2	866.3	Sekulić et al. (2018)
<i>Canna indica</i>	400	941.0	/	Cui et al. (2016)
Celery leaves	500	/	907.3	Zhang et al. (2017a)
Grape hulls	600	259.8	859.1	Trakal et al. (2014a)
Sugar cane bagasse	500	/	830.1	Ding et al. (2014)
Poultry manure	450	801.4	/	Idrees et al. (2016)
Dairy manure	350	559.6	791.5	Xu et al. (2013a)
Sesame straw	700	765.1	492.3	Park et al. (2016a)
Farmyard manure	450	681.7	/	Idrees et al. (2016)
Residue of biogas production	600	679.1	/	Bogusz et al. (2017)
Sugarcane bagasse + aerobic digestion	600	/	661.2	Inyang et al. (2011)

Table 6.1 (Continued)

Biochar origin	Temperature of pyrolysis (°C)	Maximum metal sorption		Reference
		Cd (mmol kg ⁻¹)	Pb (mmol kg ⁻¹)	
Pepper stem	600	593.4	635.6	Park et al. (2016b)
<i>Ipomoea fistulosa</i>	400	635.4	/	Goswami et al. (2016)
Residue of biogas production	400	610.5	/	Bogusz et al. (2017)
<i>Rosa damascena</i>	450	590.3	255.6	Khare et al. (2017)
<i>Canna indica</i>	300	563.3	/	Cui et al. (2016)
<i>Ipomoea fistulosa</i>	500	556.0	/	Goswami et al. (2016)
<i>Saccharina japonica</i>	700	540.0	/	K.-H. Poo et al. (2018)
<i>Ipomoea fistulosa</i>	350	493.7	/	Goswami et al. (2016)
Dairy manure	350	490.2	/	Xu et al. (2013b)
Sugar cane bagasse	500	/	419.7	Abdelhafez and Li (2016)
<i>Ipomoea fistulosa</i>	550	370.7	/	Goswami et al. (2016)
<i>Sargassum fusiforme</i>	700	330.9	/	K.-H. Poo et al. (2018)
<i>Phyllostachys pubescens</i>	700	130.6	325.5	Zhang et al. (2017b)
<i>Sida hermaphrodita</i>	700	317.7	/	Bogusz et al. (2017)
Rice straw	400	299.8	/	Han et al. (2013)
Maize cods	600	293.6	/	Moyo et al. (2016)
Wheat straw	700	289.7	/	Bogusz et al. (2017)
Dairy manure	200	280.2	/	Xu et al. (2013b)
Anaerobic digestion sludge	600	/	260.4	S.-H. Ho et al. (2017)
Peanut shell	350	/	254.8	Wang et al. (2015b)
Digested animal waste	600	30.34	250.0	Inyang et al. (2012)
Peanut shell	400	/	240.8	Wang et al. (2015b)
Salisbury (UK broadleaf hardwood)	600	/	230.0	Shen et al. (2015)
Peanut shell	300	/	206.1	Wang et al. (2015b)
Anaerobically digested dairy waste (sugar beet)	600	49.55	199.8	Inyang et al. (2012)

Table 6.1 (Continued)

Biochar origin	Temperature of pyrolysis (°C)	Maximum metal sorption		Reference
		Cd (mmol kg ⁻¹)	Pb (mmol kg ⁻¹)	
<i>Phyllostachys pubescens</i>	450	116.9	196.2	Zhang et al. (2017b)
Peanut shell	600	/	180.5	Wang et al. (2015b)
Sewage sludge + tea waste	300	177.9	/	Fan et al. (2018)
Peanut shell	500	/	166.0	Wang et al. (2015b)
Nut shells	600	40.03	150.1	Trakal et al. (2014a)
Sewage sludge	550	/	150.1	Lu et al. (2012)
Rice husk	350	70.01	140.0	Xu et al. (2013a)
Sugarcane straw	700	139.7	/	Melo et al. (2013)
Orange peel	500	/	134.5	Abdelhafez and Li (2016)
<i>Miscanthus sacchariflorus</i>	500	120.1	/	Kim et al. (2013)
<i>Miscanthus sacchariflorus</i>	600	120.1	/	Kim et al. (2013)
<i>Miscanthus sacchariflorus</i>	400	110.3	/	Kim et al. (2013)
Plum stones	600	40.03	110.0	Trakal et al. (2014a)
<i>Miscanthus sacchariflorus</i>	300	99.64	/	Kim et al. (2013)
Sugarcane straw	500	79.98	/	Melo et al. (2013)
Garden green waste residues	500	69.39	/	Frišák et al. (2015)
Sugarcane straw	600	50.00	/	Melo et al. (2013)
Pinewood sawdust	700	44.48	/	K.-H. Poo et al. (2018)
Sugarcane bagasse/ Peanut hull	600	40.03	19.98	Zhou et al. (2013)
Sugarcane straw	400	40.03	/	Melo et al. (2013)
Spruce cone	600	25.44	38.51	Saletnik et al. (2017)
Larch cone	500	21.26	37.69	Saletnik et al. (2017)
Spruce cone	500	20.02	38.42	Saletnik et al. (2017)
Larch cone	600	7.206	36.58	Saletnik et al. (2017)
Sugarcane bagasse	600	/	30.02	Inyang et al. (2011)
Hickory wood	600	20.02	19.98	Zhou et al. (2013)

Table 6.1 (Continued)

Biochar origin	Temperature of pyrolysis (°C)	Maximum metal sorption		Reference
		Cd (mmol kg⁻¹)	Pb (mmol kg⁻¹)	
Bamboo	600	20.02	9.990	Zhou et al. (2013)
Beech wood chips	500	17.70	/	Frišťák et al. (2015)
Peanut shells	350	14.82	6.593	Zama et al. (2017)
Mulberry wood	550	8.086	12.55	Zama et al. (2017)
Mulberry wood	450	6.352	12.06	Zama et al. (2017)
Mulberry wood	350	3.416	12.07	Zama et al. (2017)
Poultry manure	650	2.695	12.01	Zama et al. (2017)
Peanut shells	450	11.12	9.778	Zama et al. (2017)
Poultry manure	450	11.12	9.653	Zama et al. (2017)
Poultry manure	550	11.12	8.084	Zama et al. (2017)
Peanut shells	550	11.12	6.033	Zama et al. (2017)
Poultry manure	350	6.352	10.14	Zama et al. (2017)
Mulberry wood	650	5.925	9.894	Zama et al. (2017)
Buckwheat husk	550	3.558	9.653	Zama et al. (2017)
Buckwheat husk	350	0.605	9.556	Zama et al. (2017)
Buckwheat husk	450	8.896	6.940	Zama et al. (2017)
Buckwheat husk	650	8.896	6.897	Zama et al. (2017)
Peanut shells	650	7.410	8.523	Zama et al. (2017)
Corn cobs	450	5.231	8.137	Zama et al. (2017)
Corn cobs	650	4.679	7.703	Zama et al. (2017)
Corn cobs	550	3.701	6.892	Zama et al. (2017)
Corn cobs	350	2.865	5.314	Zama et al. (2017)

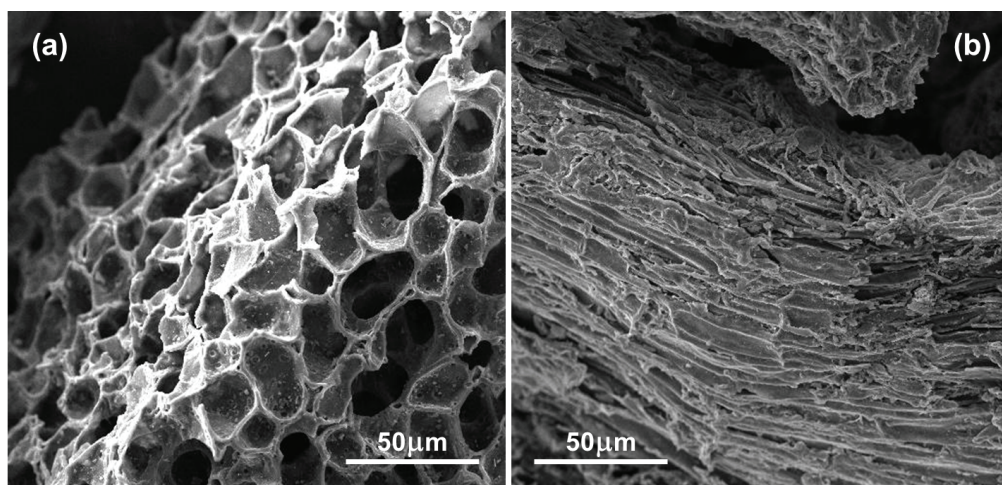


Fig. 6.1. SEM images of (A) biochar with well-developed structure (nut shields) and (B) biochar with poorly developed structure (grape husks; Trakal et al., 2014a). SEM, scanning electron microscopy.

Table 6.2 Biochar characteristics: yield of biochar from the waste material (Y), bulk density (ρ) BET surface, volume of micropores (V_{micro}), pH value and Cation Exchange Capacity (CEC; Trakal et al., 2014a).

Biochar	Y (%)	ρ (g cm ⁻³)	BET (m ² g ⁻¹)	V_{micro} (mm ³ g ⁻¹)	pH (-)	CEC (mmol kg ⁻¹)
Nut shields	21.8	0.17 ± 0.002	465	180	8.63 ± 0.04	84.4 ± 3.0
Wheat straw	18.9	0.26 ± 0.005	364	130	9.86 ± 0.05	334 ± 2
Grape stalks	30.6	0.16 ± 0.004	72	30	10.0 ± 0.1	402 ± 3
Grape husks	31.6	0.21 ± 0.003	77	32	9.98 ± 0.01	187 ± 4
Plum stones	24.7	0.22 ± 0.002	443	172	7.36 ± 0.12	121 ± 7

The pH of biochars is usually alkaline in the range 7.2-10.0 (Verheijen et al., 2010; Trakal et al., 2014a). Generally, biochar production, by pyrolysis, causes pH increases in comparison to the pH of the source material (Lu et al., 2012). The pH also increases after the pyrolysis process because the alkali salts separate from the organic matrix (at pyrolysis temperature ranging from 300 °C to 600 °C; Chen et al., 2011). This physico-chemical characteristic of biochar is usually a key factor in bivalent metal sorption from waters, mainly due to the pH-buffering effect of the biochar (Trakal et al., 2014a) affecting not only the surface charge, but also the speciation of metal ions in solution.

The cation-exchange capacity (CEC) of biochar samples is often an underestimated parameter that has considerable influence on metal-sorption efficiency, as reported by Lu et al. (2012), Zhang et al. (2013a), Ahmad et al. (2014), and Trakal et al. (2014a).

Specifically, the CEC value of biochars is closely related with: (1) the content of carboxylic groups (Harvey et al., 2011); and (2) the mineralogical composition, mainly the content of K^+ , Ca^{2+} and Mg^{2+} , which is thus important in cation release (Trakal et al., 2014a).

Fig. 6.2. shows the relationship between the metal-removal efficiency (Cd and Pb) and selected biochars characteristics. The results of various published studies were analyzed to obtain complex information about the characteristics that may be responsible for the metal-removal efficiency. Specifically, increasing the CEC significantly enhances the Pb-removal efficiency ($R = 0.90$) of various biochars. This supports the hypothesis that CEC may be one of the most important characteristics in biochar selection for metal sorption because other tested biochar characteristics (such as BET surface or temperature of pyrolysis) showed no significant relationship to the sorption efficiency of metals (represented here by Cd and Pb; Fig. 6.2; Trakal et al., 2014a).

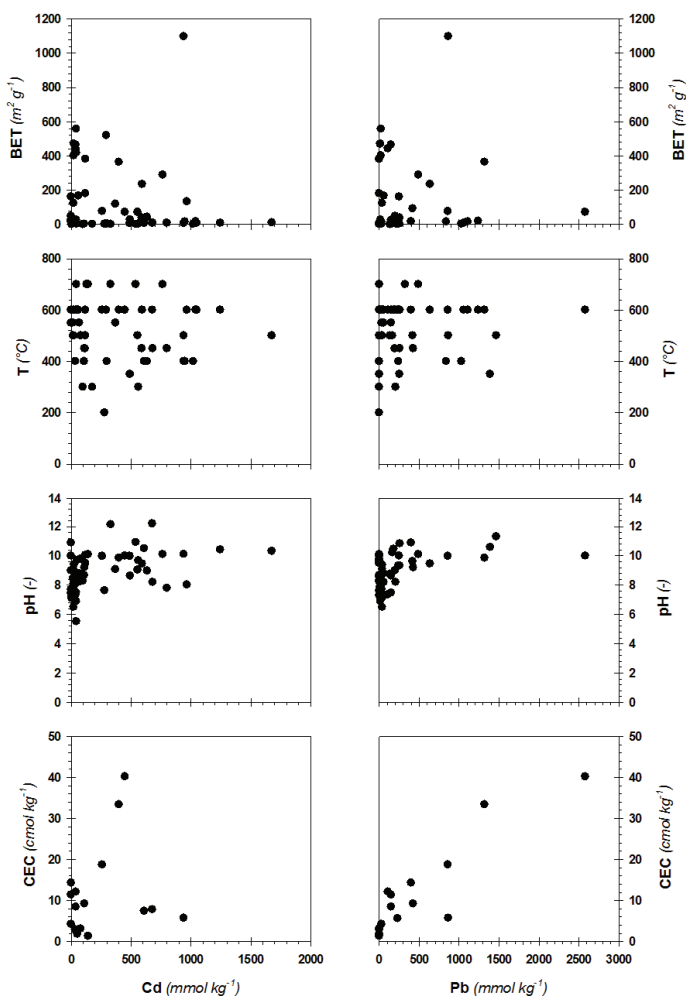


Fig. 6.2. Relationship between maximum Cd and Pb sorption on different biochars and selected biochars characteristics.

Optimization of metal sorption

The optimization of metal sorption can be implemented using batch-sorption procedures designed according to the response surface methodology (RSM). One of the main objectives of RSM is to determine optimum parameters for the control variables that result in a maximum (or a minimum) response over a certain region of interest (Khuri and Mukhopadhyay, 2010). Response surfaces could then be used to determine an optimum and to graphically illustrate the relationship between different experimental variables and their responses (Fig. 6.3). In order to determine an optimum, it is necessary for the polynomial function to contain quadratic terms. The following quadratic model (Eq. 6.1) could be used to fit experimental data (Montgomery, 2008; Khuri and Mukhopadhyay, 2010):

$$y = \beta_0 + \sum_{i=1}^k \beta_i x_i + \sum_{i=1}^k \beta_{ii} x_i^2 + \sum_{1 \leq i < j \leq k} \beta_{ij} x_i x_j + \varepsilon \quad \text{Eq. 6.1}$$

where x_1, x_2, \dots are numbers of associated control (or input) variables, y is a response of interest, β are constant coefficients referred to as parameters and ε and is a random experimental error assumed to have a zero mean. The selected independent variables X_i were coded as x_i according to the following relationship (Eq. 6.2):

$$x_i = \left(\frac{X_i - X_0}{\Delta x} \right) \quad \text{Eq. 6.2}$$

where X_0 is the uncoded value of X_i at the center point and Δx presents the step change.

In the case of metal-sorption optimization, a conventional batch-sorption experiment is employed before an experiment is designed using central composite design. The influence factors and response(s) are established and the exact number of runs (combing established factors) is then determined by Minitab software. The advantage of this approach is a limited number of runs for the following example; a design consisting of 20 experiments was used to assess the influence of 3 factors (pH of solution, dose of applied biochar, and contact time) on two responses (sorbed amount of two contrasting metals) for each biochar.

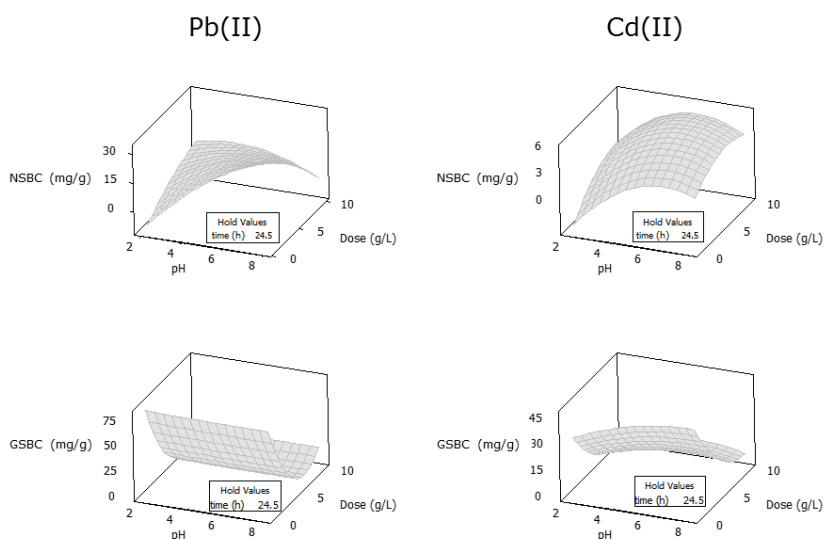


Fig. 6.3. Response surface plots of Cd(II) and Pb(II) sorption for nut shields and grape stalks biochars, respectively.

Metal-sorption mechanisms

The metal-sorption process has been described as a result of three different mechanisms (Sohi et al., 2010; Lu et al., 2012): (1) ion exchange (Ca^{2+} , K^+ , Mg^{2+} , Na^+); (2) metal complexation onto free and complexed carbonyl, carboxyl, alcoholic, hydroxyl, or phenolic hydroxyl functional groups; and (3) physical adsorption or surface precipitation caused by sorptive interaction involving delocalization of π electrons of organic carbon (Inyang et al., 2011; Lu et al., 2012; Xu et al., 2013b; Bernardo et al., 2013). As described, ion exchange, complexation, and/or physical adsorption are responsible for metal sorption to biochars. These metal-sorption mechanisms vary according to the type of biochar (group of biochars originating from similar materials) and the metal(loid).

Biochars with well-developed structures (e.g., woody biochars) sorb metals predominantly on the surface. By contrast, biochars with poorly developed structure (represented by low BET surface) exhibit metals not solely sorbed on the surface, but also bonded inside the biochar structure (in higher quantities). Fig. 6.4 shows the exact sorption mechanisms of Pb on/in two contrasting biochars. The weak π -bindings of Pb with polyorganic chains (bonding with electron-rich domains on graphene-like structures; Harvey et al., 2011) has demonstrated physical adsorption (Lu et al., 2012). The weakness of the bond was confirmed by the postdesorption test of fully metal-

loaded biochars (Trakal et al., 2014a). The presence of residual CO_3^{2-} (eventually PO_4^{3-}) in biochar together with its alkaline pH are often responsible for the formation of metal-(hydro)carbonates (and/or metal-phosphates), reflecting their surface precipitation (usually confirmed by the X-ray diffraction (XRD) patterns of metal-loaded biochars; see Fig. 6.4; Xu et al., 2013a,b; Trakal et al., 2014a).

Ion exchange, another significant sorption mechanism, was also detected in all tested biochars (Fig. 6.4). Such cation release of metals is limited predominantly to that coming from internal sites of those biochars with poorly developed structures. This could be explained by the low BET surface versus the high quantity of K and Ca (responsible for the ion exchange). The complexation with carboxylic functional groups, as the third sorption mechanism, is demonstrated in Fig. 6.4 (by the binding energy at 141 eV for the Pb). This sorption mechanism (metal-chelate creation) is nevertheless only in those biochars with poorly developed structure where the complexation is a limiting mechanism (Trakal et al., 2014a), which explains why the metal-chelate creation is insignificant in metal sorption.

Biochar with low BET surface Biochar with high BET surface

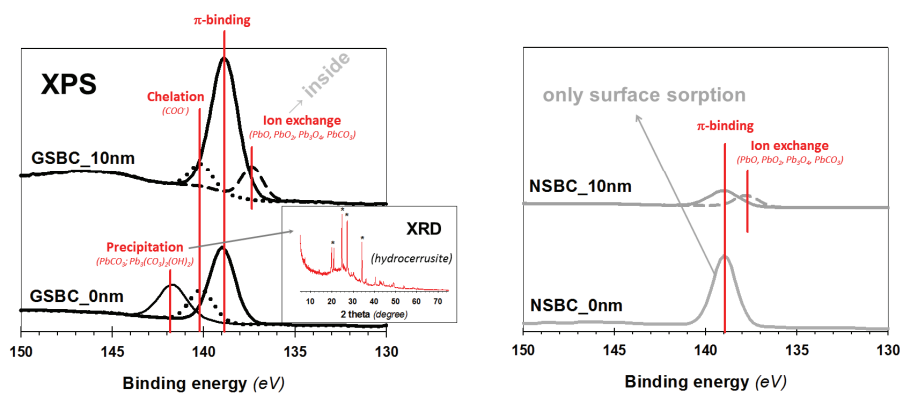


Fig. 6.4. X-ray photoelectron spectroscopy (XPS) analyses (deconvolution) of the grape stalks and nut shields biochars (on the surface and 10 nm deep) after Pb sorption and X-ray diffraction pattern of the grape stalks biochar confirming precipitation of $\text{Pb}_3(\text{CO}_3)_2(\text{OH})_2$ (hydrocerrussite; Trakal et al., 2014a).

Biochar modification

To further improve their metal-sorption efficiency, biochars can be modified before, during, and/or after the pyrolysis process (Fig. 6.5). As reviewed by Ahmed et al. (2016), there are established surface-modification methodologies such as steam activation, heat treatment, acidic/alkaline modification (chemical activation), and impregnation methods for char-based materials. Steam activation can introduce enhanced porous structures and oxygen-containing functional groups (e.g., carboxylic), whilst heat treatment can provide more basic surface functional groups for hydrocarbon sorption (Shen et al., 2008). Such modifications can effectively be regarded as turbo-boosting the existing sorption characteristics of the biochars. Acidic modification of biochars is applied by different oxidants to increase the acidic property of sorbents by removing or washing mineral elements, thereby increasing the hydrophilic nature of BC (Shen et al., 2008). Conversely, alkaline modification produces negative surface charges that, in turn, assist in adsorbing negatively charged species (Ahmed et al., 2016). Lastly, impregnation methods, by metal salts or oxides mixed with biochars, can facilitate additional physical or chemical attachment of metal ions (Ahmed et al., 2016).

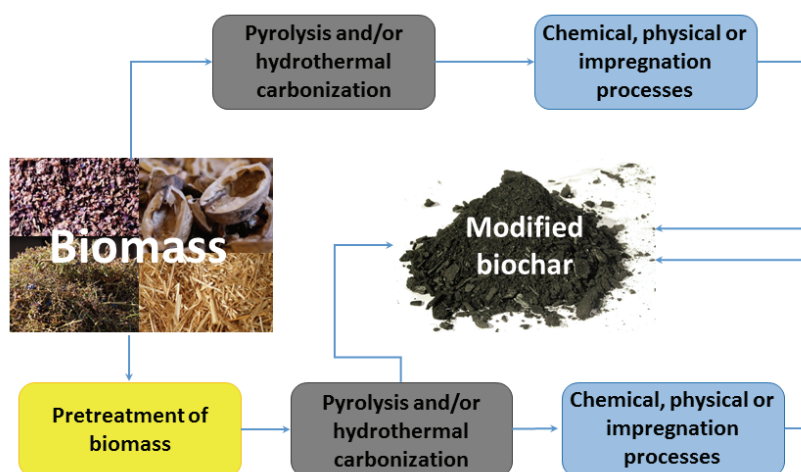


Fig. 6.5. Schematic of various biochar modifications (inspired by Ahmed et al., 2016).

Chemical activation

Chemical activation of biochars can be performed with an acidic solution or hydroxides as shown by Regmi et al. (2012) and Trakal et al. (2014b), where BC was mixed and stirred with 2 M KOH solution for 1 h at 1:250 ratio (w/v). The resulting solution was

then filtered, mixed with ultraclean water, and the pH value of BC then adjusted. Alkaline modification can improve both the physical and chemical properties of BCs. Specifically, 2 M KOH treated brewers draff BC provide significantly increased total pore volume due to the change in pore distribution, but the BET surface area was identical for both biochar samples before and after chemical activation (Table 6.3).

Table 6.3 Surface area and porosity of the pristine and chemically activated BCs using alkali modification by 2 M KOH (Trakal et al., 2014b).

Sample	BET surface ($m^2 g^{-1}$)	Pores distribution (%)				Total pore volume ($mL g^{-1}$)
		< 6nm	6 – 20nm	20 – 80nm	> 80nm	
BC	9.80 ± 0.62	/	8.23	59.8	32.0	0.01 ± 0.002
BC _{act}	11.6 ± 0.40	18.7	18.1	38.8	24.5	8.74 ± 0.18

In the context of their use as biosorbents, Cu sorption increased after this alkaline activation from 8.77 to 10.3 $mg g^{-1}$ (Trakal et al., 2014b) as a result of improved physical sorption. Furthermore, the effect of chemical activation on metal-sorption efficiency was even more significant in column leaching tests (representing a dynamic system). Here, breakthrough curves with an early increase in the c/c_i ratio (Fig. 6.6) were observed for the biochar not been previously treated by 2 M KOH. The activated biochar breakthrough curve point (BTCP; the final time step for the maximum sorption efficiency of biochar, when the ratio $c/c_i \approx 0$) occurred at 780 min, as opposed to 50 min for the pristine BC (Fig. 6.6).

Such significant differences in BTCP are most likely caused by the presence of free micropores (<6 nm) in the chemically activated biochar (BC_{act}). These pores, created predominantly during high-temperature pyrolysis (Tsai et al., 2012), are formed only in the case of BC_{act} due to the leaching out of the tar particles during alkali solution stirring. In this case, it can be assume that Cu is trapped inside these free micropores, thus replacing the previously removed tar particles.

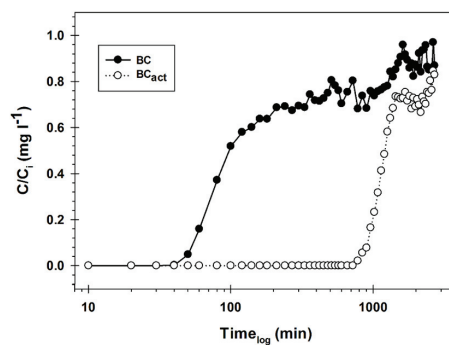


Fig. 6.6. Breakthrough curves of copper retention, obtained by a comcolumn leaching procedure (Trakal et al., 2014b).

Iron modification

Magnetic impregnation

Magnetic biochars are produced by mixing pristine biochars with a suspension of various Fe-(hydro)oxides typically when stirred under very alkaline pH (10 – 12; Mohan et al., 2015). Alternatively, other techniques such as microwave heating and chemical coprecipitation can also be applied (Mubarak et al., 2014; Trakal et al., 2016). For example, $\text{FeSO}_4 \cdot 7\text{H}_2\text{O}$ solution can be alkalinized (at $\text{pH} \approx 12$) in order to precipitate Fe-hydroxides (Trakal et al., 2016). Such created suspension is then put into a microwave, and this microwave-assisted synthesis results in the formation of iron-oxide nanoparticles with diameters ranging between 25 and 100 nm, consisting mainly of nonstoichiometric magnetite. Subsequently, ground biochar is then thoroughly mixed with the iron-oxide nanoparticles (Trakal et al., 2016). The efficiency of magnetically modified biochars as biosorbents is related to their altered surfaces, relative to pristine biochars. Firstly, magnetic modification decreases the active BET surface due to the formation of secondary iron (hydro)oxides on the surface (Mohan et al., 2015; Wang et al., 2015a), which has become more apparent in biochars with well-developed structures. Conversely, in biochars with poorly developed structures, the BET surface significantly increases (Trakal et al., 2016) due to the presence of iron oxides, which have: (1) a smaller surface area ($36.6 - 66.0 \text{ m}^2 \text{ g}^{-1}$; (Oliveira et al., 2002; Michálková et al., 2014) than that of biochars with a well-developed structure, but (2) a similar surface area to that of biochars with poorly developed structure. The magnetizing process also modified the pH value as well as the CEC, which could be explained by the presence of Fe oxides, which usually have neutral pH and rather high CEC values (in the range of 61.4 to 219 mmol kg^{-1} ; Trakal et al., 2016).

Secondly, the presence of Fe minerals can enhance the sorption efficiency of various metals (Reddy and Lee, 2014; Wang et al., 2014; Mohan et al., 2015) or metalloids (Zhang et al., 2013b; Baig et al., 2014; Wang et al., 2015a), typically fixed/sorbed on the surface of these precipitated (hydro)oxides. Therefore, magnetic biochars usually have significantly higher sorption, compared with pristine ones, of Cd(II) Pb(II) in those biochars with well-developed structure (Table 6.4), which can be explained by the presence of Fe oxides inside the structure of the biochars (Mohan et al., 2007; 2015; Zhou et al., 2013; 2014; Han et al., 2015). The improvement of metal sorption by magnetic modification is thus related to the origin of the material (especially for Pb(II)), with the well-structured biochars being most suitable for these modifications (Mohan et al., 2007, 2015; Trakal et al., 2014a; Fig. 6.7). However, the sorption efficiency of Pb^{2+} in/on biochars with poorly developed structures changed little or was reduced

compared with that of the pristine biochars (Fig. 6.7). Metal sorption is not limited to the biochar surface (Trakal et al., 2014a), but also occurs in the biochar structure. This effect is more significant for Cd(II) than for Pb(II) because of the higher affinity of Cd(II) to sorb on Fe oxides (Adriano, 2001).

Table 6.4. Cadmium- and lead-removal efficiency of biochars before and after magnetic modification from selected studies (Trakal et al., 2016).

Biochar	Magnetic modification	Biochar sorption improvement by magnetic modification (%)		References
		Cd	Pb	
Oak bark	Fe ²⁺ /Fe ³⁺ SO ₄ solution	37.0	131	Mohan et al. (2007, 2015a)
Oak wood	Fe ²⁺ /Fe ³⁺ SO ₄ solution	676	287	Mohan et al. (2007, 2015a)
Bamboo	Fine sized ZVI of <850 μm	/	67.3	Zhou et al. (2013, 2014)
Pine bark	ferrite (CoFe ₂ O ₄)	152	/	Reddy et al. (2014)
Nut shell	FeSO ₄ ·7H ₂ O	997	461	Trakal et al. (2014a, 2016)
Wheat straw	FeSO ₄ ·7H ₂ O	218	14.0	Trakal et al. (2014a, 2016)
Grape stalk	FeSO ₄ ·7H ₂ O	121	-58.4	Trakal et al. (2014a, 2016)
Grape husk	FeSO ₄ ·7H ₂ O	316	14.3	Trakal et al. (2014a, 2016)
Plum stone	FeSO ₄ ·7H ₂ O	1592	741	Trakal et al. (2014a, 2016)
Palm oil empty fruit bunch	FeCl ₃	/	-25.7	Ruthiraan et al. (2015)
Energy cane biochar	Ferric sulphate (Fe ₂ (SO ₄) ₃ ·nH ₂ O)	/	-11.2	Mohan et al. (2015b)
Romchar (Harghita, Romania)	magnetite/maghemite	/	-50.5	Han et al. (2015)
Oxford Biochar Ltd. (Dorset, UK)	magnetite/maghemite	/	139	Han et al. (2015)
Rice hull	Fe(acac) ₃ + calcination	/	-50.3	Yan et al. (2015b)
Rice hull	Fe(acac) ₃ + calcination + ZnS	/	665	Yan et al. (2015b)

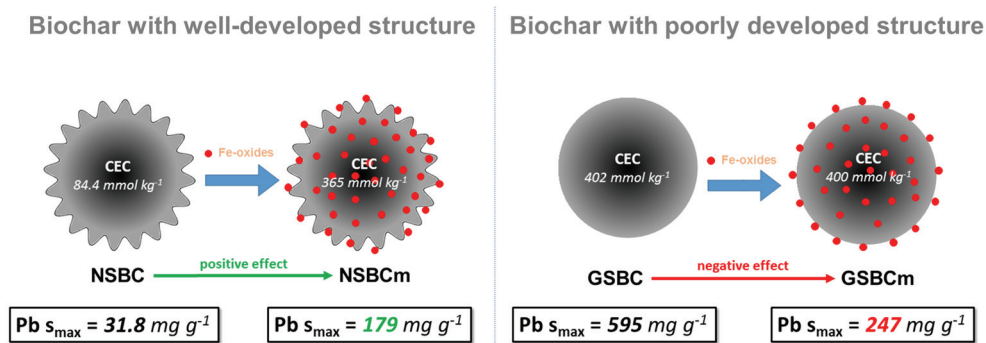


Fig. 6.7. Examples of magnetic modification on two contrasting biochars (Trakal et al., 2016).

The results of XPS analyses (Fig. 6.8) have confirmed similar Cd(II) and Pb(II) loadings for both surface and 10 nm depth against pristine biochars, where the amount of sorbed metals varied significantly between surface and subsurface (Trakal et al., 2014a). This could be explained through the attaching of Fe oxides to the biochar matrix when no clusters of these oxides appear on the surface of the biochar (Han et al., 2015). Fig. 6.8 shows that cation release and/or precipitation, represented by Pb–O binding (Xi et al., 2010), is the predominant sorption mechanism, whereas the confirmed presence of precipitated metal (hydro)carbonates were limited to the surface of pristine biochars only (Lu et al., 2012; Xu et al., 2013a,b; Trakal et al., 2014a). The slightly weak π -binding of metals with polyorganic chains demonstrated physical adsorption as a further sorption mechanism. However, this metal-sorption mechanism was suppressed at the expense of chemisorption (in comparison to the pristine biochar), mainly caused by the presence of Fe oxides in the structure of the magnetic biochars (Mohan et al., 2015). Finally, the observation of metal chelates not only on the biochar surface, but also within the interior, is in agreement with the study of Lu et al. (2012), where the magnetic modification usually enhanced the overall complexation sorption mechanism because of the presence of Fe oxides in the structure of the tested biochars.

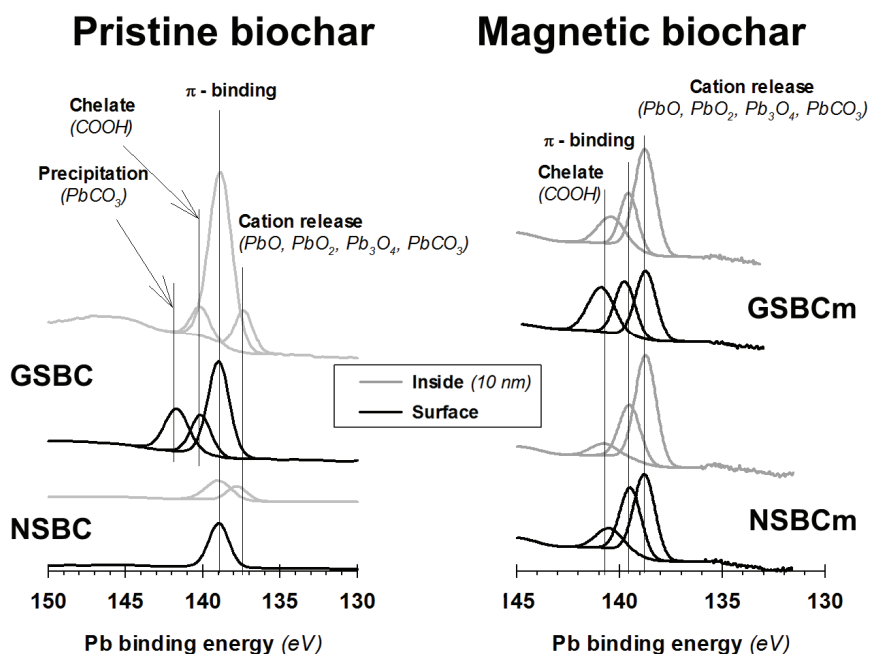


Fig. 6.8. XPS analyses of metal-loaded biochars (deconvolution of XPS bands for various Pb binding energies); GSBC - grape stalks (poorly developed) biochar; NSBC - nut shields (well-developed) biochar before and after magnetic impregnation (Trakal et al., 2016).

Nano zero-valent iron modification

Nano zero-valent iron (nZVI) has been shown to be a highly effective sorbent for various inorganic and organic contaminants in aqueous solutions. A typical core-shell structure of nZVI plays a key role in this process with Fe^0 core as a donor of electrons, offering strong reduction capability, and Fe (hydr)oxide shell (formed from the Fe^0 oxidation), allowing electron transfer that is responsible for adsorption of various contaminants (Li and Zhang, 2007; O'Carroll et al., 2013; Tosco et al., 2014; Stefaniuk et al., 2016). The nZVI particles are remarkable for their large specific surface area, high reduction capacity, low operational costs, and simple subsequent separation due to magnetic properties. On the other hand, nZVI particles have a tendency to aggregate, which decreases their specific surface area and thus their reactivity, mobility, and reduction capacity (Devi and Saroha, 2014; Tosco et al., 2014; Stefaniuk et al., 2016). When applied to soils, the high reactivity of nZVI particles could have a negative impact on soil properties, and the presence of several metal(loid)s could limit the immobilization of nZVI (Gil-Díaz et al., 2014; Su et al., 2016; Gil-Díaz et al., 2017; Vítková et al., 2017). The combination of biochar with Fe nanoparticles may give the

resulting biosorbent unique properties beneficial for selective sorption as well as for the stability of the nano-sized amendments in soils and waters (Tan et al., 2016a; Dong et al., 2017).

The nZVI-biochar composite can be produced by different synthesis methods. Generally, there are two approaches: (1) pre-coating of biomass with nZVI particles before pyrolysis and (2) biomass pyrolysis followed by impregnation of biochar with nZVI particles (Tan et al., 2016a) (Fig. 6.9). In either case, the whole synthesis needs to be conducted in an inert atmosphere to avoid O₂ dissolution during preparation (Yan et al., 2015b). The synthesis of the biochar (matrix) with functional nanomaterials can provide a unique combination of the advantages of both materials and should represent an ideal synthesis with nZVI due to: (1) better cost efficiency compared to conventional amendments, nontoxicity, and local availability of biochar; (2) ability to disperse the nanoparticles and thus enhance their stability; and (3) increasing number of oxygen-containing functional groups, an improvement in pore properties, surface active sites, and catalytic degradation ability when combined with nZVI (Figure 6.9). Therefore, this composite should exhibit an excellent ability to remove a wide range of contaminants (e.g., metals, organochlorine, or nitroaromatic compounds) from aqueous solutions, exerting simultaneous adsorption and catalytic degradation function (Peng et al., 2017; Tan et al., 2016a). Improved magnetic properties of the resulting material should allow the effective separation of the composite together with the adsorbed contaminants from the treated matrix (Trakal et al., 2016; Wang et al., 2017). Although magnetic modification may decrease the active BET surface (see Section *Magnetic Impregnation*) due to the formation of secondary iron (hydro)oxides on the surface of biochar, some metals (Cd; Trakal et al., 2016) or metalloids (As; Wang et al., 2015a) can be adsorbed more efficiently on the surface of these precipitated (hydro)oxides.

Impregnation of biochars with nZVI prevents early and excessive reaction of the nanoparticles, but allows them to use their original functionality (reduction and sorption) later in contact with aqueous solutions (Devi and Saroha, 2014; Dong et al., 2017; Peng et al., 2017). A distinct disadvantage of pristine biochars are their low efficiency for anion sorption (e.g., As) and complicated subsequent separation from the treated medium, which limits their applicability for soil and water remediation. The drawbacks of nZVI and biochar thus can be addressed by appropriate modifications. In particular, biochar supported by nZVI results in the increased stability of nZVI and improves sorption efficiency and magnetic properties of the final material. Several recent studies have reported the use of nZVI-BC composite for efficient removal of As, Cr, or organic contaminants and others from (waste)waters or aqueous solutions (Dong

et al., 2017; Peng et al., 2017; Wang et al., 2017); in particular, arsenate (Zhou et al., 2014; Wang et al., 2016a, 2017), hexavalent chromium (Zhou et al., 2014; Dong et al., 2017; Qian et al., 2017), lead (Zhou et al., 2014), pentachlorophenol and trichloroethylene (Devi and Saroha, 2014; Yan et al., 2015b; Li et al., 2017), and bromate (Wu et al., 2013). However, studies dealing with nZVI-modified biochar in soil environments are scarce (Su et al., 2016).

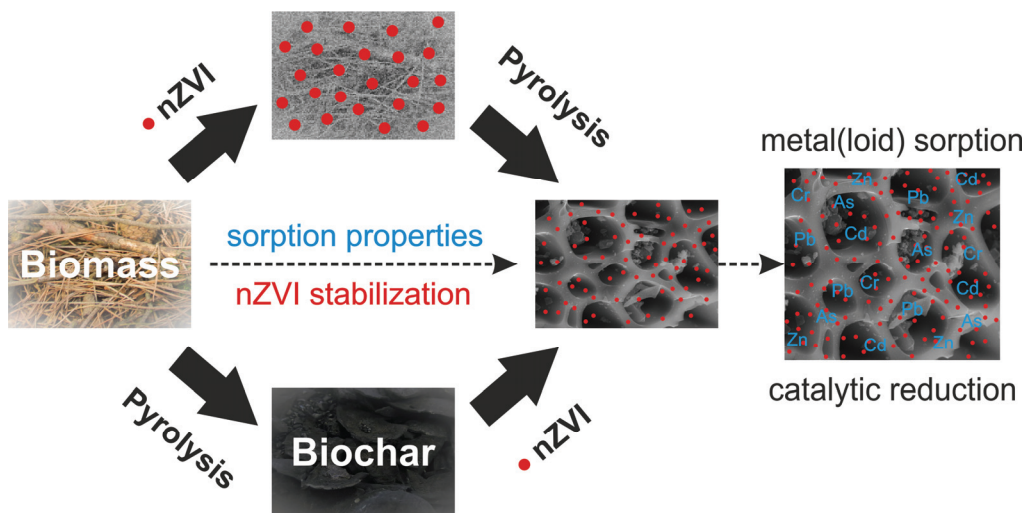


Fig. 6.9. Schematic of synthesis of the nano zero-valent iron and biochar composite and its improved functions.

Layered double-hydroxide modification

Although biochars have shown high sorption efficiency for various metal cations, their usability in waters and soils contaminated by anions, for example, arsenate, phosphate, or chromate, is limited (Wan et al., 2017). Therefore, it is necessary to provide sufficient surface modification of pristine biochars using highly effective sorbents such as layered double hydroxides (LDHs), if simultaneous sorption of cations and anions is to be achieved. Previously, LDHs have shown high sorption efficiencies for various inorganic species, for example, arsenate (Hudcová et al., 2017), arsenite (Jiang et al., 2015), chromate (Zhang et al., 2012b), phosphate (Drenkova-Tuhtan et al., 2013), sulfate (Sephehr et al., 2014) as well as metal cations (Hudcová et al., 2018). In general, anion- sorption mechanisms using LDHs are mainly influenced by surface complexation, and/or anion exchange (Hudcová et al., 2017), while metals are predominantly immobilized by surface-induced precipitation, surface complexation, and/or cation exchange (Hudcová et al., 2018). Despite excellent sorption properties of

LDHs, they have some drawbacks; aside from their relatively high cost, their stability in acidic conditions is greatly reduced. However, this could be improved by their immobilization on biochar surfaces but data are scarce as the use of LDH/biochar composites is a new topic with fewer than 15 peer-reviewed articles existing, dealing mainly with phosphate (Li et al., 2016; Wan et al., 2017; Zhang et al., 2013c; Zhang et al., 2014), arsenate (Wang et al., 2016b; Wang et al., 2016c), organics (Tan et al., 2016b; Tan et al., 2016c), nitrate (Xue et al., 2016), and metal cations (Wang et al., 2018a; Wang et al., 2018b) (ad)sorption.

Synthesis of LDH/biochar composites

LDH/biochar composites can be synthesized before or after pyrolysis. The prepyrolysis procedure consists of LDH coprecipitation on the biomass surface and subsequent pyrolysis for 2 hours at approx. 500-600°C (Tan et al., 2016b; Tan et al., 2016c; Wang et al., 2016b; Wang et al., 2016c). Alternatively, LDH precoated biomass can be also hydrothermally treated, resulting in the production of LDH/hydrochar composites (Zhang et al., 2014). The postpyrolysis procedure, which is more widely used, consists of pyrolysis of pristine biomass at conditions mentioned above and subsequent coprecipitation of LDHs on the biochar surfaces (Li et al., 2016; Wan et al., 2017; Wang et al., 2016b; Wang et al., 2016c; Wang et al., 2018a; Wang et al., 2018b; Xue et al., 2016; Zhang et al., 2013c). The synthesis prepyrolysis procedure strongly influences the specific surface area of final LDH/biochar composites, namely resulting in a decrease of the specific surface area (nearly twofold), in a higher amount of nonreacted metal species, and in a lower As(V) adsorption capacity compared to postpyrolysis products (Wang et al., 2016b; Wang et al., 2016c). In general, LDH/biochar composites exhibit a lower specific surface area compared to pristine biochar caused by filling/clogging of pores after the modification procedure, which also results in a notably rougher surface of LDH/biochar composites (Wan et al., 2017; Xue et al., 2016).

To demonstrate the structure of LDH/biochar composites, diffractograms of pristine woody biochar, Mg-Fe LDH (molar ratio Mg/Fe = 4) and Mg-Fe LDH/biochar composites are shown in Fig. 6.10A and the SEM image of LDH/biochar composites are shown in Fig. 6.10B. Diffractograms of pristine biochar (with minor phases corresponding to carbonates and/or silicates); pristine LDHs (with characteristic peaks of given intensities); and LDH/biochar composites confirmed the structure of individual materials and the successful synthesis of LDH/biochar composites. The SEM images demonstrated nonhomogeneous distribution of LDH particles on the biochar surface probably caused by the coprecipitation synthesis procedure of LDHs.

The morphology of these LDH particles corresponded to pristine LDHs as described in previous studies (Hudcová et al., 2017, 2018). LDHs were also successfully impregnated on the whole biochar surface, as confirmed by the EDX results, suggesting a high affinity of LDHs with the biochar surface that could positively influence stability/sorption properties of LDH/biochar composites.

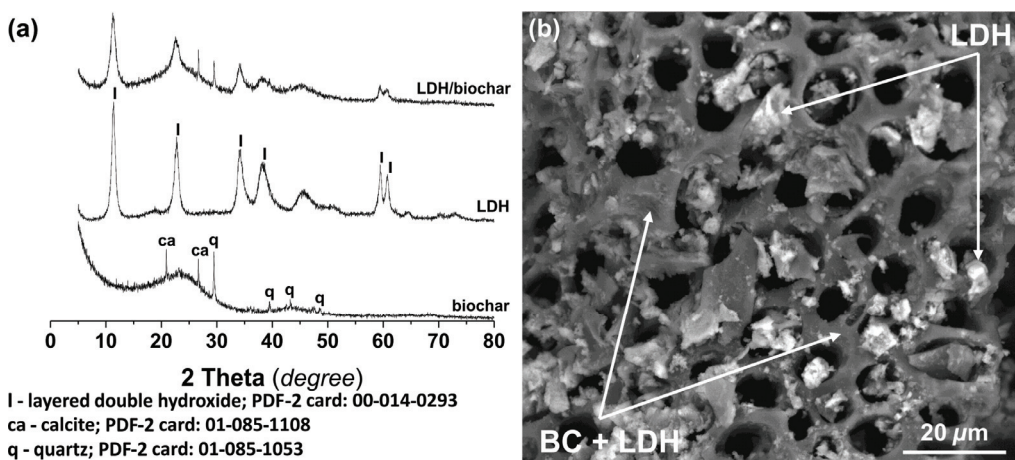


Fig. 6.10. Diffractograms of pristine woody biochar, Mg-Fe LDH and Mg-Fe LDH/biochar composites (A) and the SEM image of Mg-Fe LDH/biochar composites (B). LDH, layered double hydroxides; SEM, scanning electron microscopy.

Adsorption properties of LDH/biochar composites

Adsorption properties of LDH/biochar composites are strongly influenced by the presence of LDHs on the biochar surface. The adsorbed amounts of different inorganic species by various LDH/biochar composites are given in Table 6.5. In general, LDH/biochar composites appeared to be more effective materials for phosphate removal compared to pristine biochar, modified biochar, and many other conventional adsorbents (Li et al., 2016; Wan et al., 2017; Zhang et al., 2013a-c, 2014). The LDH/biochar composites showed even higher adsorbed amounts of phosphate compared to pristine LDHs (adsorption rate per unit weight) suggesting a synergistic effect between biochars and LDHs (Wan et al., 2017), with biochars providing an effective matrix for LDHs that increases accessibility of active adsorption sites (Zhang et al., 2013c). Adsorption mechanism of phosphate using LDH/biochar composites include surface complexation and anion exchange with interlayered anions in the structure of LDHs. At higher initial phosphate concentration precipitation with released bivalent metal cations from the surface/structure of LDHs was also observed (Li et al., 2016; Wan et al., 2017; Zhang et al., 2013c). In the case of arsenate adsorption, LDHs

significantly improved the adsorption properties compared to pristine biochars and some other pristine LDHs. Nevertheless, arsenate-adsorption is greatly influenced by the pyrolysis procedure, exhibiting significantly higher adsorbed amounts using post-pyrolysis LDH/biochar composites. The arsenate-adsorption mechanism follows the same processes as described by phosphate adsorption, except for precipitation. However, the dominant mechanism differs for prepyrolysis (physical adsorption) and postpyrolysis (chemical adsorption/anion exchange) LDH/biochar composites (Wang et al., 2016b,c). Nitrate adsorption was also significantly improved using LDH/biochar composites compared to some biochars and activated carbon. Higher selectivity for nitrate in multianion solutions containing sulfate and phosphate was also observed. The whole adsorption mechanism follows the same processes as noted for phosphate adsorption except for precipitation (Xue et al., 2016). LDH/biochar composites were found to be more effective copper and lead sorbents compared to some biochars, modified biochars, activated carbons, and other conventional sorbents. The dominant sorption mechanism has been shown to be surface precipitation caused by the buffering effect of LDH/biochar composites and the formation of chelation complexes in the case of ethylenediaminetetraacetic acid (EDTA) functionalized LDHs. Even so, the cation exchange of bivalent metal cations in the structure of LDHs by copper was also observed (Wang et al., 2018a,b).

Table 6.5. The adsorbed amounts of inorganic species using LDH/biochar composite

Biomass type	LDH type	Adsorbate	$q_{\text{MAX}} (mg g^{-1})^a$	Reference
Bamboo	Mg-Al	phosphate	172	Wan et al. (2017)
Sugarcane leaves	Mg-Al	phosphate	82	Li et al. (2016)
Cottonwood	Mg-Al	phosphate	410	Zhang et al. (2013c)
Cottonwood	Mg-Al	phosphate	386	Zhang et al. (2014)
<i>Pinus taeda</i>	Ni-Fe	arsenate	4.4	Wang et al. (2016b)
<i>Pinus taeda</i>	Ni-Fe ^b	arsenate	1.6	Wang et al. (2016b)
<i>Pinus taeda</i>	Ni-Mn	arsenate	6.5	Wang et al. (2016c)
<i>Pinus taeda</i>	Ni-Mn ^b	arsenate	0.6	Wang et al. (2016c)
Wheat straw	Mg-Fe	nitrate	25	Xue et al. (2016)
<i>Camellia oleifera</i>	Mn-Al	copper	74	Wang et al. (2018a)
Leaves ^a	Mg-Al	lead	147	Wang et al. (2018b)

^aAdsorbed amount (Langmuir model); ^bPrepyrolysis synthesis of LDH; ^cNonspecified leaves. LDH, layered double hydroxides.

To demonstrate arsenate-adsorption efficiency, the As(V) adsorption kinetics using pristine woody biochar, pristine Mg-Fe LDHs, and Mg-Fe LDH/biochar composites at controlled pH 5.5 (As(V) initial concentration of 1mM) is given in Fig. 6.11. As previously mentioned, pristine biochar showed a very low As(V) adsorption efficiency (3.1%) compared to highly effective Mg-Fe LDHs (100%) and Mg-Fe LDH/biochar composites (100%). It is worth nothing that Mg-Fe LDH/biochar composites contained only approximately 40% of LDHs on the surface/in the structure compared to pristine LDHs, suggesting a high efficiency of such composites for arsenate removal. In summary, LDH/biochar composites are efficient sorbents, but further studies focused on the stability of LDH/biochar composites at different conditions, detailed mechanistic/modelling approaches, and alternative LDH synthesis procedures to make their production more economical, are needed.

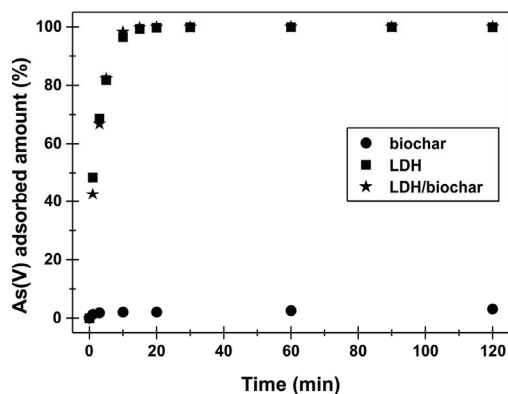


Fig. 6.11. As(V) adsorption kinetics using pristine woody biochar, Mg-Fe LDHs, and Mg-Fe LDH/biochar composites at controlled pH 5.5. LDH, layered double hydroxide.

Manganese oxide coating

Mn oxides have also been demonstrated to have very high immobilization potential for divalent metals through adsorption processes onto amphoteric surface groups of the Mn oxide, and also metalloids oxyanions due to the initial oxidation/reduction process and consequent sorption, surface complexation, and/or coprecipitation with birnessite and hydrous manganese oxide (Lenoble et al., 2004; Komárek et al., 2013). Among the various types of Mn oxides the modified sol-gel procedure of Ching et al. (1997) was used for the preparation of amorphous manganese oxide (AMO; Della Puppa et al., 2013). The AMO has previously been established as a very suitable sorbent for various metal(loid)s, but associated dissolution of AMO has resulted in excessive Mn leaching, limiting its applicability to remediation scenarios due to, amongst other concerns, Mn phytotoxicity (see Della Puppa et al., 2013; Michálková et al., 2014; Ettler et al., 2015). AMO-modified biochar, combining the advantageous properties of both AMO and pristine biochar with decreased Mn leaching and thus improved sorbent longevity, appears to be an ideal biosorbent for multimetal(loid)-contaminated wastewater

treating. Preparation of AMOchar composite involves biochar impregnated by AMO (Della Puppa et al., 2013), with the biochar added directly into the reaction mixture of 0.4 M KMnO_4 solution with 1.4 M glucose solution.

XRD analysis (Fig. 6.12B) of the AMOchar confirmed its amorphous character, where all peaks were represented by Mn-oxalate hydrate and by carbon showing the presence of the biochar skeleton. The presence of rhodochrosite was confirmed, which has been explained by Ettler et al. (2014) as a reaction of the removed Mn from oxalates of the AMO with atmospheric CO_2 . Consequently, such leached Mn could react with CO_3^{2-} groups sorbed at the surface of biochar, originating from meaningful CO_2 sorption (Xu et al., 2016) during synthesis under atmospheric conditions. Fig. 6.12 shows the structure and surface morphology of AMOchar where the AMO with Mn-oxalates coating the surface of the pristine biochar, even though porous biochar fragments associated with irregular AMO clusters, were also observed. The attraction of the AMO on the surface of pristine biochar was confirmed by deconvolution of Mn bond at binding energy 641.84 eV, which is here responsible for Mn–C_{org} bond. The pH value of the AMOchar composite was alkaline and showed a theoretically positively charged surface. The CEC the composite was similar and/or even higher than that of pure AMO (Trakal et al., 2018).

In terms of metal(loid)s removal from solution (Fig. 6.13), AMOchar was able to remove (up to 99%, 51%, and 91% of dissolved Pb(II), Cd(II), and As(V), respectively, in comparison to pristine biochar where the removal rate was limited. The leaching of Mn a during metal(loid)s sorption from the AMOchar composite was significantly reduced in comparison to the pure AMO. This demonstrates that total Mn content in AMOchar composite was lower compared to the AMO (without any limitation to metal sorption) and/or stabilization had occurred in the Mn-oxalates on the structure of AMOchar. In addition, the AMOchar composite has also been tested using a dynamic test when the cumulative leachate of As(V) from CCA (chromate-copper-arsenate) ash was significantly reduced (by sixfold compared to untreated variant after 100 minutes of intensive leaching; see the study of Trakal et al., 2018). Ongoing testing of AMOchar mixed into a variety of metal(loid) contaminated soils confirms reductions in leaching of metal(loid)s but continued instability of Mn; further refinements to the synthesis methods will be required to achieve a material with sorptive longevity.

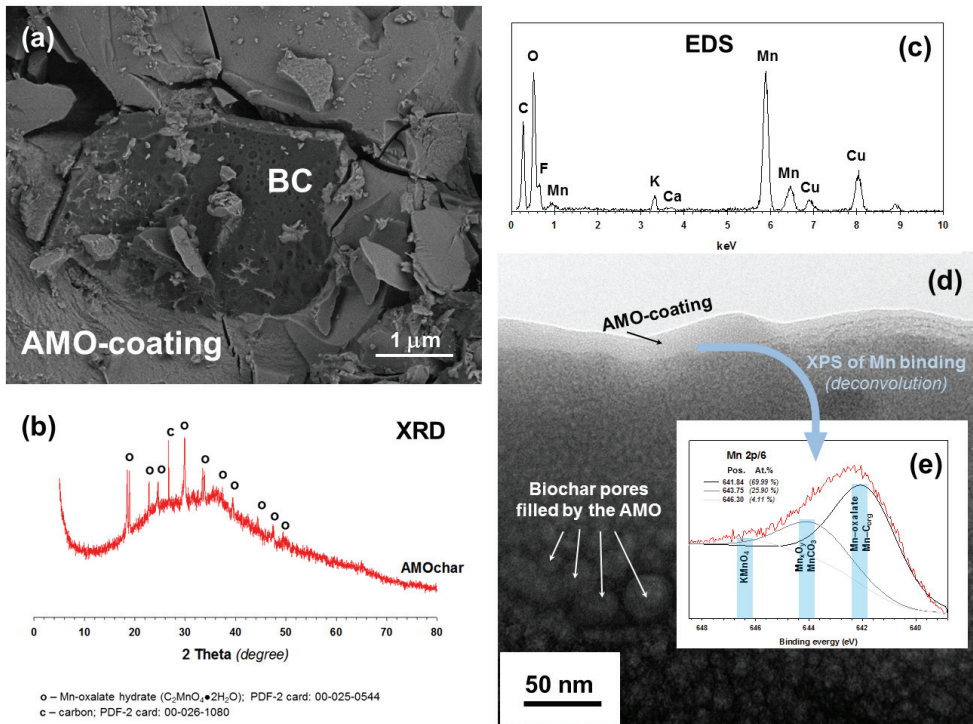


Fig. 6.12. (A) High resolution SEM of AMOchar, (B) XRD patterns, (C) energy-dispersive X-ray spectroscopy (EDS) spectra where peaks of Cu originate from the transmission electron microscopy (TEM) metal grid, (D) TEM cross-section of the AMO coating, and (E) XPS of Mn binding and the bond deconvolution of the AMOchar before sorption (Trakal et al., 2018). *SEM*, scanning electron microscopy; *XRD*, X-ray diffraction; *AMO*, amorphous manganese oxide.

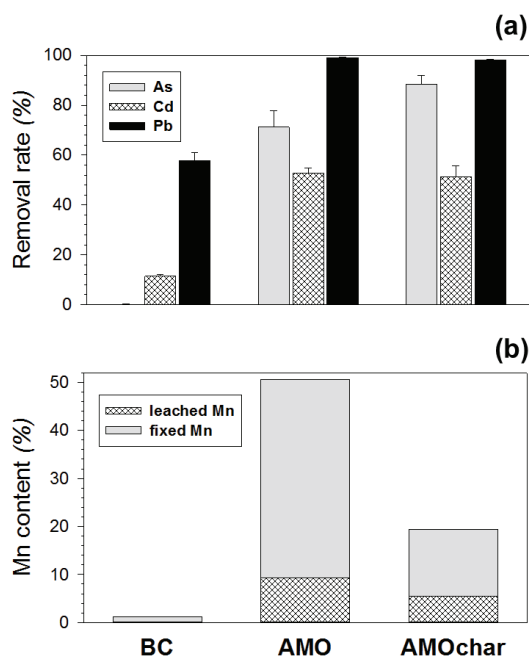


Fig. 6.13. (A) Maximum removal efficiency of As, Cd and Pb (obtained from kinetic experiment at equilibrium state; data in triplicates are presented as means \pm SD; and Mn leaching of pristine biochar, pure AMO and AMOchar; Trakal et al., 2018). *AMO*, amorphous manganese oxide.

Engineering application of modified biochars

The reutilization of agrowastes for biochar production appears to be environmentally friendly technique for metal-removal from aqueous solutions, e.g., industrial wastewaters or mine drainage (Lu et al., 2012; Zhang et al., 2013a). For that to be fully realised these materials need to be proven safe, efficient, and cost effective for environmental applications. Though the removal capacity for various metals (e.g., Cd vs Pb) was different for each tested biochar, in general those biochars with well-developed structures (reflected by high BET surface) removed lower quantities of metals in comparison to biochars with poorly developed structures, where sorbed metals are very strongly bound. By contrast, while the biochars with well-developed structure were found to be less effective for the metal sorption they proved more suitable for removal of organic pollutants (e.g., phenol; Han et al., 2013), mainly due to their high BET surface. Biochars with high BET surface are potentially more suitable for consequent modifications (impregnations) mainly due to “sufficient space” for the impregnation, thus resulting in the production of sorbents efficient both for organic and inorganic contaminant removal from waters and soils.

As has been discussed, chemical activation using various alkali solutions (e.g., 2 M KOH) can improve biochar structure by releasing tar particles, especially from micropores. This improvement could be applicable when the BET surface needs to be enlarged (e.g., for more efficient magnetic impregnation and more efficient biochars with well-developed structure).

Magnetic modification of biochar can improve sorption efficiency even for those biochars with well-developed structures. From a technological point of view, such magnetically modified biochars are generally ferromagnetic and therefore can be recovered more easily from contaminated waters after a filtration process using a magnet (Zhou et al., 2014). This property is highly desirable for the convenient recycling of contaminant-laden magnetic biochar adsorbents when their useful life is expended. Overall, the magnetic impregnation significantly

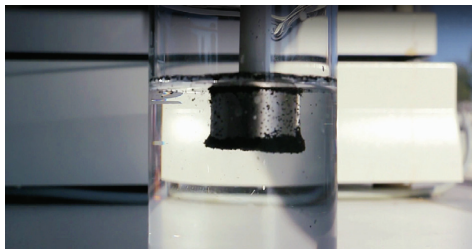


Fig. 6.14. Separation of magnetic biochar (from nut shields) previously loaded by Pb(II).

affected various biochar characteristics as well as its metal-sorption efficiency. Trakal et al. (2016) has demonstrated that the magnetic biochar could (1) sufficiently remove Cd(II) and Pb(II) and (2) be easily separated from the solution with a magnet (Fig. 6.14).

Although biochar modified by Mn oxides does not provide a ferromagnetic material, the AMOchar represents a very efficient and complex biosorbent for treatment of multimetal(loid)s contaminated waters at various pH. Usually, pristine biochars are suitable for selective sorption of particular bivalent metals as well as for multimetal loading, mainly due to their overall basic pH and negatively charged active surface (Mohan et al., 2014b). However, when different bivalent metals are sorbed to the same biochar the sorption efficiency of some metals (e.g., Cd(II) or Zn(II)) can be diminished by the sorption of metals with high affinity to organic matter (e.g., Pb(II) or Cu(II); Trakal et al., 2012, 2014a). Additionally, the efficiency of the pristine biochars to sorb oxyanions (e.g., As(V) or Cr(VI)) is usually limited, especially under alkaline conditions when such oxyanions are very mobile. In order to ensure complexity of this material to sorb various metal(loid)s as well as to ensure its universality (adsorbent that is effective under a wide range of pH and/or Eh conditions), the coating of biochar by Mn oxides represents a step forward for the treatment of waters contaminated with bivalent metals (Cd(II), Pb(II), Zn(II), etc.) and oxyanions (e.g., As(V) or Cr(VI)). Another practical advantage of this composite lies in the sole use waste materials; for example, biochar can be produced from waste biomass (prunings, off-cuts, etc.), while AMO can be produced from other organic waste materials (e.g., molasses from sugar factories) reacting with potassium permanganate. In comparison to the pure AMO, AMOchar composite represents an equally efficient sorbent with reduced Mn leaching. When improvements are made to the synthesis to further stabilize Mn the resulting biosorbent appears applicable to a wide range of environmental remediation scenarios.

Chapter VII

Summary

The first part of the thesis evaluated the (ad)sorption mechanism of As(V), Sb(V), Pb(II) and Zn(II) onto Mg-Fe LDHs in aqueous solutions using the surface complexation modeling (SCM) coupled with various solid-state analyses (XRD, SEM/EDX, HR-TEM with elemental mapping, FTIR-ATR, XPS, low-temperature ^{57}Fe Mössbauer spectroscopy). Firstly, Mg-Fe LDHs at different Mg/Fe molar ratios were synthesized by the co-precipitation method described by Seida et al. (2001) and basic characterization was provided (the structure, the morphology, the specific surface area etc.). Afterwards, the (ad)sorption rate of selected metals and metalloids onto Mg-Fe LDHs was studied by kinetic experiments fitted by pseudo-first and pseudo-second order kinetics. The basic (ad)sorption properties (e.g., adsorption capacity or affinity) were evaluated by equilibrium experiments fitted by Langmuir and Freundlich model. Moreover, the influence of different Mg/Fe molar ratios and pH values on the (ad)sorption properties of Mg-Fe LDHs were discussed. The effect of different pH values and ionic strengths was further described by the diffuse layer model (DLM) and the possible formation of monodentate and bidentate complexes was described in detail. After complex characterization of Mg-Fe LDHs, mixed oxides (CLDHs) were synthesized and basic (ad)sorption mechanism of these materials was also evaluated by adsorption kinetics and isotherms coupled with solid-state analyses (XRD, SEM/EDX and XPS). The behavior of Mg-Fe LDHs and CLDHs was further tested in real soil solutions and soils contaminated by As(V), Pb(II) and Zn(II) to evaluate the potential of these materials as stabilizing amendments in remediation technologies. Firstly, stability testing of Mg-Fe LDHs and CLDHs using deionized water and real soil solutions contaminated with As(V), Pb(II) and Zn(II) was performed. Afterwards, the influence of pH on the leaching of metals and metalloids from amended soils and the stability/stabilizing efficiency of materials in real contaminated soils were presented by the results of pH-static leaching experiments and incubation tests. The (ad)sorption mechanisms and phase transformations of Mg-Fe LDHs and CLDHs in soils were investigated using a combination of solid-state analyses and geochemical modeling. Although Mg-Fe LDHs and CLDHs have shown high stabilizing efficiency in aqueous solutions as well as in soils, drawbacks connected to the application of these materials in soils were also discussed in detail. To eliminate these negative effects, the synthesis of LDH/biochar composites was also introduced. The results of this thesis showed Mg-Fe LDHs and CLDHs as effective materials for metal and metalloid stabilization in aqueous solutions as well as in the real contaminated soils. Nevertheless, potential drawback needs to be minimalized or eliminated. The main conclusions of the proposed thesis will be further described in this chapter. Besides the specific Mg-Fe LDH and CLDH characteristics, a general approach to test a new stabilizing material to evaluate all important (ad)sorption characteristics and stability in aqueous solutions and soils

was presented in this thesis and the scheme of individual steps is given in Fig. 7.1. A presented approach should be used for newly synthesized materials to evaluate their potential as stabilizing amendment.

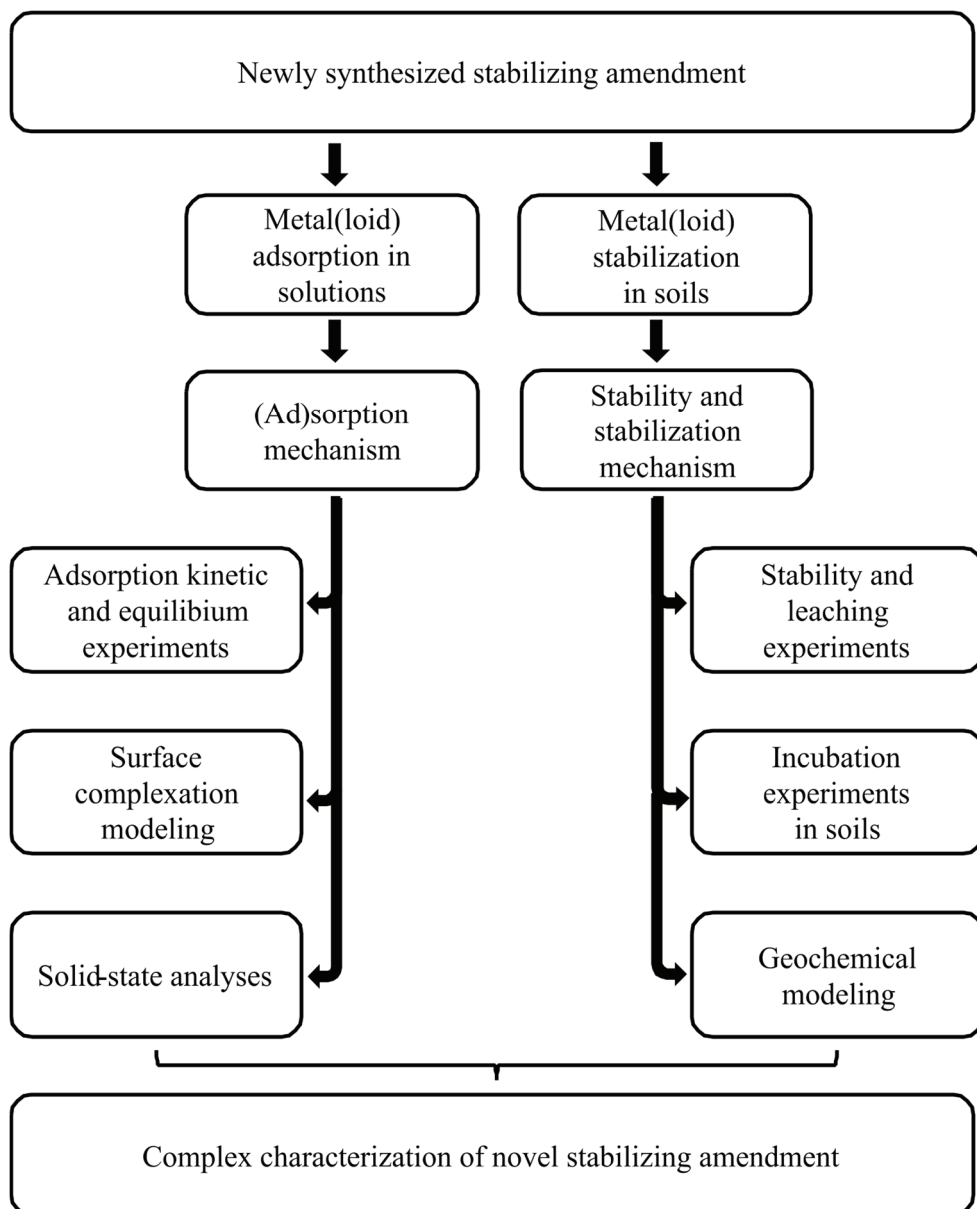


Fig. 7.1. Individual steps of novel amendment characterization.

The basic characteristics of synthesized materials are summarized in Table 7.1. The Mg-Fe LDHs were prepared by the co-precipitation method which is the oldest and most common LDH synthesis procedure. The biggest advantage of this method is a simple operation procedure; nevertheless, the properties of final products strongly depends on the experimental conditions. The final characteristics, e.g., specific surface area, M(II)/M(III) molar ratio and/or pH_{PZC} , significantly influence the (ad)sorption potential of individual materials (Chubar et al., 2017). To this date, most of the (ad)sorption studies were performed with Al-based LDHs which could have a potential drawback of Al(III) leaching from the LDH structure at low pH values (Bocclair and Braterman, 1999; Jobbágy and Regazzoni, 2011). Typically, the specific surface area of Mg-Fe LDHs occurs under $100 \text{ m}^2 \text{ g}^{-1}$ (Das et al., 2007; Kang et al., 2013; Kovanda et al., 2003; Vulic et al., 2012). Nevertheless, the value also depends on the Mg:Fe molar ratios of individual materials. Based on the XRD results, the increasing intensity of all reflections and cell parameters for LDHs with higher Mg:Fe molar ratios was observed that was corresponded to the increasing crystallinity. The increasing crystallinity means the decrease of the specific surface area (Kang et al., 2013; Seida and Nakano, 2000). Contrarily, the thermal treatment of LDHs, i.e., the formation of CLDHs, results in the increase of the specific surface area. This effect is attributed to the changes of the structural arrangements, i.e., the crystalline LDHs change to amorphous CLDHs (Kang et al., 2013). However, the further increase of the temperature leads to the formation of more crystalline material that was observed by the increasing intensity of individual peaks in the XRD diffractograms resulting in the decrease of the specific surface area. Moreover, spinel formation, which results into a further decrease of the specific surface area was observed (Hájek et al., 2017; Kovanda et al., 2003; Millange et al., 2000). Compared to LDHs, the porous structure was significantly developed during the thermal treatment caused by the structural changes, i.e., layer destruction (Zhang, 2012c). Moreover, all materials showed high pH values in water as well as high values of pH_{PZC} corresponding to a buffering effect of all materials as well as preferable positive charge on their surface (Zhang and Hou, 2007). All these characteristics influence the (ad)sorption efficiency of individual materials that is further described in detail. In the literature, the higher (ad)sorption efficiency of metals and metalloids is often assigned to a higher specific surface area (Peng et al., 2014). However, the results of this thesis showed that Mg-Fe LDHs with lower specific surface area (i.e., with higher molar Mg:Fe ratios) were more effective for metal and metalloid (ad)sorption. A higher (ad)sorption efficiency of LDHs and CLDHs with higher molar ratio towards As(V) has been presented by Kang et al. (2013). Contrarily, the effect of the molar ratios on the metal (ad)sorption onto LDHs and CLDHs has not been presented yet. In the case of thermally treated LDHs, a significant improvement

of (ad)sorption properties was corresponded to a higher specific surface area (Peng et al., 2014) as well as other structural characteristics of individual materials (Kang et al., 2013).

Table 7.1 Basic characteristics of the studied Mg-Fe LDHs and CLDHs.

Material	Mg:Fe molar ratio	Thermal treatment (°C)	S _{BET} (m ² g ⁻¹)	pH _{PZC}
LDH-2	2.4:1	-	71.2	9
LDH-3	3.5:1	-	50.6	10
LDH-4	4.6:1	-	40.1	10
CLDH-450	4.6:1	450	112	12.5
CLDH-550	4.6:1	550	92.8	12.5

The (ad)sorption capacities of Mg-Fe LDHs (Mg/Fe = 4:1) towards As(V) and Sb(V) were compared with the results from literature (Table 7.2). The (ad)sorption capacity of studied Mg-Fe LDHs showed comparable values to other studies focused on LDHs (Table 7.2); however, the (ad)sorption capacity is significantly affected by the LDH type, i.e., different composition of layers (divalent and trivalent metal cations) and interlayer region (anions). Moreover, differences between the same LDH types were also observed. In general, the (ad)sorption capacity of LDHs towards As(V) and Sb(V) varies from 0.35 to 2.70 mmol g⁻¹ and 0.18 to 2.02 mmol g⁻¹, respectively. In general, most of the As(V) and Sb(V) (ad)sorption studies were performed with Al-based LDHs which could have a potential drawback of Al(III) from the LDH structure at low pH values as has been already mentioned (Boclair and Braterman, 1999; Jobbágy and Regazzoni, 2011). However, most of the studies were performed without pH adjustment resulting in different final pH values which makes the comparison between individual materials complicated. In general, As(V) and Sb(V) (ad)sorption decreases with increasing pH values caused by the changes of the charge on the surface of solid materials as pH increases, i.e., the surface becomes less positively charged (Dzombak and Morel, 1990; Vithanage et al., 2013). Based on the different properties of individual LDHs, it is complicated to compare the effect of pH on the (ad)sorption capacity since the (ad)sorption capacity is also influenced by the properties of individual LDHs. Nevertheless, the proposed thesis presented As(V) and Sb(V) (ad)sorption on the same LDHs at controlled pH values. Based on these results, a significant decrease of the (ad)sorption capacity and (ad)sorption rate was observed at higher pH values. However, the rate coefficients describing Sb(V) (ad)sorption onto Mg-Fe LDHs were significantly lower that corresponded to the studies presented by Lee et al. (2018a, 2018b) and Lu et al. (2015). Moreover, the Sb(V) (ad)sorption showed higher pH-dependency compared to As(V) (ad)sorption that could be corresponded to the different

structural ordering of individual metalloids (Doušová et al., 2018). Compared to the literature, most of the As(V) and Sb(V) (ad)sorption studies were performed with Al-based LDHs as discussed above.

Table 7.2 (Ad)sorbed amounts of As(V) and Sb(V) onto various LDHs.

Metalloid	pH ^a	Type of anion	Sorption capacity (mmol g ⁻¹)	s/L (g L ⁻¹)	Literature
Mg-Al LDHs					
As(V)	7.0	CO ₃ ²⁻	0.44	1	Lazaridis et al. (2002)
	7.0	CO ₃ ²⁻	1.40	1	Kiso et al. (2005)
	6.0	CO ₃ ²⁻	1.30	-	Violante et al. (2009)
	7.0	Cl ⁻ /CO ₃ ²⁻	1.68	0.8	Huang et al. (2015)
	7.2	CO ₃ ²⁻ /NO ₃ ⁻	0.59	2.5	Yoshida et al. (2015)
	6.0 ^b	CO ₃ ²⁻	1.50	-	Caporale et al. (2011)
Zn-Fe LDHs					
As(V)	7.0	SO ₄ ²⁻	1.30	0.2	Lu et al. (2015)
Sb(V)	7.0	SO ₄ ²⁻	0.68	0.2	Lu et al. (2015)
Li-Al LDHs					
As(V)	5.0 ^b	Cl ⁻	0.32	1.3	Liu et al. (2006)
Mg-Fe LDHs					
As(V)	5.5 ^b	CO ₃ ²⁻	1.72	1	Hudcová et al. (2017)
	6.5 ^b	CO ₃ ²⁻	1.29	1	Hudcová et al. (2017)
	7.5 ^b	CO ₃ ²⁻	0.41	1	Hudcová et al. (2017)
	6.0 ^b	CO ₃ ²⁻	2.60	-	Caporale et al. (2011)
	7.2	CO ₃ ²⁻ /NO ₃ ⁻	0.35	2.5	Yoshida et al. (2015)
Sb(V)	5.5 ^b	CO ₃ ²⁻	0.55	1	Hudcová et al. (2019)
	6.5 ^b	CO ₃ ²⁻	0.18	1	Hudcová et al. (2019)
	7.5 ^b	CO ₃ ²⁻	0.09	1	Hudcová et al. (2019)
Zn-Al LDHs					
As(V)	8.99	SO ₄ ²⁻	2.70	10	Ardaş et al. (2013)
Sb(V)	5.4	SO ₄ ²⁻	2.02	10	Ardaş et al. (2016)
Mg-Al-Fe					
As(V)	8.0	Cl ⁻	1.20	10	Kameda et al. (2015)
Sb(V)	4.0	Cl ⁻	1.90	10	Kameda et al. (2015)

^a pH value at the beginning of the sorption experiment ^b pH controlled during the whole experiment

The (ad)sorption capacity of Mg-Fe CLDH thermally treated at 450°C towards As(V) showed only a minor increase compared to Mg-Fe LDHs (Table 7.3). However, the (ad)sorption capacity of Mg-Fe CLDH thermally treated at 550°C was significantly lower compared to the CLDH thermally treated at 450°C that could be corresponded to the changes of the structural arrangements mentioned above, i.e., by a lower specific surface area caused by the increasing crystallinity of the material treated at higher temperature. In the contrast to these results, significantly higher (ad)sorption capacities for CLDHs compared to pristine LDHs has been published due to a higher specific surface area (Peng et al., 2014). Nevertheless, a different study presented that the whole

structure of the material has a higher effect than just the value of the specific surface area. In that study, CLDHs thermally treated at different temperatures (400-500°C) provided nearly the same specific surface area; however, (ad)sorption capacities towards As(V) were different, i.e., higher for the material thermally treated at 400°C (Kang et al., 2013). Since Sb(V) (ad)sorption onto Mg-Fe CLDHs was not performed in this study, the results from the literature were compared. In general, the (ad)sorption capacities of CLDHs showed significantly higher values compared to pristine LDHs.

Table 7.3 (Ad)sorbed amounts of As(V) and Sb(V) onto various CLDHs.

Metal	pH ₀ ^a	Thermal treatment	Sorption capacity (mmol g ⁻¹)	s/L (g/L)	Literature
Mg-Al CLDHs					
As(V)	7.0	500°C	8.21	1	Lazaridis et al. (2002)
	7.0	450°C	1.33	1	Doušová et al. (2003)
	6.0	450°C	3.68	-	Violante et al. (2009)
Zn-Al CLDHs					
Sb(V)	5.4	450°C	4.54	2.5	Dore and Frau (2017)
Mg-Fe CLDHs					
As(V)	5.5 ^b	450°C	2.01	1	Hudcová et al. (2019)
	5.5 ^b	550°C	1.21	1	Hudcová et al. (2019)
	6.5	450°C	2.70	1	Carja et al. (2005)
	7.0	400°C	0.67	1	Kang et al. (2013)
	7.0	350°C	3.62	0.5	Peng et al. (2014)
Mg-Fe-Al CLDHs					
Sb(V)	5.4	450°C	4.37	2.5	Dore and Frau (2017)
Mg/Al CLDH-incorporated with polyethersulfone beads					
As(V)	7	400°C	0.10	0.5	Lee et al. (2018a)
Sb(V)	7	400°C	0.19	0.5	Lee et al. (2018a)
Mg-Al CLDHs- supported by magnetic nanoparticles					
As(V)	7	400°C	1.11	0.2	Lee et al. (2018b)
Sb(V)	7	400°C	1.49	0.2	Lee et al. (2018b)

^a pH value at the beginning of the sorption experiment ^b pH controlled during the whole experiment

The (ad)sorption capacities of Mg-Fe LDHs (Mg/Fe = 4:1) towards Pb(II) and Zn(II) were also compared with the results from literature (Table 7.4). In general, metal (ad)sorption studies using LDHs are limited compared to metalloids (Goh et al., 2008; Liang et al., 2013). The Mg-Fe LDHs presented in this thesis showed comparable (ad)sorption capacity to the published results; however, most of the studies were performed without the pH adjustment resulting in the precipitation of metal hydroxides and/or carbonates by the buffering effect of LDHs that further improved the measured immobilization capacity (González et al., 2015; Liang et al., 2013; Seida et al., 2001). Moreover, information about the final pH is also often missing in these (ad)sorption studies. The results in the proposed thesis showed that Pb(II) and Zn(II) (ad)sorption

rate without pH adjustment (the final pH reached approx. 9.5) was significantly higher compared to the controlled pH 5.5. The oversaturation of individual precipitates was further confirmed by modeling in Visual MINTEQ 3.1. In general, the metal (ad)sorption is also influenced by the LDH structure, i.e., the interlayer anions. For example, Fujji et al. (1992) and Komarneni et al. (1998) presented LDHs synthesized using the same procedure with a variation of interlayered anions presenting LDHs with CO_3^{2-} and Cl^- in the interlayer region as significantly more effective materials for metal (ad)sorption than LDHs intercalated by NO_3^- .

Table 7.4 (Ad)sorbed amounts of Pb(II) and Zn(II) onto various LDHs.

Metal	pH ₀ ^a	Type of anion	Sorption capacity (mmol g ⁻¹)	s/L (g L ⁻¹)	Literature
Mg-Al LDH					
Pb(II)	5.7	Cl ⁻	0.32	0.2	Zhao et al. (2011)
	6.0	Cl ⁻	0.53	2.5	Zhang and Hou (2007)
	5.0	CO ₃ ²⁻	0.96	10	Fujji et al. (1992)
	5.0	Cl ⁻	0.97	10	Fujji et al. (1992)
	5.0	NO ₃ ⁻	0.29	10	Fujji et al. (1992)
	5.0	Cl ⁻	0.63	1.7	González et al. (2015)
Zn(II)	4.7	CO ₃ ²⁻	4.76	2	Komarneni et al. (1998)
	4.7	NO ₃ ⁻	1.94	2	Komarneni et al. (1998)
	5.0	CO ₃ ²⁻	1.20	10	Fujji et al. (1992)
	5.0	Cl ⁻	1.02	10	Fujji et al. (1992)
	5.0	NO ₃ ⁻	0.67	10	Fujji et al. (1992)
Mg-Fe LDHs					
Pb(II)	5.5 ^b	CO ₃ ²⁻	1.65	1	Hudcová et al. (2018)
	4.5	Cl ⁻	2.03	1	Liang et al. (2009)
Zn(II)	5.5 ^b	CO ₃ ²⁻	1.44	1	Hudcová et al. (2018)

^a pH value at the beginning of the sorption experiment ^b pH controlled during the whole experiment

The (ad)sorption capacity of Mg-Fe CLDH thermally treated at 450 °C towards Zn(II) increased compared to Mg-Fe LDHs (Table 7.5). Contrarily, a minor increase was observed for Pb(II). Similarly, to As(V) (ad)sorption, Mg-Fe CLDH thermally treated at 550 °C showed significantly lower (ad)sorption capacities compared to pristine LDHs and CLDHs thermally treated at lower temperature. Nevertheless, the differences were not as significant as has been presented in the literature. For example, Sun et al. (2015a) presented that (ad)sorption capacities of CLDHs towards Zn(II) were significantly higher compared to untreated LDHs. The different (ad)sorption capacities were assigned to a higher specific surface area that means more active sites for metal cations (ad)sorption. However, studies dealing with Pb(II) and Zn(II) (ad)sorption onto CLDHs are even more limited than in the case of LDHs and; moreover, the results from the literature were also provided without pH adjustment as for As(V) (ad)sorption.

Table 7.5 (Ad)sorbed amounts of Pb(II) and Zn(II) onto various CLDHs.

Metal	pH ^{0a}	Thermal treatment	Sorption capacity (mmol g ⁻¹)	s/L (g L ⁻¹)	Literature
Mg-Al CLDHs					
Zn(II)	2.1	450°C	7.54	0.5	Sun et al. (2015a)
	2.1	450°C	7.77	0.5	Xiao et al. (2015)
Mg-Fe CLDHs					
Pb(II)	5.5 ^b	450°C	1.87	1	Hudcová et al. (2019)
	5.5 ^b	550°C	1.37	1	Hudcová et al. (2019)
Zn(II)	5.5 ^b	450°C	1.18	1	Hudcová et al. (2019)
	5.5 ^b	550°C	1.03	1	Hudcová et al. (2019)

^a pH value at the beginning of the sorption experiment ^b pH controlled during the whole experiment

A significant part of the proposed thesis was focused on metal and metalloid (ad)sorption mechanisms on Mg-Fe LDHs and CLDHs. The study was divided into the modeling part, i.e., the surface complexation modeling using the diffuse layer model (DLM), and spectroscopic/microscopic investigations. Such a comprehensive approach enabled to identify the emerging surface complexes as well as the surface precipitation and/or other mechanisms influencing metal and metalloid removal. Since the removal mechanism using Mg-Fe CLDHs was similar to that of Mg-Fe LDHs, only selected analyses were provided. At this part of the thesis, the effect of the experimental conditions on the reconstruction ability of individual Mg-Fe CLDHs was also studied. The results showed that the reconstruction ability was strongly influenced by the temperature of the thermal treatment, pH, time and metal or metalloid concentrations in the solution. Based on data from literature, studies focused on the conditions influencing the reconstruction ability of CLDHs are limited; therefore, this thesis evaluated their effect on the reconstruction ability of Mg-Fe CLDHs thermally treated at different temperatures and further explained different (ad)sorption behavior of individual CLDHs since the reconstruction ability influenced the (ad)sorption capacity of these materials through incorporation of metals and metalloids into the structure of the recovered materials. In general, the structural properties of Mg-Fe CLDH thermally treated at higher temperatures lead to the inability to reconstruct the LDH structure caused by the formation of stable spinel that further explained its lower efficiency compared to Mg-Fe CLDH thermally treated at lower temperatures.

(Ad)sorption mechanisms of As(V) and Sb(V) are given in Fig. 7.2. In general, the whole (ad)sorption mechanisms of As(V) and Sb(V) could be divided into the surface complexation and anion exchange in the case of As(V) (ad)sorption, and the surface complexation, the formation of brandholzite-like structures and a possible minor influence of the anion exchange at lower pH values in the case of Sb(V) (ad)sorption. The pH-dependent equilibrium (ad)sorption data describing the As(V) (ad)sorption

showed a visible ionic-strength dependency, i.e., the decreasing (ad)sorption by increasing ionic strength, indicating the formation of outer-sphere complexes (Hayes and Leckie, 1987; Hayes et al., 1988). Since the DLM is not able to capture outer-sphere complexes, the fitting (especially at higher pH values) showed discrepancies. Therefore, both inner-sphere and outer-sphere complexes were expected on the Mg-Fe LDH surface. Contrarily, the Sb(V) data showed ionic strength independency (except data near the pH_{PZC}); therefore, inner-sphere complexation was suggested as the predominant mechanism. However, the DLM showed also discrepancies at higher pH values that could correspond to outer-sphere complexation or possible formation of new phases as discussed by Vithanage et al. (2013, 2015). Based on the literature, the formation of inner-sphere complexes (Liu et al., 2006; Paikaray et al., 2013) as well as outer-sphere complexes (Wang et al., 2009) of As(V) on the LDH and CLDH surface was observed. Nevertheless, the simultaneous presence of both complexes was suggested by Goh et al. (2009) and Sommella et al. (2015). The As(V) (ad)sorption mechanism on the LDH and CLDH surface has been investigated by XAS measurements (Liu et al., 2006; Paikaray et al., 2013; Sommella et al., 2015; Wang et al., 2009) or XPS measurements (Goh et al., 2009). Based on the literature dealing with Sb(V) (ad)sorption, the formation of inner-sphere complexes was detected by the calculations from isotherms (Constantino et al., 2018; Kameda et al., 2015; Mitsunobu et al., 2008) and/or XPS analyses (Lee et al., 2018b; Lu et al., 2015).

In order to further evaluate the (ad)sorption mechanisms, solid state analyses were performed. The XRD diffraction confirmed the outer-sphere complexation of As(V) *via* anion exchange that was evaluated by the increase of the basal spacing of the layers and cell parameter *c*. Both parameters corresponded to the incorporation of the different anion in the LDH interlayered region (Goh et al., 2010; Huang et al., 2015; Kang et al., 2013). Moreover, the decrease of the intensity of individual peaks was also observed suggesting LDH structural changes during As(V) (ad)sorption that could be caused by the anion exchange (as mentioned above) and/or by the Mg(II) leaching that was also observed during the (ad)sorption process. On the contrary, the XRD diffractogram after Sb(V) (ad)sorption showed nearly the same intensity as the Mg-Fe LDH before the experiment suggesting the opposite effect than in the case of As(V) (ad)sorption, i.e., stabilization of Mg(II) and minor effect (or none) of anion exchange. A higher affinity of As(V) for the interlayered region compared to Sb(V) was explained by the different ionic size of individual metalloids, since the effective ionic radius of Sb(V) is higher than that of As(V); therefore, there is a higher possibility of its intercalation. Nevertheless, formation of brandholzite-like structures ($\text{pH} < 7.5$) and surface precipitation of crystalline brandholzite ($\text{pH} > 7.5$) were observed after Sb(V)

(ad)sorption by the XRD diffractograms as well as by SEM/EDX analyses confirmed the hypothesis of different (ad)sorption mechanisms that cannot be captured by the DLM (especially at higher pH values). Brandholzite is a layered mineral composed of $\text{Sb}(\text{OH})_6$ octahedra and $\text{Sb}(\text{OH})_6/\text{Mg}(\text{H}_2\text{O})_6$ octahedra connected by hydrogen bonds (Friedrich et al., 2000; Majzlan et al., 2016;). Although the formation of brandholzite-like phases has been previously presented (Ardau et al., 2016; Dore and Frau, 2018; Kameda et al., 2011, 2012, 2015), such studies expected only its formation in the interlayer region that was excluded for Mg-Fe LDHs. Therefore, more appropriate mechanism of its formation was presented in this thesis, i.e., re-(ad)sorption of positively charged Mg(II) leached from the surface/structure of LDHs (as mentioned by As(V) (ad)sorption) onto negatively charged Sb(V) complexes (ad)sorbed on the Mg-Fe LDH surface. This process resulted in the formation of individual layers corresponding to the brandholzite-like phases. Contrarily, the formation of new phases with As(V) and Mg(II) was excluded by XRD as well as SEM/EDX. Other difference between As(V) and Sb(V) (ad)sorption onto Mg-Fe LDHs was in the distribution of (ad)sorbed species. The Mg-Fe LDHs after As(V) (ad)sorption showed homogeneous distribution; contrarily, nonhomogeneous distribution was observed in the case of the material after Sb(V) (ad)sorption. The FTIR-ATR and XPS spectra further confirmed the suggested (ad)sorption mechanisms, i.e., outer-sphere complexation for As(V), brandholzite-like phases or precipitation of crystalline brandholzite for Sb(V) and the predominant effect of inner-sphere complexation for both metalloids. This part of the study showed differences between As(V) and Sb(V) (ad)sorption behavior onto the surface of Mg-Fe LDHs that has not been presented in such comprehensive approach yet.

In the case of both Mg-Fe CLDHs, the predominant effect of inner-sphere complexation was expected, since the reconstruction, i.e., the possible incorporation of As(V) in the interlayer region, of CLDHs thermally treated at 450°C took place only at low As(V) concentrations. Moreover, CLDHs treated at 550°C were not able to recover the LDH structure at any As(V) concentrations; therefore, the incorporation into the interlayer region was excluded. As has been previously mentioned, Sb(V) (ad)sorption onto Mg-Fe CLDHs was not performed in this study; however, similar (ad)sorption mechanisms as in the case of Mg-Fe LDHs are expected.

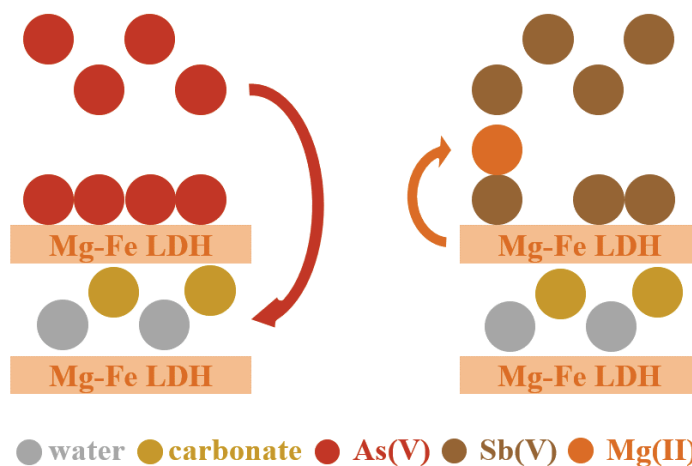


Fig. 7.2. (Ad)sorption mechanisms of As(V) and Sb(V) onto Mg-Fe LDHs.

(Ad)sorption mechanisms of Pb(II) and Zn(II) are given in Fig. 7.3. In general, the whole (ad)sorption mechanism is influenced by the surface complexation and precipitation in the case of Pb(II) (ad)sorption, and surface complexation, surface precipitation and/or a minorly by isomorphous substitution in the case of Zn(II) (ad)sorption. In contrast to As(V) (ad)sorption, the ionic-strength independency was observed for both metals. Similarly, the pH-dependent (ad)sorption was also described by the DLM to investigate the emerging inner-sphere surface complexes. In general, the pH dependent (ad)sorption of metals was divided into three main regions, i.e., a possible dissolution of LDHs and metal desorption at low pH values, surface complexation at the pH values below the saturation of metal hydroxides and/or carbonates (circumneutral pH) and the oversaturated solution for metal hydroxides and or/carbonates (higher pH values). In general, there is a lack of metal (ad)sorption studies using LDHs and CLDHs at controlled conditions (to differentiate between individual mechanisms) as well as spectroscopic/microscopic techniques dealing with different (ad)sorption mechanisms at controlled conditions. Nevertheless, few studies have been focused on Pb(II) (ad)sorption at different ionic strengths. This simple evaluation enabled to roughly differentiate between the formation of inner-sphere and/or outer-sphere complexes; however, individual inner-sphere complexes, i.e., monodentate or bidentate, cannot not be established. The preferable formation of outer-sphere complexes was observed for Mg-Al LDHs (Zhang and Hou, 2007; Zhao et al., 2011). Contrarily, Liang et al. (2009) presented the formation of inner-sphere complexes on the surface of Mg-Fe LDHs.

The whole (ad)sorption mechanism of both metals onto Mg-Fe LDHs was further investigated using various solid-state analyses since the DLM is not able to capture precipitation in the bulk solution and/or surface precipitation. In general, the surface precipitation was observed as a result of high pH values on the LDH surface resulting in the formation of metal hydroxides or carbonates at the pH values below their saturation in aqueous solution (established by Visual MINTEQ 3.1). After Pb(II) (ad)sorption, the formation of surface precipitates was observed by XRD and SEM/EDX analyses. Based on the peak position as well as characteristic hexagonally-shaped precipitates, the newly formed phases were identified as hydrocerussite and/or cerussite. The formation of these phases on the LDH surface after Pb(II) (ad)sorption was also observed by Liang et al. (2009), Park et al. (2007), Zhang and Hou (2007) and Zhao et al. (2011). In general, the precipitation of carbonates on the LDH surface is supported by atmospheric CO₂ as well as the interlayered carbonates that are available for Pb(II) precipitation on the LDH surface (Park et al., 2007). Contrarily, the XRD diffractogram after Zn(II) (ad)sorption showed nearly the same record (except lower intensities caused by a partial dissolution of LDHs as mentioned by As(V) (ad)sorption). However, newly formed amorphous structures were observed by SEM/EDX and were assigned to the precipitation of Zn oxides/hydroxides or accumulation of Zn(II) by multilayer (ad)sorption as described by Xiao et al. (2015). The most common precipitates that have been observed after Pb(II) and Zn(II) (ad)sorption in the literature, especially without the pH adjustment, are given in Table 7.6. Nevertheless, changes in cell parameter *c* after Zn(II) (ad)sorption was also observed and was assigned to isomorphic substitution in the LDH layers (Komarneni et al., 1998; Richardson and Braterman, 2009; Sun et al., 2015a). Such process was excluded for Pb(II) since the ionic radii of Pb(II) is significantly higher compared to Mg(II). The FTIR-ATR and XPS spectra further confirmed the suggested (ad)sorption mechanisms, i.e., inner-sphere complexation for both metal, surface precipitation of crystalline phases for Pb(II) and multilayer (ad)sorption and/or precipitation of amorphous Zn oxides/ hydroxides for Zn(II). The effect of isomorphic substitution was not visible using these spectroscopic techniques.

In the case of Mg-Fe CLDHs, similar mechanisms were observed; however, significant changes in the reconstruction ability at different Pb(II) and Zn(II) initial concentrations were detected. As in the case of As(V) (ad)sorption, CLDHs thermally treated at 450 °C were able to reconstruct the LDH structure at the lowest metal concentrations and; moreover, the hydrocerussite/cerussite were not detected. However, increasing Pb(II) concentrations lead to the predominant effect of the surface precipitation. In the case of Zn(II) (ad)sorption onto Mg-Fe CLDHs thermally treated at 450 °C, the

reconstruction was more successful; therefore, a possible effect of Zn(II) incorporation during this process was also expected (Sun et al., 2015a; Xiao et al., 2015). In general, studies dealing with metal (ad)sorption onto LDHs and CLDHs are rather scarce, despite a high efficiency of these materials towards metals in general.

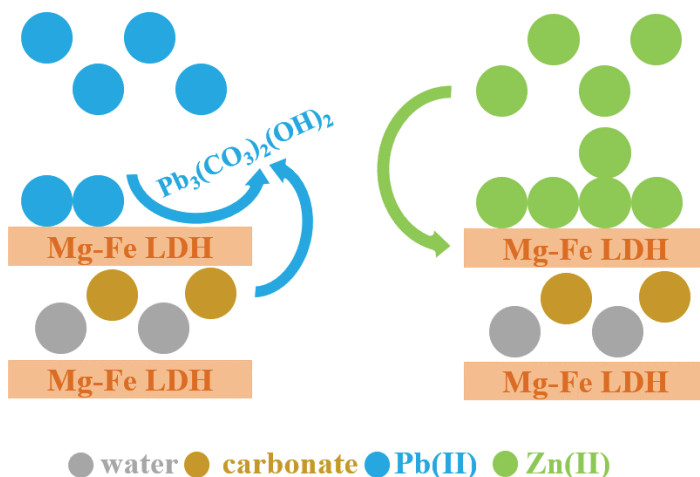


Fig. 7.3. (Ad)sorption mechanisms of Pb(II) and Zn(II) onto Mg-Fe LDHs.

Table 7.6 Precipitates occurring after Pb(II) and Zn(II) (ad)sorption onto LDHs and CLDHs.

Metal	pH ₀ ^a	Type of LDH	Precipitate	Literature
Pb(II)	5.5	Mg-Fe CO ₃ ²⁻	Pb ₃ (OH) ₂ (CO ₃) ₂	Hudcová et al. (2019)
	4.5	Mg-Fe Cl ⁻	Pb ₃ (OH) ₂ (CO ₃) ₂	Liang et al. (2009)
	-	Mg-Fe CO ₃ ²⁻	Pb(OH) ₂	Seida et al., (2001)
	6.0	Mg-Al Cl ⁻	unspecified	Zhang and Hou (2007)
	5.0	Mg-Al Cl ⁻	Pb(OH) ₂	González et al. (2015)
Zn(II)	5.0	Mg-Al Cl ⁻	ZnCl ₂ ·4Zn(OH) ₂	Fujji et al. (1992)

^a pH value at the beginning of the sorption experiment ^b pH controlled during the whole experiment

The last part of the thesis was focused on the application of Mg-Fe LDHs and CLDHs to soil solutions and soils with highly elevated As(V), Pb(II) and Zn(II) concentrations sampled in the Czech Republic. Moreover, the stability of materials at different conditions was also discussed in detail. In general, the stability of materials was established by the Mg(II) leaching during individual tests (Fe(III) leaching was not observed). Firstly, the stabilization tests in the extracted soil solutions showed Mg-Fe CLDHs as more stable materials. Moreover, all metals and metalloids in the solution, i.e., As(V), Pb(II) and Zn(II) were stabilized within the first hours of the experiment

using CLDHs that was more rapid than using Mg-Fe LDHs. Surprisingly, both Mg-Fe LDHs and CLDHs were highly effective for As(V) stabilization despite the final pH of 9-10.

The XRD diffractograms showed improvements of the Mg-Fe LDH crystallinity after the stability tests and; moreover, successful reconstruction of Mg-Fe CLDHs that further confirmed the suggested effect of pH and time on the reconstruction as has been previously mentioned. The stability and stabilization efficiency of both materials were further tested by their direct incubation in soils. Such experiments were divided into two types, i.e., pH-static leaching experiments and incubation experiments. Both experiments showed Mg-Fe LDHs as more stable and effective materials after their direct application to soils compared to aqueous solutions. Nevertheless, pH-static leaching experiments showed Mg-Fe CLDHs as more effective materials at higher pH values for As(V) and at lower pH values for Pb(II). In the case of Zn(II), both materials were not successful at lower pH values; however, Mg-Fe LDHs showed higher stabilizing efficiency at higher pH values compared to Mg-Fe CLDHs. Finally, incubation batch experiments of up to 10 weeks showed significantly higher stability of Mg-Fe LDHs at all studied time interval and a higher stabilizing efficiency towards As(V). In addition, Mg-Fe CLDH showed a decreasing ability to stabilize As(V) with the increasing time of incubation. In the case of Zn(II) stabilization, both materials were highly effective and reached up to 100% compared with the non-amended soil.

The fractionation of As(V) and Zn(II) was evaluated by sequential and simple extractions (Pb(II) was not detected). However, sequential extractions lead to the destruction of the studied Mg-Fe LDHs and CLDHs in the first step; therefore, only simple extractions were proposed as a suitable method for these systems. Based on the results of the simple extraction, the total stabilization of the Zn(II) mobile fraction was observed and was probably caused by the buffering effect of Mg-Fe LDHs and CLDHs. Moreover, the solid-state analyses of Mg-Fe LDHs and CLDHs after the incubation tests were also performed. The XRD diffractograms showed the increasing crystallinity of Mg-Fe LDHs and the successful reconstruction of Mg-Fe CLDHs in soil conditions. The stabilization of Mg(II) during the incubation was more apparent for Mg-Fe LDHs and was further explained (together with the geochemical modeling) as the formation of magnesium carbonates and magnesium silicates. Moreover, the formation of magnesium silicates, i.e., sepiolite, could further improve the (ad)sorption efficiency since sepiolite has been previously presented as an effective metal (ad)sorbent (Hu et al., 2017c).

To this date, different LDHs and CLDHs have been tested in soils contaminated by As(III) using Ca-Mg-Fe LDH (Zhou et al., 2017), Cr(VI) using a combination of electrokinetics (EK) with a CLDH-based permeable reactive barrier (PRB) (Zhang et al., 2012a) and As(V) using Mg-Al LDH (Sun et al. 2015b). In all studies, the buffering effect of LDHs and/or CLDHs in soils (Zhang et al., 2012a; Zhou et al., 2017; Sun et al. 2015b) as well as Mg(II) leaching (Zhou et al., 2017). Nevertheless, the effect on other soils properties or microorganisms were not mentioned. The possible negative influence of the buffering effect on the plant grow was discussed by Sun et al. (2015b). Nevertheless, the positive influence on the plant grown by the presence of sepiolite in soils has been also presented in this study; therefore, the newly formed sepiolite on the Mg-Fe LDH and CLDH surface after their incubation in soils could positively influence the stabilization of metals and metalloids as well as the plant grown. Nevertheless, more studies dealing with this topic need to be performed in the future.

Despite the high efficiency of Mg-Fe LDHs and CLDHs in aqueous solutions and soils, potential side effects could limit their direct application in remediation technologies. The crucial factors are the stability of materials at different conditions (especially at lower pH values), the buffering effect, the influence on nutrient cycling in soils, the effect on plants/microorganisms and the economical side of their application at a larger scale. Since LDHs and CLDHs are less stable at acidic conditions, the effect of low-molecular-weight organic acids that are exuded by plant roots needs to be tested in the future as well (Vítková et al., 2015). Nevertheless, a slight acidification by these acids could have a positive effect in the partial release of nutrients (e.g., Zn) that will be completely stabilized by Mg-Fe LDHs and CLDHs in soils. Contrarily, the strong buffering effect of Mg-Fe LDHs and CLDHs could have a positive effect on acidic soils as has been highlighted by Zhang et al. (2012a). Moreover, LDHs and CLDHs could improve the cycling of various nutrients (nitrate, phosphate) or organic acids through incorporation of these compounds into the structure of LDHs (during the synthesis) and/or CLDHs (during the reconstruction) or by the subsequent adsorption onto the LDH and/or CLDH surface. Previously, the adsorption of humic and fulvic acids onto the LDH and CLDH surface improved metal stabilizing efficiency (Benício et al., 2015; Chang et al., 2017; Fang et al., 2015, 2018). To deal with the economical side of the LDH and CLDH application, a synthesis of a composite material with a low-cost sorbent (e.g., biochar) could result in a promising material for metals and metalloid remediation technologies. In general, biochar is a low-cost material exhibiting a large specific surface area and ability to (ad)sorb metal cations, e.g., Zn or Pb (Dong et al., 2017). Moreover, the application of biochar could have a positive effect on soil properties (Lehmann and Joseph, 2009). However, its usability is limited in

water and soil contaminated by anions, e.g., arsenate or chromate (Wan et al., 2017). As the real contaminated water and soil are commonly enriched by various metals, metalloids and other contaminants (e.g., organics), LDH/biochar composites are promising materials for remediation technologies. In conclusion, the proposed thesis presented a comprehensive approach to study metal and metalloid (ad)sorption mechanisms, stability and stabilizing efficiency and the obtained results could be useful for future studies dealing with chemical stabilization using innovative solid materials.

References

- Abdelhafez, A.A., Li, J., 2016. Removal of Pb(II) from aqueous solution by using biochars derived from sugar cane bagasse and orange peel. *J. Taiwan Inst. Chem. Eng.* 61, 367–375.
- Abellán, G., Amo-Ochoa, P., Fierro, J. L. G., Ribera, A., Coronado, E., Zamora, F., 2015. Self-Assembly of 1D/2D Hybrid Nanostructures Consisting of a Cd(II) Coordination Polymer and NiAl-Layered Double Hydroxides. *Polymers* 8(1), 5.
- Abtahi, A., 1985. Synthesis of sepiolite at room temperature from SiO₂ and MgCl₂ solution. *Clay Miner.* 20, 521-523.
- Accornero, M., Marini, L., Lelli, M., 2008. The Dissociation Constant of Antimonic Acid at 10–40 °C. *Solution Chem.* 37, 785–800.
- Adriano, D.C., 2001. Trace elements in the terrestrial environments: Biogeochemistry, bioavailability, and risks of metals, 2nd edition, Springer, New York.
- Aharoni, C., Sparks, D.L., 1991. Kinetics of soil chemical reactions: A theoretical treatment, In: Sparks, D.L., Suarez, D.L. (Eds.), *Rates of Soil Chemical Processes*, SSSA Spec. Publ. 27, Soil Sci. Soc. Am., Madison, WI., pp. 1–18.
- Ahmad, M., Rajapaksha, A.U., Lim, J.E., Zhang, M., Bolan, N., Mohan, D., Vithanage, M., Lee, S.S., Ok, Y.S., 2014. Biochar as a sorbent for contaminant management in soil and water: A review. *Chemosphere* 99, 19–33.
- Ahmed, M.B., Zhou, J.L., Ngo, H.H., Guo, W., Chen, M., 2016. Progress in the preparation and application of modified biochar for improved contaminant removal from water and wastewater. *Bioresour. Technol.* 214, 836–851.
- Alexander, M.R., Thompson, G.E., Beamson, G., 2000. Characterization of the oxide/hydroxide surface of aluminium using x-ray photoelectron spectroscopy: a procedure for curve fitting the O 1s core level. *Surf. Interface Anal.* 29, 468-477.
- Alias, S.S., Mohamad, A.A., 2014. *Synthesis of Zinc Oxide by Sol-Gel Method for Photoelectrochemical Cells*, Springer, Singapore.
- Andreozzi, G.B., Princivalle, F., Skogby, H., Della Giusta, A., 2000. Cation ordering and structural variations with temperature in MgAl₂O₄ spinel: an Xray single crystal study. *Am. Mineral.* 85, 1164–1171.

- Arakha, M., Saleem, M., Mallick, B.C., Jha, S., 2015. The effects of interfacial potential on antimicrobial propensity of ZnO nanoparticle. *Sci. Rep.* 5, 1-10.
- Ardau, C., Frau, F., Lattanzi, P., 2013. New data on arsenic sorption properties of Zn-Al sulphate layered double hydroxides: Influence of competition with other anions. *Appl. Clay Sci.* 80-81, 1-9.
- Ardau, C., Frau, F., Lattanzi, P., 2016. Antimony Removal from Aqueous Solutions by the Use of Zn-Al Sulphate Layered Double Hydroxide. *Water Air Soil Pollut.* 227, 344.
- Atkins, P., de Paula, J., 2010. *Physical Chemistry*, 9th edition, Oxford Univ. Press, Oxford.
- Bahfenne, S., Frost, R.L., 2010. A Review of the Vibrational Spectroscopic Studies of Arsenite, Antimonite, and Antimonate Minerals. *Appl. Spectrosc. Rev.* 45, 101-129.
- Baig, S.A., Zhu, J., Muhammad, N., Sheng, T., Xu, X., 2014. Effect of synthesis methods on magnetic Kans grass biochar for enhanced As (III, V) adsorption from aqueous solutions. *Biomass Bioenerg.* 71, 299–310.
- Baltrusaitis, J., Chen, H., Rubasinghege, G., Grassian, V.H., 2012. Heterogeneous atmospheric chemistry of lead oxide particles with nitrogen dioxide increases lead solubility: environmental and health implications. *Environ. Sci. Technol.* 46 (23), 12806-12813.
- Benício, L. P. F., Silva, R. A., Lopes, J. A., Eulálio, D., dos Santos, R. M. M., de Aquino, L. A., Vergütz, L., Novais, R. F., da Costa, L. M., Pinto, F. G., Tronto, J., 2015. Layered double hydroxides: Nanomaterials for applications in agriculture. *R. Bras. Ci. Solo* 39, 1-13.
- Bernardo, M., Mendes, S., Lapa, N., Goncalves, M., Mendes, B., Pinto, F., Lopes, H., Fonseca, I., 2013. Removal of lead (Pb²⁺) from aqueous medium by using chars from co-pyrolysis. *J. Colloid Interface Sci.* 409, 158–165.
- Biesinger, M.C., Payne, B.P., Grosvenor, A.P., Lau, L.W.M., Gerson, A.R., Smart, R.S.C., 2011. Resolving surface chemical states in XPS analysis of first row transition metals, oxides and hydroxides: Cr, Mn, Fe, Co and Ni. *Appl. Surf. Sci.* 257, 2717-2730.

- Blanchard, M., Morin, G., Lazzeri, M., Balan, E., Dabo, I., 2012. First-principles simulation of arsenate adsorption on the (1 1 2) surface of hematite. *Geochim. Cosmochim. Ac.* 86, 182–195.
- Bocclair, J.W., Braterman, P.S., 1999. Layered Double Hydroxide Stability. 1. Relative Stabilities of Layered double Hydroxides and Their Simple Counterparts. *Chem. Mater.* 111, 298-302.
- Bogusz, A., Nowak, K., Stefaniuk, M., Dobrowolski, R., Oleszczuk, P., 2017. Synthesis of biochar from residues after biogas production with respect to cadmium and nickel removal from wastewater. *J. Environ. Manage.* 201, 268–276.
- Bohn, H. L., Strawn, D.G., O'Connor, G.A., 2015. *Soil Chemistry*, 4th edition, John Wiley & Sons, West Sussex, UK.
- Bolan, N., Kunhikrishnan, A., Thangarajan, R., Kumpiene, J., Park, J., Makino, T., Kirkham, M.B., Scheckel, K., 2014. Remediation of heavy metal(loid)s contaminated soils-to mobilize or to immobilize? *J. Hazard. Mater.* 266, 141-166.
- Borůvka, L., Vácha, R., 2006. Litavka river alluvium as a model area heavily polluted with potentially risk elements, In: Morel, J.L., Echevarria, G., Goncharova, N. (Eds.) *Phytoremediation of Metal-contaminated Soils*, Springer, Dordrecht, pp. 267-298.
- Boyd, G.E., Adamson, A.W., Myers, Jr L.S., 1947. The Exchange Adsorption of Ions from Aqueous Solutions by Organic Zeolites. II. Kinetics. *J. Am. Chem. Soc.* 69, 2836-2848.
- Broadley, M.R., White, P.J., Hammond, J.P., Zelko, I., Lux, A., 2007. Zinc in plants. *New Phytol.* 173, 677-702.
- Brown, G.E., 1990. Spectroscopic studies of chemisorption reaction mechanisms at oxide - water interfaces. *Rev. Mineral.* 23, 309-363.
- Bruna, F., Celis, R., Pavlovic, I., Barriga, C., Cornejo, J., Ulibarri, M.A., 2009. Layered double hydroxides as adsorbents and carriers of the herbicide (4-chloro-2-methylphenoxy) acetic acid (MCPA): systems Mg–Al, Mg–Fe and Mg–Al–Fe. *J. Hazard Mater.* 168, 1476-1481.
- Cai, Y., Li, L., Zhang, H., 2015. Kinetic modeling of pH-dependent antimony (V) sorption and transport in iron oxide-coated sand. *Chemosphere* 138, 758-764.

- Cao, X., Ma, L., Gao, B., Harris, W., 2009. Dairy-manure derived biochar effectively sorbs lead and atrazine. *Environ. Sci. Technol.* 43, 3285–3291.
- Cao, X., Ma, L.Q., Rhue, D.R., Appel, C.S., 2004. Mechanisms of lead, copper, and zinc retention by phosphate rock. *Environ. Pollut.* 131(3), 435–444.
- Caporale, A.G., Pigna, M., Dynes, J.J., Cozzolino, V., Zhu, J., Violante, A., 2011. Effect of inorganic and organic ligands on the sorption/desorption of arsenate on/from Al–Mg and Fe–Mg layered double hydroxides. *J. Hazard Mater.* 198, 291-298.
- Carja, G., Lehotu, G., Dartu, L., Mertens, M., Cool, P., 2012. Layered double hydroxides reconstructed in calcium glutamate aqueous solution as a complex delivery system. *Appl. Clay Sci.* 65-66, 37-42.
- Carja, G., Nakamura, R., Niiyama, H., 2005. Tailoring the porous properties of iron containing mixed oxides for As (V) removal from aqueous solutions. *Micropor. Mesopor. Mat.* 83, 94-100.
- Carrow, R.N., Waddington, D.V., Rieke, P.E., 2001. *Turfgrass Soil Fertility & Chemical Problems: Assessment and Management*. Wiley, Hoboken.
- Cavani, F., Trifirò, F., Vaccari, A., 1991. Hydrotalcite-type anionic clays: preparation, properties and applications. *Catal. Today* 11, 173-301.
- CEN/TS 14997, 2006. *Characterization of Waste - Leaching Behaviour Tests - Influence of pH on Leaching with Continuous pH-Control*. CEN, Brussels.
- Cha, J.S., Park, S.H., Jung, S.C., Ryu, C., Jeon, J.K., Shin, M.C., Park, Y.K., 2016. Production and utilization of biochar: A review. *J. Ind. Eng. Chem.* 40, 1-15.
- Chang, K., Li, X., Liao, Q., Hu, B., Hu, J., Sheng, G., Linghu, W., Huang, Y., Asiri, A.M., Alamry, K.A., 2017. Molecular insights into the role of fulvic acid in cobalt sorption onto graphene oxide and reduced graphene oxide. *Chem. Eng. J.* 327, 320-327.
- Chang, K., Li, X., Liao, Q., Hu, B., Hu, J., Sheng, G., Linghu, W., Huang, Y., Asiri, A.M., Alamry, K.A., 2017d. Molecular insights into the role of fulvic acid in cobalt sorption onto graphene oxide and reduced graphene oxide. *Chem. Eng. J.* 327, 320-327.

- Chapman, D.L., 1913. A contribution to the theory of electrocapillarity. *Philos. Mag.* 25(6), 475–481.
- Charlet, L., Manceau, A.A., 1992. X-ray absorption spectroscopic study of the sorption of Cr(III) at the oxide-water interface. II. Adsorption, coprecipitation, and surface precipitation on hydrous ferric oxide. *J. Colloid Interf. Sci.* 148(2), 442–458.
- Chen, X., Chen, G., Chen, L., Chen, Y., Lehmann, J., McBride, M.B., Hay, A.G., 2011. Adsorption of copper and zinc by biochars produced from pyrolysis of hardwood and corn straw in aqueous solution. *Bioresour. Technol.* 102, 8877–8884.
- Ching, S., Petrovay, D.J., Jorgensen, M.L., 1997. Sol–gel synthesis of layered birnessite-type manganese oxides. *Inorg. Chem.* 36, 883–890.
- Chubar, N., Gilmour, R., Gerda, V., Mičušík, M., Omastova, M., Heister, K., Man, P., Fraissard, J., Zaitsev, V., 2017. Layered double hydroxides as the next generation inorganic anion exchangers: Synthetic methods versus applicability. *Adv. Colloid Interface Sci.* 245, 62–80.
- Cocheci, L., Barvinschi, P., Pode, R., Popovici, E., Seftel, E. M., 2010. Structural characterization of some Mg/Zn-Al type hydrotalcites prepared for chromate sorption from wastewater, *Chem. Bull. “POLITEHNICA” Univ.* 55, 40–45.
- Constantino, L.V., Quirino, J.N., Monteiro, A.M., Abrão, T., Parreira, P.S., Urbano, A., Santos, M.J., 2017. Sorption-desorption of selenite and selenate on Mg-Al layered double hydroxide in competition with nitrate, sulfate and phosphate. *Chemosphere* 181, 627–634.
- Constantino, L.V., Quirino, J.N., Abrão, T., Parreira, P.S., Urbano, A., Santosa, M.J., 2018. Sorption–desorption of antimony species onto calcined hydrotalcite: Surface structure and control of competitive anions. *J. Hazard. Mater.* 344, 649–656.
- Cui, X., Fang, S., Yao, Y., Li, T., Ni, Q., Yang, X., He, Z., 2016. Potential mechanisms of cadmium removal from aqueous solution by *Canna indica* derived biochar. *Sci. Total Environ.* 562, 517–525.
- Cullity, B.D., 1978. *Elements of X-Ray Diffraction*, 2nd edition, Addison-Wesley Publishing Company, Inc., Reading, MA.

- da Silva, V., Mangrich, A.S., Wypych, F., 2014. Nitrate release from layered double hydroxides as potential slow-release fertilizers. *Rev. Bras. Ciênc. Solo*. 38, 821-830.
- Das, J., Das, D., Dash, G. P., Das, D. P., Parida, K. M., 2004. Studies on Mg/Fe hydrotalcite-like-compound (HTlc)—II. Removal of chromium(VI) from aqueous medium. *Int. J. Environ. Stud.* 61 (5), 605-616.
- Das, J., Sairam Patra, B., Baliarsingh, N., Parida, K.M., 2007. Calcined Mg-Fe-CO(3) LDH as an adsorbent for the removal of selenite. *J. Colloid Interf. Sci.* 316, 216-223.
- Davis, J.A., and Leckie, J.O., 1978. Surface ionization and complexation at the oxide/water interface. 2. Surface properties of amorphous iron oxyhydroxide and adsorption of metal ions. *J. Colloid Interf. Sci.* 67, 90-107.
- De Gisi, S., Lofrano, G., Grassi, M., Notarnicola, M., 2016. Characteristics and adsorption capacities of low-cost sorbents for wastewater treatment: A review. *Sus. Mater. Technol.* 9, 10-40.
- de Roy, A., Forano, C., Besse, J. P., 2001. Layered Double Hydroxides: Synthesis and Post-Synthesis Modification, In: Rives, V. (Eds.), *Layered Double Hydroxides: Present and Future*, Nova Science Publishers, Inc., New York, pp. 1-39.
- Della Puppa, L., Komárek, M., Bordas, F., Bollinger, J.C., Joussein, E., 2013. Adsorption of copper cadmium, lead and zinc onto a synthetic manganese oxide, *J. Colloid Interface Sci.* 399, 99-106.
- Delorme, F., Seron, A., Bizi, M., Jean-Prost, V., Martineau, D., 2006. Effect of time on the reconstruction of the $Mg_4Al_2(OH)_{12}CO_3 \cdot 3H_2O$ layered double hydroxide in a Na_2CO_3 solution. *J. Mater. Sci.* 41, 4876-4882.
- Deng, R.-J., Jin, C.-S., Ren, B.-Z., Hou, B.-L., Hursthouse, A., 2017. The Potential for the Treatment of Antimony-Containing Wastewater by Iron-Based Adsorbents. *Water* 9(10), 794.
- Devi, P., Saroha, A.K., 2014. Synthesis of the magnetic biochar composites for use as an adsorbent for the removal of pentachlorophenol from the effluent. *Bioresour. Technol.* 169, 525-531.
- Ding, W., Dong, X., Ime, I.M., Gao, B., Ma, L.Q., 2014. Pyrolytic temperatures impact lead sorption mechanisms by bagasse biochars. *Chemosphere* 105, 68-74.

Dong, H., Deng, J., Xie, Y., Zhang, C., Jiang, Z., Cheng, Y., Hou, K., Zeng, G., 2017. Stabilization of nanoscale zero-valent iron (nZVI) with modified biochar for Cr(VI) removal from aqueous solution. *J. Hazard. Mater.* 332, 79-86.

Dore, E., Frau, F., 2018. Antimonate uptake by calcined and uncalcined layered double hydroxides: effect of cationic composition and M²⁺/M³⁺ molar ratio. *Environ. Sci. Pollut. Res.* 25(1), 916-929.

Doušová, B., Lhotka, M., Filip, J., Koloušek, D., 2018. Removal of arsenate and antimonate by acid-treated Fe-rich clays. *J. Hazard. Mater.* 357, 440-448.

Doušová, B., Lhotka, M., Grygar, T., Machovič, V., Herzogová, L., 2011. In situ co-adsorption of arsenic and iron/manganese ions on raw clays. *Appl. Clay Sci.* 54, 166-171.

Doušová, B., Machovč, V., Koloušek, D., Kovanda, F., Dorničák, V., 2003. Sorption of As(V) species from aqueous systems. *Water Air Soil Pollut.* 149(1-4), 251-267.

Drahota, P., Kulakowski, O., Culka, A., Knappová, M., Rohovec, J., Veselovský, F., Racek, M., 2018. Arsenic mineralogy of near-neutral soils and mining waste at the Smolotely-Lišnice historical gold district, Czech Republic. *Appl. Geochem.* 89, 243-254.

Drenkova-Tuhtan, A., Mandel, K., Paulus, A., Meyer, C., Hutter, F., Gellermann, C., Sextl, G., Franzreb, M., Steinmetz, H., 2013. Phosphate recovery from wastewater using engineered superparamagnetic particles modified with layered double hydroxide ion exchangers. *Water Res.* 47, 5670-5677.

Dzombak, D. A., Morel, F. M. M., 1990. *Surface Complexation Modeling: Hydrous Ferric Oxide*, John Wiley & Sons, Toronto, Canada.

Echigo, S., Itoh, S., Kuwahara, M., 2007. Bromide removal by hydrotalcite-like compounds in a continuous system. *Wat. Sci. Tech.* 56 (11), 117-122.

Elhalil, A., Qourzal, S., Mahjoubi, F.Z., Elmoubarki, R., Farnane, M., Tounsadi, H., Sadiq, M., Abdennouri, M., Barka, N., 2016. Defluoridation of groundwater by calcined Mg/Al layered double hydroxide. *Emerging Contaminants* 2, 42-48.

- Ettler, V., Knytl, V., Komárek, M., Della Puppa, L., Bordas, F., Mihaljevič, M., Klementová, M., Šebek, O., 2014. Stability of a novel synthetic amorphous manganese oxide in contrasting soils, *Geoderma* 214–215, 2–9.
- Ettler, V., Mihaljevič, M., Šebek, O., Molek, M., Grygar, T., Zeman, J., 2006. Geochemical and Pb isotopic evidence for sources and dispersal of metal contamination in stream sediments from the mining and smelting district of Příbram, Czech Republic. *Environ. Pollut.* 142, 409-417.
- Ettler, V., Tomášová, Z., Komárek, M., Mihaljevič, M., Šebek, O., Michálková, Z., 2015. The pH-dependent long-term stability of an amorphous manganese oxide in smelter-polluted soils: Implication for chemical stabilization of metals and metalloids. *J. Hazard. Mater.* 286, 386-394.
- Evans, D. G., Slade, X., 2006. Structural Aspects of Layered Double Hydroxides, In: Evans, D.G., Slade, X. (Eds.), *Layered Double Hydroxides*, Springer, Berlin, pp. 1-87.
- Everaert, M., Warrinnier, R., Baken, S., Gustafsson, J.P., De Vos, D., Smolders, E., 2016. Phosphate-Exchanged Mg–Al Layered Double Hydroxides: A New Slow Release Phosphate Fertilizer, *ACS Sustainable Chem. Eng.* 4, 4280-4287.
- Fan, G., Li, F., Evans, D. G., Duan, X., 2014. Catalytic applications of layered double hydroxides: recent advances and perspectives. *Chem. Soc. Rev.* 43, 7040-7066.
- Fan, S., Li, H., Wang, Y., Wang, Z., Tang, J., Tang, J., Li, X., 2018. Cadmium removal from aqueous solution by biochar obtained by co-pyrolysis of sewage sludge with tea waste. *Res. Chem. Intermed.* 44, 135–154.
- Fang, L., Li, W., Chen, H., Xiao, F., Huang, L., Holm, P.E., Hansen, H.C.B., Wang, D., 2015. Synergistic effect of humic and fulvic acids on Ni removal by the calcined Mg/Al layered double hydroxide. *RSC Adv.* 5, 18866-18874.
- Fang, L., Hou, J., Xu, C., Wang, Y., Li, J., Xiao, F., Wang, D., 2018. Enhanced removal of natural organic matters by calcined Mg/Al layered double hydroxide nanocrystalline particles: Adsorption, reusability and mechanism studies. *Appl. Surf. Sci.* 442, 45-53.
- Febrianto, J., Kosasih, A.N., Sunarso, J., Ju, Y.-H., Indraswati, N., Ismadji, S., 2009. Equilibrium and kinetic studies in adsorption of heavy metals using biosorbent: A summary of recent studies. *J. Hazard. Mater.* 162, 616-645.

- Ferreira, O. P., de Moraes, S. G., Duran, N., Cornejo, L., Alves, O. L., 2006. Evaluation of boron removal from water by hydrotalcite-like compounds. *Chemosphere* 62(1), 80-88.
- Fierro, V., Torné-Fernández, V., Montané, D., Celzard, A., 2008. Adsorption of phenol onto activated carbons having different textural and surface properties. *Microporous Mesoporous Mater.* 111, 276-284.
- Filella, M., Belzile, N., Chen, Y.W., 2002a. Antimony in the environment: a review focused on natural waters I. Occurrence. *Earth-Sci. Rev.* 57, 125-176.
- Filella, M., Belzile, N., Chen, Y.W., 2012b. Antimony in the environment: a review focused on natural waters: II. Relevant solution chemistry. *Earth-Sci. Rev.* 59, 265-285.
- Fiol, N., Villaescusa, I., 2009. Determination of sorbent point zero charge: usefulness in sorption studies. *Environ. Chem. Lett.* 7, 79-84.
- Fondell, M., Gorgoi, M., Boman, M., Lindblad, A., 2018. Surface modification of iron oxides by ion bombardment – Comparing depth profiling by HAXPES and Ar ion sputtering. *J. Electron. Spectros. Relat. Phenomena* 224, 23-26.
- Foo, K.Y., Hameed, B.H., 2010. Insights into the modeling of adsorption isotherm systems. *Chem. Eng. J.* 156, 2-10.
- Ford, R.G., Sparks, D.L., 2000. The nature of Zn precipitates formed in the presence of pyrophyllite. *Environ. Sci. Technol.* 34, 2479-2483.
- Freundlich, H.M.F., 1906. Über Die Adsorption in Lösungen. *Z. Phys. Chem.* 57, 385-470.
- Friedrich, A., Wildner, M., Tillmanns, E., Merz, P.L., 2000. Crystal chemistry of the new mineral brandholzite, $Mg(H_2O)_6[Sb(OH)_6]_2$, and of the synthetic analogues $M_2+(H_2O)_6[Sb(OH)_6]_2$ ($M_2+ = Mg, Co$). *Am. Mineral.* 85, 593-599.
- Friel, J.J., Lyman, C.E., 2006. X-ray mapping in electron-beam instruments. *Microsc. Microanal.* 12(1), 2-25.

- Frišták, V., Pipiška, M., Lesný, J., Soja, G., Friesl-Hanl, W., Packová, A., 2015. Utilization of biochar sorbents for Cd²⁺, Zn²⁺, and Cu²⁺ ions separation from aqueous solutions: comparative study. *Environ. Monit. Assess.* 187, 4093.
- Frost, R.L., Čejka, J., Sejkora, J., Ozdín, D., Bahfenne, S., Keeffe, E.C., 2009. Raman spectroscopic study of the antimonate mineral brandholzite Mg[Sb₂(OH)₁₂]·6H₂O. *J. Raman Spectrosc.* 40, 1907–1910.
- Fujji, S., Sugie, Y., Kobune, M., Touno, A., 1992. Uptakes of Cu²⁺, Pb²⁺ and Zn²⁺ on synthetic hydrotalcite in aqueous solution. *J. Jpn. Chem. Soc.* 1992, 1504-1507.
- García-Sánchez, A., Alvarez-Ayuso, E., Rodríguez-Martín, F., 2002. Sorption of As(V) by some oxyhydroxides and clay minerals. Application to its immobilization in two polluted soils. *Clay Miner.* 37, 187-194.
- Gaya, U., 2014. *Heterogeneous Photocatalysis Using Inorganic Semiconductor Solids*, Springer, Netherlands.
- Gier, S., Johns, W.D., 2000. Heavy metal-adsorption on micas and clay minerals studied by X-ray photoelectron spectroscopy. *Appl. Clay Sci.* 16, 289-299.
- Gil-Díaz, M., Alonso, J., Rodríguez-Valdés, E., Pinilla, P., Lobo, M.C., 2014. Reducing the mobility of arsenic in brownfield soil using stabilised zero-valent iron nanoparticles. *J. Environ. Sci. Health A* 49, 1361-1369.
- Gil-Díaz, M., Pinilla, P., Alonso, J., Lobo, M.C., 2017. Viability of a nanoremediation process in single or multi-metal(loid)contaminated soils. *J. Hazard. Mater.* 321, 812-819.
- Giles, C.H., Smith, D., Huitson, A., 1974. A general treatment and classification of the solute adsorption isotherm. I. Theoretical. *J. Colloid Interf. Sci.* 47, 755–765.
- Goh, K. H., Lim, T. T., Dong, Z., 2008. Application of layered double hydroxides for removal of oxyanions: A review. *Water Res.* 42, 1343-1368.
- Goh, K. H., Lim, T. T., Dong, Z., 2009. Enhanced arsenic removal by hydrothermally treated nanocrystalline Mg/Al layered double hydroxide with nitrate intercalation. *Environ. Sci. Technol.* 43(7), 2537-2543.

Goh, K. H., Lim, T. T., Dong, Z., 2010. Removal of arsenate from aqueous solution by nanocrystalline Mg/Al layered double hydroxide: sorption characteristics, prospects, and challenges. *Water Sci. Technol.* 61 (6), 1411-1417.

Goldberg, S., 1992. Use of surface complexation models in soil chemical systems. *Adv. Agron.* 47, 233–329.

Goldberg, S., Criscenti, L. J., Turner, D. R., Davis, J. A., Cantrell, K. J., 2007. Adsorption–desorption processes in subsurface reactive transport modeling. *Vadose Zone J.* 6, 407-435.

Goldberg, S., 2014. Application of surface complexation models to anion adsorption by natural materials. *Environ. Toxicol. Chem.* 33(10), 2172-2180.

González, M.A., Pavlovic, I., Barriga, C., 2015. Cu(II), Pb(II) and Cd(II) sorption on different layered double hydroxides. A kinetic and thermodynamic study and competing factors. *Chem. Eng. J.* 269, 221-228.

Goswami, R., Shim, J., Deka, S., Kumari, D., Katak, R., Kumar, M., 2016. Characterization of cadmium removal from aqueous solution by biochar produced from *Ipomoea fistulosa* at different pyrolytic temperatures. *Ecol. Eng.* 97, 444–451.

Gouy, G., 1910. Sur la constitution de la charge électrique à la surface d'un électrolyte. *J. Phys. Theor. Appl.*, 9(1), 457-468.

Gräfe, M., Nachtegaal, M., Sparks, D.L., 2004. Formation of metalarsenate precipitates at the goethite–water interface. *Environ. Sci. Technol.* 38(24), 6561–6570.

Grünewald, G., Kaiser, K., Jahn, R., 2008. Hydrotalcite-a potentially significant sorbent of organic matter in calcareous alkaline soils. *Geoderma* 147, 141-150.

Guo, X., Wu, Z., He, M., Meng, X., Jin, X., Qiu, N., Zhang, J., 2014. Adsorption of antimony onto iron oxyhydroxides: Adsorption behavior and surface structure. *J. Hazard. Mat.* 276, 339-345.

Gupta, S. S., Bhattacharyya, K. G., 2011. Kinetics of adsorption of metal ions on inorganic materials: A review. *Adv. Colloid Interfac.* 162, 39-58.

Gustafsson, J. P., 2013. Visual MINTEQ. Version 3.1.; Division of Land and Water Resources, Royal Institute of Technology: Stockholm, Sweden.

- Ha, H.N.N., Phuong, N.T.K., An, T.B., Tho, N.T.M., Thang, T.N., Minh, B.Q., Du, C.V., 2016. Arsenate removal by layered double hydroxides embedded into spherical polymer beads: Batch and column studies. *J. Environ. Sci. Health A Tox. Hazard. Subst. Environ. Eng.* 51(5), 403-413.
- Hadnadjev, M., Vulic, T., Marinkovic-Neducin, R., Suchorski, Y., Weiss, H., 2008. The iron oxidation state in Mg–Al–Fe mixed oxides derived from layered double hydroxides: An XPS study. *Appl. Surf. Sci.* 254, 4297–4302.
- Hájek, M., Kocík, J., Frolich, K., Vávra, A., 2017. Mg-Fe mixed oxides and their rehydrated mixed oxides as catalysts for transesterification. *J. Clean. Prod.* 161, 1423-1431.
- Han, D. S., Batchelor, B., Abdel-Wahab, A., 2013. XPS analysis of sorption of selenium(IV) and selenium(VI) to mackinawite (FeS). *Environ. Prog. Sustain. Energy* 32, 84–93.
- Han, Y., Boateng, A.A., Qi, P.X., Lima, I.M., Chang, J., 2013. Heavy metal and phenol adsorptive properties of biochars from pyrolyzed switchgrass and woody biomass in correlation with surface properties. *J. Environ. Manage.* 118, 196–204.
- Han, Z., Sani, B., Mroziak, W., Obst, M., Beckingham, B., Karapanagioti, H.K., Werner D., 2015. Magnetite impregnation effects on the sorbent properties of activated carbons and biochars. *Water Res.* 70, 394–403.
- Hanauer, T., Felix-Henningsen, P., Steffens, D., Kalandadze, B., Navrozashvili, L., Urushadze, T., 2011. In situ stabilization of metals (Cu, Cd, and Zn) in contaminated soils in the region of Bolnisi, Georgia. *Plant Soil* 341, 193-208.
- Harvey, O.R., Herbert B.E., Rhue, R.D., Kuo, L.-J., 2011. Metal Interactions at the Biochar-Water Interface: Energetics and Structure-Sorption Relationships Elucidated by Flow Adsorption Microcalorimetry. *Environ. Sci. Technol.* 45, 5550–5556.
- Hashim, M.A., Mukhopadhyay, S., Sahu, J.N., Sengupta, B., 2011. Remediation technologies for heavy metal contaminated groundwater. *J. Hazard. Mater.* 92, 2355-2388.
- Hayes, K.F., Leckie, J.O., 1987. Modeling ionic strength effects on cation adsorption at hydrous oxide/solution interfaces. *J. Colloid Interface Sci.* 115, 564–572.

- Hayes KF, Papelis C., Leckie, J.O., 1988. Modeling ionic strength effects on anion adsorption at hydrous oxide/solution interfaces. *J. Colloid Interface Sci.* 125, 717–726.
- Hayes, K. F., Redden, G., Ela, W., Leckie, J. O., 1991. Surface complexation models: an evaluation of model parameter estimation using FITEQL and oxide mineral titration data. *J. Colloid Interface Sci.* 142 (2), 448-469.
- He, L.M., Zelazny, L.W., Martens, D.C., Baligar, V.C., Ritchey, K.D., 1997. Ionic Strength Effects on Sulfate and Phosphate Adsorption on γ -Alumina and Kaolinite: Triple-Layer Model. *Soil Sci. Soc. Am. J.* 61, 784-793.
- Heinrich, H.T.M., Bremer, P.J., McQuillan, A.J., Daughney, C.J., 2008. Modelling of the acid-base properties of two thermophilic bacteria at different growth times. *Geochim. Cosmochim. Acta* 72, 4185-4200.
- Herbelin, A. L., Westall, J., 1999. FITEQL - A Computer Program for Determination of Chemical Equilibrium Constants from Experimental Data, Dept of Chemistry Rep 99–01, Oregon State University, Corvallis, OR, USA.
- Ho, Y.S., McKay, G., 1998. A Comparison of Chemisorption Kinetic Models Applied to Pollutant Removal on Various Sorbents. *Process Saf. Environ.* 76, 332-340.
- Ho, Y.S., McKay, G., 1999. Pseudo-second order model for sorption processes. *Process Biochem.* 34(5), 451-465.
- Ho, Y.S., 2006. Review of second-order models for adsorption systems. *J. Hazard. Mater.* 136(3), 681-689.
- Ho, S.H., Chen, Y.D., Yang, Z.K., Nagarajan, D., Chang, J.S., Ren, N.Q., 2017. High-efficiency removal of lead from wastewater by biochar derived from anaerobic digestion sludge. *Bioresour. Technol.* 246, 142–149.
- Hu, B., Ye, F., Jin, C., Ma, X., Huang, C., Sheng, G., Ma, J., Wang, X., Huang, Y., 2017a. The enhancement roles of layered double hydroxide on the reductive immobilization of selenate by nanoscale zero valent iron: Macroscopic and microscopic approaches. *Chemosphere* 184, 408-416.
- Hu, B., Huang, C., Li, X., Sheng, G., Li, H., Ren, X., Ma, J., Wang, J., Huang, Y., 2017b. Macroscopic and spectroscopic insights into the mutual interaction of graphene oxide, Cu(II), and Mg/Al layered double hydroxides. *Chem. Eng. J.* 313, 527-534.

- Hu, B., Hu, Q., Chen, C., Sun, Y., Xu, D., Sheng, G., 2017c. New insights into Th(IV) speciation on sepiolite: Evidence for EXAFS and modeling investigation. *Chem. Eng. J.* 322, 66-72.
- Hu, B., Chen, G., Jin, C., Hu, J., Huang, C., Sheng, J., Sheng, G., Ma, J., Huang, Y., 2017d. Macroscopic and spectroscopic studies of the enhanced scavenging of Cr(VI) and Se(VI) from water by titanate nanotube anchored nanoscale zero-valent iron. *J. Hazard. Mater.* 336, 214-221.
- Huang, P. P., Cao, C. Y., Wei, F., Sun, Y. B., Song, W. G., 2015. MgAl layered double hydroxides with chloride and carbonate ions as interlayer anions for removal of arsenic and fluoride ions in water. *RSC Adv.* 5, 10412–10417.
- Hudcová, B., Veselská, V., Filip, J., Číhalová, S., Komárek, M., 2017. Sorption mechanisms of arsenate on Mg-Fe layered double hydroxides: A combination of adsorption modeling and solid state analysis. *Chemosphere* 168, 539-548.
- Hudcová, B., Veselská, V., Filip, J., Číhalová, S., Komárek, M., 2018. Highly effective Zn(II) and Pb(II) removal from aqueous solutions using Mg-Fe layered double hydroxides: Comprehensive adsorption modeling coupled with solid state analyses, *J. Clean. Prod.* 171, 944-953.
- Hudcová, B., Vítková, M., Ouředníček, P., Komárek, M., 2019. Stability and stabilizing efficiency of Mg-Fe layered double hydroxides and mixed oxides in aqueous solutions and soils with elevated As(V), Pb(II) and Zn(II) contents. *Sci. Total Environ.* 648, 1511-1519.
- ICDD, PDF-2 Database, Release 2003, 2003. International Centre for Diffraction Data. Newton Square, PA, USA.
- Idrees, M., Batool, S., Hussain, Q., Ullah, H., Al-Wabel, M.I., Ahmad, M., Kong, J., 2016. High-efficiency remediation of cadmium (Cd²⁺) from aqueous solution using poultry manure-and farmyard manure-derived biochars. *Sep. Sci. Technol.* 51, 2307–2317.
- Inyang, M., Gao, B., Ding, W., Pullammanappallil, P., Zimmerman, A.R., Cao X., 2011. Enhanced lead sorption by biochar derived from anaerobically digested sugarcane bagasse. *Sep. Sci. Technol.* 46, 1950–1956.

Isaacs-Paez, E.D., Leyva-Ramos, R., Jacobo-Azuara, A., Martinez-Rosales, J.M., Flores-Cano, J.V., 2014. Adsorption of boron on calcined AlMg layered double hydroxide from aqueous solutions. Mechanism and effect of operating conditions. *Chem. Eng. J.* 245, 248-257.

Izumi, Y., Kiyotaki, F., Minato, T., Seida, Y., 2002. X-ray Absorption Fine Structure Combined with Fluorescence Spectrometry for Monitoring Trace Amounts of Lead Adsorption in the Environmental Conditions. *Anal. Chem.*, 74, 3819-3823.

Izumi, Y., Kiyotaki, F., Minato, T., Masih, D., Seida, Y., 2005. Monitoring trace amounts of lead and arsenic adsorption by x-ray absorption fine structure combined with fluorescence spectrometry. *Phys. Scripta.* T115, 933–935.

Jaiswal, A., Gautam, R. K., Chattopadhyaya, M. C., 2014. Layered Double Hydroxides and the Environment: An Overview 3, In: Tiwari, A., Syväjärvi, M. (Eds.), *Advanced Materials for Agriculture, Food and Environmental Safety*, John Wiley & Sons, Inc., Hoboken, New Jersey, pp. 1-26.

Jeppu, G.P., Clement, T.P., 2012. A modified Langmuir-Freundlich isotherm model for simulating pH-dependent adsorption effects. *J. Contam. Hydrol.* 129–130, 46–53.

Jiang, T.-Y., Jiang, J., Xu, R.-K., Li, Z., 2012. Adsorption of Pb(II) on variable charge soils amended with rice-straw derived biochar. *Chemosphere* 89, 249–256.

Jiang, J.-Q., Ashekuzzaman, S.M., Hargreaves, J.S.J., McFarlane, A.R., Badruzzaman, A.B.M., Tarek, M.H., 2015. Removal of Arsenic (III) from groundwater applying a reusable Mg-Fe-Cl layered double hydroxide. *J. Chem. Technol. Biotechnol.* 90, 1160–1166.

Jiao, F.P., Shuai, L., Yu, J.G., Jiang, X.Y., Chen, Y.Q., Du, S.L., 2014. Adsorption of glutamic acid from aqueous solution with calcined layered double Mg–Fe–CO₃ hydroxide. *Trans. Nonferrous Met. Soc. China* 24, 3971-3978.

Jobbágy, M., Regazzoni, A.E., 2011. Dissolution of nano-size Mg-Al-Cl hydrotalcite in aqueous media. *Appl. Clay Sci.* 51, 366-369.

Jolstera, R., Gunneriusson, L., Forsling, W., 2010. Adsorption and surface complex modeling of silicates on maghemite in aqueous suspensions. *J. Colloid Interface Sci.* 342 (2), 493–498.

- Kameda, T., Saito, S., Umetsu, Y., 2005. Mg-Al layered double hydroxide intercalated with ethylene-diaminetetraacetate anion: Synthesis and application to the uptake of heavy metal ions from an aqueous solution. *Sep. Purif. Technol.* 47, 20-26.
- Kameda, T., Honda, M., Yoshioka, T., 2011. Removal of antimonate ions and simultaneous formation of a brandholzite-like compound from magnesium–aluminum oxide. *Sep. Purif. Technol.* 80, 235-239.
- Kameda, T., Nakamura, M., Yoshioka, T., 2012. Removal of antimonate ions from an aqueous solution by anion exchange with magnesium–aluminum layered double hydroxide and the formation of a brandholzite-like structure. *J. Environ. Sci. Health A Tox. Hazard. Subst. Environ. Eng.* 47(8), 1146-1151.
- Kameda, T., Kondo, E., Yoshioka, T., 2015. Equilibrium and kinetics studies on As(V) and Sb(V) removal by Fe²⁺-doped Mg-Al layered double hydroxides. *J. Environ. Manage* 151, 303-309.
- Kameda, T., Oba, J., Yoshioka, T., 2017. Removal of boron and fluoride in wastewater using Mg-Al layered double hydroxide and Mg-Al oxide. *J. Environ. Manage.* 188, 58-63.
- Kang, D., Yu, X., Tong, S., Ge, M., Zuo, J., Cao, C., Song, W., 2013. Performance and mechanism of Mg/Fe layered double hydroxides for fluoride and arsenate removal from aqueous solution. *Chem. Eng. J.* 228, 731-740.
- Khare, P., Dilshad, U., Rout, P.K., Yadav, V., Jain, S., 2017. Plant refuses driven biochar: application as metal adsorbent from acidic solutions. *Arab J Chem* 10, 3054–3063.
- Khuri, A.I., Mukhopadhyay, S., 2010. Response Surface Methodology, In: Wegman, E.J., Said, Y.H., Scott, D.W. (Eds.), *Wiley Interdisciplinary Reviews - Computational Statistics*, Vol. 2, No 2. Wiley, Hoboken, New Jersey, pp. 128-149.
- Kim, W.-K., Shim, T., Kim, Y.-S., Hyun, S., Ryu, C., Park, Y.-K., Jung, J., 2013. Characterization of cadmium removal from aqueous solution by biochar produced from a giant *Miscanthus* at different pyrolytic temperatures. *Bioresour. Technol.* 138, 266–270.

Kiso, Y., Jung, Y. J., Yamada, T., Nagai, M., Min, K.S., 2005. Removal properties of arsenic compounds with synthetic hydrotalcite compounds. *Water Sci. Technol.: Water Supply* 5 (5), 75-81.

Klemkaite, K., Prosycevas, I., Taraskevicius, R., Khinsky, A., Kareiva, A., 2011. Synthesis and characterization of layered double hydroxides with different cations (Mg, Co, Ni, Al), decomposition and reformation of mixed metal oxides to layered structures. *Cent. Eur. J. Chem.* 9(2), 275-282.

Kloprogge, J.T., Frost, R.L., 2010. Infrared and Raman Spectroscopic Studies of Layered Double Hydroxides (LDHs), In: Rives, V. (Eds.), *Layered Double Hydroxides: Present and Future*, Nova Science Publishers, Inc., New York, pp. 153-215.

Klug, H.P., Alexander, L.E., 1954. *X-ray diffraction procedures for polycrystalline and amorphous materials*, John Wiley & Sons, New York.

Kołodyska, D., Wnętrzak, R., Leahy, J.J., Hayes, M.H.B., Kwapiński, W., Hubicki, Z., 2012. Kinetic and adsorptive characterization of biochar in metal ions removal. *Chem. Eng. J.* 197, 295–305.

Komárek, M., Vaněk, A., Ettler, V., 2013. Chemical stabilization of metals and arsenic in contaminated soils using oxides - A review. *Environ. Pollut.* 172, 9-22.

Komárek, M., Koretsky, C. M., Stephen, K. J., Alessi, D. S., Chrastný, V., 2015. Competitive Adsorption of Cd(II), Cr(VI), and Pb(II) onto Nanomaghemite: A Spectroscopic and Modeling Approach. *Environ. Sci. Technol.* 49 (21), 12851-12859.

Komárek, M., Antelo, J., Králová, M., Veselská, V., Čihalová, S., Chrastný, V., Ettler, V., Filip, J., Yu, Q., Fein, J.B., Koretsky, C.M., 2018. Revisiting models of Cd, Cu, Pb and Zn adsorption onto Fe(III) oxides. *Chem. Geol.* 493, 189-198.

Komarneni, S., Kozai, N., Roy, R., 1998. Novel function for anionic clays: selective transition metal cation uptake by diadochy. *J. Mater. Chem.* 8, 1329-1331.

Koretsky, C., 2000. The significance of surface complexation reactions in hydrologic systems: a geochemist's perspective. *J. Hydrol.* 230, 127-171.

- Kovanda, F., Balek, V., Dorničák, V., Martinec, P., Mašláň, M., Bílková, L., Koloušek, D., Bountsewa, I.M., 2003. Thermal behaviour of syntetic pyroaurite-like anionic clay. *J. Therm. Anal. Calorim.* 71, 727-737.
- Kumpiene, J., Lagerkvist, A., Maurice, C., 2008. Stabilization of As, Cr, Cu, Pb and Zn in soil using amendments - A review. *Waste Manage.* 28, 215-225.
- Kumpiene, J., Ore, S., Renella, G., Mench, M., Lagerkvist, A., Maurice, C., 2006. Assessment of zerovalent iron for stabilization of chromium, copper, and arsenic in soil. *Environ. Pollut.* 144, 62-69.
- Kuśtrowski, P., Sułkowska, D., Chmielarz, L., Olszewski, P., Rafalska-Łasocha, A., Dziembaj, R., 2005. Effect of rehydration conditions on the catalytic activity of hydrotalcite-derived Mg-Al oxides in aldolization of acetone. *React. Kinet. Catal. Lett.* 85, 383-390.
- Lagergren, S., 1898. Zur theorie der sogenannten adsorption gelöster stoffe. *Kungliga Svenska vetenskapsakademiens handlingar* 24, 1-39.
- Lamb, D.T., Ming, H., Megharaj, M., Naidu, R., 2009. Heavy metal (Cu, Zn, Cd and Pb) partitioning and bioaccessibility in uncontaminated and long-term contaminated soils. *J. Hazard. Mater.* 171, 1150-1158.
- Langmuir, I., 1918. The adsorption of gases on plane surfaces of glass, mica, and platinum. *J. Am. Chem. Soc.* 40, 1361-1403.
- Lazaridis, N. K., Hourzemanoglou, A., Matis, K. A., 2002. Flotation of metal-loaded clay anion exchangers. Part II: the case of arsenates. *Chemosphere* 47 (3), 319-324.
- Lee, S.-H., Choi, H., Kim, K.-W., 2018a. Removal of As(V) and Sb(V) in aqueous solution by Mg/Al layered double hydroxide-incorporated polyethersulfone polymer beads (PES-LDH). *Environ. Geochem. Health.* 40(5), 2119-2129.
- Lee, S.-H., Choi, H., Kim, K.-W., 2018b. Removal of As(V) and Sb(V) in water using magnetic nanoparticle-supported layered double hydroxide nanocomposites. *J. Geochem. Explor.* 184 (2018b) 247-254.
- Leftheriotis, G., Papaefthimiou, S., Yianoulis, P., Siokou, A., Kefalas, D., 2003. Structural and electrochemical properties of opaque sol-gel deposited WO₃ layers. *Appl. Surf. Sci.* 218, 275-280.

- Lehmann, J., Joseph, S., 2009. Biochar for environmental management: an introduction, In: Lehmann, J., Joseph, S. (Eds.), *Biochar for Environmental Management*, Earthscan, USA, pp. 1–12.
- Lenoble, V., Laclautre, C., Serpaud, B., Deluchat, V., Bollinger, J.-C., 2004. As(V) retention and As(III) simultaneous oxidation and removal on a MnO₂-loaded polystyrene resin. *Sci. Total Environ.* 326, 197–207.
- Leuz, A.K., Monch, H., Johnson, C.A., 2006. Sorption of Sb (III) and Sb (V) to goethite: influence on Sb (III) oxidation and mobilization. *Environ. Sci. Technol.* 40, 7277– 7282.
- Li, X.Q., Zhang, W.X., 2007. Sequestration of metal cations with zerovalent iron nanoparticles – a study with high resolution X-ray photoelectron spectroscopy (HR-XPS). *J. Phys. Chem. C* 111, 6939-6946.
- Li, R., Wang, J.J., Zhou, B., Awasthi, M.K., Ali, A., Zhang, Z., Gaston, L.A., Lahori, A.H., Mahar, A., 2016. Enhancing phosphate adsorption by Mg/Al layered double hydroxide functionalized biochar with different Mg/Al ratios. *Sci. Tot. Environ.* 559, 121–129.
- Li, S., Wang, W., Liang, F., Zhang, W.X., 2017. Heavy metal removal using nanoscale zero-valent iron (nZVI): Theory and application. *J. Hazard. Mater.* 322: 163–171.
- Liang, X., Hou, W., Xu, J., 2009. Sorption of Pb(II) on Mg-Fe Layered Double Hydroxide. *Chinese J. Chem.* 27, 1981-1988.
- Liang, X., Hou, W., Xu, Y., Sun, G., Wang, L., Sun, Y., Qin, X., 2010. Sorption of lead ion by layered double hydroxide intercalated with diethylenetriaminepentaacetic acid. *Colloids Surf., A* 366, 50-57.
- Liang, X., Zang, Y., Xu, Y., Tan, X., Hou, W., Wang, L., Sun, Y., 2013. Sorption of metal cations on layered double hydroxides. *Colloid. Surf. A* 433, 122-131.
- Limousin, G., Gaudet, J. P., Charlet, L., Szenknect, S., Barthès, V., Krimissa, M., 2007. Sorption isotherms: A review on physical bases, modeling and measurement. *Appl. Geochem.* 22, 249–275.
- Liu, Y. T., Wang, M. K., Chen, T. Y., Chiang, P. N., Huang, P. M., Lee, J. F., 2006. Arsenate sorption on lithium/aluminum layered double hydroxide intercalated by

chloride and on gibbsite: sorption isotherms, envelopes, and spectroscopic studies. *Environ. Sci. Technol.* 40 (24), 7784–7789.

Low, M.J.D., 1960, Kinetics of chemisorption of gases on solids. *Chem. Rev.* 60, 267-312.

Lu, H., Zhang, W., Yang, Y., Huang, X., Wang, S., Qiu, R., 2012. Relative distribution of Pb²⁺ sorption mechanisms by sludge-derived biochar. *Water Res.* 46, 854–862.

Lu, H., Zhu, Z., Zhang, H., Zhu, J., Qiu, Y., 2015. Simultaneous removal of arsenate and antimonate in simulated and practical water samples by adsorption onto Zn/Fe layered double hydroxide. *Chem. Eng. J.* 276, 365–375.

Lu, H., Zhu, Z., Zhang, H., Zhu, J., Qiu, Y., 2015. Simultaneous removal of arsenate and antimonate in simulated and practical water samples by adsorption onto Zn/Fe layered double hydroxide. *Chem. Eng. J.* 276, 365–375.

Luengo, C.V., Volpe, M.A., Avena, M.J., 2017. High sorption of phosphate on Mg-Al layered double hydroxides: Kinetics and equilibrium. *J. Environ. Chem. Eng.* 5, 4656-4662.

Majzlan, J., Števkó, M., Lánczos, T., 2016. Soluble secondary minerals of antimony in Pezinok and Kremnica (Slovakia) and the question of mobility or immobility of antimony in mine waters. *Environ. Chem.* 13, 927–935.

Martínez-Lladó, X., de Pablo, J., Giménez, J., Ayora, C., Martí, V., Rovira, M., 2008. Sorption of Antimony (V) onto Synthetic Goethite in Carbonate Medium. *Solvent Extr. Ion. Exc.* 26, 289-300.

Maurice, P.A., 2009. *Environmental Surfaces and Interfaces from the Nanoscale to the Global Scale.* John Wiley and Sons, Hoboken, NJ.

McBride, M.B., 1994. *Environmental Chemistry of Soils,* Oxford University Press, New York.

McBride, M.B., 1997. A critique of diffuse double layer models applied to colloid and surface chemistry. *Clays Clay Miner.* 45, 598–608.

- McCann, C.M., Gray, N.D., Tourney, J., Davenport, R.J., Wade, M., Finlay, N., Hudson-Edwards, K.A., Johnson, K.L., 2015. Remediation of a historically Pb contaminated soil using a model natural Mn oxide waste. *Chemosphere* 138, 211-217.
- McComb, K.A., Craw, D., McQuillan, A.J., 2007. ATR-IR Spectroscopic Study of Antimonate Adsorption to Iron Oxide. *Langmuir* 23, 12125-12130.
- Melo, C. R., Riella, H. G., Kuhnen, N. C., Angioletto, E., Melo, A. R., Bernardin, A. L. M., da Rocha M. R., da Silva, L., 2012. Synthesis of 4A Zeolites from Kaolin for obtaining 5A Zeolites through Ionic Exchange for Adsorption of Arsenic. *Mater. Sci. Eng. B*, 345–349.
- Michálková, Z., Komárek, M., Šillerová, H., Della Puppa, L., Joussein, E., Bordas, F., Vaněk, A., Vaněk, O., Ettler, V., 2014. Evaluating the potential of three Fe- and Mn-(nano)oxides for the stabilization of Cd, Cu and Pb in contaminated soils. *J. Environ. Manage.* 146, 226-234.
- Michálková, Z., Komárek, M., Veselská, V., Číhalová, S., 2016a. Selected Fe and Mn (nano)oxides as perspective amendments for the stabilization of As in contaminated soils. *Environ. Sci. Pollut. Res.* 23, 10841-10854.
- Michálková, Z., Komárek, M., Vítková, M., Řečínská, M., Ettler, V., 2016b. Stability, transformations and stabilizing potential of an amorphous manganese oxide and its surface-modified form in contaminated soils. *Appl. Geochem.* 75, 125-136.
- Millange, F., Walton, R.I., O'Hare, D., 2000. Time-resolved in situ X-ray diffraction study of the liquid-phase reconstruction of Mg-Al-carbonate hydrotalcite-like compounds. *J. Mater. Chem.* 10, 1713-1720.
- Mills, S., Christy, A., Genin, J.-M., Kameda, T., Colombo, F., 2012. Nomenclature of the hydrotalcite supergroup: natural layered double hydroxides. *Mineral. Mag.* 76, 1289–336.
- Mitsunobu, S., Takahashi, Y., Sakai, Y., Inumaru, K., 2008. Interaction of Synthetic Sulfate Green Rust with Antimony(V). *Environ. Sci. Technol.* 43(2), 318-323.
- Miyata, S., 1983. Anion-exchange properties of hydrotalcite-like compounds. *Clay Miner.* 31, 305–311.

- Mohan, D., Pittman, C.U., 2007. Arsenic removal from water/wastewater using adsorbents-A critical review. *J. Hazard. Mater.* 142(1-2), 1-53.
- Mohan, D., Pittman Jr., C.U., Bricka, M., Smith, F., Yancey, B., Mohammad, J., Steele, P.H., Alexandre-Franco, M.F., Gómez-Serrano, V., Gong, H., 2007. Sorption of arsenic, cadmium, and lead by chars produced from fast pyrolysis of wood and bark during bio-oil production. *J. Colloid Interface Sci.* 310, 57-73.
- Mohan, D., Sarswat, A., Ok, Y.S., Pittman Jr., C.U., 2014a. Organic and inorganic contaminants removal from water with biochar, a renewable, low cost and sustainable adsorbent – A critical review. *Bioresour. Technol.* 160, 191–202.
- Mohan, D., Kumar, H., Sarswat, A., Alexandre-Franco, M., Pittman Jr., C.U., 2014b. Cadmium and lead remediation using magnetic oak wood and oak bark fast pyrolysis biochars. *Chem. Eng. J.* 236, 513–528.
- Mohan, D., Kumar, H., Sarswat, A., Alexandre-Franco, M., Pittman Jr., C.U., 2015. Cadmium and lead remediation using magnetic oak wood and oak bark fast pyrolysis bio-chars. *Chem. Eng. J.* 236, 513–528.
- Moyo, M., Lindiwe, S.T., Sebata, E., Nyamunda, B.C., Guyo, U., 2016. Equilibrium, kinetic, and thermodynamic studies on biosorption of Cd(II) from aqueous solution by biochar. *Res. Chem. Intermed.* 42, 1349–1362.
- Mubarak, N., Kundu, A., Sahu, J., Abdullah, E., Jayakumar, N., 2014. Synthesis of palm oil empty fruit bunch magnetic pyrolytic char impregnating with FeCl₃ by microwave heating technique. *Biomass Bioenerg.* 61, 265–275.
- Nachtegaal, M., Sparks, D.L., 2004. Effect of iron oxide coatings on zinc sorption mechanisms at the clay-mineral/water interface. *J. Colloid Interface Sci.* 276, 13-23.
- O'Carroll, D., Sleep, B., Krol, M., Boparai, H., Kocur, C., 2013. Nanoscale zero valent iron and bimetallic particles for contaminated site remediation. *Adv. Water Resour.* 51, 104–122.
- Oliveira, L.C.A., Rios, R.V.R.A., Fabris, J.D., Garg, V., Sapag, K., Lago, R.M., 2002. Activated carbon/iron oxide magnetic composites for the adsorption of contaminants in water. *Carbon* 40, 2177–2183.

- Paikaray, S., Hendry, M. J., Essilfie-Dughan, J., 2013. Controls on arsenate, molybdate, and selenate uptake by hydrotalcite-like layered double hydroxides. *Chem. Geol.* 345, 130-138.
- Palmer, S. J., Soissonard, A., Frost, R. L., 2009. Determination of the mechanism(s) for the inclusion of arsenate, vanadate, or molybdate anions into hydrotalcites with variable cationic ratio. *J. Colloid Interface Sci.* 329, 404–409.
- Park, M., Choi, C. L., Seo, Y. J., Yeo, S. K., Choi, J., Komarneni, S., Lee, J. H., 2007. Reactions of Cu²⁺ and Pb²⁺ with Mg/Al layered double hydroxide. *Appl. Clay Sci.* 37, 143-148.
- Park, J.Y., Kim, J.H., 2011. Characterization of adsorbed arsenate on amorphous and nano crystalline MgFe-layered double hydroxides. *J. Nanopart. Res.* 13, 887-894.
- Park, J.H., Cho, J.S., Ok, Y.S., Kim, S.H., Kang, S.W., Choi, I.W., Heo, J.S., DeLaune, R.D., Seo, D.C., 2015. Competitive adsorption and selectivity sequence of heavy metals by chicken bone-derived biochar: Batch and column experiment. *J. Environ. Sci. Health A.* 50, 1194–1204.
- Park, J.H., Ok, Y.S., Kim, S.H., Cho, J.S., Heo, J.S., Delaune, R.D., Seo, D.C., 2016a. Competitive adsorption of heavy metals onto sesame straw biochar in aqueous solutions. *Chemosphere* 142, 77-83.
- Park, J.H., Cho, J.S., Ok, Y.S., Kim, S.H., Heo, J.S., Delaune, R.D., Seo, D.C., 2016b. Comparison of single and competitive metal adsorption by pepper stem biochar. *Arch. Agron. Soil Sci.*, 62, 617–632.
- Parkhurst, D.L., Appelo, C.A.J., 2013. Description of Input and Examples for PHREEQC Version 3 - a Computer Program for Speciation, Batch-reaction, One-dimensional Transport, and Inverse Geochemical Calculations. U.S. Geological Survey Techniques and Methods, Denver.
- Peng, F., Luo, T., Yuan, Y., 2014. Controllable synthesis of Mg–Fe layered double hydroxide nanoplates with specific Mg/Fe ratios and their effect on adsorption of As(V) from water. *New J. Chem.* 38, 4427-4433.
- Peng, X., Liu, X., Zhou, Y., Peng, B., Tang, L., Luo, L., Yao, B., Deng, Y., Tang, J., Zeng, G., 2017. New insights into the activity of a biochar supported nanoscale

zerovalent iron composite and nanoscale zero valent iron under anaerobic or aerobic conditions. *RSC Adv.* 7, 8755-8761.

Poo, K.-M., Son, E.-B., Chang, J.-S., Ren, X., Choi, Y.-J., Chae, K.-J., 2018. Biochars derived from wasted marine macro-algae (*Saccharina japonica* and *Sargassum fusiforme*) and their potential for heavy metal removal in aqueous solution. *J. Environ. Manage.* 206, 364–372.

Prucek, R., Tuček, J., Kolařík, J., Filip, J., Marušák, Z., Sharma, V. K., Zbořil, R., 2013. Ferrate(VI)-Induced Arsenite and Arsenate Removal by In-Situ Structural Incorporation into Magnetic Iron(III) Oxide Nanoparticles. *Environ. Sci. Technol.* 47, 3283–3292.

Qi, P., Pichler, T., 2016. Sequential and simultaneous adsorption of Sb(III) and Sb(V) on ferrihydrite: Implications for oxidation and competition. *Chemosphere* 145, 55-60.

Qian, L., Zhang, W., Yan, J., Han, L., Chen, Y., Ouyang, D., Chen, M., 2017. Nanoscale zero-valent iron supported by biochars produced at different temperatures: Synthesis mechanism and effect on Cr(VI) removal. *Environ. Pollut.* 223, 153-160.

Quevauviller, P.H, 1998. Operationally defined extraction procedures for soil and sediment analysis I. Standardization. *Trends Anal. Chem.* 17, 289-298.

Rakshit, S., Sarkar, D., Datta, R., 2015. Surface complexation of antimony on kaolinite. *Chemosphere* 119, 349–354.

Rauret, G., Lopez-Sanchez, J.F., Sahuquillo, A., Barahona, E., Lachica, M., Ure, A.M., Davidson, C.M., Gomez, A., Luck, D., Bacon, J., Yli-Halla, M., Muntau, H., Quevauviller, P., 2000. Application of a modified BCR sequential extraction (three-step) procedure for the determination of extractable trace metal contents in a sewage sludge amended soil reference material (CRM 483), complemented by a three-year stability study of acetic acid and EDTA extractable metal content. *J. Environ. Monit.* 2, 228-233.

Reddy, D.H.K., Lee, S.-M., 2014. Magnetic biochar composite: Facile synthesis, characterization, and application for heavy metal removal. *Colloid Surf. A-Physicochem. Eng. Asp.* 454, 96-103.

- Regmi, P., Garcia Moscoso, J.L., Kumar, S., Cao, X., Mao, J., Schafran, G., 2012. Removal of copper and cadmium from aqueous solution using switchgrass biochar produced via hydrothermal carbonization process. *J. Environ. Manage.* 109, 61-69.
- Reich, T. J., Koretsky, C. M., 2011. Adsorption of Cr(VI) on γ -alumina in the presence and absence of CO₂: Comparison of three surface complexation models. *Geochim. Cosmochim. Acta* 75 (22), 7006–7017.
- Reich, T.J., Das, S., Koretsky, C.M., Lund, T.J., Landry, C.J., 2010. Surface complexation modeling of Pb(II) adsorption on mixtures of hydrous ferric oxide, quartz and kaolinite. *Chem. Geol.* 275, 262-271.
- Richardson, M.C., Braterman, P.S., 2009. Cation exchange by anion-exchanging clays: the effects of particle aging. *J. Mater. Chem.* 19, 7965-7975.
- Rojas Delgado, R., Arandigoyen Vidaurre, M., De Pauli, C. P., Ulibarri, M. A., Avena, M. J., 2004. Surface-charging behavior of Zn–Cr layered double hydroxide. *J. Colloid Interface Sci.* 280, 431-441.
- Rojas Delgado, R., De Pauli, C. P., Barriga Carrasco, C., Avena, M.J., 2008. Influence of MII/MIII ratio in surface-charging behavior of Zn–Al layered double hydroxides. *Appl. Clay Sci.* 40, 27-37.
- Ropp, R.C., 2013. *Encyclopedia of the Alkaline Earth Compounds*. Elsevier, Oxford.
- Saeidnia, S., Asadollahfardi, G., Darban, A.K., Mohseni, M., 2016. Simulation of antimony adsorption on nano-zero valent iron and kaolinite and analyzing the influencing parameters. *Water Sci. Technol.* 73(10), 2493-2500.
- Saletnik, B., Zagula, G., Grabek-Lejko, D., Kasprzyk, I., Bajcar, M., Czernicka, M., Puchalski, C., 2017. Biosorption of cadmium(II), lead(II) and cobalt(II) from aqueous solution by biochar from cones of larch (*Larix decidua* Mill. subsp. *decidua*) and spruce (*Picea abies* L. H. Karst). *Environ. Earth Sci.* 76, 574.
- Santona, L., Castaldi, P., Melis, P., 2006. Evaluation of the interaction mechanisms between red muds and heavy metals. *J. Hazard. Mater.* 136, 324-329.
- Sato, T., Onai, S., Yoshioka, T., Okuwaki, A., 1993. Causticization of sodium carbonate with rock-salt type magnesium aluminium oxide formed by the thermal

decomposition of hydrotalcite-like layered double hydroxide. *J. Chem. Technol. Biot.* 57, 137–140.

Seida, Y., Nakano, Y., 2000. Removal of humic substances by layered double hydroxide containing iron. *Water Res.* 34(5), 1487-1494.

Seida, Y., Nakano, Y., Nakamura, Y., 2001. Rapid removal of dilute lead from water by pyroaurite-like compound. *Water Res.* 35, 2341-2346.

Sejkora, J., Ozdín, D., Ďuďa, R., 2010. The supergene mineral association with brandholzite from Pernek, Malé Karpaty Mountains, Slovak Republic. *J. Geosci.* 55, 149–160.

Sekulić, M.T., Pap, S., Stojanović, Z., Bošković, N., Radonić, J., Knudsen T.Š., 2018. Efficient removal of priority, hazardous priority and emerging pollutants with *Prunus armeniaca* functionalized biochar from aqueous wastes: Experimental optimization and modelling. *Sci. Total Environ.* 613–614, 736–750.

Sepehr, M.N., Yetilmeszooy, K., Marofi, S., Zarrabi, M., Ghaffari, H.R., Fingas, M., Foroughi, M., 2014. Synthesis of nanosheet layered double hydroxides at lower pH: Optimization of hardness and sulfate removal from drinking water samples. *J. Taiwan Inst. Chem. Eng.* 45, 2786-2800.

Shen, W., Li, Z., Liu, Y., 2008. Surface chemical functional groups modification of porous carbon. *Recent Patents Chem. Eng.* 1, 27–40.

Shen, Z., Jin, F., Wang, F., McMillan, O., Al-Tabbaa, A., 2015. Sorption of lead by Salisbury biochar produced from British broadleaf hardwood. *Bioresour. Technol.*, 193, 553–556.

Simonin, J. P., 2016. On the comparison of pseudo-first order and pseudo-second order rate laws in the modeling of adsorption kinetics. *Chem. Eng. J.* 300, 254-563.

Singh, S., Thiyagarajan, P., Kant, K.M., Anita, D., Thirupathiah, S., Rama, N., Tiwari, B., Kottaisamy, M., Rao, M.S.R., 2007. Structure, microstructure and physical properties of ZnO based materials in various forms: bulk, thin film and nano. *J. Phys. D: Appl. Phys.* 40, 6312-6327.

- Singh, R., Singh, S., Parihar, P., Singh V.P., Prasad, S.M., 2015. Arsenic contamination, consequences and remediation techniques: A review. *Ecotox. Environ. Safe.* 112, 247-270.
- Smith, K.S., 1999. Metal sorption on mineral surfaces: An overview with examples relating to mineral deposits. *Review in Economic Geology* 6A, 161-182.
- Sohi, S.P., Krull, E., Lopez-Capel, E., Bol, R., 2010. A review of biochar and its use and function in soil. *Adv. Agron.* 105, 47–82.
- Sommella, A., Caporale, A. G., Denecke, M. A., Mangold, S., Pigna, M., Santoro, A., Terzano, R., Violante, A., 2015. Nature and reactivity of layered double hydroxides formed by coprecipitating Mg, Al and As(V): Effect of arsenic concentration, pH, and aging. *J. Hazard. Mater.* 35, 504-512.
- Sparks, D.L., 2003. *Environmental soil chemistry*, 2nd edition, Academic Press, San Diego.
- Sposito, G., 1989. *The Chemistry of Soils*, Oxford Univ. Press, New York.
- Stefaniuk, M., Oleszczuk, P., Ok, Y.S., 2016. Review on nano zerovalent iron (nZVI): From synthesis to environmental applications. *Chem. Eng. J.* 287, 618–632.
- Stern, O., 1924. Zur Theorie der Elektrolytischen Doppelschicht. *Z. Elektrochem.* 30, 508–516.
- Sternlieb, M.P., Pasteris, J.D., Williams, B.R., Krol, K.A., Yoder, C.H., 2010. The structure and solubility of carbonated hydroxyl and chloro lead apatites. *Polyhedron* 29, 2364-2372.
- Stumm, W., Kummert, K., and Sigg, L., 1980. A ligand exchange model for the adsorption of inorganic and organic ligands at hydrous oxide interfaces. *Croat. Chem. Acta* 53, 291–312.
- Su, H., Fang, Z., Tsang, E.T., Zheng, L., Cheng, W., Fang, J., Zhao, D., 2016. Remediation of hexavalent chromium contaminated soil by biochar-supported zero-valent iron nanoparticles. *J. Hazard. Mater.* 318, 533-540.

Sumin de Portilla, V. I., 1974. Infrared spectroscopic investigations of the structure of some natural arsenates and the nature of H-bonds in their structures. *Can. Mineral.* 12, 262-268.

Sun, M., Xiao, Y., Zhang, L., Gao, X., Yan, W., Wang, D., Su, J., 2015a. High uptake of Cu²⁺, Zn²⁺ or Ni²⁺ on calcined MgAl hydroxides from aqueous solutions: Changing adsorbent structures. *Chem. Eng. J.* 272, 17-27.

Sun, Y., Liu, R., Zeng, X., Lin, Q., Bai, L., Li, L., Su, S., Wang, Y., 2015b. Reduction of arsenic bioavailability by amending seven inorganic materials in arsenic contaminated soil. *J. Integr. Agr.* 14, 1414–1422.

Šrámek and Zeman, 2004. Introduction to environmental hydrogeochemistry, Vydavatelství MU, Brno.

Tan, K. H., 2010. Principles of Soil Chemistry, 4th edition, CRC Press, Boca Raton, FL, USA.

Tan, X., Liu, Y., Zeng, G., Wang, X., Hu, X., Gu, Y., Yang, Z., 2015. Application of biochar for the removal of pollutants from aqueous solutions. *Chemosphere* 125, 70–85.

Tan, X.F., Liu, Y.G., Gu, Y.L., Xu, Y., Zeng, G.M., Hu, X.J., Liu, S.B., Wang, X., Liu, S.M., Li, J., 2016a. Biochar-based nano-composites for the decontamination of wastewater: A review. *Bioresour. Technol.* 212, 318-333.

Tan, X.F., Liu, Y.G., Gu, Y.L., Liu, S.B., Zeng, G.M., Cai, X., Hu, X.J., Wang, H., Liu, S.M., Jiang, L.H., 2016b. Biochar pyrolyzed from MgAl-layered double hydroxides pre-coated ramie biomass (*Boehmeria nivea* (L.) Gaud.): Characterization and application for crystal violet removal. *J. Environ. Manage.* 184, 85-93.

Tan, X.F., Liu, S.B., Liu, Y.G., Gu, Y.L., Zeng, G.M., Cai, X.X., Yan, Z.L., Yang, C.P., Hu, X.J., Chen, B., 2016c. One-pot synthesis of carbon supported calcined-Mg/Al layered double hydroxides for antibiotic removal by slow pyrolysis of biomass waste. *Sci. Rep.* 6, 39691.

Teixeira, T.P.F., Aquino, S.F., Pereira, S.I., Dias, A., 2014. Use of calcined layered double hydroxides for the removal of color and organic matter from textile effluents: kinetic, equilibrium and recycling studies. *Braz. J. Chem. Eng.* 31(1), 19-26.

Terry, P.A., 2009. Removal of nitrates and phosphates by ion exchange with hydrotalcite. *Environ. Eng. Sci.* 26, 691-696.

Thommes, M., Kaneko, K., Neimark, A.V., Olivier, J.P., Rodriguez-Reinoso, F., Rouquerol, J., Sing, K.S.W., 2015. Physisorption of gases, with special reference to the evaluation of surface area and pore size distribution (IUPAC Technical Report). *Pure Appl. Chem.* 87, 1051-1069.

Tiberg, C., Kumpiene, J., Gustafsson, J.P., Marsz, A., Persson, I., Mench, M., Kleja, D.B., 2016. Immobilization of Cu and As in two contaminated soils with zero-valent iron - long-term performance and mechanisms. *Appl. Geochem.* 67, 144-152.

Tokoro, C., Sakakibara, T., Suzuki, S., 2015. Mechanism investigation and surface complexation modeling of zinc sorption on aluminum hydroxide in adsorption/coprecipitation processes. *Chem. Eng. J.* 279, 86-92.

Tonkin, J.W., Balistrieri, L.S., Murray, J.W., 2004. Modeling sorption of divalent metal cations on hydrous manganese oxide using the diffuse double layer model. *Appl. Geochem.* 19, 29-53.

Torres-Dorante, L.O., Lammel, J., Kuhlmann, H., Witzke, T., Olf, H.W., 2008. Capacity, selectivity, and reversibility for nitrate exchange of a layered double-hydroxide (LDH) mineral in simulated soil solutions and in soil. *J. Plant. Nutr. Soil. Sci.* 171, 777-784.

Tosco, T., Papini, M.P., Viggli C.C., Sethi P., 2014. Nanoscale zerovalent iron particles for groundwater remediation: a review. *J. Clean. Prod.* 77, 10–21.

Trakal, L., Komárek, M., Száková, J., Zemanová, V., Tlustoš, P., 2011. Biochar application to metal-contaminated soil: Evaluating of Cd, Cu, Pb and Zn sorption behavior using single- and multi-element sorption experiment. *Plant. Soil Environ.* 57, 372–380.

Trakal, L., Komárek, M., Száková, J., Tlustoš, P., Tejnecký, V., Drábek, O., 2012. Sorption behaviour of Cd, Cu, Pb and Zn and their interactions in phytoremediated soil. *Int. J. Phytoremediat.* 14, 806–819.

Trakal, L., Bingöl, D., Pohořelý, M., Hruška, M., Komárek, M., 2014a. Geochemical and spectroscopic investigations of Cd and Pb sorption mechanisms on contrasting biochars: Engineering implications. *Bioresour. Technol.* 171, 442–451.

- Trakal, L., Šigut, R., Šillerová, H., Faturíková, D., Komárek, M., 2014b. Copper removal from aqueous solution using biochar: Effect of chemical activation. *Arab. J. Chem.* 7, 43–52.
- Trakal, L., Veselská, V., Šafařík, I., Vítková, M., Číhalová, S., Komárek, M., 2016. Lead and cadmium sorption mechanisms on magnetically modified biochars. *Bioresour. Technol.* 203, 318–324.
- Trakal, L., Michálková, Z., Beesley, L., Vítková, M., Ouředníček, P., Barceló, A.P., Ettler, V., Číhalová, S., Šillerová, H., Komárek, M., 2018. AMOchar: Amorphous manganese oxide coating of biochar improves its efficiency at removing metal(loid)s from aqueous solutions. *Sci. Total Environ.* 625, 71–78.
- Tsai, W.T., Liu, S.C., Chen, H.R., Chang, Y.M., Tsai, Y.L., 2012. Textural and chemical properties of swine-manure-derived biochar pertinent to its potential use as a soil amendment. *Chemosphere* 89, 198–203.
- Türk, T., Alp, I., Deveci, H., 2009. Adsorption of As(V) from water using Mg-Fe-based hydrotalcite (FeHT). *J. Hazard. Mater.* 171, 665-670.
- Turner, B. F., Fein, J. B., 2006. Protonfit: A program for determining surface protonation constants from titration data. *Comput. Geosci.* 32 (9), 1344-1356.
- Undabeytia, T., Nir, S., Rytwo, G., Serban, C., Morillo, E., Maqueda, C., 2002. Modeling adsorption-desorption processes of Cu on edge and planar sites of montmorillonite. *Environ. Sci. Technol.* 36(12), 2677-2683.
- Verheijen, F.G.A., Jeffery, S., Bastos, A.C., van der Velde, M., Diafas, I., 2010. Biochar Application to Soils — A Critical Scientific Review of Effects on Soil Properties, Processes and Functions. EUR 24099 EN, Luxembourg.
- Veselská, V., Fajgar, R., Číhalová, S., Bolanz, R. M., Göttlicher, J., Steininger, R., Siddique, J. A., Komárek, M., 2016. Chromate adsorption on selected soil minerals: surface complexation modeling coupled with spectroscopic investigation. *J. Hazard. Mater.* 318, 433-442.
- Violante, A., Pucci, M., Cozzolino, V., Zhu, J., Pigna, M., 2009. Sorption/desorption of arsenate on/from Mg–Al layered double hydroxides: Influence of phosphate. *J. Colloid Interface Sci.* 333, 63-70.

- Vithanage, M., Rajapaksha, A.U., Dou, X., Bolan, N.S., Yang, J.E., Ok, Y.S., 2013. Surface complexation modeling and spectroscopic evidence of antimony adsorption on iron-oxide-rich red earth soils. *J. Colloid Interface Sci.* 406, 217–224.
- Vithanage, M., Rajapaksha, A.U., Ahmad, M., Uchimiya, M., Dou, X., Alessi, D.S., Ok, Y.S., 2015. Mechanisms of antimony adsorption onto soybean stover-derived biochar in aqueous solutions. *J. Environ. Manage.* 151, 443-449.
- Vítková, M., Komárek, M., Tejnecký, V., Šillerová, H., 2015. Interactions of nano-oxides with low-molecular-weight organic acids in a contaminated soil. *J. Hazard. Mater.* 293, 7-14.
- Vítková, M., Rákosová, S., Michálková, Z., Komárek, M., 2017. Metal(loid)s behaviour in soils amended with nano zero-valent iron as a function of pH and time. *J. Environ. Manage.* 186, 268-276.
- Vulic, T.J., Reitzmann, A.F.K., Lázár, K., 2012. Thermally activated iron containing layered double hydroxides as potential catalyst for N₂O abatement, *Chem. Eng. J.* 207-208, 913-922.
- Wan, S., Wang, S., Li, Y., Gao, B., 2017. Functionalizing biochar with Mg–Al and Mg–Fe layered double hydroxides for removal of phosphate from aqueous solutions. *J. Ind. Eng. Chem.* 47, 246-253.
- Wan, S., Wang, S., Li, Y., Gao, B., 2017. Functionalizing biochar with Mg–Al and Mg–Fe layered double hydroxides for removal of phosphate from aqueous solutions. *J. Ind. Eng. Chem.* 47, 246-253.
- Wang, Y., Gao, H., 2006. Compositional and structural control on anion sorption capability of layered double hydroxides (LDHs). *J. Colloid Interface Sci.* 301, 19–26.
- Wang, S. L., Liu, C. H., Wang, M. K., Chuang, Y. H., Chiang, P. N., 2009. Arsenate adsorption by Mg/Al–NO₃ layered double hydroxides with varying the Mg/Al ratio. *Appl. Clay Sci.* 43, 79-85.
- Wang, S., Peng, Y., 2010. Natural zeolites as effective adsorbents in water and wastewater treatment. *Chem. Eng. J.* 156, 11-24.

- Wang, S.-y., Tang, Y.-k., Li, K., Mo, Y.-y., Li, H.-f., Gu, Z.-q., 2014. Combined performance of biochar sorption and magnetic separation processes for treatment of chromium-contained electroplating wastewater. *Bioresour. Technol.* 174, 67–73.
- Wang, S., Gao, B., Zimmerman, A.R., Li, Y., Ma, L., Harris, W.G., Migliaccio, K.W., 2015a. Removal of arsenic by magnetic biochar prepared from pinewood and natural hematite. *Bioresour. Technol.* 175, 391–395.
- Wang, Z., Liu, G., Zheng, H., Li, F., Ngo, H.H., Guo, W., Liu, C., Chen, L., Xing, B., 2015b. Investigating the mechanisms of biochar's removal of lead from solution. *Bioresour. Technol.*, 177, 308-317.
- Wang, S., Gao, B., Li, Y., Creamer, A.E., He, F., 2016a. Adsorptive removal of arsenate from aqueous solutions by biochar supported zero-valent iron nanocomposite: Batch and continuous flow tests. *J. Hazard. Mater.* 322, 172-181.
- Wang, S., Gao, B., Li, Y., Zimmerman, A.R., Cao, X., 2016b. Sorption of arsenic onto Ni/Fe layered double hydroxide (LDH)-biochar composites. *RSC Adv.* 6, 17792-17799.
- Wang, S., Gao, B., Li, Y., 2016c. Enhanced arsenic removal by biochar modified with nickel (Ni) and manganese (Mn) oxyhydroxides. *J. Ind. Eng. Chem.* 37, 361-365.
- Wang, S., Gao, B., Li, Y., Creamer, A.E., He, F., 2017. Adsorptive removal of arsenate from aqueous solutions by biochar supported zero-valent iron nanocomposite: Batch and continuous flow tests. *J. Hazard. Mater.* 322, 172-181.
- Wang, T., Li, C., Wang, C., Wang, H., 2018a. Biochar/MnAl-LDH composites for Cu (II) removal from aqueous solution. *Colloids Surf. A Physicochem. Eng. Asp.* 538, 443–450.
- Wang, C., Wang, H., 2018b. Pb(II) sorption from aqueous solution by novel biochar loaded with nano-particles. *Chemosphere* 192, 1–4.
- Watts, J.F., Wolstenholme, J., 2003. *An Introduction to Surface Analysis by XPS and AES*, John Wiley & Sons Ltd., The Atrium, Southern Gate, Chichester, West Sussex, UK.
- Webber, T.W., Chakkravorti, R.K., 1974. Pore and solid diffusion models for fixed-bed adsorbers, *AIChE J.* 20, 228–238.

- Weber, W.J., Morris, J.C., 1963. Kinetics of adsorption on carbon from solutions. *J. Sanitary Eng. Div. Am. Soc. Civ. Eng.* 89, 31–60.
- Wenzel, W.W., Kirchbaumer, N., Prohaska, T., Stingeder, G., Lombi, E., Adriano, D.C., 2001. Arsenic fractionation in soils using an improved sequential extraction procedure. *Anal. Chim. Acta* 436, 309–323.
- Wu, X., Yang, Q., Xu, D., Zhong, Y., Luo, K., Li, X., Chen, H., Zeng, G., 2013. Simultaneous adsorption/reduction of bromate by nanoscale zerovalent iron supported on modified activated carbon. *Ind. Eng. Chem. Res.* 52, 12574–12581.
- Xiao, Y., Sun, M., Zhang, L., Gao, X., Su, J., Zhu, H., 2015. The co-adsorption of Cu^{2+} and Zn^{2+} with adsorption sites surface-lattice reforming on calcined layered double hydroxides. *RSC Adv.* 5, 28369–28378.
- Xu, X., Cao, X., Zhao, L., 2013a. Comparison of rice husk- and dairy manure-derived biochars for simultaneously removing heavy metals from aqueous solutions: Role of mineral components in biochars. *Chemosphere* 92, 955–961.
- Xu, X., Cao, X., Zhao, L., Wang, H., Yu, H., Gao, B., 2013b. Removal of Cu, Zn, and Cd from aqueous solutions by the dairy manure-derived biochar. *Environ. Sci. Pollut. Res.* 20, 358–368.
- Xu, X., Kan, Y., Zhao, L., Cao X., 2016. Chemical transformation of CO_2 during its capture by waste biomass derived biochars. *Environ. Pollut.* 213, 533–540.
- Xue, L., Gao, B., Wan, Y., Fang, J., Wang, S., Li, Y., Muñoz-Carpena, R., Yang, L., 2016. High efficiency and selectivity of MgFe-LDH modified wheat-straw biochar in the removal of nitrate from aqueous solutions. *J. Taiwan Inst. Chem. Eng.* 63, 312–317.
- Yan, L. G., Yang, K., Shan, R. R., Yu, H. Q., Du, B., 2015a. Calcined ZnAl- and $\text{Fe}_3\text{O}_4/\text{ZnAl}$ -layered double hydroxides for efficient removal of Cr(VI) from aqueous solution. *RSC Adv.* 5, 96495–96503.
- Yan, J., Han, L., Gao, W., Xue, S., Chen, M., 2015b. Biochar supported nanoscale zerovalent iron composite used as persulfate activator for removing trichloroethylene. *Bioresour. Technol.* 175, 269–274.
- Yan, L., Song, J., Chan, T.-S., Jing, C., 2017. Insights into antimony adsorption on {001} TiO_2 : XAFS and DFT study. *Environ. Sci. Technol.* 51(11), 6335–6341.

Yang, W. S., Kim, Y., Liu, P. K. T., Sahimi, M., Tsotsis, T. T., 2002. A study by in situ techniques of the thermal evolution of the structure of a Mg–Al–CO₃ layered double hydroxide. *Chem. Eng. Sci.* 57, 2945-2953.

Yang, L., Shahrivari, Z., Liu, P. K. T., Sahimi, M., Tsotsis, T. T., 2005. Removal of Trace Levels of Arsenic and Selenium from Aqueous Solutions by Calcined and Uncalcined Layered Double Hydroxides (LDH). *Ind. Eng. Chem. Res.* 44(17), 6804-6815

Yang, Y., Wei, Z., Zhang, X., Chen, X., Yue, D., Yin, Q., Xiao, L., Yang, L., 2014. Biochar from *Alternanthera philoxeroides* could remove Pb(II) efficiently. *Bioresour. Technol.* 171, 227–232.

Yang, F., Sun, S., Chen, X., Chang, Y., Zha, F., Lei, Z., 2016. Mg-Al layered double hydroxides modified clay adsorbents for efficient removal of Pb²⁺, Cu²⁺ and Ni²⁺ from water. *Appl Clay Sci.* 123, 134-140.

Yoshida, M., Koilraj, P., Qiu, X., Hirajima, T., Sasaki, K., 2015. Sorption of arsenate on MgAl and MgFe layered double hydroxides derived from calcined dolomite. *Chem. Eng. J.* 3, 1614-1621.

Yoshitake, H., 2012. Functionalization of Periodic Mesoporous Silica and its Application to the Adsorption of Toxic Anions, In: Fryxell, G.E., Cao, G. (Eds.), *Environmental Applications of Nanomaterials*, Imperial College Press, 2nd Edition, London, UK, pp. 287-325

Yu, X. Y., Luo, T., Jia, Y., Xu, R. X., Gao, C., Zhang, Y. X., Liu, J. H., Huang, X. J., 2012. Three-dimensional hierarchical flower-like Mg–Al-layered double hydroxides: highly efficient adsorbents for As(V) and Cr(VI) removal. *Nanoscale* 4, 3466–3474.

Yue, X., Liu, W., Chen, Z., Lin, Z., 2016. Simultaneous removal of Cu(II) and Cr(VI) by Mg–Al–Cl layered double hydroxide and mechanism insight. *J. Environ. Sci.* 53, 16-26.

Zama, E.F., Zhu, Y.-G., Reid, B.J., Sun, G.-X., 2017. The role of biochar properties in influencing the sorption and desorption of Pb(II), Cd(II) and As(III) in aqueous solution. *J. Clean. Prod.* 148, 127–136.

Zhang, S.Q., Hou, W.G., 2007. Sorption removal of Pb(II) from solution by uncalcined and calcined MgAl-Layered double hydroxides. *Chin. J. Chem.* 25, 1455-1460.

Zhang, S., Li, X. Y., Chen, J. P., 2010. An XPS study for mechanisms of arsenate adsorption onto a magnetite-doped activated carbon fiber, *J. Colloid Interf. Sci.* 343, 232–238.

Zhang, J., Xu, Y., Li, W., Zhou, J., Zhao, J., Qian, G., Xu, Z. P., 2012a. Enhanced remediation of Cr(VI)-contaminated soil by incorporating a calcined-hydrotalcite-based permeable reactive barrier with electrokinetics. *J. Hazard. Mater.* 239-240, 128-134.

Zhang, J., Li, Y., Zhou, J., Chen, D., Qian, G., 2012b. Chromium (VI) and zinc (II) waste water co-treatment by forming layered double hydroxides: Mechanism discussion via two different processes and application in real plating water. *J. Hazard. Mater.* 205–206, 111–117.

Zhang, T., Li, Q., Xiao, H., Lu, H., Zhou, Y., 2012c. Synthesis of Li–Al Layered double hydroxides (LDHs) for efficient fluoride removal. *Ind. Eng. Chem. Res.* 51, 11490-11498.

Zhang, X., Wang, H., He, L., Lu K., Sarmah, A., Li, J., Bolan, N.S., Pei, J., Huang, H., 2013a. Using biochar for remediation of soils contaminated with heavy metals and organic pollutants. *Environ. Sci. Pollut. Res.* 20, 8472–8483.

Zhang, M., Gao, B., Varnoosfaderani, S., Hebard, A., Yao, Y., Inyang, M., 2013b. Preparation and characterization of a novel magnetic biochar for arsenic removal. *Bioresour. Technol.* 130, 457–462.

Zhang, M., Gao, B., Yao, Y., Inyang, M., 2013c. Phosphate removal ability of biochar/MgAl-LDH ultra-fine composites prepared by liquid-phase deposition. *Chemosphere* 92, 1042–1047.

Zhang, M., Gao, B., Fang, J., Creamer, A.E., Ullman, J.L., 2014. Self-assembly of needle-like layered double hydroxide (LDH) nanocrystals on hydrochar: characterization and phosphate removal ability. *RSC Adv.* 4, 28171–28175.

Zhang, T., Zhu, X., Shi, L., Li, J., Li, S., Lü, J., Li, Y., 2017a. Efficient removal of lead from solution by celery-derived biochars rich in alkaline minerals. *Bioresour. Technol.* 235, 185–192.

- Zhang, C., Shan, B., Tang, W., Zhu, Y., 2017b. Comparison of cadmium and lead sorption by *Phyllostachys pubescens* biochar produced under a low-oxygen pyrolysis atmosphere. *Bioresour Technol.* 238, 352–360.
- Zhao, D., Sheng, G., Hu, J., Chen, C., Wang, X., 2011. The adsorption of Pb(II) on Mg₂Al layered double hydroxide. *Chem. Eng. J.* 171, 167-174.
- Zhao, L., Li, X., Hao, C., Raston, C.L., 2012. SO₂ adsorption and transformation on calcined NiAl hydrotalcite-like compounds surfaces: An in situ FTIR and DFT study. *Appl. Catal. B-Environ.* 117-118, 339-345.
- Zheng, W., Guo, M., Chow, T., Bennett, D.N., Rajagopalan, N., 2010. Sorption properties of greenwaste biochar for two triazine pesticides. *J. Hazard. Mater.* 181, 121–126.
- Zhou, Y., Gao, B., Zimmerman, A.R., Fang, J., Sun, Y., Cao, X., 2013. Sorption of heavy metals on chitosan-modified biochars and its biological effects. *Chem. Eng. J.* 231, 512–518.
- Zhou, Y., Gao, B., Zimmerman, A.R., Chen, H., Zhang, M., Cao, X., 2014. Biochar-supported zerovalent iron for removal of various contaminants from aqueous solutions. *Bioresour. Technol.* 152, 538–542.
- Zhou, J., Shu, W., Gao, Y., Cao, Z., Zhang, J., Hou, H., Zhao, J., Chen, X., Pan, Y., Qian, G., 2017. Enhanced arsenite immobilization via ternary layered double hydroxides and application to paddy soil remediation, *RSC Adv.* 7, 20320-20326.
- Žák, T., Jirásková, Y., 2006. CONFIT: Mössbauer spectra fitting program. *Surf. Interf. Anal.* 38, 710–714.

**Curriculum vitae
&
List of publications**

Barbora Hudcová

Born: September 5, 1989, Prague (Czech Republic)

E-mail: hudcovab@fzp.czu.cz

Education

- 2014 – present: Czech University of Life Sciences Prague - Faculty of Environmental Sciences
Ph.D. Environmental Modeling
Ph.D. topic “The use of layered double hydroxides and mixed oxides for stabilization of metals and metalloids in contaminated soils”
- 2012 – 2014: University of Pardubice - Faculty of Chemical Technology
MSc. Technical Physical Chemistry
MSc. topic “Structure and activity analysis of Mg/Al and Zn/Al mixed oxides in aldolization and transesterification”
- 2009 – 2012: University of Pardubice - Faculty of Chemical Technology
BSc. Environment Protection Management
BSc. topic “Treatment of energy crops to value-added chemicals”

Fellowships

- Fulbright-Masaryk Visiting Scholar at University of Notre Dame, Indiana, USA (2018)

Awards

- Rector's Prize for Ph.D. Research and Publication (2018)
- Early Career Scientist's Travel Support at the General Assembly of the European

- Geosciences Union (2018)
- Travel award at the International Conference on the Biogeochemistry of Trace Elements conference (2017)
 - Prize of Technical University of Liberec at Innovative remediation technologies – research and experience (2015)
 - Prize of the Knauf Praha Company for excellent BSc. thesis (2012)

Publications

- Hudcová, B.**, Veselská, V., Filip, J., Číhalová, S., Komárek, M., 2017. Sorption mechanisms of arsenate on Mg-Fe layered double hydroxides: A combination of adsorption modeling and solid-state analysis. *Chemosphere* 168, 539-548.
- Hudcová, B.**, Veselská, V., Filip, J., Číhalová, S., Komárek, M., 2018. Highly effective Zn(II) and Pb(II) removal from aqueous solutions using Mg-Fe layered double hydroxides: Comprehensive adsorption modeling coupled with solid state analyses. *Journal of Cleaner Production* 171, 944-953.
- Hudcová, B.**, Vítková, M., Ouředníček, P., Komárek, M., 2019. Stability and stabilizing efficiency of Mg-Fe layered double hydroxides and mixed oxides in aqueous solutions and soils with elevated As(V), Pb(II) and Zn(II) contents. *Science of The Total Environment* 648, 1511-1519.
- Trakal, L., Vítková, M., **Hudcová, B.**, Beesley, L., Komárek, M., 2018. Biochar and its Composites for Metal (loid) Removal From Aqueous Solutions, In: Ok, Y., Tsang, D., Bolan, N., Novak J. (eds.), *Biochar from Biomass and Waste*, Elsevier, United Kingdom, pp. 113-141.

Submitted articles and manuscripts in preparation

- Hudcová, B.**, Erben, M., Vítková, M., Komárek, M., 2019. Antimonate (ad)sorption onto Mg-Fe layered double hydroxides in aqueous solutions at different pH values: Investigation of the mechanism supported by surface complexation modeling and solid-state analyses. Submitted to *Applied Surface Science*.

Grants and projects

- Co-worker on grant: Innovative use of nanoiron-modified biochar: advanced geochemical testing for metal(loid) stabilisation in soils
Project no. 18-24782Y (Czech Science Foundation)
- Co-worker on grant: Application of modified waste biomaterials for mine water remediation
Project no. TJ01000015 (2018-2019; Technology Agency of the Czech Republic)
- Principal investigator on grant: Synthesis and use of innovative adsorbents for stabilization of metals and metalloids in contaminated soils
CIGA no. 20154202 (2015-2016; Czech University of Life Sciences Prague)
- Principal investigator on grant: Simulation of Zn sorption processes in soil using geochemical modelling
IGA no. 4240013123159 (2015-2017; Internal Grant Agency of the Faculty of Environmental Sciences, Czech University of Life Sciences Prague)
- Co-investigator on grant: Development and production of innovative materials from waste products for stabilization of metals and metalloids: A comprehensive experimental and model approach
CIGA no. 20174204 (2017-2018; Czech University of Life Sciences Prague)
- Co-investigator on grant: Interactions of arbuscular mycorrhiza with nano zero-valent iron and their influence on metal(loid) behavior in plant - soil system
CIGA no. 20174205 (2017-2018; Czech University of Life Sciences Prague)

Teaching activities

- Environmental Soil Chemistry – Practical Course
- Field Practice for Environmental Geosciences
- Supervisor of 8 defended bachelor theses

• Voluntary activities

- Laboratory work with grammar school students in the frame of Science to Schools program
- Summer school for students